Per Instructions:
Following pages removed
3-80
3-81
3-82

R-600

CONTROL, GUIDANCE AND NAVIGATION FOR ADVANCED MANNED MISSIONS

(Final) Report on Task II of Contract NAS-9-6823)

VOL. IV INERTIAL SUBSYSTEMS (STRUCTURE MOUNTED STUDIES)

INSTRUMENTATION LABORATORY

MASSACHUSETTS INSTITUTE OF TECHNOLOGY

Cambridge 39, Mass.

R-600

CONTROL, GUIDANCE, AND NAVIGATION FOR ADVANCED MANNED MISSIONS

(Final Report on Task II of Contract NAS-9-6823)

VOL. IV INERTIAL SUBSYSTEMS

SEPTEMBER 1968

INSTRUMENTATION LABORATORY
MASSACHUSETTS INSTITUTE OF TECHNOLOGY
CAMBRIDGE, MASSACHUSETTS

Approved: _____ Date: 11 Sept. 1968
JAMES H. FLANDERS, DIRECTOR, ADVANCED CG&N
APOLLO GUIDANCE AND NAVIGATION PROGRAM

Approved: _____ Date: 11 Sep 68
DAVID G. HOAG, DIRECTOR
APOLLO GUIDANCE AND NAVIGATION PROGRAM

Approved: _____ Date: 13 Sept 68
RALPH R. RAGAN, DEPUTY DIRECTOR
INSTRUMENTATION LABORATORY

ACKNOWLEDGEMENT

This report was prepared under DSR Project 55-29430, sponsored by the Manned Spacecraft Center of the National Aeronautics and Space Administration through Contract NAS 9-6823 with the Instrumentation Laboratory at Massachusetts Institute of Technology in Cambridge, Massachusetts.

The publication of this report does not constitute approval by the National Aeronautics and Space Administration of the findings or the conclusions contained therein. It is published only for the exchange and stimulation of ideas.

This volume is the combined effort of the following authors, with their section of interest indicated in parentheses after each name.

Chapter 1

A.J. Boyce (1.3)
J.H. Flanders (1.2)
Dr. D.C. Fraser (1.2)
J.P. Gilmore (1.1 - 1.5)
F.D. Grant (1.2)

Chapter 2

G.J. Bukow (2.4)
W.S. Ewing (2.3.4 & 2.3.6)
J.P. Gilmore (2.1, 2.3 - 2.5)
J.R. Keenan (2.5)
C.B. Lory (2.3.5 & 2.6)
R.A. McKern (2.2)

Chapter 3*

G.J. Bukow (3.4)
J. Feldman (3.3)
J.P. Gilmore (3.1 - 3.4)

*Data and test result contributions to this chapter were provided by: R. Dauwalter, E.J. Hall, P. R. Kerrigan, H. McArdle, and B. Rowe

Chapter 4

A.H. Arpiarian (4.3.4)
J.H. Barker (4.5.3 - 4.5.6)
D.G. Brown (4.4)
J.P. Gilmore (4.1 - 4.6)
J.R. Keenan (4.4)
R.A. McKern (4.6)
G.L. Trousil (4.5.6)
J.M. Watson (4.6)

Chapter 5

J. P. Gilmore

Appendix

J.P. Gilmore (A)
G.J. Bukow (B)

R-600

CONTROL, GUIDANCE AND NAVIGATION FOR ADVANCED MANNED MISSIONS

(Final Report on Task II of Contract NAS-9-6823)

ABSTRACT

This is a study of Navigation, Guidance, and Control for Advanced Manned Space Missions, It is divided into the areas of systems, computer subsystems, radiation subsystems, and inertial subsystems. From a system aspect a study is made of guidance and navigation requirements imposed by the different phases of interplanetary missions. A representative system is described as a design model. Detailed descriptions are provided of analytical and development work on advanced concepts in computer, radiation, and structure-mounted inertial subsystems.

It is shown that required system performance advances are will within reason but that the requirements for reliability will demand new standards in design concepts, quality assurance, maintainability, and quiescent failure rates.

Guidelines for further developments in this direction are set forth.

January 1968

PRECEDING PAGE BLANK NOT FILMED.

TABLE OF CONTENTS

Section			Page
1.	SYSTEM AND INSTRUMENT MECHANIZATION CONCEPTS		1-1
	1.1	Introduction	1-1
	1.2	Performance Model	1-4
	1.3	Multisensor Configuration	1-20
	1.4	Modular Instrument Configuration	1-38
	1.5	Strapdown System-Spacecraft Testing	1-43
2.	ATTITUDE ALOGRITHM AND INSTRUMENT MODEL DEVELOPMENT		2-1
	2.1	Introduction	2-1
	2.2	Transformation Alogrithm Study	2-3
	2.3	Single-Degree-of-Freedom Gyro Dynamics	2-16
		2.3.1 General Equations	2-16
		2.3.2 Simplified SDF Gyro Equation of Motion	2-19
		2.3.3 Output Axis Equations	2-21
		2.3.4 Error Sources	2-23
		2.3.5 Output Axis Coupling	2-29
		2.3.6 Numerical Error Analysis	2-31
	2.4	Pendulous Accelerometer Dynamics in a Rotating Frame	2-39
	2.5	Gyro Pulse-Torque Model and Simulation	2-44
	2.6	Improvements in Pulse-Rebalanced Instruments	2-54
3.	INERTIAL COMPONENT EVALUATIONS 18 IRIG MOD B AND 16 PM PIP		3-1
	3.1	Introduction	3-1
	3.2	Evaluation Summary and Recommendations	3-2
	3.3	18 Integrating Inertial Gyro MOD B (IRIG MOD B)	3-6
		3.3.1 Introduction	3-6
		3.3.2 Physical Description	3-6
		3.3.3 Principles of Operation	3-8

TABLE OF CONTENTS, (Cont.)

Section			Page
	3.3.4	Dynamic Errors	3-14
	3.3.5	Torque Generator	3-18
	3.3.6	Signal-Generator Noise	3-41
	3.3.7	Gas-Bearing Design Consideration	3-44
	3.3.8	Gas-Bearing Reliability	3-49
	3.3.9	Other Design Improvement Activity	3-52
	3.3.10	Gyro-Evaluation Testing	3-52
3.4	16 Permanent-Magnet-Pulsed-Integrating Pendulous Accelerometer (16 PM PIP)		3-79
	3.4.1	Introduction	3-79
	3.4.2	Physical Description	3-79
	3.4.3	Theory of Operation	3-84
	3.4.4	Test Program	3-87
	3.4.5	Test Setup	3-88
	3.4.6	Scale Factor and Bias Stability	3-94
	3.4.7	Moding and Double-Pulsing	3-102
	3.4.8	Frequency of Interrogation	3-104
	3.4.9	Sensitivity Testing	3-108
4.	BODY MOUNTED TEST PACKAGE AND REAL-TIME ALOGRITHM TEST AND EVALUATION		4-1
	4.1	Introduction	4-1
	4.2	Summary	4-2
	4.3	Test Package and Supporting Hardware	4-6
	4.4	Real-Time - Alogrithm Computational Capabilities	4-29
	4.5	Pulse Torque Control Loop and Power Supply Support Electronics	4-45
	4.6	Test Program and Concepts	4-63
	4.7	Ground Support Equipment	4-81
5.	SUMMARY AND CONCLUSIONS		5-1
	5.1	System Mechanization and Performance Model	5-1
	5.2	Instrument Model and Algorithm Development	5-2
	5.3	Instrument Evaluations	5-3
	5.4	Body-Mounted Test Package and Real-Time Algorithm Test Evaluation	5-4
Appendix			
A	Quaternions		A-1
B	Effects of Double Pulsing on Count Stability		B-1

LIST OF ILLUSTRATIONS

Figure		Page
1.2-1	Transplanetary injection error model	1-7
1.2-2	Entry profile	1-12
1.2-3	Roll attitude vs time - entry phase	1-13
1.3-1	Instrument input axes orientation relative to the instrument frame triad and the dodecahedron	1-22
1.3-2	Hexad-array strap-down system implementation	1-32
1.3-3	Hexad-array strap-down configuration package	1-34
1.3-4	Component alignment with spin axes normal to z axis	1-36
1.3-5	Reliability plots, self-contained failure isolation	1-37
1.4-1	Gyro module	1-39
1.4-2	Gyro module thermal strap-in mount	1-40
1.5-1	Schematic, conceptual model combined radiation and inertial sensor assembly	1-45
1.5-2	Design layout of combined radiation and inertial sensor assembly	1-46
2.2-1	Normalized coning response	2-9
2.2-2	Coning performance response	2-10
2.2-3	Alogrithm coning drift vs coning frequency	2-14
2.3-1	Line schematic diagram of single-degree-of-freedom floated integrating gyro unit	2-17
2.3-2	Sensitivity to output-axis sinusoid	2-33
2.5-1A	Simplified ternary torquing loop	2-46
2.5-1B	Gyro float as torque summing device	2-46
2.5-2	MAC coding for integration loop	2-47
2.5-3	Gyroscope loop simulator program	2-49
2.5-4	Normalized gyro response to a single torque pulse command	2-50
2.5-5	"Moding" for constant rate input	2-52
2.5-6	"Moding" for constant rate input	2-53
2.6-1	Idealized pulse-rebalance loop	2-56
2.6-2	Idealized system equivalent to Fig. 2.6-1	2-56
2.6-3	Idealized system with one-half clock period prediction added	2-57
2.6-4	Linearized, single-axis model of a pulse-rebalanced gyroscope	2-58

LIST OF ILLUSTRATIONS, (Cont.)

Figure		Page
2.6-5	Pulse-rebalanced gyroscope model with separate rebalance branch	2-59
2.6-6	Comparison of ideal and actual systems	2-60
2.6-7	Response of uncompensated system to initial condition $\Delta = 5\Delta\theta$	2-63
2.6-8	Response of compensated system to initial condition $\Delta = 5\Delta\theta$	2-64
2.6-9	Response of uncompensated system to ramp to one-half maximum rate	2-65
2.6-10	Response of compensated system to ramp to one-half maximum response	2-66
3.3-1	18 IRIG MOD B cutaway view	3-7
3.3-2	A single-degree-of-freedom gyro operating in a single-axis inertially stabilized test control loop	3-15
3.3-3	Servo mode gyro drift test positions	3-16
3.3-4	Perspective view of s ngle pole section of permanent magnet torquer	3-19
3.3-5	Block diagram-18 IRIG closed loop	3-20
3.3-6	Torquer coil reaction effect for 2 pole PM torque generator	3-23
3.3-7	Magnet assembly-8 PMT 1.730-1B	3-25
3.3-8	Air gap flux density vs magnet pole angle	3-27
3.3-9	TG scale factor sensitivity vs float angle	3-28
3.3-10	Scale factor-radial sensitivity	3-29
3.3-11	Bias stability across PM magnetization 18 IRIG MOD B #411	3-30
3.3-12	Torque vs angle, stop bias reaction torque variation with float angle	3-32
3.3-13	Resistance vs frequency 8 PMT 1.73-2A (18 IRIG MOD B)	3-34
3.3-14	Normalized frequency sensitivity-titanium coil holder	3-35
3.3-15	Normalized frequency sensitivity-plastic vs beryllium coil holder	3-36
3.3-16	Reaction torque vs angle and frequency	3-37
3.3-17	Reaction torque vs angle and frequency	3-38
3.3-18	Signal generator magnetic modulation	3-43
3.3-19	18 IRIG MOD B gas bearing wheel assembly	3-45
3.3-20	18 IRIG MOD B slew rate tests, case B, design parameters	3-46
3.3-21	18 IRIG MOD B, effect of clearance on ΔK (helium atmosphere)	3-47

LIST OF ILLUSTRATIONS, (Cont.)

Figure		Page
3.3-22	Effect of clearance on slew rate capability (helium atmosphere)	3-48
3.3-23	Wheelspeed & SG frequency vs wheel voltage changes	3-51
3.3-24	Stop bias hysteresis, 18 IRIG MOD B #411	3-55
3.3-25	Servo performance tests, six day period	3-56
3.3-26	Table rate deviation, 2 consecutive 36 hr IA vertical servo runs (unit #411, 7/10/67)	3-57
3.3-27	Gyro test area	3-59
3.3-28	Unit 0411, 18 MOD B	3-60
3.3-29	Unit 0411, 18 MOD B, scale factor vs float angle	3-62
3.3-30	Unit 0411, 18 MOD B, scale factor vs temperature	3-63
3.3-31	Unit 0411, 18 MOD B, scale factor vs radial displacement	3-64
3.3-32	Unit 0411, 18 MOD B, sacle factor vs axial displacement	3-65
3.3-33	Ternary pulse torque switching	3-66
3.3-34	Gyro in pulse torquing electronic test setup	3-69
3.3-35	SG output vs time	3-72
3.3-36	Pulse torque SF stability, 18 IRIG MOD B #411	3-75
3.3-37	Pulse torque SF stability, 18 IRIG MOD B #411	3-76
3.3-38	Scale factor linearity, unit 411	3-77
3.3-39	Scale factor linearity, unit 411	3-78
3.4-1	Cutaway view of 16 PM PIP	3-80
3.4-2	Line schematic of the 16 PM PIP	3-81
3.4-3	Block diagram 16 PM PIP closed loop	3-85
3.4-4	Ternary pulse torque switching	3-89
3.4-5	Block diagram - PIP, pulse torque electronics and test equipment	3-91
3.4-6	PM PIP laboratory area	3-92
3.4-7	Close-up of PM PIP and test fixture	3-93
3.4-8	PIP scale factor stability vs time	3-95
3.4-9	PIP average scale factor stability vs time	3-96
3.4-10	Bias stability vs time, PM PIP #9 (9600 pps interrogation rate	3-97
3.4-11	Bias measurements - input axis orientations	3-103
3.4-12	Double pulsing	3-105
3.4-13	Stability run, PM PIP #14, 9600 Hz, September 1967	3-107
3.4-14	Bias variations vs test sequence PM PIP #9, July 1967	3-109
4.2-1	Body-mounted real time test facility	4-3

LIST OF ILLUSTRATIONS, (Cont.)

Figure		Page
4.2-2	Body-mounted real time test facility.	4-4
4.3-1	Gyro test package, Y and Z gyro view	4-7
4.3-2	Gyro test package, X and Z gyro view	4-8
4.3-3	4-axis test table	4-9
4.3-4	Gyro test package mounted to 16" table via alignment plate.	4-10
4.3-5	Frame prior to final machining	4-12
4.3-6	Gyro mounting flat misalignment angles wrt reference cure . .	4-13
4.3-7	Gyro alignment fixture, front view	4-14
4.3-8	18 IRIG MOD B gyro in alignment fixture with integral normalizing electronics (SG end view)	4-16
4.3-9	18 IRIG MOD B gyro in alignment fixture with integral normalizing electronics (TG end view)	4-17
4.3-10	Gyro frame mounted proportional temperature controller . . .	4-18
4.3-11	Variable thermal resistance	4-20
4.3-12	Frame variable coolant controller (front view)	4-21
4.3-13	Frame variable coolant controller (rear view)	4-22
4.3-14	Schematic pictorial of strapdown system (freehand perspective)	4-24
4.3-15	Completely assembled test package on 16" table	4-25
4.3-16	Cut-away view gyro-package development test configuration . .	4-26
4.3-17	Test facility - optical alignment references	4-27
4.3-18	System reference cube alignment using Kern DKM-3 theodolite (autocollimation).	4-28
4.4-1	Test computer	4-30
4.4-2	Computer with interface modification	4-39
4.4-3	Memory drawer with interface hardware outlined	4-40
4.4-4	Functional - block diagram gyro counter interface	4-41
4.4-5	Typical input/output instruction I/O control signal timing (typical)	4-42
4.4-6	Timing chart for gyro counter interface equipment	4-44
4.5-1	Support electronics console	4-46
4.5-2	Ducosyn 9600 cps power supply	4-48
4.5-3	± 15v supply	4-49
4.5-4	Three-axis pulse torque control drawer	4-52
4.5-5	Block diagram - ternary pulse torque electronics.	4-53
4.5-6	Interrogator logic and timing	4-55

LIST OF ILLUSTRATIONS, (Cont.)

Figure		Page
4.5-7	Current switch	4-56
4.5-8	DC current loop	4-58
4.5-9	Block diagram - PM pulse torque electronics	4-59
4.6-1	Orientation for determining θ_{OA}	4-67
4.6-2	Orientation for determining θ_{SA}	4-69
4.6-3	Calibration positions for determining the gyro drift terms; NBD, ADOA, ADSRA, and ADIA	4-71
4.6-4	Test package gyro axes orientation	4-78
4.6-5	Coning of the Z-gyro IA due to synchronized oscillations about X and Y	4-79
4.7-1	Front panel layout of modified optics inertial analyzer	4-82
4.7-2	Front panel layout of modified computer test set	4-83
4.7-3	Clock and scaler	4-84
4.7-4	Multiplex control drawer	4-86
4.7-5	Mode control, mech. diagram	4-87
4.7-6	DUM scan control	4-88
4.7-7	Data acquisition mechanization	4-90
4.7-8	Signal and control harness interface and block diagram - GSE for AGC and N System	4-91

1. SYSTEM AND INSTRUMENT MECHANIZATION CONCEPTS

1.1 Introduction

In accordance with the work statement objectives, the development effort described in this report is oriented towards consideration of a body-mounted, strapdown, inertial subsystem for Advanced Manned Missions. It is appropriate at the beginning of this report to review the factors which led to the emphasis placed on the strapdown configuration of inertial subsystems for this type of application. Accordingly, the following paragraphs are devoted to this subject.

Characteristically, the strapdown and the familar Apollo inertial-platform mechanization differ primarily in the implementation of an inertial reference frame for accumulating specific-force measurements.

In the inertial-platform gimbal mechanization the gyros are used in gimbal-drive nulling loops. The gimbal drives operate in response to the gyro outputs, appropriately resolved, to null all angular motion of the stable member, i.e., to space stabilize the instrument package from vehicle motion ; and thus the stable member is a direct physical representation of the inertial reference frame. The corresponding advantage of a relatively passive instrument environment, in which the the accelerometer information is physically resolved into the desired inertial-coordinate frame, is apparent.

In contrast, in the strapdown system the sensor package is mounted directly to the vehicle. Sensor measurements represent specific force and angular rates in the vehicle coordinate frame. Thus, the instruments encounter the full dynamic environment. Further, in order to maintain the inertial reference frame an analytical computational algorithm must be implemented that numerically processes the gyro outputs. The accelerometer data may then be resolved into the inertial-frame coordinate system and processed by guidance algorithms in the digital computer.

Apart from academic interest, the motivations for the successful attainment of a strapdown inertial-guidance mechanization stems from some of its inherent potential advantages. Perhaps the majority of these advantages result from the elimination of the mechanical complexities of the gimbal-system structure. Minimum configuration constraints result and efficient packaging is possible. Thus, for an equivalent sensor package significant size, weight and power reductions appear to be attainable. Further, the elimination of the rigid physical gimbal restraints allows packaging concepts to be formulated that facilitate system maintenance and in-flight repair.

Improved reliability is also generally cited as a major advantage of the strapdown mechanization. The increased complexity of the strapdown inertial-sensor torque-rebalance loop is easily offset by the elimination of the gimbal mechanical complexities and its associated angle readouts, servo drives, slip rings, etc. The reliability considerations associated with the impact of the additional attitude algorithm computational load is debatable. It is considered, however, that the reliability index of a guidance and control system computer conceived to function with a strapdown sensor package does not differ significantly from that of one mechanized to operate with an inertial platform. In addition to reliability increases resulting from component count and relative design complexities is the strapdown mechanization's ease of adaptability to redundancy reliability techniques.

An inherent strapdown implementation operational advantage is the direct output of wide-band body-rate data. This is a desirable feature for autopilot control functions especially if the vehicle evidences significant body-bending modes. In addition, relative to the three-gimbal stable-platform mechanization, the strapdown computational algorithm is free of gimbal-lock operational restrictions.

Clearly, for advanced manned space missions, the strapdown inertial-configuration potential advantages are significant. Long-duration flights strain state-of-the-art reliability and would be enhanced by in-flight repair capabilities. Similarly, payload restrictions necessitate economic allocation of weight, size, and power. Thus, this Advanced Manned Mission inertial-system study and development effort has pursued the following basic objectives:

1. The formulation of concepts that would achieve an optimal harvest of the strapdown mechanization's advantages.
2. The in-depth evaluation of the performance capabilities and limitation of the strapdown inertial configuration.

Consistent with these objectives the tasks outlined below were formulated to encompass conceptual system definition and theoretical investigation balanced by state-of-the-art sensor, sensor package, and algorithm test and evaluations.

Inertial System Task Outline

I	System and Instrument Mechanization Concepts
II	Algorithm and Instrument Model Development
III	State-of-the-Art Instrument Development and Evaluation
IV	Body-Mounted Test Package and Realtime Algorithm Test and Evaluation

This report presents the status of activity after ten months' effort on each of these subtasks and, as such, it is interim in nature. Although many individual goals have been achieved and are described, continued support to assume the fulfillment of the overall objectives is merited.

The remainder of this chapter presents various aspects of strapdown system mechanization concepts. They include: an instrument and system performance model based upon limited mission studies and instrument and control loop performance that appears to be realizable, a multisensor configuration for ultra-reliability with self-contained failure detection and isolation concepts, and a modular instrument concept that is consistent with in-flight repair objectives.

The remaining chapters of this volume cover:

Chapter 2 - A review of algorithm and instrument model development studies.

Chapter 3 - A review of 18 IRIG and 16 PM PIP inertial component development and test evaluations.

Chapter 4 - A review of the status and capabilities of the real-time strapdown system test and evaluation activities (including the body mounted package, electronics, and test facility descriptions).

1.2 / Performance Model

1.2.1 Introduction

The nature of the inertial system mechanization is intimately keyed to the gross mission definition, spacecraft propulsion system, and the intended mission functions of the inertial equipment, i.e., control, guidance, and navigation. Within the frameworks of Advanced Manned Missions it is reasonable to project certain basic constraints that allow a realistic conceptual formulation.

The primary objective of Advanced Manned Missions studies is the realization of interplanetary space exploration. Applications overlap into post-Apollo-type earth orbital operation and lunar exploration is also probable. Manned mission trajectory studies considering Mars, Venus, and Dual plane flybys, Mars orbital and landing operations in the years 1975-90 have been conducted.[1, 2] The North American Rockwell study configures itself about current Saturn booster and Apollo spacecraft technology while Boeing considers use of the Nerva II nuclear engine. Although radically different in engine design, a common fundamental feature represents a basis for uniform inertial subsystem design concepts. Both are impulsive propulsion engines; thus the guidance operation and spacecraft steering and control is of brief duration compared to extended free-fall coast periods.

Examination of the midcourse velocity corrections called for by the navigation and guidance algorithm used in the requirements study (see Vol. I) showed that only 5 to 10 velocity corrections were required with increments on the order of tens of feet per second. Guidance errors were reviewed for these midcourse corrections but only the tail-off uncertainty in the propulsion system seemed critical. Accordingly, attention was turned to the transplanetary injection and earth entry phases.

The transplanetary phase described by Boeing was selected because of duration of the burn, 2303 sec with a velocity change of 19, 149 ft/sec. The entry phase appeared to represent the most severe dynamic environment imposing loads of up to 10 g and manuever rates of up to 0.37 rad/sec.

For both studies a "best guess" instrument and inertial system parameter estimate was projected for the mid-1970 time frame. Error models were formulated for each mission phase. The study results then developed position and velocity error sensitivities for each inertial system error model parameter. The error analysis work was performed under the systems task reported on in Volume I, Chapter 1 of R-600. The following paragraphs describe the error models and review the error analysis findings.

1.2.2 Transplanetary Injection

A) General

A statistical error analysis of the injection into an interplanetary path from an earth orbit was performed in order to define the demands upon the inertial subsystem during this phase of operation. No externally derived information was used during the burn.

The reference trajectory was generated in each case using the required velocity concept together with a cross-product steering law[3, 4]. This was implemented with a modified version of a computer program which was originally written for the Apollo translunar injection by Phillíou[5]. The required velocity is defined as that velocity which will cause the vehicle to arrive at a specified time at a preselected inertial target and is computed as a solution to a Lambert problem.

No effort was made in this study to optimize either the guidance or targeting schemes. The criterion for an acceptable scheme was that the sensitivity of position and velocity errors to individual inertial component errors should not exhibit first-order influences by minor changes in the reference trajectory. All data necessary to characterize the vehicle and engine was extracted from references 1 and 2.

The strapdown inertial measurement unit was assumed to be installed such that the X input axis aligned with space vehicle X or roll axis. The instrument package configuration assumed was an orthogonal triad of three single-degree-of-freedom gyroscopes and accelerometers. Each instrument operated in a torque-to-balance control loop with quantized output that represents an incremental measurement of velocity or a rotational angle. The Y and Z gyros are mounted with their output axes along the vehicle X axis. For this alignment a suitable body-fixed system error model was developed and included in the statistical error analysis for the referenced trajectory.

B) Simplified Error Model

For the purposes of describing the problem, one accelerometer is assumed to be aligned with the desired velocity vector V_I and it controls the propulsion system cut-off on the basis of its velocity-gained measurement. Similarly, the two orthogonal accelerometers are nulling out velocity build-up on their axes by the steering law. (It is not necessary in the actual system to assign specific accelerometers and align the strapdown package so that X is collinear with the velocity vector. It is convenient for this simplified model. One

may, however, visualize hypothetical accelerometers in the software which are so assigned that they are subject to some performance and alignment errors.)

For the particular alignment concept we may express our error in terms of the orientation error (E) of an actual (V_A) velocity measurement relative to the desired velocity (V_I). A velocity error (V_E) may also be defined that corresponds to the scalar difference in magnitudes of the desired and actual velocity.

$$V_E = V_A \cos E - V_I \qquad (1.2.1)$$

The angular error (E) may be defined in terms of several sources and is formulated on an RMS basis (expressed in degrees).

$$E = \sqrt{E_{opt}^2 + E_{mech}^2 + E_{drift}^2 + E_{CA}^2} \qquad (1.2.2)$$

where

E_{opt} = the angular error introduced when the body frame and strapdown inertial frame were initialized in the computer using optical techniques

E_{mech} = angular error corresponding to the mechanical misalignment of the accelerometer on the body-mounted frame

E_{drift} = angular error in the inertial frame resulting from gyro drift terms, non-sensitive bias, and acceleration sensitive bias

E_{CA} = angular error due to bias output of the orthogonal accelerometer Y and Z, i.e., the vehicle steers to null their outputs

Figure 1.2-1 illustrates a worst-case orientation error build-up for a two-axis representation.

To determine the velocity error as defined in (1.2.1), we consider the relationship between the measured velocity (V_M) indicated by the X accelerometer and the actual velocity change along this axis.

$$V_M = \pm A_{bx} t_f + V_A(1 \pm U_{SFX}) \qquad (1.2.3)$$

where

A_{bx} = the bias uncertainty of the X accelerometer

t_f = the burn time

V_A = the magnitude of the actual velocity input along the X axis

U_{SFX} = the X accelerometer scale factor uncertainty expressed as a fraction of the calibrated scale factor.

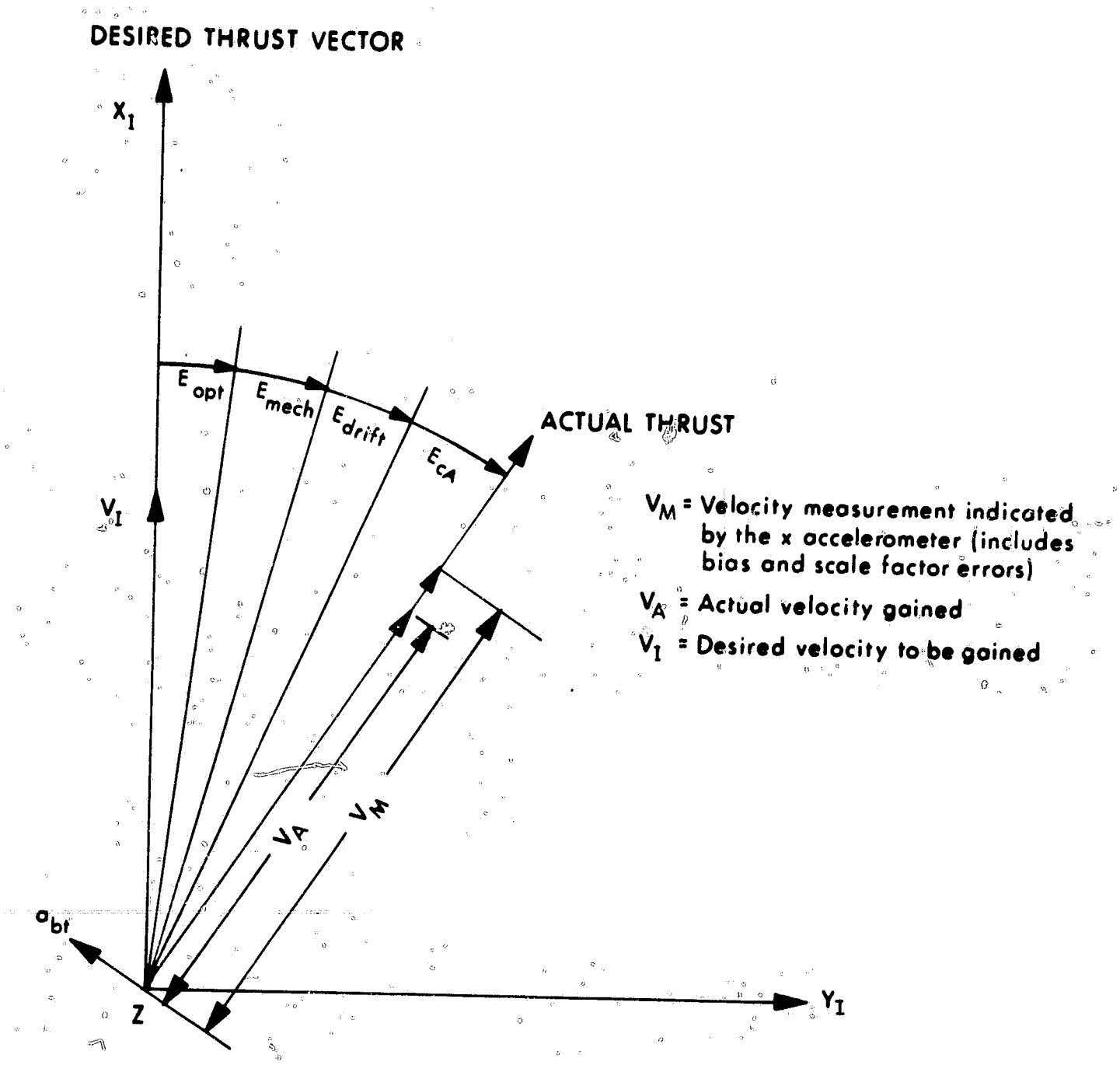

Fig. 1.2-1 Transplanetary injection error model.

The actual velocity measured by the X instrument corresponds to:

$$V_A = \frac{V_I \pm A_{bx} t_f}{1 \pm U_{SFX}} \qquad (1.2.4)$$

Note that the engine cutoff was assumed to occur when the measured velocity equaled the desired velocity. By substituting (1.2.4) into (1.2.1) we can define the scalar velocity error in terms of the desired velocity magnitude, the burn-time instrument uncertainties, and the vector orientation error.

Representative nominal and high-low limits for orientation errors due to the initialization and accelerometer mechanical misalignment uncertainties were defined and are listed in Table 1.2-1B. The drift orientation error results from the bias and acceleration sensitive terms of the cross axis gyros. For the figure shown, the drift corresponds only to the influence of the Z gyro on the orientation of X accelerometer reference frame. The actual E_{drift} used corresponds to the RMS of the Z and Y gyro influence; their individual terms were assumed equal.

$$E_{drift} = \frac{\sqrt{2}\, W_{IE} \times 10^{-3}}{3600} \left[\pm \mathrm{NBD}\,(t_p + t_f) + (\mathrm{ADOA}) \int_o^{t_f} F\, dt \right]$$

where

NBD = nonsensitive bias drift uncertainty expressed in meru units, i.e.: earth rate, $W_{IE} \times 10^{-3}$

ADOA = acceleration sensitivity drift uncertainty of Y or Z gyro due to specific force along its output axis, i.e., the Y and Z gyros were assumed aligned with their output axes along X

F = the specific force seen by the gyros; vehicle thrust along X

t_p = the total time in seconds between initialization and the beginning of engine burn

t_f = the engine on time

$\frac{W_{IE} \times 10^{-3}}{3600}$ = conversion constant (meru to degrees/sec);

The rms velocity vector misalignment resulting from the influence of Y and Z axis accelerometers on the steer law (equal bias levels is assumed for all instruments) is:

$$E_{CA_z} = E_{CA_y} = \tan^{-1}\left(\pm \frac{A_b t_f}{V_A} \right) \qquad (1.2.5)$$

These equations were mechanized in a statistical trajectory error analysis program. Computational algorithm error modeling was not included in these runs due to lack of specific dynamic rate (vibration, etc.) environment information.

The Boeing vehicle and trajectory were characterized by:

TABLE 1.2-1A
VEHICLE PARAMETERS

Exhaust Velocity	=	27,400 feet per second
Thrust	=	600,000 pounds
Initial Weight	=	2,313,760 pounds
Mass Flow Rate	=	705 pounds per second

The total velocity change was 19,149 ft/sec and the burn time was 2,302 sec. A one-hour prealignment time, t_p, was assumed.

The nominal instrument and subsystem parameters with the extremes that were used in the study were:

TABLE 1.2-1B
SYSTEM PARAMETERS

Parameter	High	Nominal	Low
E_{OPT}(secs)	90	60	30
E_{mech}(secs)	30	20	10
NBD (meru)	5.0	1.5	0.5
ADOA (meru/g)	1.5	1.0	0.3
a_b (cm/sec^2)	0.20	0.10	0.05
U_{SFX} (PPM)	150	50	20

The position and velocity errors resulting from any given parameter variation were essentially linear. Table 1.2-1C presents the slopes of these linear functions at the end of the burn for each of the above error sources. (A more complete discussion of the trajectory analysis program and statistical error modeling is presented in Vol I.)

As might be anticipated the most significant instrument error sensitivity corresponds to accelerometer bias. Reference frame orientation drift during the one hour prealignment was the next largest error source. The error sensitivity resulting from velocity algorithm computational round-off with a 30-bit word length and 10g scaling is approximately 0.5 mile for as many as 1000 updates per second.

TABLE 1.2-1C

SENSITIVITY COEFFICIENTS AT 2302 SECONDS

Source	Position Error Sensitivity	Velocity Error Sensitivity
Accelerometer Bias	31 miles/cm/sec^2	147 fps/cm/sec^2
Accelerometer Scale Factor Error	0.0089 mile /ppm	0.045 fps/ppm
NBD	0.41 mile /meru	3.8 fps/meru
NBD with 1 hour prealign time	1.94 miles/meru	14.2 fps/meru
ADOA	0.14 mile /meru/g	1.38 fps/meru/g
Initial Misalignment or Mechanical Misalignment	0.035 mile /arc-second	0.22 fps/arc-second

1.2.3 Mars-Earth Entry

Error sensitivity studies were also conducted for a Mars-Earth entry trajectory. Although the mission studies were limited, it does appear that the entry phase represents the most stringent dynamic environment on the accelerometers and gyroscopes.

The reference trajectory was generated using an entry steering scheme which is essentially the same as that used for Apollo Earth atmospheric entry[6]. The only modification is that the constant drag phase was modified to decrease the g-loading by decreasing drag with velocity. This analysis is based, therefore, on the assumption that an Apollo-type earth entry module would be used and is sized to allow the heat shield to cope with return velocities of up to 55,000 ft/sec. The maximum acceleration was between 9 and 10 g's for approximately 60 sec. The entry was initiated at 400,000 feet and terminates at 24,000 ft (chute deployment). Its duration was 13.5 minutes. The nominal reference trajectory and vehicle characteristics that were used in this analysis were:

Initial Velocity	=	50,000 feet per second
Entry Angle (γ)	=	-7 degrees
Lift to Drag Ratio (L/D)	=	0.5
Range	=	2,500 nautical miles

The acceleration versus velocity profile is shown in Fig. 1.2-2. This profile differs from Fig. 1.2-26, Vol. 1, since the initial left vector was assumed down. The roll maneuver time history for the entry trajectory is shown in Fig. 1.2-3.

The strapdown package, a triad instrument configuration, was assumed to be mounted such that its X-axis was aligned parallel to the drag vector (minus relative velocity) and Z was along the lift vector. This configuration was selected for convenience since the primary control spacecraft maneuvers were about the relative velocity vector, $\overline{V}$. Thus, the major rate maneuvers occurred along one reference triad axis (a maximum roll rate of 0.37 radian/sec).

The analysis program accounts for the strapdown implementation by using the instrument errors in body coordinates and transforming them into an inertial frame. The effective inertial acceleration error is then processed by successive integrations to yield corresponding trajectory position

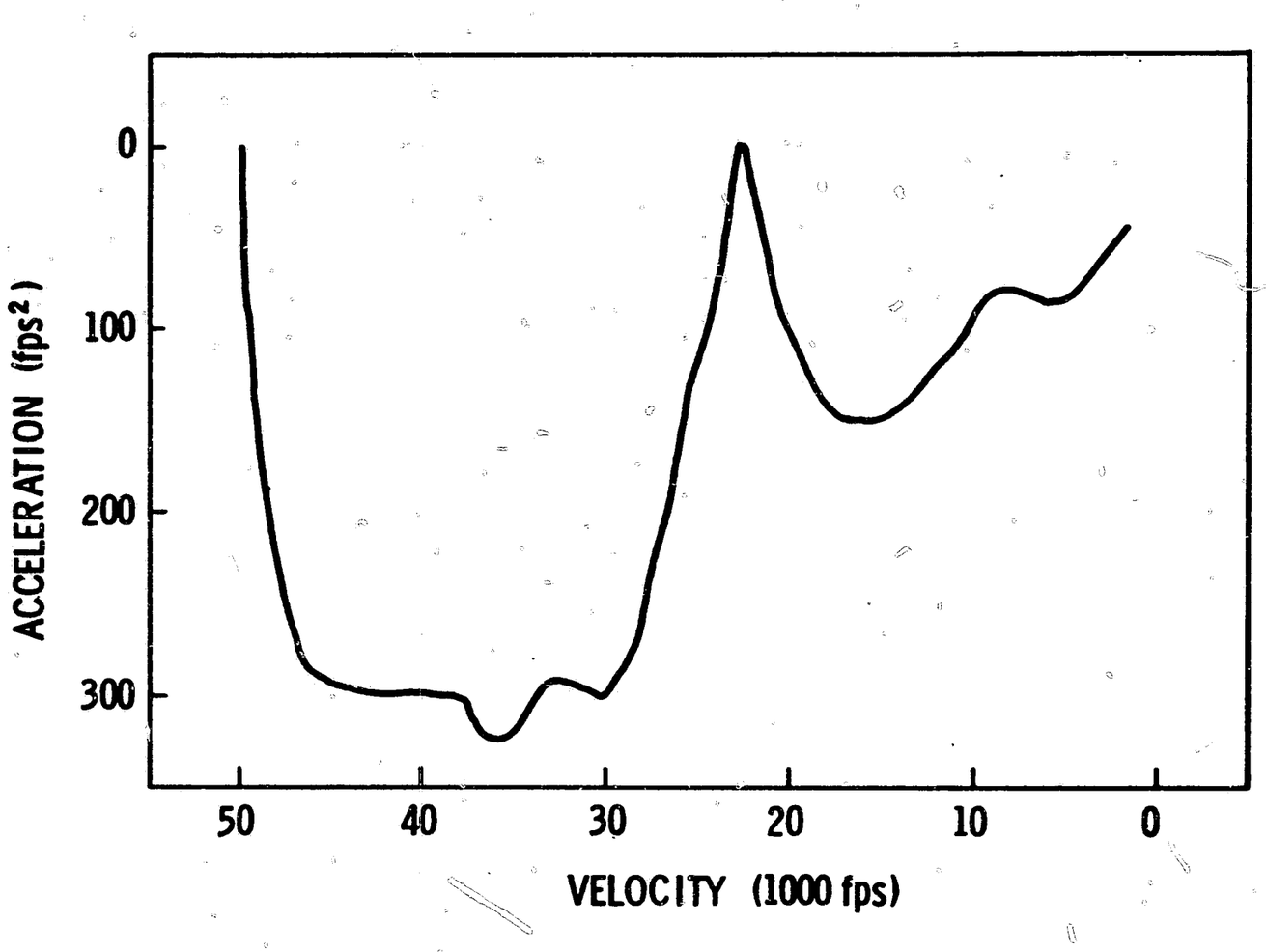

Fig. 1.2-2 Entry profile.

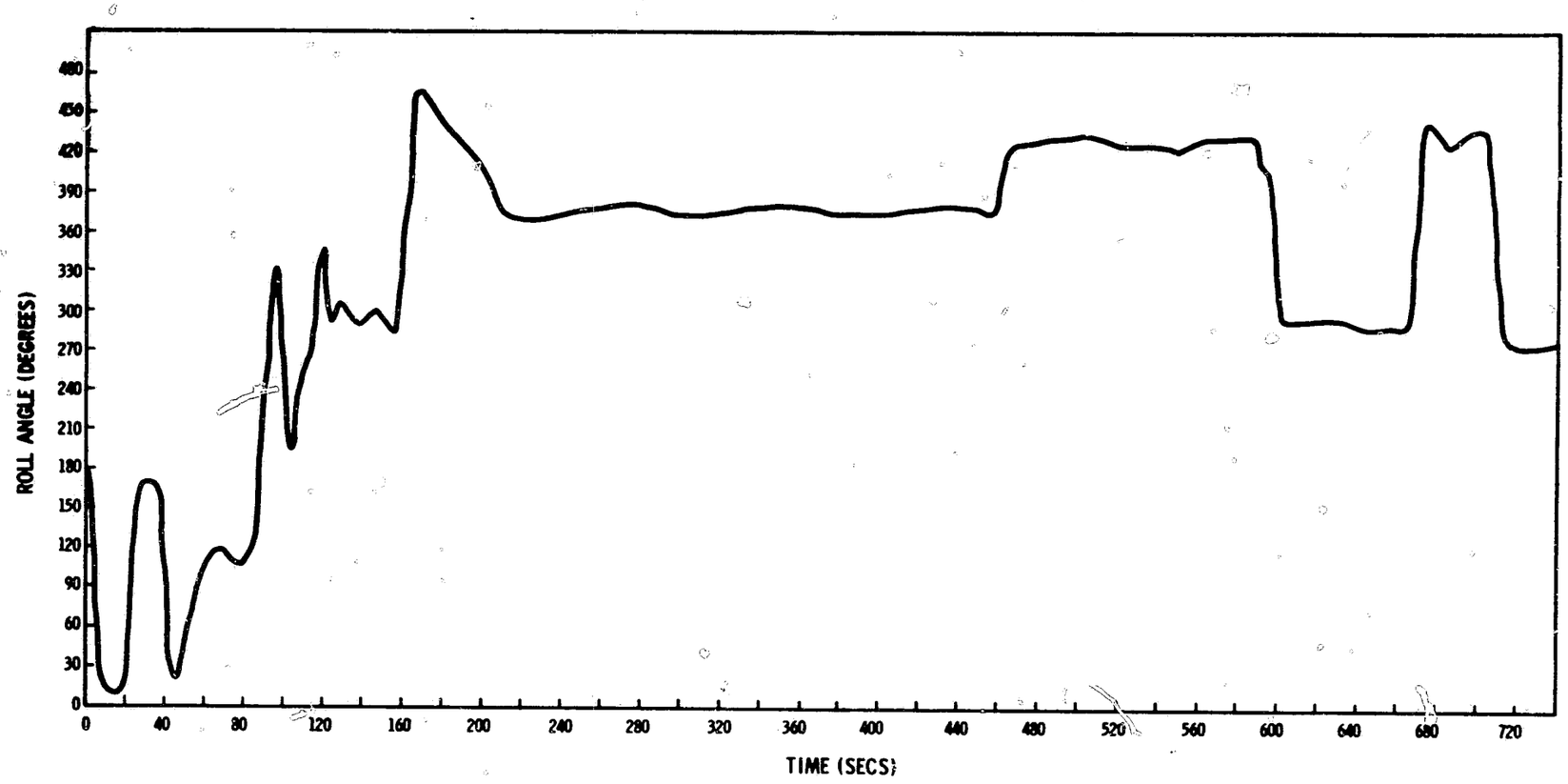

Fig. 1.2-3 Roll attitude vs time - entry phase.

and velocity errors. The position and velocity errors are then transformed into a local vertical frame. The local vertical frame is defined as:

Altitude - outwards along $\bar{R}$ at event time

Track - along $\bar{V} \times \bar{R}$

Range - along $\overline{\text{Altitude}} \times \overline{\text{Track}}$

The computational result for the entry trajectory is a linearized tabulation of altitude, track and range error at termination for each instrument error source.

In addition to basic instrument errors, the influence of the computational attitude algorithm error propagation was also included. A first-order direction-cosine algorithm was postulated and errors were modeled on the basis of coning, rate slew, and computational round-off. The coning environment was projected using Apollo simulation data, where a pitch and yaw damping oscillation frequency is exhibited during entry. The oscillation is essentially a function of the aerodynamic spring constants and vehicle mass. The frequency is characterized by:

$$f \simeq \frac{1}{\pi}\sqrt{g} \qquad (1.2.6)$$

where

f is the oscillation frequency in radians/second
g is the vehicle acceleration expressed in units of earth gravity.

The coning angle is essentially defined by autopilot considerations and for the sinusoid model using a maximum angular rate limit of two degrees per second the coning angle a, is:

$$a = \frac{2\pi}{180f} \text{ radians} \qquad (1.2.7)$$

The dynamic coning environment was then generated using the acceleration profile of Fig. 1.2-2. A worst-case condition was assumed, i.e.: the pitch and yaw oscillations were defined as being phased displaced by 90^{o}. For the mounting configuration selected the coning error is reflected as an equivalent drift rate about the X-axes that is represented by:

$$\omega_D = \frac{1}{12} a^2 (2\pi f)^3 \Delta t^2 \qquad (1.2.8)$$

where:

Δt corresponds to the computer update interval.

Rate slew errors were modeled as the attitude algorithm error that results for vehicle maneuvers. These were essentially about the roll axis (X-axis) and correspond to :

$$\theta_E = \frac{\Delta\theta^3}{3} \qquad (1.2.9)$$

where:

$\Delta\theta$ is the accumulated rotational angle in a computational interval Δt.

For these studies Δt was set to 1×10^{-3} sec (similar to a DDA serial implementation). Round-off errors were developed using a 30-bit wordlength. They were generated on a worse-case basis, a cumulative error based on the sense of rotation.

These algorithm errors were also generated in the analysis program on an iterative basis to yield the effect on trajectory position and velocity errors. The error analysis results for both the instrument and attitude algorithm error model are tabulated in Table 1.2-2. For comparison purposes a stable platform (gimbal system) mechanization was also implemented for the same trajectory with the same initial conditions. Although dynamic instrument errors (e.g., anisoinertia and output axis coupling) or a vibration environment (that could have resulted in a larger coning error) were not included in the analysis, several significant aspects of strapdown error propagation were evidenced.

In both the strapdown and the gimbal system implementations sizeable but essentially equivalent errors are introduced by the initial platform or algorithm misalignment. Similarly, the errors due to bias drift uncertainty for an assumed one-hour free-fall period between initialization and start of the entry phase are also equivalent. It is interesting to note that the sensitivity of the strapdown system to accelerometer misalignment, bias and scale factor errors is considerably reduced, e.g., misalignment of Y about Z and Z about X in the strapdown corresponds to a track and range error of 222 and 197 feet, respectively. In the platform case the errors were 1941 and 1306 feet, respectively. The reduced sensitivity in the strapdown implementation is probably due to cancelling effects arising from the body motion with respect to the acceleration vector. In contrast the strapdown implementation has a marked sensitivity to gyro IA misalignments, eg. a 4497-foot track error results from a 20-sec misalignment of Y about Z and a 6748-foot range error for a 20-sec misalignment of Z about Y.

TABLE 1.2-2

ENTRY ERROR ANALYSIS

Strapdown System Uncertainties	RMS Uncertainty	Position Uncertainty (feet)		Velocity Uncertainty feet/sec		
		Track	Range	Alt	Track	Range
I Initial Alignment X	60 $\widehat{\text{sec}}$	-1419	27	.012	-5.96	+0.17
(Optics-ISS- Y	60 $\widehat{\text{sec}}$	104	2081	-19.54	0.09	1.31
Algorithm) Z	60 $\widehat{\text{sec}}$	5824	-167	0	8.59	-0.25
II Accelerometers						
a) IA Misalignment						
X about Y	20 $\widehat{\text{sec}}$	14	77	2.31	0	0.01
X about Z	20 $\widehat{\text{sec}}$	-	-	-	-	-
Y about X	20 $\widehat{\text{sec}}$	-111	119	0.05	-0.48	0.15
Y about Z	20 $\widehat{\text{sec}}$	222	-237	-0.11	0.96	-0.29
Z about X	20 $\widehat{\text{sec}}$	-	-	-	-	-
Z about Y	20 sec	-171	-197	-0.11	-0.07	-0.92
b) Bias Error						
X	0.1 cm/sec^2	-14	73	-2.54	-0.01	-0.05
Y	0.1 cm/sec^2	-540	226	0.12	-1.2	0.28
Z	0.1 cm/sec^2	-149	-607	-0.28	0.03	-1.53
c) Scale Factor						
X	50 ppm	15	-79	2.38	-	-
Y	50 ppm	-	-	-	-	-
Z	50 ppm	44	51	0.03	0.02	0.24
III Gyros						
a) Gyro IA Misalignment						
X about Y	20 $\widehat{\text{sec}}$	-	-	-	-	-
X about Z	20 $\widehat{\text{sec}}$	-	-	-	-	-
Y about X	20 $\widehat{\text{sec}}$	-	-	-	-	-
Y about Z	20 $\widehat{\text{sec}}$	4497	-341	-0.26	3.55	-0.82
Z about X	20 $\widehat{\text{sec}}$	-	-	-	-	-
Z about Y	20 $\widehat{\text{sec}}$	570	-6748	3.00	2.00	-10.9

TABLE 1.2-2 (Cont'd)

ENTRY ERROR ANALYSIS

Strapdown System Uncertainties		RMS Uncertainty	Position Uncertainty feet		Velocity Uncertainty feet/sec		
			Track	Range	Alt	Track	Range
b) Bias Drift**							
X Intl		1.5 meru	-1921	37	0.02	-8.07	0.23
Entry			-4	15	0.01	-0.01	0.03
Y Intl		1.5 meru	141	3792	-26.5	0.12	1.77
Entry			200	437	0.19	0.27	1.03
Z Intl		1.5 meru					
Entry			7884	-226	-	11.62	-0.34
			-398	298	0.15	-0.82	0.64
c) Accel Sensitive Drift							
(Combined effect)*	X	ADIA, ADSRA 5 meru/g	29	120	0.05	0.08	0.21
	Y	ADOA 1 meru/g	838	64	-	1.12	0.49
	Z		221	1198	0.53	0.97	2.30
Accel. Squared Sensitive Drift	X	1 meru/g^2	-36	164	0.07	-0.07	0.27
	Y	1 meru/g^2	529	-162	-0.09	0.60	-0.22
	Z	1 meru/g^2	20	764	0.32	-0.24	1.36
d) Scale Factor	X	50 ppm	-33	-43	0.03	-0.03	0.17
	Y	50 ppm	-	-	-	-	-
	Z	50 ppm	-	-	-	-	-
IV Algorithm							
Coning		Eq. 1.2-9	-0.01	0.03	-	-	-
Slew		Eq. 1.2-10	-0.02	0.03	-	-	-
Round-off		(30 Bits)	-0.6	-7.4	-0.01	-0.3	-0.3
Strapdown Total Error (RSS)			10854	8605			
Inertial Platform Total (RSS)			11062	5149			

* ADIA dominant effect in error result.

** Bias drift is divided into two phases; Intl- corresponding to an assumed one-hour period between system optical alignment and the actual entry maneuver phase, Entry - corresponding to the actual entry phase.

The level of these errors is consistent with cross-coupling error propagation for the severe dynamic roll environment depicted in Fig. 1.2-3.

Errors associated with gyro scale factor uncertainty, which are commonly thought of as being one of the major strapdown design problems, were negligible. Similarly, algorithm error propagation effects were also insignificant, even though a relatively low performance algorithm was used. It is interesting to note that the overall rms error for the strapdown configuration was essentially identical to the stable platform mechanization in track and somewhat poorer in range performance for this entry trajectory. Although this study was not comprehensive, i.e., it was not possible to review all of the various entry trajectory and alignment conditions, it does appear that the projected strapdown system mechanization performance is adequate for successful space mission applications.

1.2.4 Performance Design Model

The preceding sections described some of the trajectory error analysis findings associated with various inertial subsystem performance parameters. The details of the overall guidance and navigation requirements study were reported on in Volume I.

The transplanetary error model considered first order error sources in a simplified error model. The entry analysis was more extensive and considered all instrument errors using the same linearized techniques employed in similar Apollo studies. Table 1.2-3 lists instrument, control loop and algorithm parameters that appear to be realizable during the time frame considered in the mission studies. As indicated by the error sensitivities of the mission phases described in the previous sections and Volume I these performance parameters are compatible with the anticipated Advanced Manned Mission objectives.

TABLE 1.2-3
REALIZABLE PERFORMANCE PARAMETERS

Gyro Performance		
Bias - NBD		1.5 meru
Acceleration Sensitive Terms	ADIA	2 meru/g
	ADSRA	2 meru/g
	ADOA	0.5 meru/g
Acceleration Sensitive Squared		1 meru/g^2
Scale Factor Linearity (.01-.3 rad/sec)		50/ppm
Scale Factor Stability (2^o/sec)		20/ppm
Operational Range		1 radian/sec
Accelerometer Performance		
Bias		0.1 cm/sec^2
Scale Factor Linearity (.01-1g's)		50 ppm
Scale Factor Uncertainty		10 ppm
Acceleration Squared Indication Error		10 mg/g^2
Mechanical Alignment		
Instrument Nonorthogonality		20 arc-seconds
Optical Alignment-Initialization		60 arc-seconds

The algorithm requirements were sized to allow for a more severe body bending coning environment. Anticipated algorithm requirements consistent with one-meru performance over coning input ranges of $1/2^o$ cone at 4-10 cps and as much as 1 rad/sec 3-axis slew rate are tabulated below.

TABLE 1.2-4
ANTICIPATED ALGORITHM REQUIREMENTS

	General Purpose Third-Order	DDA First-Order
Update Rate	(100-250)/sec	(1500-4000)/sec
Quantization	(2-6) $\widehat{sec}$	(2-6) $\widehat{sec}$
Word Length	34 bits	34 bits

The coning inputs represents the more severe criteria in all cases.

1.3 Multisensor Configuration

1.3.1 Introduction

High reliability is perhaps the most significant guidance system requirement for extended mission applications. Reliability may be viewed in the statistical sense and, as important, in absolute terms. A mean-time-to-failure statistic of 10^6 hours, for example, does not preclude the possibility of an instrument failure. The need for alternate guidance provisions is clear but the concept of back-up systems that are "inherently" more reliable is questionable. Generally, the back-up concept implies reduced sophistication (elimination of operational capabilities) as the means for reliability improvement. For extended missions this approach does not represent a wise trade-off; i.e., terminating the most fruitful portion of an interplanetary mission because of the reduced capability of a back-up system is ludicrous. Moreover, a reduction in sophistication does not guarantee an improvement in reliability. Too often cost and performance compromises are made because it is "only" a back-up system and marginal reliability results.

Redundant usage within the primary system or redundant application of primary systems such that mission objectives are not compromised by performance degradation or failure is the preferred system concept for extended missions. Redundancy, however, in itself is not a cure-all; the reliability of each element in the system must be consistent with the mission environment and duration.

The guidance and control system may be functionally segmented into the computer and the inertial reference sensor package. Volume II of this report presents a multiprocessor computer concept. The multiprocessor employs redundant techniques using multiple-element implementation as well as adaptive coding methods for error detection and correction processing. For the inertial reference unit a variety of redundant implementations are possible. Within a single system they evolve about the sensor mechanization; i.e., redundant use of sensors on common orthogonal axes or redundant measurement data via the use of skewed multiple-sensor configurations. Consideration of redundant usage of primary systems represents another level of reliability enchancement.

The introduction of in-flight repair concepts is also warranted. Mission reliability objectives, however, should not be predicated on the use of in-flight repair.

1.3.2 Design Model Concept

The design model selected for the extended mission application is based upon the use of a skewed redundant sensor implementation. The sensor configuration employs six gyros and accelerometers whose input axes are collinear with the normals to the faces of a regular dodecahedron. (See Fig. 1.3-1.) (This concept was developed in full detail in a Master's thesis by Gilmore[7] and is reviewed here for completeness.) This array is unique in that complete symmetry is evidence; i.e., the acute angle (2α) measured between any two axes defined by the dodecahedron normals is equal ($63^{\circ}26'.8''$). The preferred orientation of these axes with respect to the orthogonal triad is also shown in Fig. 1.3-1.
Note that input axis pairs are located in triad planes (XZ, XY, YZ) and are displaced by an angle α ($31^{\circ}43'2.8''$) about each positive triad axis. For this configuration the relationship between angular rate or specific force inputs along the triad frame and each of the respective dodecahedron axes A, B, C, D, E, F, respectively is:

$$\underline{m} = \underline{H}\,\underline{b} \qquad (1.3.1)$$

where:

$$\underline{m} = \begin{bmatrix} m_a \\ m_b \\ m_c \\ m_d \\ m_e \\ m_f \end{bmatrix} \quad \underline{H} = \begin{bmatrix} \sin\alpha & 0 & \cos\alpha \\ -\sin\alpha & 0 & \cos\alpha \\ \cos\alpha & \sin\alpha & 0 \\ \cos\alpha & -\sin\alpha & 0 \\ 0 & \cos\alpha & \sin\alpha \\ 0 & \cos\alpha & -\sin\alpha \end{bmatrix} \quad \underline{b} = \begin{bmatrix} \omega_x \\ \omega_y \\ \omega_z \end{bmatrix} \text{ or } \begin{bmatrix} f_x \\ f_y \\ f_z \end{bmatrix}$$

$$\cos\alpha = \left(\frac{\sqrt{5}+5}{10}\right)^{1/2} \simeq 0.85$$

$$\sin\alpha = \left(\frac{5-\sqrt{5}}{10}\right)^{1/2} \simeq 0.526$$

Here m is either the rate input, ω, or the specific force input, f, seen by gyros or accelerometers whose input axes lie along respective dodecahedron axes.

As seen from the equation each instrument provides a measure of redundant data. For example, instruments A, B, C, D all sense a component of input along the X triad axis. Similarly one may algebraically manipulate the equations and obtain corresponding solutions for equivalent inputs

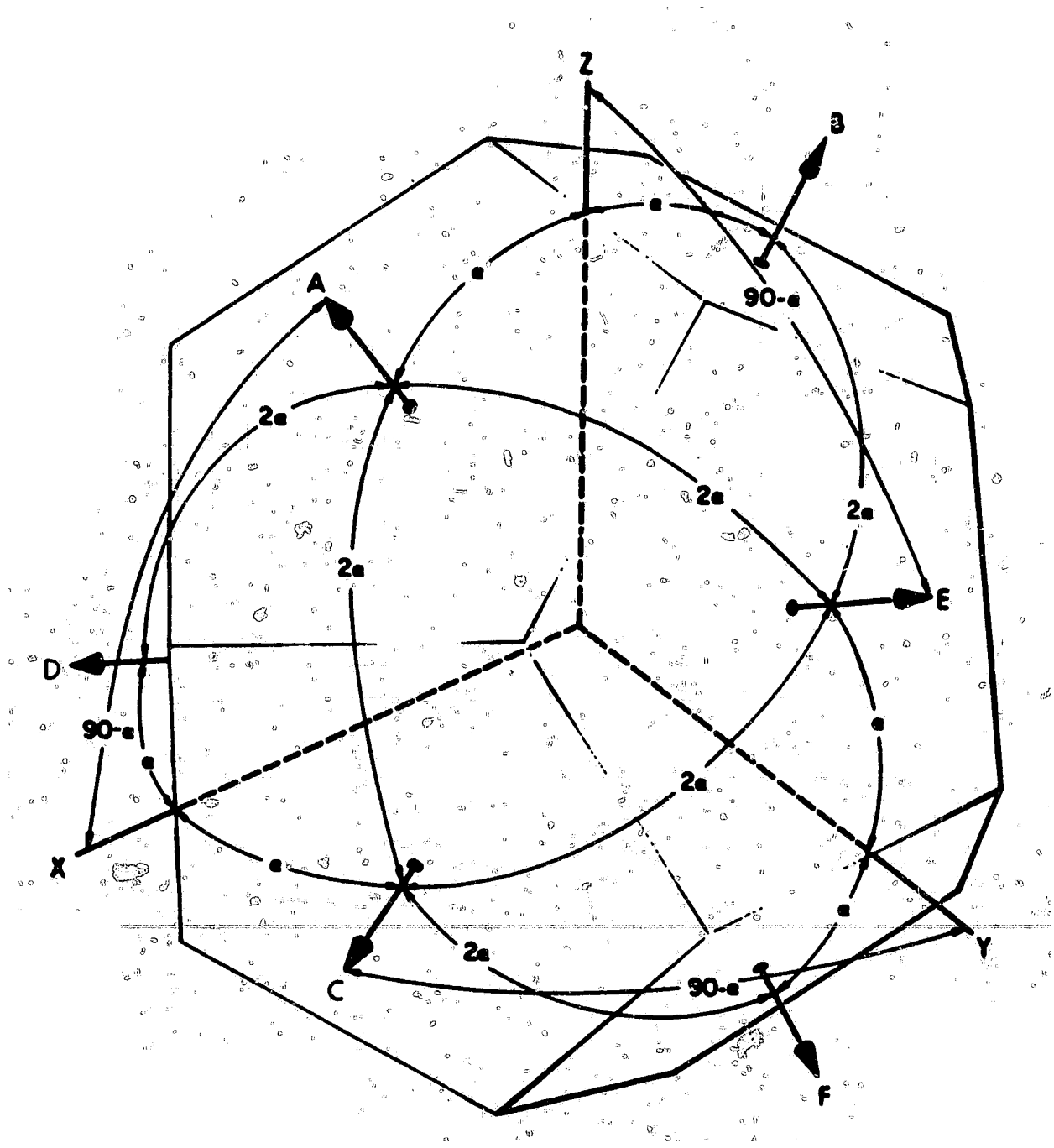

Fig. 1.3-1 Instrument input axes orientation relative to the instrument frame triad and the dodecahedron.

along the triad axes based on the sensed instrument inputs. From analysis of the equation format one observes that a solution for equivalent X, Y, Z inputs is attainable from any three of the six gyros or accelerometers. Thus, assuming a means exists for determining the failed sensors, an equivalent triad solution for guidance and control utilization is attainable from any three gyros and accelerometers. In an arrangement employing duplex redundancy on orthogonal axes failure of two gyros or accelerometers on the same axis is catastrophic.

The dodecahedron array also provides self-contained failure detection and isolation capabilities. Failure detection is not limited to a catastrophic failure; it includes a measure of instrument performance degredation. The mechanization allows isolation of any two gyro or accelerometer failures and the detection of a third failure. In general, self-contained failure detection and isolation requires some sort of majority voting or error coding scheme. Clearly in an orthogonal configuration employing two gyros per triad axis a single gyro failure is detectable. It is not possible, however, unless the environment is known or a catastrophic failure occurs, to determine which of the two gyros or accelerometers is functioning correctly. After a performance type failure is detected, no basis for isolation is available unless diagnostic sensing aids are also implemented (wheel speed detector, scale factor current monitor, etc.). On the other hand, with the dodecahedron six-instrument concept complete symmetry is achieved. For each instrument set, gyros or accelerometers, none of the input axes are colinear, no three axes are coplanar, and each axis is skewed with respect to the orthogonal reference frame. Isolation is, therefore, attainable for a single, or even dual, failure.

In essence, the dodecahedron array implementation allows a comprehensive redundant usage of six gyros and accelerometers and their associated control electronics. In absolute terms its ultimate backup capability exceeds that of a nine-instrument orthogonal instrument configuration since it can tolerate any three gyro or accelerometer failures and still yield useful data.

1.3.3 Data Processing

Equation 1.3.1 may be manipulated to determine the triad solution for every three-fold subset of instruments. Each of the twenty characteristic solutions for each possible instrument grouping is itemized in Gilmore's thesis. A statistical index for each solution may be obtained considering the solution variance relative to the performance of a single instrument. We may view this index as a measure of the error-spread of the equivalent orthogonal instrument frame solutions relative to a triad configuration using the same instruments. For normal distribution slightly more than 95% of the measurement instrument error spread is included in the one-σ limits. Assuming identical limits for all instruments allows an analysis of the geometric properties of the dodecahedron array solutions. Interestingly, the twenty instrument combinations may be identified with the four distinct total variance groups shown in Table 1.3-1.

TABLE 1.3-1 THREE-INSTRUMENT COMBINATION SOLUTION VARIANCES

Instrument Group				Variance			Solution Mean-Squared-Errors
I				$1.82\sigma^2$	$8.35\sigma^2$	$0.69\sigma^2$	$10.86\sigma^2$
	II			$1.82\sigma^2$	$1.65\sigma^2$	$0.69\sigma^2$	$4.16\sigma^2$
		III		$3.62\sigma^2$	$3.62\sigma^2$	$3.62\sigma^2$	$10.86\sigma^2$
			IV	$1.38\sigma^2$	$1.38\sigma^2$	$1.38\sigma^2$	$4.15\sigma^2$
ABC&AED AEF&BEF CDE&CDF				x z y	y x z	z y x	
	ABE&ABF CEF&DEF ACD&BCD			x z y	y x z	z y x	
		ACF ADE BCE BDF		x	y	z	
			ACE ADF BCF BDE	x	y	z	

Group I corresponds to those three-instrument combinations that exhibit the most error propagation due to geometric resolution. For example, in the triad solution corresponding to gyros ABC or AED the Y-axis solution error amplification corresponds to a variance of 8.35 times that of a single instrument. In contrast a skewed configuration obtained by rotating two orthogonal triads apart by three 45^{o} Euler angle rotations yields a corresponding worst-case variance amplification of approximately 100.

The thesis also demonstrates that, relative to the geometric error propogation characteristics, the symmetrical dodecahedron array yields an optimum statistical performance solution (covariance matrix of $1/2\ \sigma^2 \underline{I}$) when all six instruments are used. Further, the performance index for all combinations of five instruments is still superior and four-instrument combinations yield performance indexes that are essentially equivalent to that of an orthogonal triad solution.

A generalized weighted least-squares best-estimate solution for the dodecahedron configuration is:

$$\underline{\hat{b}} = (\underline{H}^T \psi^{-1} \underline{H})^{-1}\ \underline{H}^T \psi^{-1}\ \underline{m} \qquad (1.3.2)$$

The covariance matrix ψ is:

$$\begin{bmatrix} \frac{1}{\sigma_1^2} & 0 & 0 & 0 & 0 & 0 \\ 0 & \frac{1}{\sigma_2^2} & 0 & 0 & 0 & 0 \\ 0 & 0 & \frac{1}{\sigma_3^2} & 0 & 0 & 0 \\ 0 & 0 & 0 & \frac{1}{\sigma_4^2} & 0 & 0 \\ 0 & 0 & 0 & 0 & \frac{1}{\sigma_5^2} & 0 \\ 0 & 0 & 0 & 0 & 0 & \frac{1}{\sigma_6^2} \end{bmatrix}$$

If all instruments are weighted with equal variance and the errors are statistically independent, (1.3.2) reduces to:

$$\underline{\hat{b}} = (\underline{H}^T \underline{H})^{-1}\ \underline{H}^T \underline{m} \qquad (1.3.3)$$

Manipulation of (1.3.3) for a solution using all six instruments is expressable as a linear combination of equations:

$$x = \frac{1}{2}\left[(m_a - m_b)\, s(\alpha) + (m_c + m_d)\, c(\alpha)\right]$$

$$y = \frac{1}{2}\left[(m_c - m_d)\, s(\alpha) + (m_e + m_f)\, c(\alpha)\right] \qquad (1.3.4)$$

$$z = \frac{1}{2}\left[(m_e - m_f)\, s(\alpha) + (m_a + m_f)\, c(\alpha)\right]$$

where

$$s(\alpha) = \sin(\alpha) \quad , \quad c(\alpha) = \cos(\alpha)$$

Similar equations may be defined for the five-and four-gyro combinations. They correspond in (1.3.2) to setting the variance associated with the instrument not considered to ∞.

The corresponding solution forms are listed for triad rate solutions in Tables 3.4 and 3.6 of the referenced thesis. For a specific system the variance of each instrument may be defined from extensive component testing and, thus, individual instrument weighting as identified in (1.3.2) is possible. The application of such statistical weighting represents a trade-off between mission performance requirements and computational complexity. In some applications, a simpler approach to solution processing may be warranted.

It may be argued that statistical processing is superfluous if performance is adequate when only three instruments are operative. (Note that the mean-squared error for certain three-instrument combinations in Table 1.3-1 corresponds to $10.86\sigma^2$.) One could develop solutions using an arbitrary selection criterion when more than three instruments are available. For example, in (1.3.1), although all instruments are operative, we could restrict the solution to reduced processing by considering only solutions associated with:

$$x = (m_c + m_d)\ \frac{1}{2}\ c(\alpha)$$

$$y = (m_e + m_f)\ \frac{1}{2}\ c(\alpha) \qquad (1.3.5)$$

$$z = (m_a + m_b)\ \frac{1}{2}\ c(\alpha)$$

Similarly, if instrument D were "suspect" an equally simple processing scheme for the x-solution could be used:

$$x = (m_a - m_b)\ \frac{1}{2}\ s(\alpha) \qquad (1.3.6)$$

As long as four instruments are available, the most lengthy solution involves a single axis and is of the form:

$$x = \frac{-s(\alpha)}{2c^2(\alpha)}\ (m_e + m_f) + \frac{m_c}{c(\alpha)} \qquad (1.3.7)$$

(For (1.3.7) instruments A or B, but not both,and C, E, and F could be performing satisfactorily, but only C, E, and F would be used.)

Ultimately the selection of a solution algorithm represents a trade-off decision between the power (speed and memory) and "graceful degradation" capabilities of the multiprocessor computer and the mission performance requirements.

1.3.4 Failure Isolation and Detection

In the previous discussion methods for obtaining equivalent triad solutions of frame rate or velocity were identified. Implicit in these discussions was the assumption that a suitable technique can be defined that allows detection and failure isolation. Failure may be defined as being catastrophic or a performance degradation malfunction; either may invalidate the mission objective.

Catastrophic failures are usually detectable with simple detection schemes; e.g., a spin-motor detector in a gyro, a signal generator null monitor, a ΔV monitor in free-fall, etc. Thus, for catastrophic failures rapid failure isolation with a corresponding change in the processing algorithm is readily mechanized. Even in powered flight, where previously a catastrophic failure would have represented a safety hazard, the direct filtering influence of the multiple-sensor processing configuration assures tolerable operations during the detection and processing-reorganization interval.

Performance degradation is not as simply evidenced or detected. In some spacecraft applications external failure detection and isolation is possible. Diagnostic procedures using on-board celestial sensors or ground-based tracking may allow detection and identification of the faulty instrument. For a variety of mission phases diagnostic procedures are impractical and the need for a self-contained failure detection and isolation capability is apparent.

Self-contained failure isolation in a redundant-sensor implementation is clearly evidenced if one considers majority voting, e.g., three instruments all along the same triad axis. In the non-orthogonal array, however, no two instrument outputs correspond. Thus, to achieve an output comparison for the hexad array, as in the case of the triad solution processing, a multi-sensor output comparison algorithm must be defined. Several techniques were explored in the referenced thesis. The direct approach that comes to mind is simply to compute triad solutions using individual three instrument combinations, effect solution comparisons, and then use those that appear to agree. The direct application of this approach was shown to be unwieldy,

but due to the unique geometry this basic deterministic concept was refined to yield a simple set of direct instrument comparison "parity equations". Another more sophisticated technique would be to use the best estimate solution $\hat{b}$ (Eq 1.3.2) of the instrument triad solution to estimate what the respective instrument outputs should be. One may then compare the instrument output estimate with its actual output and isolate an instrument failure by the measure of its deviation from that estimate.

The "parity" equation implementation is simply mechanized in a computer and represents a minimal impact in both processing and memory requirements. "Parity" equation refers to the identity equations listed in Table 1.3-2 (for derivation refer to T-472). These equations correspond to geometric relationships uniquely satisfied by the multisensor array. The equations are mechanized on the basis of four instrument output comparisons which should yield a resultant zero output. For example, if a gyro configuration is considered, the term A corresponds to the accumulated $\Delta\theta$ count in some comparison interval of the instrument in the A position of the multisensor array. For ideal instruments and no malfunctions all equations would null. If we consider only a single failure, gyro A for example, we note that equations 1 through 10 would not indicate correctly and equations 11 through 15 would. Thus, a failure of gyro A is detected and isolated by a check of the parity equations. If a second instrument fails, inspection of the remaining equations (11 through 15) would allow another level of detection and isolation. If three instruments fail, none of the equations are satisfied and the failure is detected; but self-contained isolation (except for catastrophic types) is no longer possible.

In practice, it would not be necessary to inspect all fifteen equations at each parity test time. If one considers that no two failures will occur in the same test interval, the parity test can be reduced considerably. The reference identifies a series of truth tables that allow single-failure isolation in a sequential manner such that inspection of fewer equations at any one test time is possible. If we consider monitoring equations 1, 3, 6, 10, 11, and 15, we can directly isolate a single failure and detect a dual failure. In Table 1.3-3, for example, we note that for each individual instrument failure, a "go-no-go" combination of parity equations (the 1 indicates a non-zero result) result that is not duplicated by any other failure or failure combination. If a dual failure occurs (i.e. no equation set matches), one may then resort to the full equation set in Table 1.3-2. Once a single failure occurs and is isolated, another group of the parity equations may then be used for further fault isolation. Other economies are also possible; e.g.,

TABLE 1.3-2

FAILURE DETECTION PARITY EQUATIONS

No.	Instrument	Equation
1	ABCD	$(A - B)c - (C + D)s = 0$
2	ABCE	$(B + C)c - (A + E)s = 0$
3	ABCF	$(C - A)c + (B - F)s = 0$
4	ABDE	$(D - A)c + (B - E)s = 0$
5	ABDF	$(B + D)c - (A - F)s = 0$
6	ABEF	$(E - F)c - (A + B)s = 0$
7	ACDE	$(D + E)c - (A - C)s = 0$
8	ACDF	$(F - C)c + (A + D)s = 0$
9	ACEF	$(A + F)c - (C + E)s = 0$
10	ADEF	$(E - A)c + (D - F)s = 0$
11	BCDE	$(E - C)c + (D - B)s = 0$
12	BCDF	$(F + D)c + (B - C)s = 0$
13	BCEF	$(B - E)c + (C + F)s = 0$
14	BDEF	$(B + F)c + (D - E)s = 0$
15	CDEF	$(D - C)c + (E - F)s = 0$

$$c = \cos(\alpha) = \left(\frac{\sqrt{5} + 5}{10}\right)^{1/2} \simeq 0.85065$$

$$s = \sin(\alpha) = \left(\frac{5 - \sqrt{5}}{10}\right)^{1/2} \simeq 0.52574$$

by analysis of the signs of the terms in the "no-go" parity equation test, the number test equations can even be further reduced.

TABLE 1.3-3

PRIMARY PARITY TEST - FAILURE DETECTION

Gyro Failure	Parity Equation					
	15	10	6	3	1	11
A	0	1	1	1	1	0
B	0	0	1	1	1	1
C	1	0	0	1	1	1
D	1	1	0	0	1	1
E	1	1	1	0	0	1
F	1	1	1	1	0	0

Thus far the discussion has assumed an idealized instrument set. Clearly, errors associated with instrument uncertainties require that the measure of satisfactory parity equation test be defined by some tolerance. The determination of this tolerance is highly dependent on the instrument error model and performance statistics. The parity tolerance and measurement comparison must allow for random errors, possible ramping performance deterioration, low-level jump shifts, and unacceptable short-term performance tolerances.

The parity tolerance for low-level ramping deterioration or jump shifts would best be achieved by a comparison after a long-term count accumulation (here random error accumulations would tend to average out). Unacceptable performance, i.e. a large SF or bias shift which is intolerable even for short durations, can be detected using a much wider tolerance but with parity tests affected over shorter accumulation intervals. A specific mechanization is definable only when the mission performance requirements are known and an adequate instrument error model is synthesized.

One interesting adaptive consideration in the parity equations is that for single instrument performance shifts it may be possible to make an effective measure of the change and correct for it. Thus, a measure of self-calibration is feasible and overall system reliability is further enhanced. Similarly, an instrument exhibiting low-level ramping tendencies which was previously taken off-line in the equation processing structure could be reinstated to provide satisfactory short-term performance when a catastrophic failure occurs.

1.3.5 Multisensor Mechanization

Having established a data processing and failure isolation scheme, we may now integrate the multisensor concept within the framework of a system package and electronics mechanization. Thus far the defined symmetrical array of six single-degree-of-freedom instruments is applicable to either a gimballed platform or a strapdown system mechanization. Although previous discussions implied computer usage for the data processing, it is equally possible to mechanize a comparable analog scaling and switching system that would reduce the gyro outputs to signals equivalent to the stable member triad signals normally used through the platform resolution system and fed to the torque motors. Although the instrument redundancy is retained, the complexities in the analog computational scaling are sizable; and if these elements are not to compromise system reliability, they must also be redundant. Similarly, the gimbal system servo, resolver, and slipring mechanization all require some redundant treatment if a single fault is not to compromise the entire system. The attendant gimbal weight structure penalty is likely to be overwhelming. In contrast, the relative ease of adaptability to a strapdown configuration is apparent. Mechanical complexity and configuration constraints are minimal and the size, weight and power penalties do not increase out of proportion. With respect to the additional computer processing burden, the strapdown implementations represent additional interface channels and a relatively small percentage increase in the memory capacity. Further, with the computer multiprocessor structure presented in Volume II of R-600, redundancy is inherently defined and thus the fundamental reliability of the entire concept is preserved.

Figure 1.3-2 illustrates the adaptation of the six-gyro configuration to a strapdown system implementation. A similar block diagram is applicable to the accelerometers. Note that a pulse-restrained torquing loop is identified and each single-degree-of-freedom instrument is configured with its own thermal controller and torque loop (thereby further extending the redundant instrument mechanization).

A pulse-restrained torquing loop was selected as opposed to the use of single-axis platforms. Relative advantages of reduced complexity, higher reliability, and lower power and weight are cited. A performance advantage is often attributed to the single axis platforms, generally in the area of dynamic range[8]. However, the realizable performance of torque-to-balance instrument control loops (Section 1.2.4) appears to more than adequately satisfy the mission application requirements (Section 1.2 and Volume I).

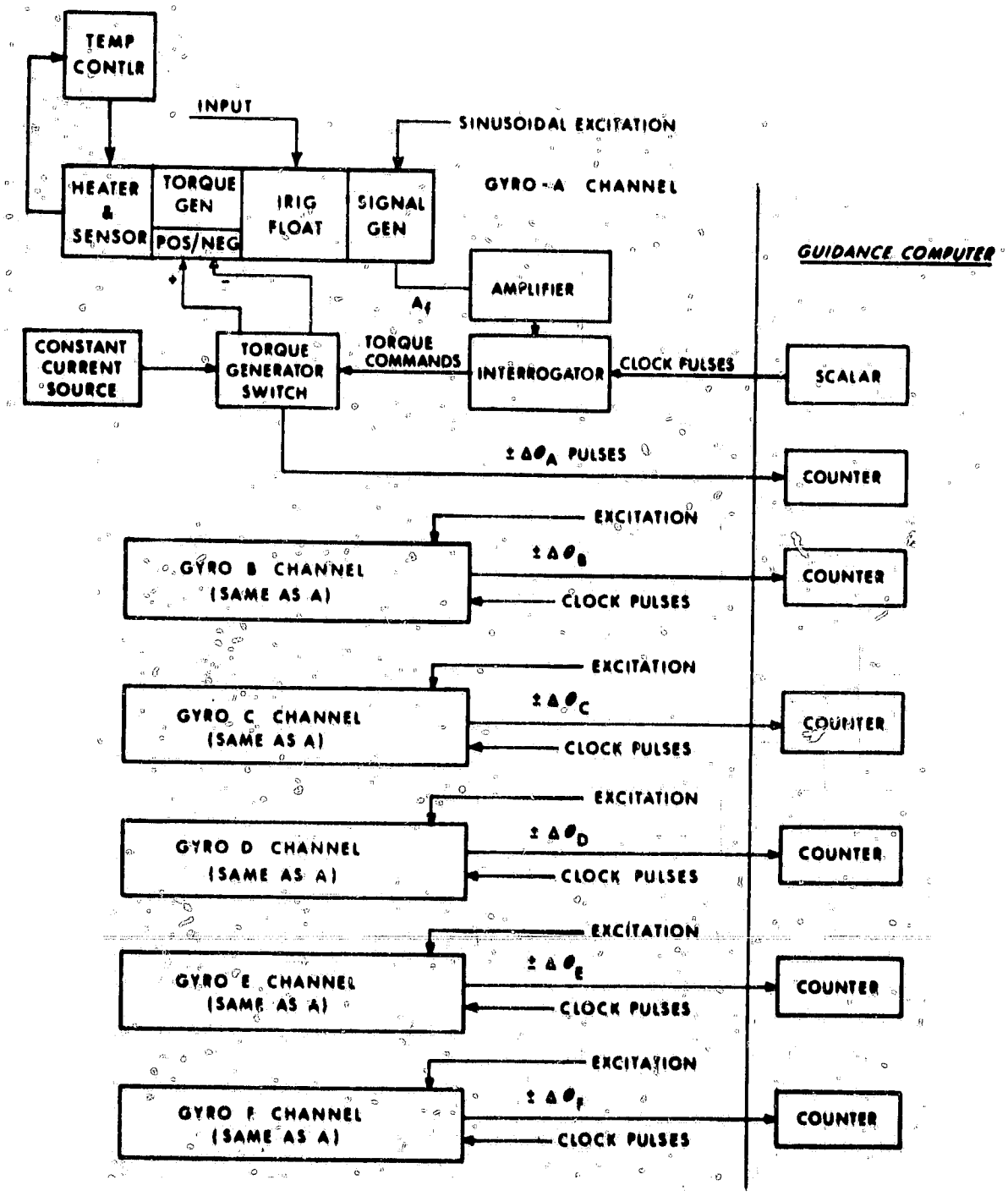

Fig. 1.3-2 Hexad-array strap-down system implementation.

The incremental output of each instrument and control loop is stored in a separate input counter in the computer. If a serial interface is defined (as in the case of the multiprocessor), the counters shown in the figure can assume the role of local accumulators with redundant serial interface provisions for data transmission to the computer. (An alternate mechanization could be defined using a redundant multiplexed-time-shared pulse-restrained torque loop configuration[9].) Finally, to achieve the overall system reliability goals (redundant gyro wheel, suspension, etc.), power supplies must be defined. The relative reliability of these elements is significantly greater than that of the basic inertial instrument. Thus, more conventional duplex type of redundant implementations with self-contained failure monitor and switching provisions should suffice.

Thus far orientation constraints have been defined only for the input axes of the inertial instruments. Within this basic constraint we are free to consider the instrument placement within a mounting configuration. Several orientation choices are possible. Figure 1.3-3 illustrates one in which maximum density packaging objectives are satisfied. The instrument outlines depicted correspond to the 16 PM PIP accelerometer and 18 IRIG gyro (Ref Chapter 3), both single-degree-of-freedom pulse-restrained instruments. This layout would yield a reasonably compact assembly using a conventional mounting frame design. The mounting configuration shown allows identical prealignment of all instruments and the final input-axis orientation array is achieved by placing the instrument OA's in an orthogonal mounting configuration. Note that, since the OA's are all orthogonal, the data processing triad solutions may be used directly for OA dynamic corrections (Ref Section 2.3 and 2.4) without requiring any additional geometric resolution. In this arrangement, however, four gyros are mounted such that all of their acceleration sensitivities may be exhibited during thrusting. (Assume, for example, that X corresponds to the thrust or g-vector; then instruments A, B, C, and D all have relative specific force components along IA and SA.)

Consideration can also be given to orienting the instrument OA's in a manner such that some preferred orientations are defined that minimize or eliminate some of the acceleration sensitive term effects. For most space applications, the majority of the mission time is spent in a free-fall environment. Generally, accelerating flight phases are of brief duration and, if the instrument performance is within reasonable tolerances (see Section 1.2.3), only minor performance advantages are obtained with a special orientation. For these applications, packaging efficiency will be the dominant consideration. For land navigation applications, however, (transport aircraft missions dependent upon the

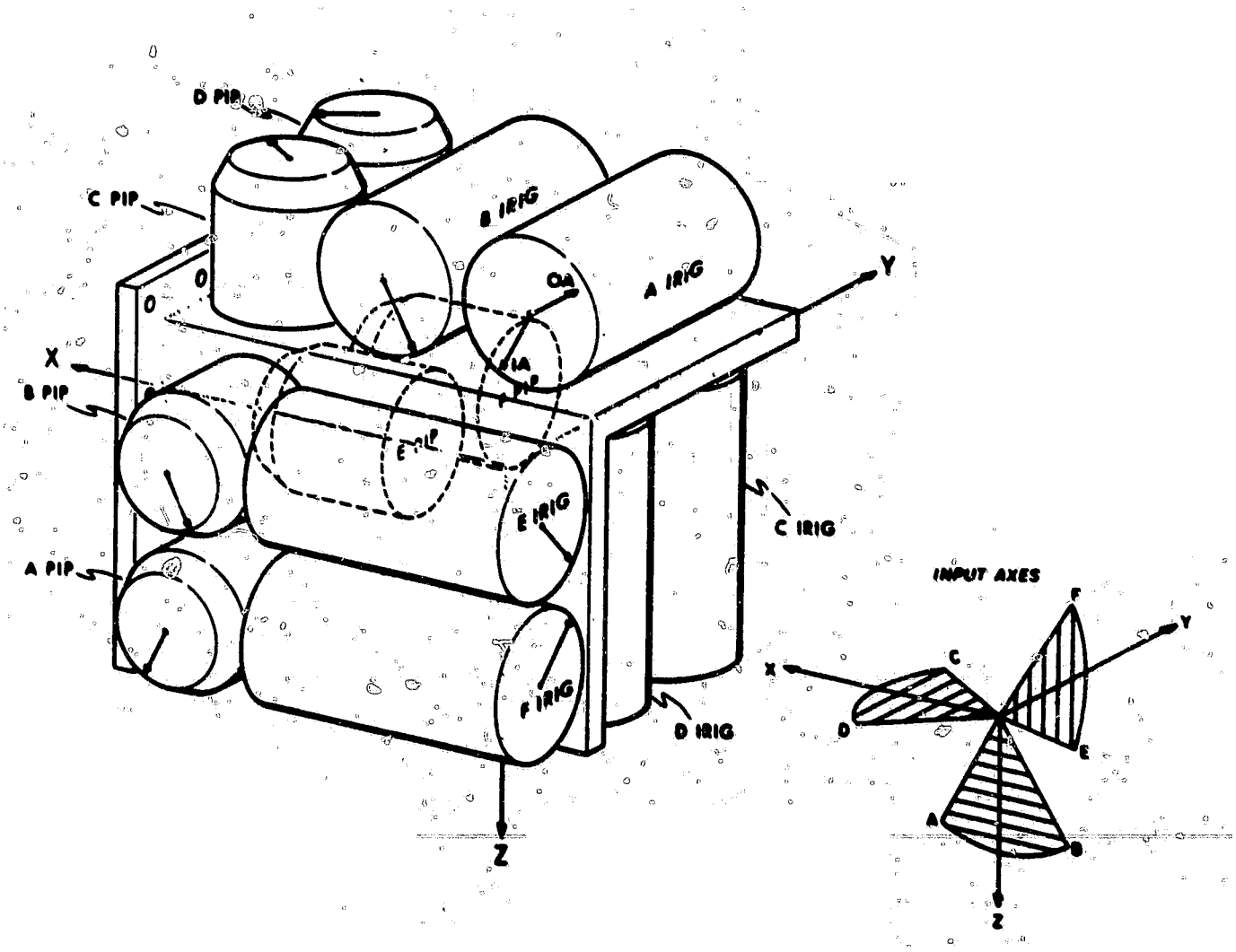

Fig. 1.3-3 Hexad-array strap-down configuration package.

instrument tolerances) it may be desirable to align the instruments to minimize the gravity influence on instrument drift sensitivities. If we consider mounting OA in non-orthogonal planes (for example, those defined by the faces of a dodecahedron with the IA's normal to the faces), it is possible to achieve an instrument alignment in which all spin axes are perpendicular to a triad frame axis (z) corresponding to the nominal g-vector (Fig. 1.3-4).

1.3.6 Reliability Models

A variety of reliability models for comparisons of the multisensor reliability statistics were developed and described in the referenced thesis. In general, it was shown that a significant reliability advantage is attainable over other comparative redundant instrument and system configurations. Figure 1.3-5 illustrates these findings. Normalized reliability trend statistics are plotted. They correspond to the use of identical instruments in different redundant configurations. For example, reliability plots compare three triad systems mechanized so that continued mission success is attained by majority agreement, a similar majority agreement scheme using a single system mechanization with three instruments on each triad axes, the multisensor configuration with parity voting allowing two failures, and the multisensor array using a standby concept. The standby concept assumes only five instruments are normally operative and when a failure is detected and isolated the remaining sixth unit, which was in a standby (inoperative) status, is activated. No data loss occurs during the activation phase since the other four good units are fully operational. The newly activated instrument simply provides the fifth instrument necessary for operation with continued failure detection and isolation capabilities.

The normalized abscissa used in the plot corresponds to the product of the failure rate (λ) of a single instrument in the system and time of operation for each system. If identical instruments are used in each system, the reliability for the same operational time is given by the projection of the (λt) point on the abscissa to the corresponding system configuration curve. Similarly, if the instrument λ is 100×10^{-6} failures per million hours, $0.2\,\lambda t$ corresponds to 2000 hours of system operation. The basic hexad array instrument configuration reliability is approximately 0.9 for this period even when all six instruments are assumed to be continuously operating. This is significantly better than any comparitive system mechanization even though they use a larger quantity of instruments.

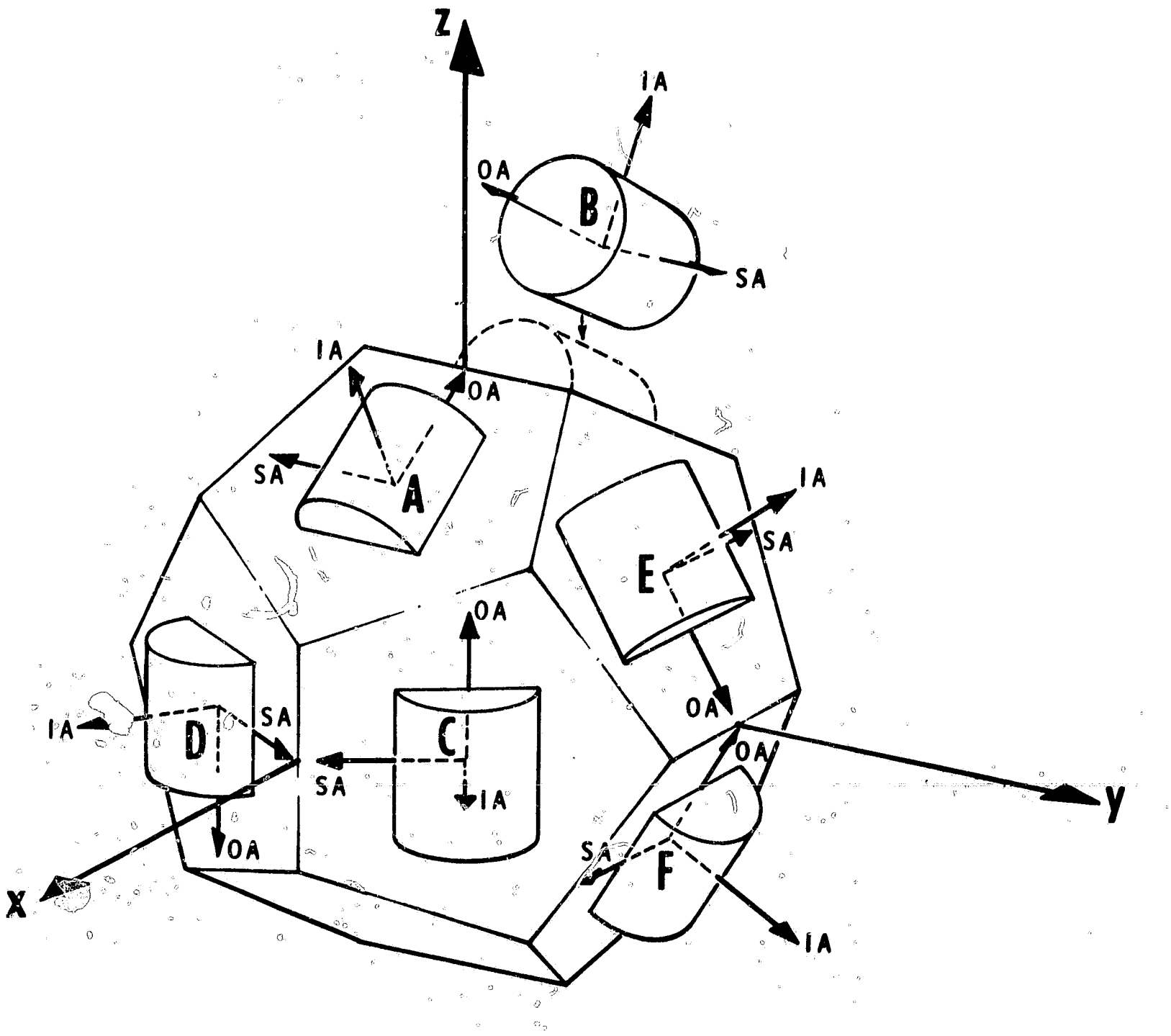

Fig. 1.3-4 Component alignment with spin axes normal to z axis.

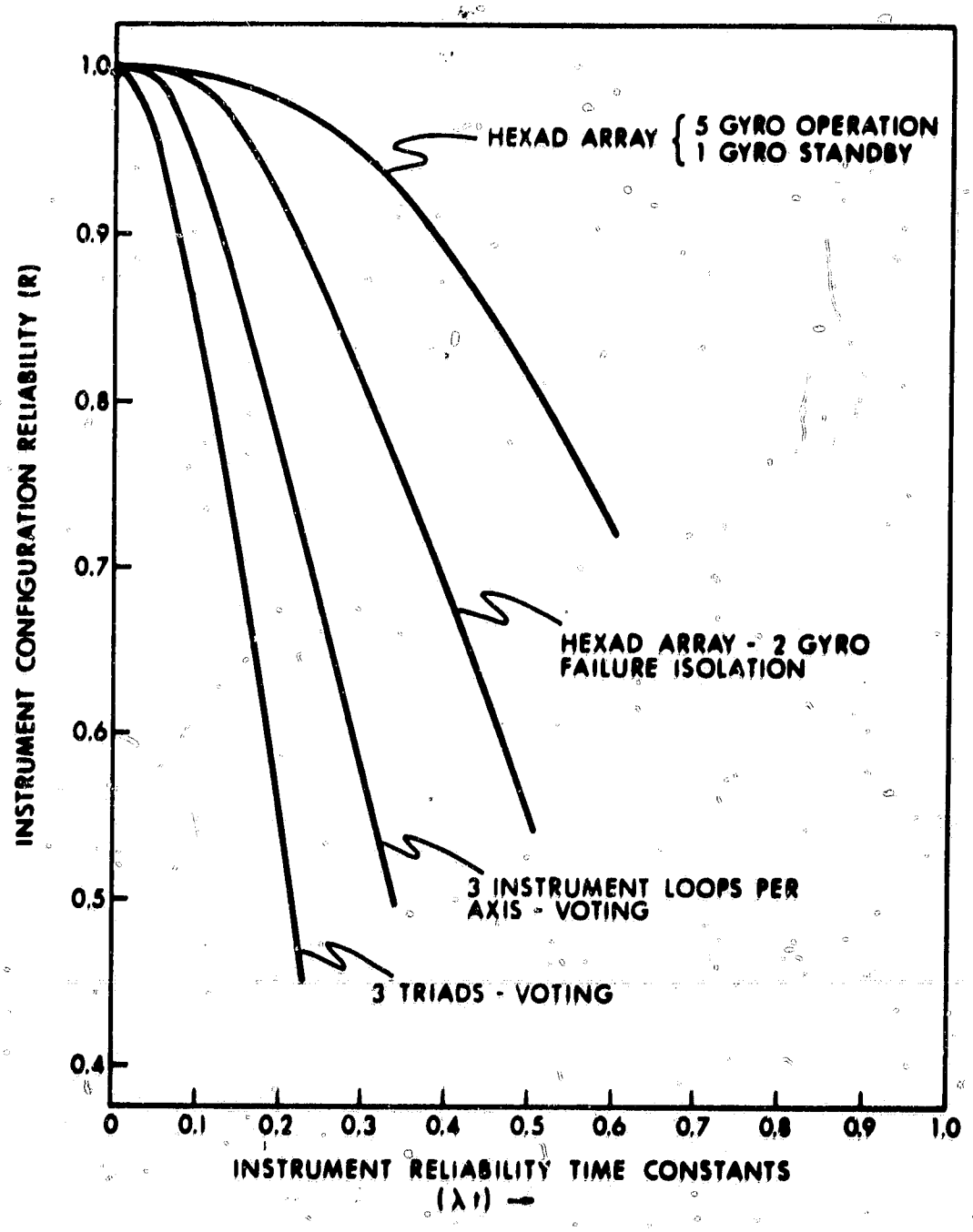

Fig. 1.3-5 Reliability plots, self-contained failure isolation.

1.4 Modular Instrument Configuration

Enhancement of maintainability design features has been cited in previous discussions as one of the potentials of the structure-mounted configuration. Inertial instrument replacement for suspect performance or potential failure hazards (in accordance with prediction criteria[10]) has been a continuous problem in the Apollo Guidance and Navigation System programs. Each replacement necessitates removal of the Inertial Measurement Unit from the spacecraft. Rigid cleanliness and inspection procedures (since the gimbal covers must be removed for instrument replacement) are required and extensive subsystem recertification testing is conducted assure that other hazards have not been induced and that a satisfactory replacement has been achieved. Clearly the maintainability problem is a question of accessibility of the inertial sensor package and the instruments within the package and of final design for maintainability.

The strapdown system implementation removes the obvious constraint of gross instrument inaccessibility by the elimination of the gimbal system structure. Design for ease of access and instrument removal in a gimbal structure generally conflicts with packaging density objectives and, as such, tends to be negated to avoid substantial weight and volume penalties. Structure-mounted design allows more flexible consideration of packaging concepts that are consistent with modularity design features typically employed in electronic assemblies. Modularity design features are a necessary requirement if comprehensive inertial subsystem in-flight repair is to be realized. For the inertial-grade instrument, however, modular in-flight interchangeability represents an unrealized goal.

Unlike the electronic module, the nature of the inertial component and its application requirements necessitate precise mechanical alignment, thermal control, and electronic design compatibility. In the strapdown configuration these precision requirements are significantly more severe than a comparative gimbal system. For the same application, superior alignment and torquing performance is an absolute requirement (see Section 1.2.3). Thus, although strapdown allows consideration of modular concepts, it also imposes more severe requirements on the module design.

Initial studies were conducted to develop modular design concepts for inertial gyros. The layouts shown in Figs. 1.4-1 and 1.4-2 represent some of the concepts that were reviewed. These figures illustrate a modular design centered about the 18 IRIG MOD B, a single-degree-of-freedom pulse-restrained gyro developed for strapdown application (see Chapter 3). Self-contained within the module are the gyro pulse-torquing electronics, temperature controllers with thermoelectric control elements, suspension and quadrature adjustment components, digital-to-analog conversion channels for direct signal-conditioning monitoring, and mechanical alignment adjustment provisions. The inclusion of the torquing electronics and suspension

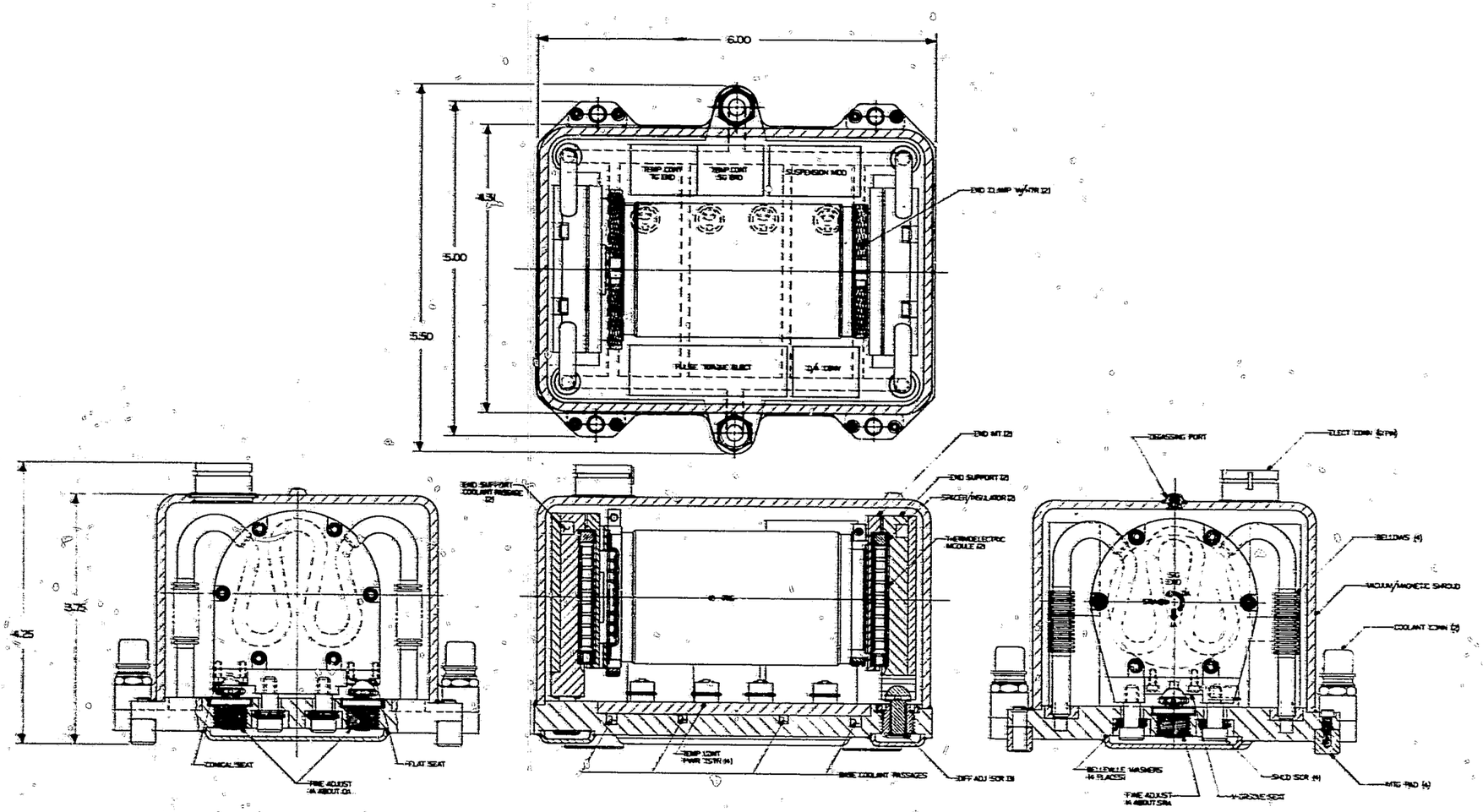

Fig. 1.4-1 Gyro module.

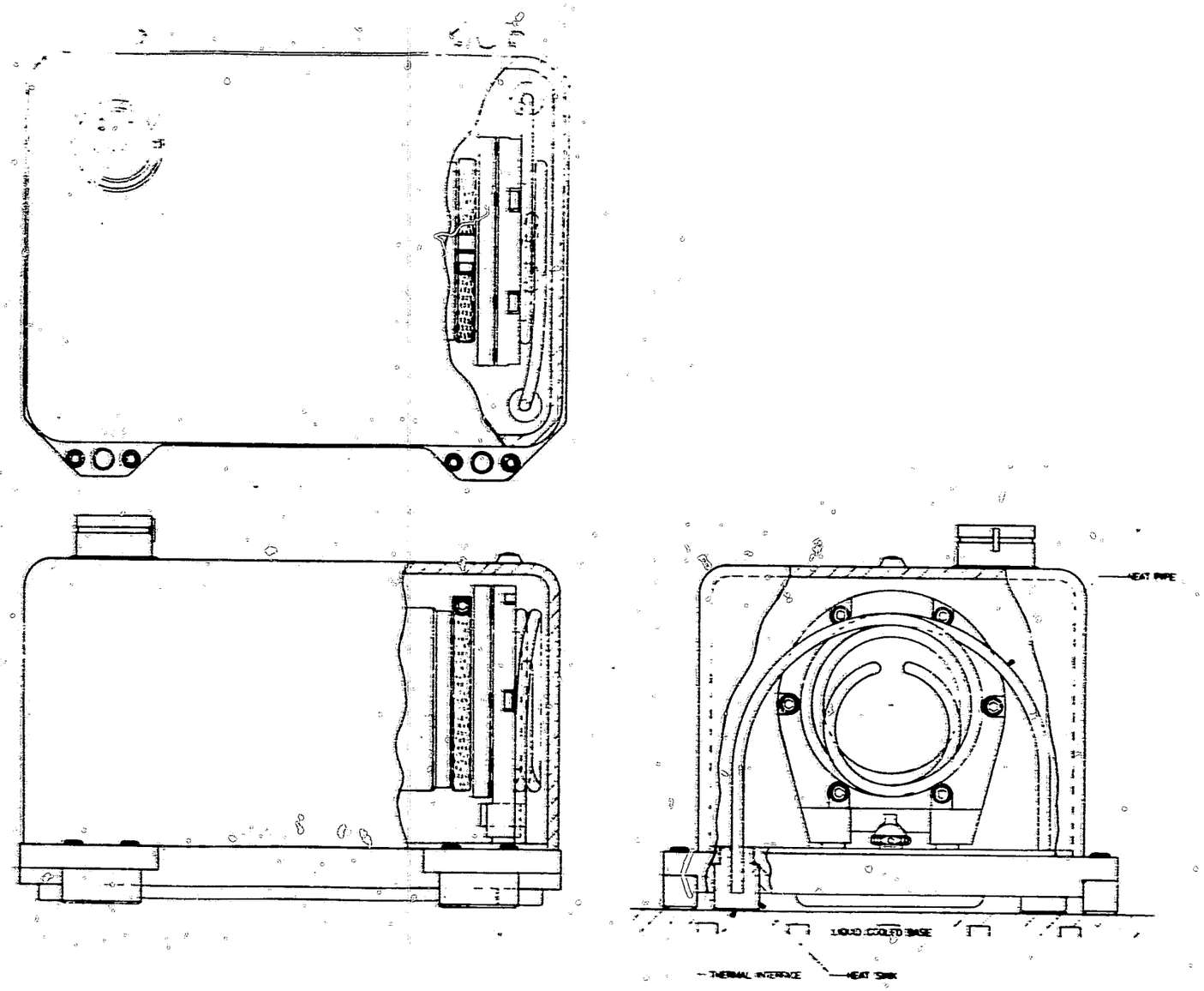

Fig. 1.4-2 Gyro module thermal strap-in mount.

components within the module allows a compatible electronic normalization of the instrument for interchangeability. Normally adjusted parameters to account for torquer scale factor and tuning, instrument transfer function, etc, are thereby self-contained within the functional assembly. The primary electronic interfaces then reduce to power, clock, and output data lines which are identical for all units. Inclusion of the digital-analog conversion module implies self-contained monitoring and signal conditioning. The digital monitoring interface allows for onboard data management using the computer and facilitates test and maintenance procedures.

The thermal design shown (consistent with studies described in Volume I, Section 2, 2, 7, and Appendix A) considered the use of thermoelectric materials for the control elements. The studies have shown that the thermoelectric elements exhibit a higher performance coefficient compared to conventional heaters. For example, in a test in which a 10^{o} difference existed between the heat sink and the desired instrument temperature the thermoelectric device used one-third the power of an equivalent conventional heater. The device is also bidirectional, and therefore allows heating or cooling depending upon the environment.

Figure 1, 4-1 shows integral coolant passages within the gyro module tied directly to heat sinks that are attached to the instrument with thermal isolation and control provided by the thermoelectric modules. Figure 1, 4-2 shows the end-mount heat sink tied to a liquid cold plate (or system heatsink) via thermal straps (heat-pipes are shown since they represent a potential thermal short circuit). The use of separate temperature controllers for each instrument end was considered to correct for asymetric heat dissipation due to the large currents required by the gyro torquer at 1-radian-per-second input rates. Torquer magnet improvements (Section 3, 3, 5D) should eliminate this consideration. The overall thermal module design features in both illustrations are compatible with system variable thermal resistance design concepts described in Chapter 4, Section 4, 3. In total, the thermal mechanization allows adaptability to a variable environment while maximizing thermal control power efficiency.

Finally, the module design illustrates a mechanical alignment concept for the gyro. Note that the instrument alignment and thermal control function are essentially separated. The instrument alignment adjustment is achieved by rotating the entire gyro cradled between its two end-support heat sinks. A flat and conical seat is located on the base of one end support and a V groove on the other. They form a three-point kinematic mount. Adjustment is achieved by rotating the fine screws in the module base which advance or retract the balls that mate with the seats on the end supports. Differential rotation of the two screws at one of the base adjust the gyro IA about OA, while adjustment of the screw on the V-groove end adjusts the gyro IA about SRA.

The module illustrations represent a first-cut conceptual design. As such, considerable improvements are realizable, and other design approaches should be reviewed. They do, however, serve to illustrate many of the design considerations that are essential to the attainment of modular-inertial-instrument in-flight interchangeability.

1.5 Strapdown System-Spacecraft Testing

Apollo experience has shown that for an extended period of time prior to vehicle launch the inertial subsystem is installed in the spacecraft. During this period the system is used in combined spacecraft-systems integration testing. It is in this phase of operations in which the spacecraft is earth-fixed that a gimballed inertial subsystem's (IMU) orientation flexibility is advantageous. For example, in the spacecraft stacked configuration IMU gimbal rotations may be commanded so that accelerometer and the corresponding gimbal angle sensor outputs provide stimuli for functional spacecraft system tests (thrust vector and reaction control system phasing and scaling). Further, this gimbal orientation flexibility allows the stable member to be rotated so that inertial components may be oriented with respect to the earth-rate vector and local vertical. Thus, the inertial instrument parameters (bias, acceleration sensitive bias, etc.) may be monitored[11] during the extended spacecraft buildup and pre-launch phases and a high degree of performance confidence is assured prior to launch. In contrast, the same measure of confidence with current[12] strapdown system configuration concepts can only be achieved by removal of the sensor package and subsequent laboratory testing. This single factor can represent a serious constraint on spacecraft operations. Procedural system removal and test implies that the spacecraft installation is such that the package is readily accessable and easily removed. Extremely durable electrical and coolant interconnection interfaces are also required to withstand the hazards of periodic package removal and test.

One obvious solution to this constraint is to mount the strapdown package on a navigation base that incorporates a provision for rotation of the package in the spacecraft, i.e., "put the package on a gimbal". This does not imply that a multiaxis gimbal structure, which would nullify all of the advantages cited for the strapdown system, is required. A satisfactory solution may be achieved with a single-degree-of-freedom gimbal that is manually oriented to detent positions or, at most, driven to desired positions by a stepper motor. The multisensor configuration, by virtue of the non-orthogonal instrument orientations, is readily adaptable to a high confidence instrument test with only a single degree of rotational freedom. Further, its self-contained comparative capabilities coupled with non-orthogonallity with respect to the earth rate and local vertical vectors assures a considerable level of instrument performance confidence without any rotational test freedom. If one were to consider implementing a single test gimbal only, limited motion would be required and sliprings, etc. would not be needed. In mission operations the gimbal would be locked and not affect the system reliability.

A more sophisticated approach which combines the radiation sensor system and the inertial sensors was conceptually investigated as part of the Advanced Control

Guidance, and Navigation study. The instrument is schematically illustrated in Fig. 1.5-1. The radiation sensors and concepts are fully described in Vol. III of the study report. Briefly, the radiation sensor configuration depicts a dual-line-of-sight automatic photometric sextant that has four degrees of freedom and allows maximum spherical coverage. The sensor assembly incorporates photometers and star trackers and utilizes a vidicon for functional astronaut monitoring.

With regard to the inertial subsystem, the mechanization shows the inertial instruments mounted on the outer hemisphere. In this study a triad of three 16 PM PIRG's and three 18 MOD B IRIG's were used. The hemisphere, which is also the outer motion isolation gimbal of the radiation sensor package, constitutes the equivalent of the navigational base between the optical and inertial references. Both sensor systems can be thought of as operating cooperatively for mutual measurement back-up and calibration.

In the case of the inertial sensors, their calibration can be achieved by using the radiation sensor system to orient and precisely define the instrument axes, via the rotation of the outer gimbal and its sensor readouts. The inertial instrument alignments were selected in the conceptual model such that the instrument IA triad was configured about the axis of rotation of the outer gimbal. The IA's are orthogonal but the gimbal axis is set so that it is angularly equidistant from each axis, (approximately 54^{o}). With this orientation, if we consider the sensor package installed on the side of the vehicle with the outer rotational axis essentially perpendicular to local vertical, a series of rotations may be defined that orient instrument axes with respect to earth rate and local vertical. The use of this set of orientations enables an accurate determination of each instrument's parameters.

Figure 1.5-2 is a design layout of the combined sensor assembly in which two of the inertial instruments are shown. Electrical interconnections are made using a flexible cable assembly. Inertial instrument access in this case would be attained by removal of the cover or cover plates on the assembly. This section of the instrument assembly is within the spacecraft compartment.

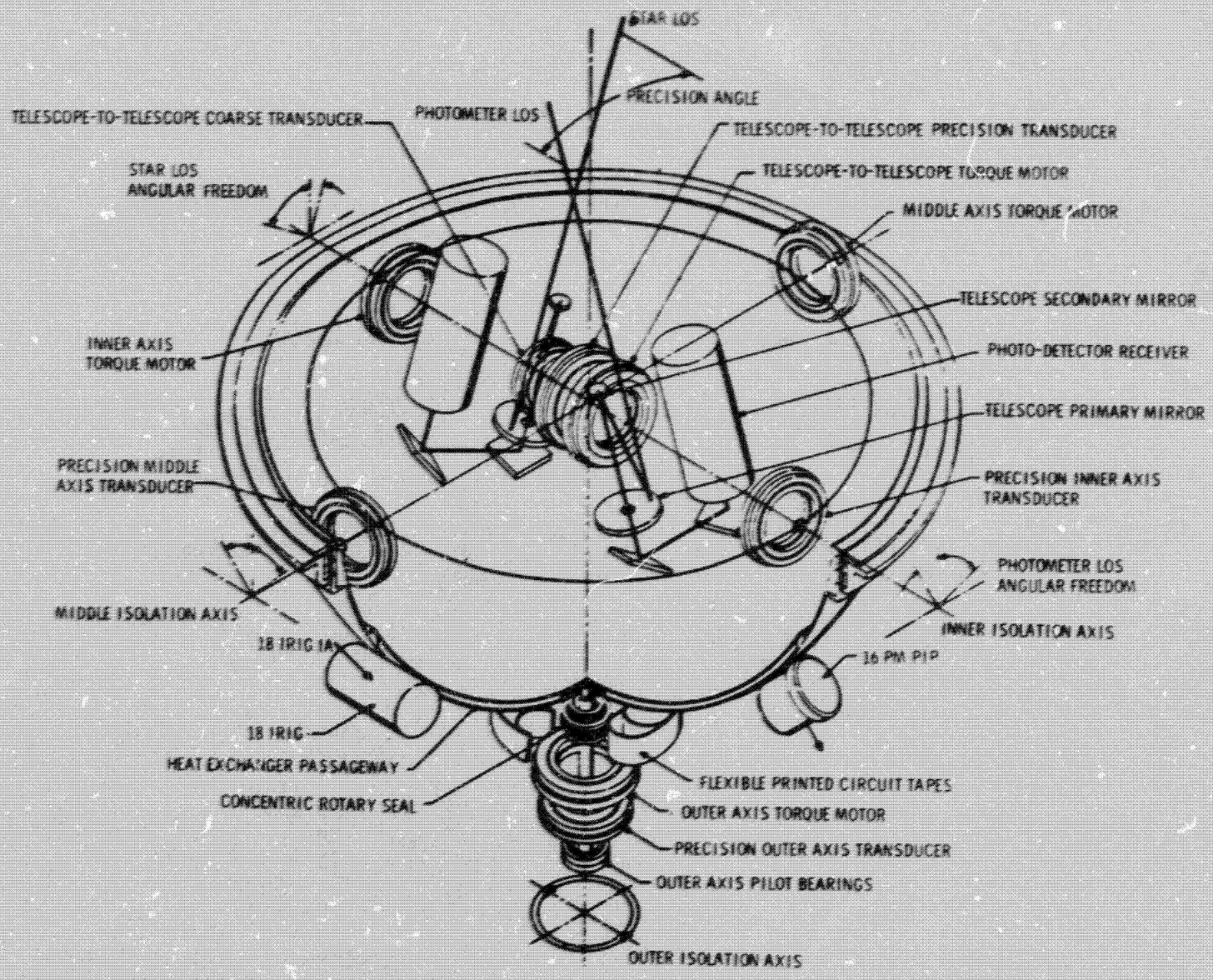

Fig. 1.5-1 Schematic, conceptual model combined radiation and inertial sensor assembly.

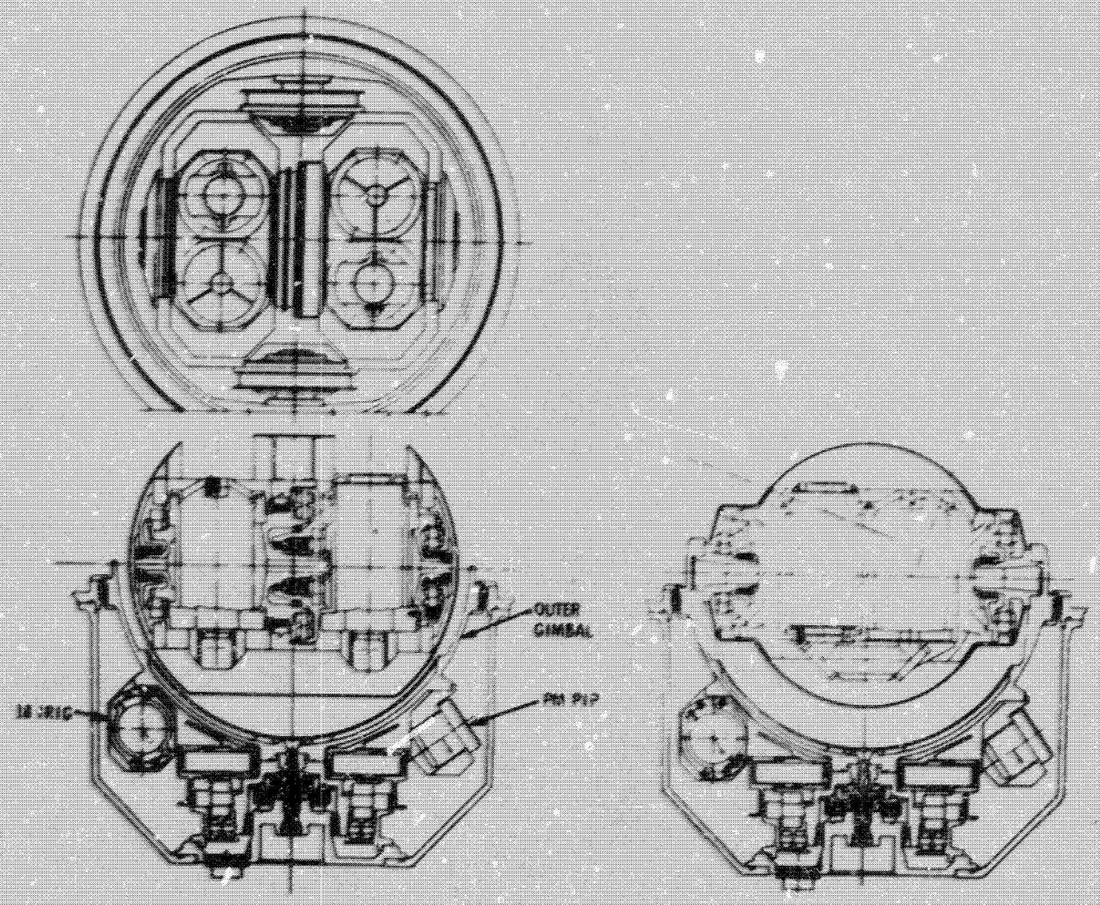

Fig. 1.5-2 Design layout of combined radiation and inertial sensor assembly.

2. ATTITUDE ALGORITHM AND INSTRUMENT MODEL DEVELOPMENT

2.1 Introduction

This chapter summarizes analysis studies conducted to provide a foundation for strapdown system development and, in addition, as direct support for the three axis test evaluation program described in Chapter IV. Specifically, the development of suitable computational attitude algorithms, instrument dynamic error models and dynamic models of the combined pulse-restrained-instrument control loop were undertaken.

In the area of attitude algorithms, the quaternion and direction cosine matrix was studied. Emphasis was placed on the development of whole-number algorithms suitable for implementation in general-purpose computer. Whole-number algorithms were clearly more compatible with the multi-processor concepts developed under the computer study portion (Vol. II) of the overall Advanced CG&N program. Further, they may be flexibly adapted in available small-general-purpose computer. First and third-order quaternion and direction cosine algorithms were developed and comparitive error analysis for constant slew rates and coning inputs were formulated. Algorithm parameters that were evaluated are: computational update rates, data quantization, and word length. These studies are described in section 2.2 of this chapter; the relative advantages of each algorithm are also discussed. In general, the analysis studies showed that a third-order algorithm operating at moderate update rates would satisfy all anticipated system requirements. For example, in a coning environment of $1/2^{o}$ amplitude at 4 cps, a 34-bit third-order algorithm operating at 100 computer update per second with a gyro quantization of 6 arc seconds would result in better than one meru attitude drift performance.

Sections 2.3 and 2.4 formulate simplified equations of motion describing the single-degree-of-freedom gyroscope and pendulous accelerometer. The equation development is oriented towards defining and providing an understanding of some of the major single-degree-of-freedom instrument error sources encountered in the full dynamic environment of the strapdown application.

The gyro dynamic errors are then numerically evaluated for representative environment and test inputs using the design parameters of the 18 IRIG (Chapter III). A separate derivation of the output-axis coupling error equation that accounts for the radial motion freedom of the gyro in a magnetically suspended-floated instrument is also included. This treatment shows the frequency response characteristics of the output axis coupling equation.

Combined gyro-pulse-torque-to-balance model and simulations are described in section 2.5. These studies and simulations served to illustrate the dynamic interplay of the control-loop and gyro parameters. The simulations for example, clearly demonstrated that the gyro float response limitations cause the ternary-torque-to-balance control-loop to issue pulse bursts in lieu of regularly spaced torquing pulses for constant input rates. The pulse bursting takes place because only a small percentage of a single torque pulse's final-value float motion occurs in a control-loop sampling period. This phenomenon was subsequently corroborated during instrument testing. These findings stimulated further investigations of control development techniques to eliminate pulse-bursting and minimize float hang-off. Development of an improved torquing loop with a new approach to loop dynamic compensation is described in section 2.6. Analog simulations illustrating the potential improvements for various test inputs are included.

2.2 Transformation Algorithm Study

The term "algorithm" is defined by Webster[13] as "a rule of procedure for solving a recurrent mathematical problem". A transformation algorithm represents a recurrent mathematical form with which data can be transformed from one coordinate frame to another.

Since the ideal transformation equation would involve trigonometric terms and would, in general, not only be a function of angular velocity but also the derivatives of angular velocity over a sampling time interval, certain approximations are required to implement the transformation algorithms.

Formulation of an algorithm for use in general purpose digital computers differs considerably from an algorithm for use in a DDA (Digital Differential Analyzer). Both approaches have been investigated, however, for this study. Compatibility with the general purpose digital-computer multiprocessor concept[14] is developed in detail. The performance attained is then compared with that obtained using a first-order DDA mechanization. The DDA is capable of very high data-processing rates but is limited by hardware complexity when algorithms of higher than first-order are considered. The DDA attempts to reduce rectangular integration errors by the use of high processing rates. The practical limit of this approach is the sampling speed with which meaningful incremental angles can be extracted from the gyro loop. The digital computer is more compatible with higher-order algorithm approximations which can be updated at a much slower repetition rate. In higher-order algorithms, the integration errors are smoothed between updates by using both past and current gyro-output information.

For comparison purposes a first-order DDA algorithm mechanization program has been reviewed for use on the Honeywell DDP-516 computer. Types of DDA mechanization of the first-order direction cosine algorithm have been considered. Bumstead and Vander Velde[15] proposed an alternating-order serial-updating method reversing the order each update time. This reduces errors associated with both limit-cycle and constant-rate inputs when compared to a straight serial updating. Hession presents a serial-parallel mechanization requiring three sample times for a complete update in which sets of direction cosine elements are updated each sampling time. Broxmeyer[16] has shown a grouping algorithm mechanization to reduce the error in the off-diagonal elements. A summary of the types of DDA mechanizations suggested for the first-order direction cosine matrix is presented by Ball.[17]

The information which follows is concerned with the development of higher-order whole-number algorithm expansions and is extracted from McKern.[18] Full details and derivations are included in this reference which was prepared as Master's thesis conducted under the auspices of this program.

2.2.1 Higher Order Algorithms

Several transformation methods have been investigated, such as Euler angles, vector transformations and Cayley-Klein parameters. Only the direction cosine matrix and the quaternion offer transformations that are completely describable at all possible orientations and have linear differential equations that enable higher order expansion development.

The quaternion transformation and the direction-cosine matrix are discussed in this text. The quaternion and its associated algebra is discussed later in some explanatory detail since it is rarely referred to in current literature. (See Appendix A.) It does, however, offer some interesting advantages for strapdown attitude algorithm applications.

A) Quaternion of Transformations

The quaternion of transformation represents the rotation of the body frame with respect to the inertial frame. Visualize a rotation of the body frame about the inertial frame described by some angle α about the rotational axis $\bar{l}_n$. Then a unit quaternion describing this rotation is defined as:

$$q = \cos\alpha/2 + \bar{n}\sin\alpha/2 \qquad (2.2.1)$$

The conjugate which corresponds to the opposite rotation can be represented as:

$$q^* = \cos\alpha/2 - \bar{n}\sin\alpha/2 \qquad (2.2.2)$$

Notice by the unit quaternion definition above a constraint has been imposed such that the scalar squared plus the vector-magnitude squared is equal to one. A similarity transformation using the quaternion can now be formed which will describe an arbitrary vector being transformed from the body frame into the inertial frame as:

$$\bar{v}^I = q\bar{v}^b q^* \qquad (2.2.3)$$

where $\bar{v}^I$ is an arbitrary vector in the inertial frame and $\bar{v}^b$ is the same vector represented in the body frame. The rate of change of the quaternion is defined by:

$$\dot{q} = (\dot{\lambda} + \dot{\bar{\rho}}) = 1/2\, q\bar{\omega}^b = q\Omega \qquad (2.2.4)$$

where Ω has the quaternion form

$$\left(0 + \frac{\bar{\omega}^b}{2}\right)$$

The Taylor-series expansion for the quaternion is:

$$q(t + \Delta t) = q(t) + \dot{q}(t)\,\Delta t + \ddot{q}(t)\,\frac{\Delta t^2}{2} + \dddot{q}(t)\,\frac{\Delta t^3}{6} + \ldots \qquad (2.2.5)$$

where

$$\dot{q} = q\Omega; \qquad \ddot{q} = (q\dot{\Omega} + \Omega\dot{q}) = q(\dot{\Omega} + \Omega\Omega); \qquad (2.2.6)$$

$$\dddot{q} = q\,(\ddot{\Omega} + \dot{\Omega}\,\Omega + 2\,\Omega\dot{\Omega} + \Omega^3) \qquad (2.2.7)$$

The information available from the gyro-loop outputs over a Δt interval can also be expressed as:

$$\theta(\Delta t) = \int_t^{t+\Delta t} \omega(\tau)\,d\tau \qquad (2.2.8)$$

$$\theta\ (\Delta t) = \int_t^{t+\Delta t} \left[\omega(t) + \dot{\omega}(t)\,(\tau - t) + \ddot{\omega}(t)\,\frac{(\tau - t)^2}{2} + \ldots\right] d\tau \qquad (2.2.9)$$

and by expanding $\omega_1(\tau)$ as a Taylor series:

The first-, second-, and third-order quaternion algorithm expansion can be expressed in terms of the present incremental gyro inputs $(\theta\Delta t)$ and the last gyro output $\theta^*(\Delta t)$ as:

$$q(t + \Delta t) = q(t)\,U(t, \Delta t) \qquad (2.2.10)$$

where for:

First Order Expansion

$$U(t, \Delta t) = \left(1 + \frac{\bar{\theta}}{2}\right) \qquad (2.2.11)$$

Second Order Expansion

$$U(t, \Delta t) = \left[1 + \frac{\bar{\theta}}{2} - \frac{1}{2}\left(\frac{\bar{\theta}}{2} \cdot \frac{\bar{\theta}}{2}\right)\right] \qquad (2.2.12)$$

Third Order Expansion

$$U(t, \Delta t) = 1 + \frac{\bar{\theta}}{2} - \frac{1}{2}\left(\frac{\bar{\theta}}{2} \cdot \frac{\bar{\theta}}{2}\right) - \frac{1}{6}\left(\frac{\bar{\theta}}{2} \cdot \frac{\bar{\theta}}{2}\right)\frac{\bar{\theta}}{2} - \frac{1}{6}\left(\frac{\bar{\theta}}{2}^* \times \frac{\bar{\theta}}{2}\right) \qquad (2.2.13)$$

The incremental velocity transformation can be made using the similarity transformation as:

$$\Delta\bar{V}^i = \Delta\bar{V}^b + 2\lambda\bar{\rho} \times \Delta\bar{V}^b + 2\bar{\rho} \times (\bar{\rho} \times \Delta\bar{V}^b) \qquad (2.2.14)$$

B) Direction Cosines

Similar expansions can be written for the direction cosine matrix. The differential equation of the direction-cosine matrix is:

$$\dot{C}(t) = C(t)\Omega \qquad (2.2.15)$$

where C(t) is the direction cosine matrix and Ω is the anti-symmetric matrix representation of the angular velocity vector in the body frame, or:

$$\Omega = \begin{bmatrix} 0 & -\omega_Z(t) & +\omega_Y(t) \\ +\omega_Z(t) & 0 & -\omega_X(t) \\ -\omega_Y(t) & +\omega_X(t) & 0 \end{bmatrix} \qquad (2.2.16)$$

To propagate the direction-cosine matrix over some interval,an expansion is found of the form:

$$C(t + \Delta t) = C(t)\, M\,(t, \Delta t) \qquad (2.2.17)$$

where M(t,Δt) is a matrix which represents the incremental attitude information obtained from the gyro loops. Knowledge of the M(t,Δt) matrix would permit the recursive calculation of the current value of C(t) represented as C(t+Δt) The Taylor series expansion of C(t) can be shown as:

$$C(t + \Delta t) = C(t) + \dot{C}(t)\Delta t + \ddot{C}(t)\frac{\Delta t^2}{2} + \dddot{C}(t)\frac{\Delta t^3}{6} + \ldots \qquad (2.2.18)$$

where:

$$\dot{C} = C\Omega \qquad (2.2.19)$$

$$\ddot{C} = C[\Omega^2 + \dot{\Omega}] \qquad (2.2.20)$$

$$\dddot{C} = C[\Omega^3 + \dot{\Omega}\Omega + 2\Omega\dot{\Omega} + \dot{\Omega}\dot{}] \qquad (2.2.21)$$

Again by using the gyro-loop output information over two adjacent intervals the required matrix M(t,Δt) can now be formed as:

<u>0th-Order Expansion</u>

$$C(t + \Delta t) = C(t)\, M_0\, (t, \Delta t) \qquad (2.2.22)$$

where,

$M_o(t, \Delta t)$ is the unity matrix.

First Order Expansion

$$C(t + \Delta t) = C(t)\, M^{I}(t, \Delta t) \tag{2.2.23}$$

where,

$$M^{I}(t, \Delta t) = \left[I + \Omega\ \Delta t\right] = \begin{bmatrix} 1 & -\theta_Z & \theta_Y \\ \theta_Z & 1 & -\theta_X \\ -\theta_Y & \theta_X & 1 \end{bmatrix} \tag{2.2.24}$$

Second Order Expansion

$$C(t + \Delta t) = C(t) M^{II}(t, \Delta t) \tag{2.2.25}$$

$$M^{II}(t, \Delta t) = M^{I}(t, \Delta t) + \frac{1}{2}\begin{bmatrix} -(\theta_Y^2 + \theta_Z^2) & \theta_X\theta_Y & \theta_X\theta_Z \\ \theta_X\theta_Y & -(\theta_X^2 + \theta_Z^2) & \theta_Y\theta_Z \\ \theta_X\theta_Z & \theta_Y\theta_Z & -(\theta_X^2 + \theta_Y^2) \end{bmatrix} \tag{2.2.26}$$

Third Order Expansion

$$C(t + \Delta t) = C(t)\, M^{III}(t, \Delta t) \tag{2.2.27}$$

$$M^{III}(t, \Delta t) = M^{III}(t + \Delta t) + \frac{1}{12}\begin{bmatrix} 0 & 2\theta^2\theta_Z + \theta_X\theta_Y^* - \theta_Y\theta_X^* & -2\theta^2\theta_Y + \theta_X\theta_Z^* - \theta_Z\theta_X^* \\ -2\theta^2\theta_Z + \theta_Y\theta_X^* - \theta_X\theta_Y^* & 0 & 2\theta^2\theta_X + \theta_Y\theta_Z^* - \theta_Z\theta_Y^* \\ 2\theta^2\theta_Y + \theta_Z\theta_X^* - \theta_X\theta_Z^* & -2\theta^2\theta_X + \theta_Z\theta_Y^* - \theta_Y\theta_Z^* & 0 \end{bmatrix} \tag{2.2.28}$$

These expansions are then evaluated for various types of dynamic inputs.

2.2.2 Algorithm Evaluation

A comparison of both the direction-cosine matrix and quaternion algorithms through the first three orders of expansion is made for a theoretical coning motion. A similar evaluation is made for constant three-axis slewing and the constraint conditions associated with each transformation are evaluated. All evaluations are made over a single iteration time. The coning environment

is generated by applying equal sine and cosine inputs to two of the algorithm axes and monitoring the coning error which is shown about the third axis. Figure 2.2-1 shows a normalized response of all three orders of algorithm expansion to a coning input. It was found that both the quaternion and direction-cosine transformations yield identical results to coning half-amplitudes of 5 degrees or less. The first- and second-order algorithms shown agree well with computer simulations made by Otten.[19] The third-order curve was confirmed by computer simulations conducted on this program. Both curves were developed analytically from basic coning-geometry considerations. The large improvement in drift error shown in the third-order expansion is directly due to the use of both past and present incremental gyro outputs in the algorithm. The point $f\Delta t = 0.5$ represents the limit in the ability of any algorithm to recognize coning (i.e., at least two samples for each cycle of a sinusoidal input are required for any recognition of the actual input by the algorithm).

Figure 2.2-2 shows the equivalent information where the cone half-angle is assumed to be one degree. In this figure the coning frequency is plotted against the computer update speed. Lines of equivalent constant-algorithm drift are shown to relate the required computer-update rate for various coning input frequencies.

Table 2.2-1 shows the drift errors for constant slewing rates over a single iteration time for the first-, second-, and third-order direction-cosine algorithms. It also shows the magnitude of the errors which can be expected from the degradation of the six orthogonality constraints. Table 2.2-2 shows similar results using the quaternion. The quaternion has only a unit-length constraint. Comparing both tables, the quaternion performance is superior to the direction-cosine matrix in all orders. For example, the third-order quaternion slew error is one-sixteenth that of the direction cosine third-order slew error. A comparison of computer timing requirements is shown in Table 2.2-3 using actual programs mechanized for use on the Honeywell 516 test-system computer (ref. Chapter 4). These programs represent each algorithm mechanized in double-precision using two fifteen-bit words (a twenty-nine-bit word length with a sign bit). The ΔV transformations are also assumed to require double-precision calculations. In actual practice, the ΔV-transformation-update rate requirements may be less than that of the attitude algorithm update transformation. As such, the velocity update could be run in parallel with the attitude transformation or interleaved with attitude updates.

Figure 2.2-3 shows the effects of gyro-loop quantization and the computer word length upon the performance of both the first- and third-order algorithm to a coning input.

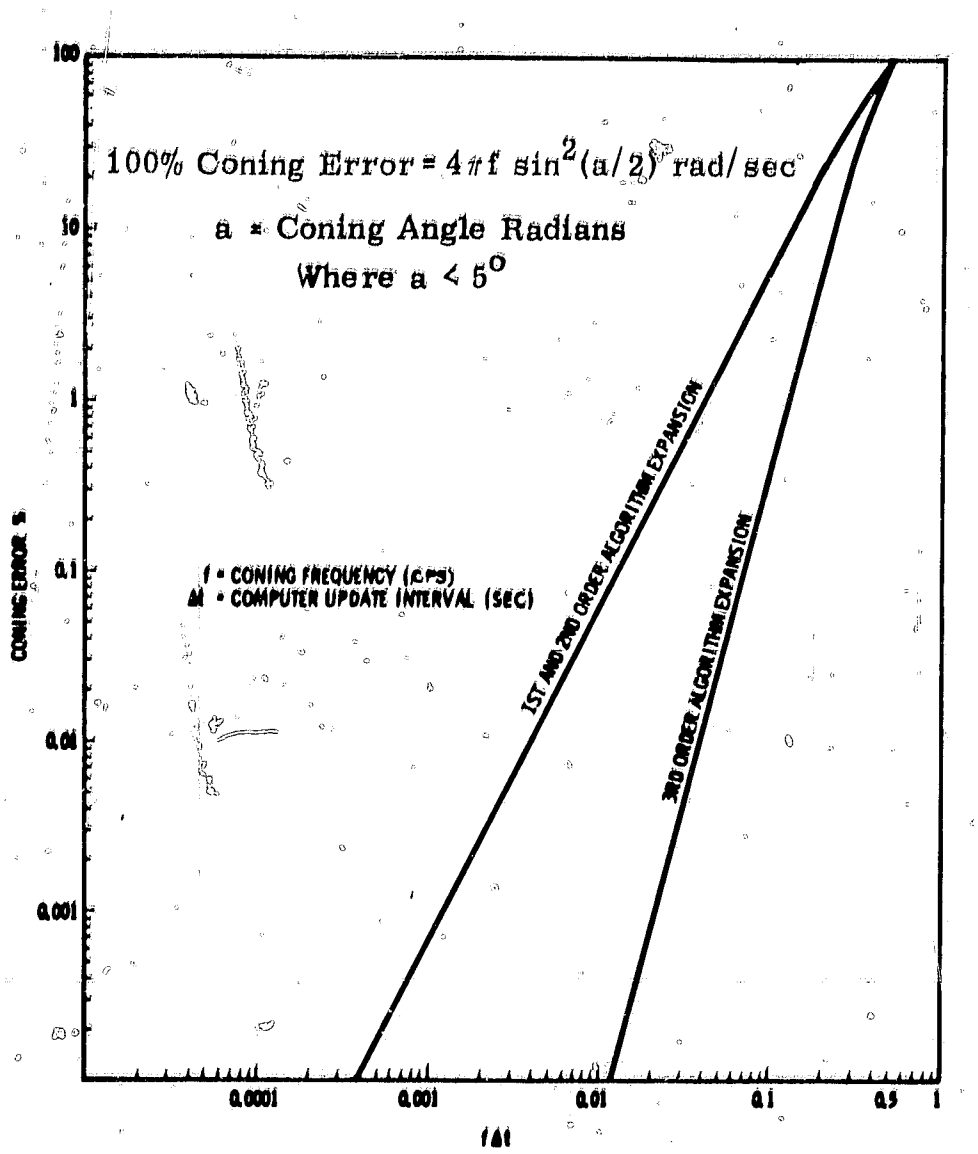

Fig. 2.2-1 Normalized coning response.

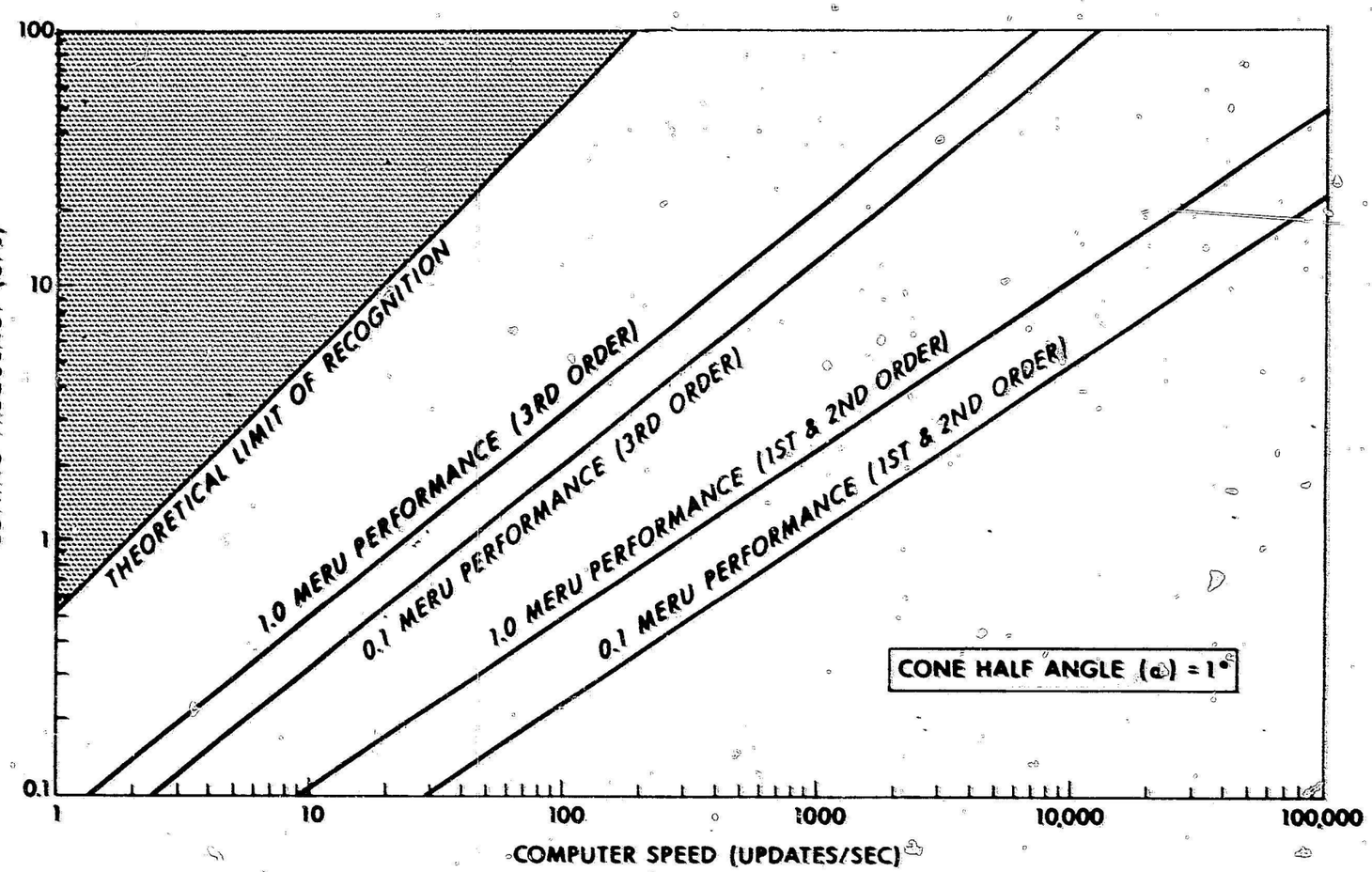

Fig. 2.2-2 Coning performance response.

TABLE 2.2-1

CONSTANT SLEW RATE - DIRECTION COSINE ALGORITHM

ALGORITHM ORDER N	THREE AXIS SLEWING ERROR	MATRIX ORTHOGONALITY ERRORS					
		LENGTH OF M^N			PERPENDICULARITY OF M^N		
		M^N_{3j}	M^N_{2j}	M^N_{3j}	$M^N_{1j} \perp M^N_{2j}$	$M^N_{1j} \perp M^N_{3j}$	$M^N_{2j} \perp M^N_{3j}$
I	$\frac{\theta^3}{3}$	θ^2_{1j}	θ^2_{2j}	θ^2_{3j}	$\theta_x\theta_y$	$\theta_x\theta_z$	$\theta_y\theta_z$
II	$\frac{\theta^3}{6}$	$\frac{\theta^2}{4}\theta^2_{1j}$	$\frac{\theta^2}{4}\theta^2_{2j}$	$\frac{\theta^2}{4}\theta^2_{3j}$	$\frac{\theta^2}{4}\theta_x\theta_y$	$\frac{\theta^2}{4}\theta_x\theta_z$	$\frac{\theta^2}{4}\theta_y\theta_z$
III	$\frac{\theta^5}{30}$	$\frac{\theta^2}{12}(1-\frac{\theta^2}{3})\theta^2_{1j}$	$\frac{\theta^2}{12}(1-\frac{\theta^2}{3})\theta^2_{2j}$	$\frac{\theta^2}{12}(1-\frac{\theta^2}{3})\theta^2_{3j}$	$\frac{\theta^2}{12}(1-\frac{\theta^2}{3})\theta_x\theta_y$	$\frac{\theta^2}{12}(1-\frac{\theta^2}{3})\theta_x\theta_z$	$\frac{\theta^2}{12}(1-\frac{\theta^2}{3})(\theta_y\theta_z)$

θ IS THE TOTAL ANGLE TRAVELED OVER A SINGLE Δt UPDATE INTERVAL

$j = 1, 2, 3$

$$\theta^2_{1j} = (\theta^2_y + \theta^2_z)$$

$$\theta^2_{2j} = (\theta^2_x + \theta^2_z)$$

$$\theta^2_{3j} = (\theta^2_x + \theta^2_y)$$

TABLE 2.2-2

CONSTANT SLEW RATE - QUATERNION ALGORITHM

ALGORITHM ORDER	THREE AXIS SLEWING ERROR	UNIT LENGTH DEGRADATION ERROR
1	$\frac{\theta^3}{12}$	$\frac{\theta^2}{4}$
2	$\frac{\theta^3}{24}$	$\frac{\theta^4}{64}$
3	$\frac{\theta^5}{480}$	$\frac{\theta^4}{192}\left(1-\frac{\theta^2}{12}\right)$

θ IS THE TOTAL ANGLE TRAVELED OVER A SINGLE Δt UPDATE INTERVAL

TABLE 2.2-3
ALGORITHM TIMING AND MEMORY REQUIREMENTS

ALGORITHM	RELATIVE COMPLEXITY	COMPUTER REQUIREMENTS		
		MEMORY (WORDS)		ACTUAL UPDATE TIME (μsec)
		PROGRAM	DATA	
DIRECTION COSINE MATRIX				
FIRST ORDER	36A + 36MPY + 72LS	207	46	544
SECOND ORDER	54A + 78MPY + 156LS	402	54	985
THIRD ORDER	78A + 114MPY + 216LS	519	63	1292
ΔV TRANSFORMATION	18A + 18MPY + 39LS	100	17	271
QUATERNION				
FIRST ORDER	24A + 24MPY + 48LS	148	23	382
SECOND ORDER	30A + 31MPY + 62LS	180	25	466
THIRD ORDER	45A + 52MPY + 98LS	273	31	704
ΔV TRANSFORMATION	57A + 45MPY + 75LS	267	31	693

A = ADDS
MPY = MULTIPLYS
LS = LOAD AND STORES

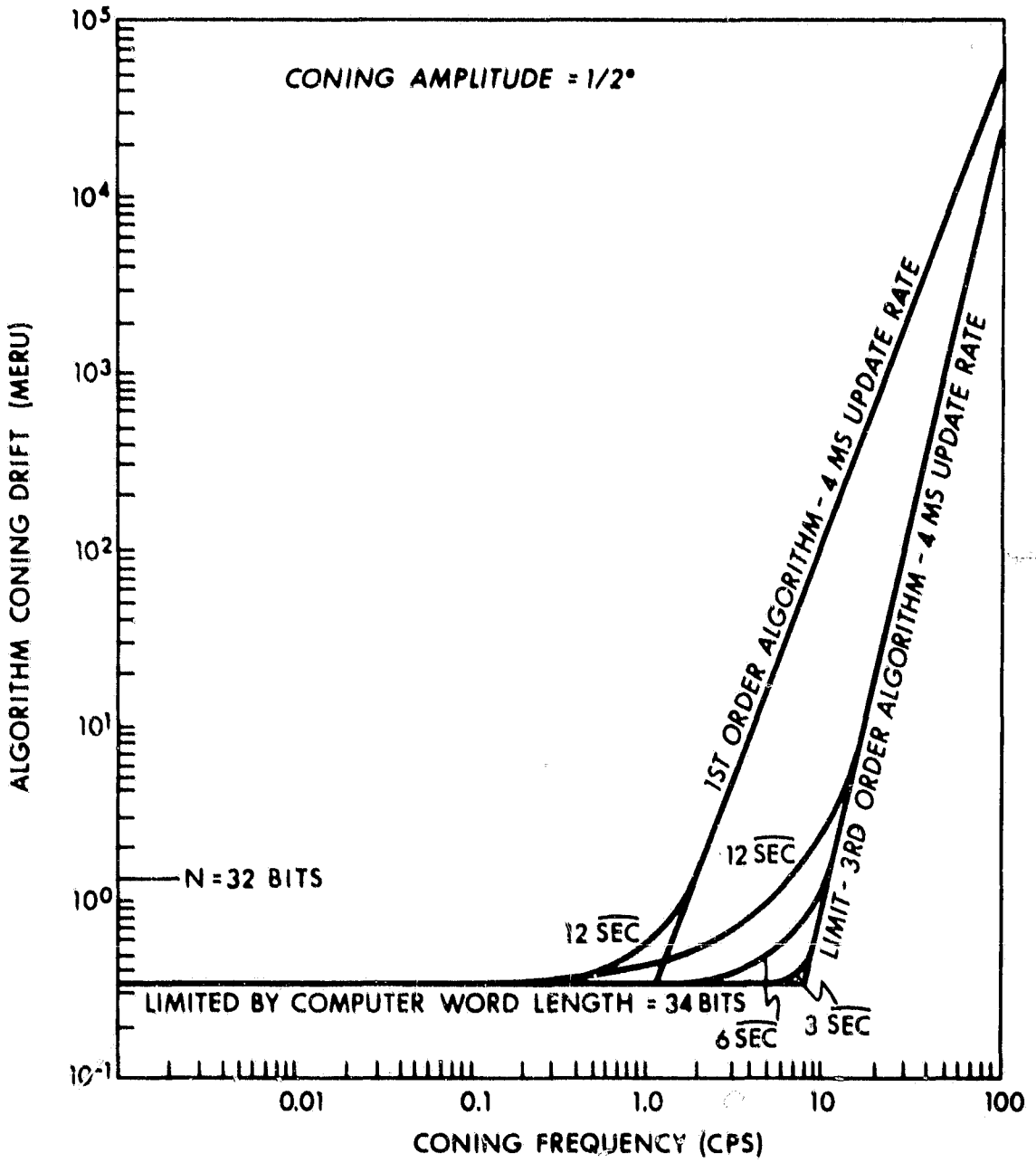

Fig. 2.2-3 Algorithm coning drift vs coning frequency.

2.2.3 Summary

The results of this study demonstrate that a third-order algorithm operating at low processing rates in a general-purpose computer yields drift-error performance that is comparable with extremely high DDA processing rates using a first-order algorithm. For example, from Fig. 2.2-2 it is seen that one-meru performance is attained at a ten-cycle-per-second coning frequency with a first-order algorithm operating at a processing rate of 10,000 updates per second. The equivalent performance for a third-order algorithm requires a processing rate of 500 updates per second. Similarly, for constant slew rates up to 0.3 radian per second, the equation in Table 2.2-1 can be used to show that the third-order direction-cosine algorithm operating at 100 updates per second yields better performance than its corresponding first-order algorithm at 10,000 updates per second. The constraint degradation errors of the third-order algorithm are also reduced in two ways. Smaller errors are propagated during each update interval. Fewer updates are required for the same general performance and therefore, for the same operational period, fewer errors are introduced. Finally, the general purpose computer allows flexibility in programming algorithm selection in accordance with mission requirements.

The comparison of transformation methods using the quaternion or the direction-cosine matrix shows no overwhelming advantage for either transformation. The quaternion of transformation, however, has a single-length constraint to normalize rather than the complete reorthogonalization of the direction-cosine matrix. The normalization of unit length in the quaternion can be accomplished on the Honeywell DDP-516 computer (double-precision) in 192 microseconds. The orthogonalization of the direction-cosine matrix is more involved and care must be taken in determining the order of the orthogonality corrections. No clear choice of orthogonalization equations was found in this study, for the method used should be modeled to the mission requirements. The third-order quaternion transformation constant slew errors were less than the direction cosine matrix. The coning frequency response of both algorithms are essentially identical. The processing time found using a Honeywell DDP-516 computer is nearly equivalent assuming both attitude and ΔV transformations are required at each update time. The quaternion attitude algorithm has useful testing advantage since the actual attitude is visualized by an inspection of the four quaternion elements. In dynamic testing, if real-time comparisons were desired, four elements must be read out of the computer at each comparison time as compared to a possible minimum of six direction-cosine matrix elements. Thus, the output processing required while the algorithm operation continues is reduced.

2.3 Single-Degree-of-Freedom Gyro Dynamics

The purpose of this section is to provide a background treatment of dynamic errors associated with the single-degree-of-freedom (SDF) floated-inertial gyroscope. The various dynamic errors are then evaluated for representative inputs. Special treatment is given to the output axis coupling functions so that its frequency response characteristics will be clearly evidenced. A numerical error summary using 18 IRIG gyroscope parameters is also included.

2.3.1 General Equations

The principle of operation of the gyroscope is formulated in terms of angular momentum. Equations describing the motion of the gyroscope are defined in both case (C) and gimbal element (f-float) coordinate frame. A pictorial schematic illustrating the float case frame is shown in Fig. 2.3-1. The applied torque $\overline{M}^f$ expressed in the float coordinate frame is:

$$\overline{M}^f = \left(\frac{d\overline{H}^f}{dt}\right)_i \qquad (2.3.1)$$

where:

$\overline{H}_f$ = float angular momentum in the float coordinate frame (Upper subscripts correspond to reference coordinate frames; lower subscripts indicate the frame with respect to which an operation vector is defined.)

It is convenient to express the rate of change of angular momentum in terms of the equation of Coriolis:

$$\overline{M}^f = \left(\frac{d\overline{H}^f}{dt}\right)_f + \overline{W}^f_{if} \times \overline{H}^f \qquad (2.3.2)$$

where:

$\overline{W}^f_{if}$ = the angular rate of the float with respect to inertial space.

The angular momentum of the gyro may be expressed in terms of its spinning element ($\overline{H}_s$ - the wheel) and its non-spinning gimbal structure ($\overline{H}_{ns}$).

$$\overline{M}^f = p_f \overline{H}^f_s + p_f \overline{H}^f_{ns} + \overline{W}^f_{if} \times \overline{H}^f_s + \overline{W}^f_{if} \times \overline{H}^f_{ns} \qquad (2.3.3)$$

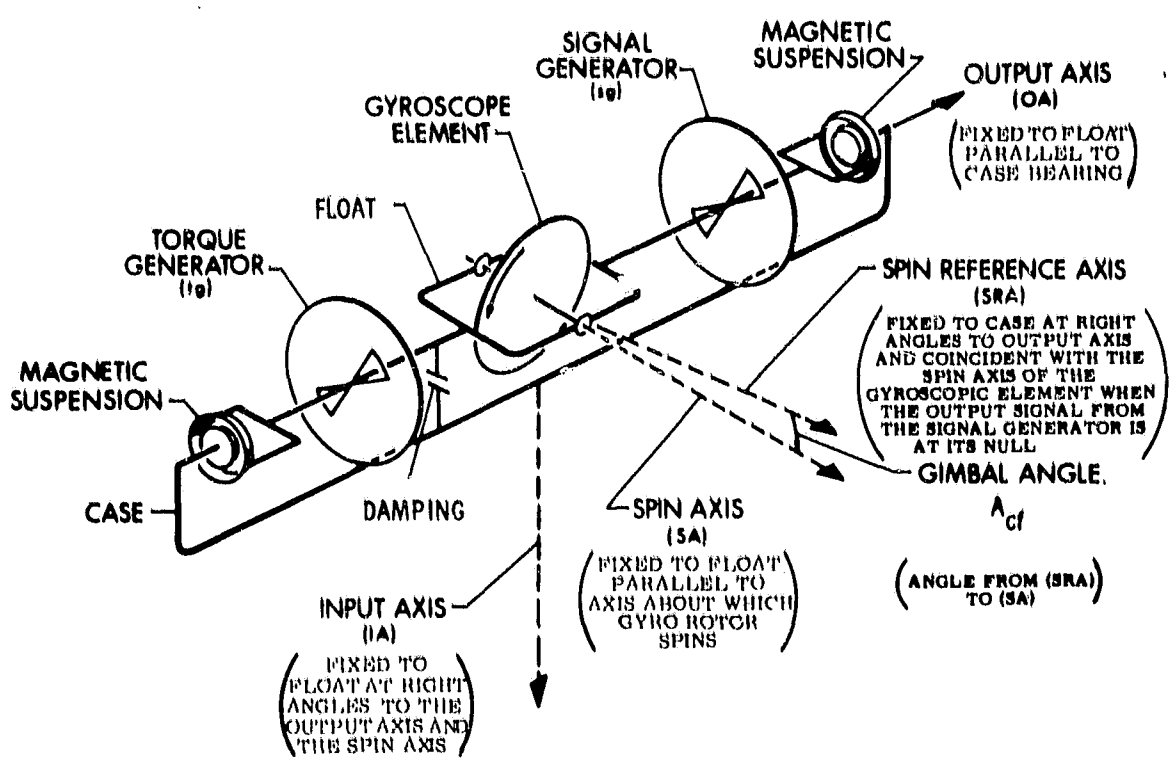

NOTES:

1. POSITIVE SENSES SHOWN BY THE ARROWS ARE CHOSEN SO THAT (IA), (SRA), AND (OA) FORM A RIGHT-HANDED SYSTEM.

CASE - (c) - THE STRUCTURE THAT GIVES SUPPORT FOR THE INTERNAL WORKING PARTS OF THE GYRO UNIT, ENCLOSES THE PARTS, AND CARRIES PROVISIONS FOR EXTERNAL CONNECTIONS OF ALL KINDS.

TORQUE GENERATOR - (tg) - COMPONENT FOR RECEIVING INPUT SIGNALS AND PRODUCING CORRESPONDING OUTPUT TORQUE APPLIED TO THE FLOAT ABOUT THE OUTPUT AXIS.

DAMPING - (Float to case) FOR ANGULAR VELOCITY OF THE FLOAT WITH RESPECT TO THE CASE A RETARDING TORQUE ACTING ON THE FLOAT WITH A MAGNITUDE PROPORTIONAL TO THE MAGNITUDE OF THE ANGULAR VELOCITY OF THE FLOAT WITH RESPECT TO THE CASE.

SIGNAL GENERATOR -(sg)- COMPONENT FOR RECEIVING THE ANGLE OF THE SPIN AXIS WITH RESPECT TO THE CASE AS INPUT AND PRODUCING A CORRESPONDING SIGNAL THAT SERVES AS THE OUTPUT SIGNAL FROM THE GYRO UNIT.

FLOAT - STRUCTURE CARRYING THE BEARINGS FOR THE SPINNING ROTOR OF THE GYROSCOPIC ELEMENT, ROTORS FOR THE TORQUE GENERATOR AND SIGNAL GENERATOR, PART OF THE DAMPER, FLOAT SEALS AND STRUCTURE, BALANCE ADJUSTMENTS, STOPS, PIVOTS, ETC.

Fig. 2.3-1 Line schematic diagram of single-degree-of-freedom floated integrating gyro unit.

where:

$$\overline{W}_{if}^{f} = \begin{bmatrix} W_{SA} \\ W_{IA} \\ W_{OA} \end{bmatrix} , \quad \overline{M}^{f} = \begin{bmatrix} M_{SA} \\ M_{IA} \\ M_{OA} \end{bmatrix}$$

$$\overline{H}_{s}^{f} = \begin{bmatrix} H_{s} \\ 0 \\ 0 \end{bmatrix} , \quad \overline{H}_{ns}^{f} = \underline{I}\,\overline{W}_{if}^{f}, \quad \underline{I} = \begin{bmatrix} I_{SA} & 0 & 0 \\ 0 & I_{IA} & 0 \\ 0 & 0 & I_{OA} \end{bmatrix}$$

(The operator p is introduced for the derivative expression.)

The float axes are defined as the spin (SA), input (IA), and output (OA), and are selected to correspond to the principal axes of inertia, I. The case axes are defined as spin reference (SRA), input reference (IRA), and output reference (ORA).

The angular rate of the float may be defined in terms of the case inertial rates ($\overline{W}_{ic}^{c}$) and the relative rates between the float and the case ($\overline{W}_{cf}^{f}$).

$$\overline{W}_{if}^{f} = \left[R_{c}^{f} \right] \overline{W}_{ic}^{c} + \overline{W}_{cf}^{f} \qquad (2.3.4)$$

where:

$$\overline{W}_{ic}^{c} = \begin{bmatrix} W_{SRA} \\ W_{IRA} \\ W_{ORA} \end{bmatrix} , \quad \overline{W}_{cf}^{f} = \begin{bmatrix} \dot{A}_{SA} \\ \dot{A}_{IA} \\ \dot{A}_{OA} \end{bmatrix}$$

$\left[R_{c}^{f} \right]$ is a transform matrix that relates the case rates in the case coordinate frame to corresponding rates in the float coordinate frame. (Brackets or a bar below a letter will be used to denote a matrix representation.)

Torques are generally applied to the float with respect to the case by suspension forces and fluid damping. The corresponding torque equation is:

$$\overline{M}^{f} = - \left[C \right] \overline{W}_{cf}^{f} - \left[K \right] \overline{A}_{cf}^{f} + \overline{M}_{g2}^{f} + \overline{M}_{TG}^{f} \qquad (2.3.5)$$

$$+ M_{g}^{f} + M_{b}^{f}$$

Where C is the float damping, K represents the suspension and other elastic spring restraints, M^f_{g2} represents anisoelastic torques, and M^f_{TG} represents the command or control torques from the instrument torque generator. M^f_g and M^f_b are acceleration sensitive and the bias (acceleration sensitive) torques respectively. For the remaining sections they are omitted since they are not dynamic error sources in the sense of these derivations.

2.3.2 Simplified SDF Gyro Equation of Motion:

As a starting point it is desirable to develop the equations of motion of the float for a simplified gyro representation. The simplifying assumptions are:

1. All internal rotations of the float within the case are about OA; no other relative rotations exist. Thus, the C and F frames are aligned when the gyro is at a null. (The float OA and case ORA axes are coincident.)

2. There are no spring restraints about OA, ie: no signal generator, flex lead, suspension, or torquer elastic restraints.

3. There is no bearing friction between the float and case or between the wheel and float.

4. The wheel mount is perfectly rigid within the float, ie: there is no compliance, and the gimbal structure is perfectly rigid.

We may develop the float equations directly from (2.3.3):

$$M_{SA} = I_{SA}\,\dot{W}_{SA} + (I_{OA} - I_{IA})\,(W_{OA}\,W_{IA}) + \dot{H}_s$$

$$M_{IA} = I_{IA}\,\dot{W}_{IA} + (I_{SA} - I_{OA})\,W_{OA}\,W_{SA} + W_{OA}\,H_s \qquad (2.3.6)$$

$$M_{OA} = I_{OA}\,\dot{W}_{OA} + (I_{IA} - I_{SA})\,W_{IA}\,W_{SA} - W_{IA}\,H_s$$

The pertinent angular inputs to the SDF gyro are the inertial rates that are applied to the case. In the strapdown application the torque generator, M_{TG}, about the ORA is used as a measure of the angular rate applied about the case input reference axis, W_{IRA}. Equation (2.3.4) may be used to relate the case rates to the float rates.

Using the simplifying assumptions allows one to define $\underline{R}^f_c$ and $\overline{W}^f_{cf}$ in terms of the angle and angular rate between the case ORA and float OA axes.

$$\underline{R}_c^f = \begin{bmatrix} \cos\theta & \sin\theta & 0 \\ -\sin\theta & \cos\theta & 0 \\ 0 & 0 & 1 \end{bmatrix} \qquad (2.3.7)$$

$$\overline{W}_{cf}^f = \begin{bmatrix} 0 \\ 0 \\ \dot{\theta} \end{bmatrix} \qquad (2.3.8)$$

where: $\dot{\theta} = \dot{A}_{OA}$

Substituting (2.3.7) and (2.3.8) into (2.3.4) yields:

$$\begin{aligned} W_{SA} &= W_{SRA}\cos\theta + W_{IRA}\sin\theta \\ W_{IA} &= W_{IRA}\cos\theta - W_{SRA}\sin\theta \\ W_{OA} &= W_{ORA} + \dot{\theta} \end{aligned} \qquad (2.3.9)$$

Substituting (2.3.9) into (2.3.6) and then using a small angle approximation gives:

(Note that $\dot{W}_{IA} = \dot{W}_{IRA}\cos\theta - W_{IRA}\dot{\theta}\sin\theta - \dot{W}_{SRA}\sin\theta - W_{SRA}\dot{\theta}\cos\theta$)

$$\begin{aligned} M_{SA} &= I_{SA}(\dot{W}_{SRA} - \dot{\theta}\,\theta\,W_{SRA} + \dot{W}_{IRA}\,\theta + W_{IRA}\,\dot{\theta}) \\ &\quad + (I_{OA} - I_{IA})(W_{ORA} + \dot{\theta})(W_{IRA} - W_{SRA}\,\theta) + \dot{H}_s \\ M_{IA} &= I_{IA}(\dot{W}_{IRA} - \dot{\theta}\,\theta\,W_{IRA} - \dot{W}_{SRA}\,\theta - \dot{\theta}\,W_{SRA}) \\ &\quad + (I_{SA} - I_{OA})(W_{ORA} + \dot{\theta})(W_{SRA} + W_{IRA}\,\theta) + H_s(W_{ORA} + \dot{\theta}) \\ M_{OA} &= I_{OA}(\dot{W}_{ORA} + \ddot{\theta}) + (I_{IA} - I_{SA})(W_{IRA} - W_{SRA}\,\theta)(W_{SRA} + W_{IRA}\,\theta) \\ &\quad - H_s(\dot{W}_{IRA} - W_{SRA}\,\theta) \end{aligned} \qquad (2.3.10)$$

These equations represent the torques on the float M_{SA}, M_{IA}, M_{OA} in terms of input rates about the case axes, W_{IRA}, W_{SRA}, W_{ORA}.

A further idealization of the gyro (not listed in the original set of assumptions) would have been to consider $I_{SA} = I_{IA} = I_{OA}$. Clearly this would have eliminated the corresponding anisoinertia terms in each of the three equations.

The output axis equation is of major interest and its characteristics will now be reviewed.

2.3.3 Output Axis Equations

The output axis torques derived from (2.3.5) using the same assumptions as in the previous section are:

$$M_{OA} = - C_{OA} \dot{\theta} + M_{TG} + M_{g^2OA} \qquad (2.3.11)$$

The anisoelastic torque may be formulated by relaxing the previous section's assumption that the wheel suspension was perfectly stiff and that a finite compliance ($\underline{k}$) of the wheel within the float exists. A linear acceleration $\bar{a}$ of the gyroscope would then produce a corresponding gyroscopic torque. For example, the force resulting from the acceleration of the wheel mass (m) produces a deflection of the wheel CG along all three float axes:

$$\bar{d} = \underline{k}\, \bar{F}$$

where:

$$\bar{F} = m \begin{bmatrix} a_S \\ a_I \\ a_O \end{bmatrix} \qquad (2.3.12)$$

The resultant $M_g^f 2$ sensitive torque is:

$$M_g^f 2 = \bar{d} \times \bar{F} = \underline{k}\, \bar{F} \times \bar{F} \qquad (2.3.13)$$

The wheel compliances are represented in matrix notation:

$$\underline{k} = \begin{bmatrix} k_{SS} & k_{SI} & k_{SO} \\ k_{IS} & k_{II} & k_{IO} \\ k_{OS} & k_{OI} & k_{OO} \end{bmatrix} \qquad (2.3.14)$$

Each element k_{mn} is defined such that the subscript m denotes the deflection direction and the subscript n denotes the direction of the force. Evaluation of (2.3.13) using the compliance matrix for the float output axis torque yields:

$$M_{g^2OA} = m^2 \left[a_S a_I (k_{SS} - k_{II}) - a_S{}^2 k_{IS} + a_I{}^2 k_{SI} - a_O a_I k_{IO} + a_O a_S k_{SO} \right] \qquad (2.3.15)$$

Adding (2.3.15) to (2.3.11) and equating the torque equation to the output axis equation of (2.3.10) results in the total output axis dynamic equations. (The second order terms in θ^2 are omitted, note that the terms θ and A_{OA} are used interchangeably in these equations.)

$$I_{OA} \frac{d^2 A_{OA}}{dt^2} + C_{OA} \frac{d A_{OA}}{dt} = H_s W_{IRA} + M_{TG} - H_s W_{SRA} A_{OA} - I_{OA} \dot{W}_{ORA} + (I_{SA} - I_{IA}) \left[W_{IRA} W_{SRA} + (W_{IRA}^2 - W_{SRA}^2) A_{OA} \right] + m^2 \left[a_S a_I (k_{SS} - k_{II}) - a_S{}^2 k_{IS} + a_I{}^2 k_{SI} - a_O a_I k_{IO} + a_O a_S k_{SO} \right] \qquad (2.3.16)$$

where:

- $I_{(\ )}$ = the moment of inertia of the float about each of its principal axes (SA, IO, OA).
- C_{OA} = the viscous damping coefficient of the float about OA
- H_s = the spin angular momentum of the wheel
- A_{OA} = the angle about OA (θ), of the float with respect to the case
- $W_{(\ )}$ = the angular velocity of the gyro case about each of its respective reference axes (SRA, IRA, ORA).
- $a_{(\ )}$ = the linear acceleration of the gyro along float axes (S, I, O).
- $k_{m,n}$ = the compliance of the wheel within the float along the mth axis due to force along the nth axis.

The terms on the left correspond to the float rotational dynamic response. The first and second terms on the right correspond to the desired input rate and measurement control torque. The remaining terms on the right side represent measurement error sources corresponding to:

$H_s W_{SRA} A_{OA}$ - axis crosscoupling

$I_{OA} \dot{W}_{ORA}$ - output axis coupling

$(I_{SA} - I_{IA}) \left[W_{IRA} W_{SRA} + \ldots \right]$ - anisoinertia

$-m^2 \left[a_S a_I (k_{SS} - k_{II}) - \ldots \right]$ - anisoelastic

(Torques arising from float mass unbalance, etc., that result in acceleration sensitive torques are not considered in this dynamic analysis; they are discussed in Chapter 3.) The most simplified representation of the gyroscopic behavior corresponds to equating the restraining torque M_{TG} to the input axis case rate and neglecting float rotational dynamics (a steady-state, constant-rate solution is inferred).

$$M_{TG} = H_s W_{IRA} \qquad (2.3.17)$$

A linearized analysis may be applied to the output axis equation described in (2.3.16) so that solutions for $\dot{\theta}$ can be developed independently for each input and error source term on the right hand side of the equation. The total $\dot{\theta}$ solution is then the sum of all individual solutions. It represents the float rate that would be measured and quantized as an input to a strapdown attitude algorithm. Dependent upon the attitude performance desired it may be necessary to dynamically correct for these error terms. To provide some insight into the character of each error source, time dependent solutions for various rate and acceleration conditions (steps, ramps, and sinusoids) expressed in terms of an equivalent input error rate are outlined in the following subsections. The equivalent input rate is defined as:

$$W_D = \frac{C_{OA}}{H_s} \dot{\theta} \qquad (2.3.18)$$

2.3.4 Error Sources

A) Basic Input Response

To provide a base line consider the gyro response equation:

$$I_{OA} \ddot{\theta} + C_{OA} \dot{\theta} = H_s W_{IRA} \qquad (2.3.19)$$

The output float rate response may then be defined for each of the following input rates, when the initial float conditions are:

$$t = 0,\ \dot{\theta} = 0,\ \ddot{\theta} = 0 \qquad (2.3.20)$$

1) $W_{IRA} = W_I\, U_{-1}(t)$

a step of rate at t = 0

$$\dot{\theta} = W_I \frac{H_s}{C_{OA}} \left[1 - e^{-t/\tau} \right] \qquad (2.3.21)$$

where $\tau = \dfrac{I_{OA}}{C_{OA}}$

2) $W_{IRA} = W_I\, U_{-2}(t)$,

a ramp of rate at t = 0

$$\dot{\theta} = W_I \frac{H_s}{C_{OA}} \left[t + \tau\ (e^{-t/\tau} - 1) \right] \qquad (2.3.22)$$

3) $W_{IRA} = W_I \sin \omega t$

If $\omega\tau << 1$ then $\cos \omega\tau \simeq 1$ and

$$\dot{\theta} \simeq W_I \frac{H_s}{C_{OA}} \left[\sin(\omega t - \psi) + \tau\, \omega e^{-t/\tau} \right]$$

$$\simeq W_I \frac{H_s}{C_{OA}} \left[\sin \omega t + \tau\, \omega (e^{-t/\tau} - \cos \omega t) \right]$$

where: $\psi = \tan^{-1}(\tau\omega)$ (2.3.23)

(The 18 IRIG Mod B time constant equals 450 μsec.)

Equations (2.3.21) through (2.3.23) demonstrate that the float dynamics introduce measurement errors in the form of an exponential transient in the case of step and ramp input. For an oscillatory input both an exponential transient and phase lag is introduced.

B) Output Axis Coupling

This error term is principally introduced by the inertia of the float output axis. Physically we may view this effect as the tendency of the float to remain at rest when the case is accelerated about the output axis. (A more comprehensive treatment of output axis coupling that evidences the interaction of the float input and output axis dynamics is presented in Section 2.3.5).

The applicable gyro response equation is:

$$I_{OA}\,\ddot{\theta} + C_{OA}\,\dot{\theta} = -\,I_{OA}\,\dot{W}_{ORA} \qquad (2.3.24)$$

The float response expressed as an equivalent input rate error, W_D, is presented for each of the following rate functions applied at t = 0 about the case output axis when the initial conditions are:

$$t = 0,\ \dot{\theta} = 0,\ \ddot{\theta} = 0 \qquad (2.3.25)$$

1) $W_{ORA} = W_O\,U_{-1}(t)$, a step rate at t = 0

$$W_D = \frac{-W_O}{H_s} C_{OA}\,e^{-t/\tau} \qquad (2.3.26)$$

where: $\tau = I_{OA}/C_{OA}$

2) $W_{ORA} = \alpha_0\,U_{-2}(t)$, a ramp of increasing rate applied at t = 0 and constant slope, α_0.

$$W_D = -\frac{\alpha_0}{H_s}\,I_{OA}\,(1 - e^{-t/\tau}) \qquad (2.3.27)$$

3) $W_{ORA} = W_O \sin \omega t$, a sinusoid applied at t = 0, for $(\omega\tau)^2 \ll 1$

$$W_D \simeq \frac{W_O}{H_s}\,I_{OA}\left[\omega e^{-t/\tau} - \omega(\cos \omega t - \psi)\right] \qquad (2.3.28)$$

where: $\psi = \tan^{-1}(\tau\,\omega)$

If $\tau\,\omega \ll 1$

$$W_D \simeq W_O\,\frac{I_{OA}}{H_s}\left[\omega e^{-t/\tau} - \omega \cos \omega t\right] \qquad (2.3.29)$$

Equations (2.3.26) through (2.3.29) demonstrate that the output-axis errors introduce

for a step-rate input a decaying exponential rate transient error,

for a steady-state constant angular acceleration a constant rate error, and

for a sinusoidal input a quadrature error that is proportional to the frequency of oscillation of the applied sinusoid input and a decaying exponential rate transient error.

C) Anisoinertia Error

As indicated previously the anisoinertia terms arise from the difference in the inertia of the float spin and input axes. To simplify our analysis the $(I_{SA} - I_{IA})(W_{IRA}^2 - W_{SRA}^2)\,\theta$ term will be neglected(θ is controlled to be small, less than 10 sec).

The applicable gyro response equation is:

$$I_{OA}\,\ddot{\theta} + C_{OA}\,\dot{\theta} = (I_{SA} - I_{IA})\,W_{IRA}\,W_{SRA} \qquad (2.3.30)$$

The float response expressed as an equivalent input rate error, W_D, is presented for each of the following rate functions applied at t = 0 with the inertial float conditions t = 0, $\dot{\theta} = 0$, and $\ddot{\theta} = 0$.

1) $W_{IRA} = W_I\,U_{-1}(t)$, $W_{SRA} = W_S\,U_{-1}(t)$, step inputs about each axis at t = 0

The combined input corresponds to a step whose magnitude is $W_I\,W_S$ and the equivalent input rate error is:

$$W_D = \frac{(I_{SA} - I_{IA})\,W_I\,W_S}{H_s}\left[1 - e^{-t/\tau}\right] \qquad (2.3.31)$$

2) $W_{IRA} = W_I \sin \omega t$, $W_{SRA} = W_S \sin(\omega t + z)$, sinusoids about each axis applied at t = 0.

Trigonometric identities may be used to express the product of the two sinusoids as:

$$\sin \omega t \quad \sin(\omega t + z) = \frac{1}{2}\left[\cos z - \cos(2\,\omega t + z)\right] \qquad (2.3.32)$$

$$W_D = \frac{W_I W_S (I_{SA} - I_{IA})}{2H} \left[(1 - e^{-t/\tau}) \cos z + e^{-t/\tau} \cos (z - \psi) - \cos (2\omega t + z - \psi) \right]$$

$$\text{where: } \psi = \tan^{-1} (2\omega\tau), \ \tau = \frac{I_{OA}}{C_{OA}} \qquad (2.3.33)$$

D) Anisoelasticity

As derived previously the anisoelastic terms arise from the compliance of the wheel within the float. Resultant error torques arise when components of acceleration are seen along the float input axes.

The applicable gyro response equation is:

$$I_{OA} \ddot{\theta} + C_{OA} \dot{\theta} = m^2 \left[a_S a_I (k_{SS} - k_{II}) - a_S^2 k_{IS} + a_I^2 k_{SI} - a_O a_I k_{IO} + a_O a_S k_{SO} \right] \qquad (2.3.34)$$

The float response expressed as an equivalent input rate error, W_D, is presented for a three axis acceleration step and sinusoid. These forcing functions are applied at t = 0 with initial float conditions of $\theta = \dot{\theta} = 0$.

1) $\bar{a} = \begin{bmatrix} a_S \\ a_I \\ a_O \end{bmatrix} U_{-1}(t)$, a three axis step of acceleration

$$W_D = \frac{m^2}{H} \left[a_S a_I (k_{SS} - k_{II}) - a_S^2 k_{IS} + a_I^2 k_{SI} - a_O a_I k_{IO} + a_O a_S k_{SO} \right] \left[1 - e^{-t/\tau} \right] \qquad (2.3.35)$$

2) $\bar{a} = \begin{bmatrix} a_S \sin \omega t \\ a_I \sin (\omega t + z) \\ a_O \sin (\omega t + \lambda) \end{bmatrix}$, a sinusoidal input of the same frequency

but phase displaced applied along each float axis. (The time averaged error term is tabulated below. The complete transient response is quite lengthy.)

$$W_D = \frac{m^2}{2H} \left[a_S a_I (k_{SS} - k_{II}) \cos z - a_S^2 k_{IS} + a_I^2 k_{SI} - a_O a_I k_{IO} \cos (z - \lambda) + a_O a_S k_{SO} \cos \lambda \right] \qquad (2.3.36)$$

E) Coning

This error does not correspond to one of the dynamic error sources derived in the previous sections. It is included here for completeness and is evidenced when one considers simultaneous phase-displaced oscillatory rates about the float output and spin axes. The error is a kinematic drift rectification which results from the geometric characteristics of a single-degree-of-freedom gyroscope. This error source is particularly significant if one considers a strapdown platform subjected to angular vibrations. (Coning is discussed in detail in MIT/IL report E-1399, August 1963.)

Consider a vibratory input of the form:

$$W_{OA} = A\ \omega \cos \omega t$$

$$W_{SA} = B\ \omega \cos (\omega t + \delta) \qquad (2.3.37)$$

where: A and B are the respective magnitudes and ω corresponds to the oscillatory rate expressed in radians/sec. The resultant kinematic rectification corresponds to:

$$W_D = \frac{A\ B\ \omega \sin \delta}{2} \qquad (2.3.38)$$

2.3.5 Output Axis Coupling

This section develops a more comprehensive treatment of output axis coupling so that a better understanding of the output axis transient response is afforded. We may formulate the desired analysis by considering (2.3.5) and (2.3.6) and relaxing the restriction that rotation exists only about OA.

To allow a manageable analysis we will, however, simplify the equations by assuming that anisoinertia and cross-coupling effects are negligible, i.e. $|\overline{A}|$ is small and $(I_{SA} - I_{IA}) = (I_{SA} - I_{OA}) = 0$. (Compliance torques will also be neglected.) These approximations linearize the equations and decouple the SRA equation, leaving the output axis term intact.

The removal of the float rotational restriction allows us to formulate the float input and output axis rates in terms of the inertial rates applied to the case and the relative motion of the float with respect to the case.

$$\begin{aligned} W_{IA} &= W_{IRA} + \dot{A}_{IA} \\ W_{OA} &= W_{ORA} + \dot{A}_{OA} \end{aligned} \qquad (2.3.39)$$

It also allows us to formulate the input axis torque equation in terms of the suspension radial spring constant (K_{IA}) and damping (C_{IA}).

$$M_{IA} = -K_{IA} A_{IA} - C_{IA} \dot{A}_{IA} \qquad (2.3.40)$$

Equating (2.3.5) and (2.3.6), accounting for the linearizing assumptions and substituting (2.3.39) and (2.3.40) as required yields (The transform operator p is introduced as the differential operator.):

$$(I_{IA} p^2 + C_{IA} p + K_{IA}) A_{IA} = H(W_{ORA} + p A_{OA}) - I_{IA} p W_{IRA} \qquad (2.3.41A)$$

$$(I_{OA} p^2 + C_{OA} p) A_{OA} = H(W_{IRA} + p A_{IA}) - I_{OA} p W_{ORA} + M_{TG} \qquad (2.3.41B)$$

Solving for A_{IA} (2.3.41A), substituting the solution in (2.3.41B), and clearing fractional notation results in the output axis equation:

$$(P_{IA} P_{OA} + H^2 p^2) A_{OA} = H(C_{IA} p + K_{IA}) W_{IRA} - (I_{OA} P_{IA} + H^2) p W_{ORA} \qquad (2.3.42)$$

where:

$$P_{IA} = (I_{IA}p^2 + C_{IA}p + K_{IA})$$
$$P_{OA} = (I_{OA}p^2 + C_{OA}p)$$

The output axis transfer function response to an input about ORA is then given by:

$$A_{OA} = \frac{-(I_{OA}P_{IA} + H^2)}{(P_{IA}P_{OA} + H^2p^2)} \; p\,W_{ORA} \qquad (2.3.43)$$

Substituting the values for P_{IA} and P_{OA} yields:

$$A_{OA} = -\left[\frac{I_{OA}(I_{IA}p^2 + C_{IA}p + K_{IA}) + H^2}{(I_{IA}p^2 + C_{IA}p + K_{IA})(I_{OA}p + C_{OA}) + H^2p}\right] W_{ORA} \qquad (2.3.44)$$

The next stage in the analysis is to selectively simplify the equation so that the significant dynamics may be visualized. If we divide the numerator and denominator by $C_{IA}I_{OA}$:

$$A_{OA} = \frac{-\left(\frac{I_{IA}}{C_{IA}}p^2 + p + \frac{K_{IA}}{C_{IA}} + \frac{H^2}{I_{OA}C_{IA}}\right)}{\left[\left(\frac{I_{IA}}{C_{IA}}p^2 + p + \frac{K_{IA}}{C_{IA}}\right)\left(p + \frac{C_{OA}}{I_{OA}}\right) + \frac{H^2}{I_{OA}C_{IA}}p\right]} \qquad (2.3.45)$$

Since the $\frac{I_{IA}}{C_{IA}} << 1$ (for the 18 IRIG MOD B I_{IA} is 436 gm-cm^2 and $C_{IA} >> C_{OA}$ = 500,000 dyne-cm-sec), the p^2 terms may be neglected. We may further simplify the equation by noting that:

$$\frac{C_{OA}}{I_{OA}} >> \frac{K_{IA}}{C_{IA}} > \frac{H^2}{I_{OA}C_{IA}} \; . \qquad (2.3.46)$$

That is, manipulating (2.3.45) after removing the $p^2\left(\frac{I_{IA}}{C_{IA}}\right)$ terms and using the relationships in (2.3.46) allows one to neglect the $H^2/I_{OA}C_{IA}$ in the denominator of (2.3.45). This last simplification yields the

following form:

$$\frac{A_{OA}}{W_{ORA}} = -\frac{\left[p + \alpha_I \left(1 + \frac{H^2}{I_{OA} K_{IA}}\right)\right]}{(p + \alpha_I)(p + \alpha_O)} \qquad (2.3.47)$$

where:

$$\alpha_I = \frac{K_{IA}}{C_{IA}} \qquad \alpha_O = \frac{C_{OA}}{I_{OA}}$$

For the 18 IRIG MOD B:

$$\tau_I = 1 / \alpha_I \simeq 10 \text{ sec}$$

$$\tau_O = 1 / \alpha_O \simeq 450 \,\mu\text{sec}$$

$$H^2 / I_{OA} K_{IA} \simeq 0.2$$

The frequency response of the output axis function is obtained by substituting $p = 2\pi Jf$ into eq. 2.3.47. The magnitude of the resultant function is shown in Fig. 2.3-2. Note that at extreme low frequencies the response magnitude includes an "effective output axis inertia term" $(I_{OA} + H^2/K_{IA})$. For all higher frequency ranges only the float inertia, I_{OA}, influences the response.

2.3.6 Numerical Error Analysis

A numerical error analysis of the Apollo 18 IRIG gyroscope errors for various dynamic environment conditions was constructed. The results of this analysis are provided in Tables 2.3-1 through 2.3-5.

The Apollo 18 IRIG is a single-degree-of-freedom torqued-to-null gyroscope. Its basic parameters are:

$$H_s = 1.51 \times 10^5 \text{ (gm-cm}^2\text{) /sec}$$

$$C_{OA} = 5.02 \times 10^5 \text{ dyne-cm/rad/sec}$$

$$\tau = 450 \ \mu \text{ sec}$$

$$\frac{H_s}{C_{OA}} = 0.296$$

$$I_{OA} = 225 \text{ gm-cm}^2$$

$$(I_{SA} - I_{IA}) \leq 0.03 \, I_{OA}$$

In addition, the compliance drift rate has been experimentally determined to be on the order of 0.8 meru/g^2.

Suggested Dynamic Environment Inputs:

1. Angular Rates:

   Maximum maneuvering rate - $\frac{1}{10}$ rad/sec

   Normal maneuvering rate - $\frac{1}{100}$ rad/sec

   Residual rate - 10^{-5} rad/sec

2. Angular Acceleration:

   Maximum - $\frac{1}{10}$ rad/sec^2

   Normal - $\frac{1}{200}$ rad/sec^2

3. Linear Acceleration:

   Boost - 4 g

   Maneuver - 1 g

4. Oscillatory Environment:

Body bending -(thrust) -	limit cycle - 1/10 degree P-P frequency 2 Hz
Slosh effect -(thrust) -	limit cycle - 1 degree P-P frequency 1/2 Hz
Basic autopilot deadzone -	limit cycle - 1 degree P-P frequency - 1/20 Hz

These rates represent an educated guess to the Apollo dynamic environment.

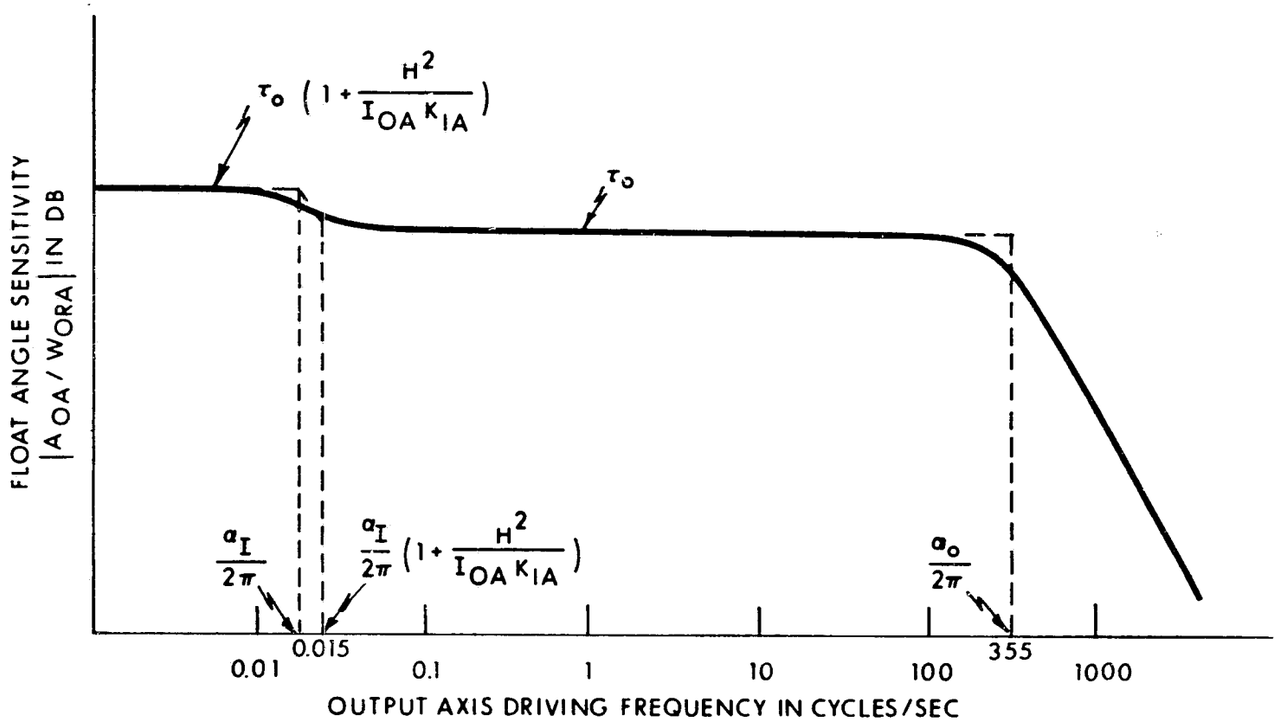

Fig. 2.3-2 Sensitivity to output-axis sinusoid.

TABLE 2.3-1
SUMMARY OF DRIFT ERROR FORMULAE

TORQUE	FORM	REQUIRES	INPUT	EQUIVALENT DRIFT RATE $\langle\omega_D\rangle$ ERROR
OA Coupling	$-I_{OA}\ \frac{dW_{ORA}}{dt}$	Angular Acceleration About OA	$\omega_{ORA} = \alpha_O U_{-2}(t)$	$-\frac{\alpha_O}{H_S}\ I_{OA}\ (1 - e^{t/\tau})\ dt \quad \tau = IOA/COA$
Anisoinertia	$(I_{SA} - I_{IA})\ \omega_{IRA}\ \omega_{SRA}$	Angular Rates about IRA & SRA	$\omega_{IRA} = \text{Const} = \omega_I$ $\omega_{SRA} = \text{Const} = \omega_S$	$\frac{\omega_I \omega_S\ (I_{SA} - I_{IA})}{H_S}$ *
	"	"	$\omega_{IRA} = A \sin \omega f$ $\omega_{SRA} = B \sin (\omega t + \xi)$	$\frac{AB\ (I_{SA} - I_{IA}) \cos \xi}{2H_S}$ *
Anisoelasticity	$m^2[a_S a_I (k_{SS} - k_{II})] - k_{IS}\ a_s^2$ $+ k_{SI}\ a_I^2 - k_{IO} a_O a_I + k_{SO} a_O a_S]$	Trans-lational Acceleration	a = Constant	$\frac{m^2}{H_S}[a_S a_I\ (k_{SS} - k_{II}) - k_{IS} a_S^2 + k_{SI} a_I^2$ * $- k_{IO}\ a_O\ a_I + k_{SO}\ a_O\ a_S]$
		"	$a_S = a \sin \omega t$ $a_I = b \sin (\omega t + \xi)$ $a_O = c \sin (\omega t + \lambda)$	$\frac{m^2}{H_S}[ab\ (k_{SS} - k_{II}) \cos \xi + ac\ k_{SO} \cos \lambda$ * $-a^2 k_{IS} + b^2 k_{SI} - bc\ k_{IO} \cos (\xi \quad \lambda)]$
Coning	--------	Sinusoidal Vibration about OA & SA	$\omega_{OA} = A\ \omega \sin \omega t$ $\omega_{SA} = B \omega \cos (\omega t + \xi)$	$\frac{AB\omega}{2} \sin \xi$

*Steady State Solution.

TABLE 2.3-2

OA COUPLING - NUMERICAL EVALUATION OF EQUIVALENT DRIFT RATE

ANGULAR ACCELERATION			$\langle \omega_D \rangle$
INPUT	TYPE	MAGNITUDE	(Meru)
MAXIMUM	CONSTANT	$\frac{1}{10}\ \frac{\text{rad}}{\text{sec}^2}$	2.05×10^3
NORMAL	CONSTANT	$\frac{1}{200}\ \frac{\text{rad}}{\text{sec}^2}$	1.025×10^2

Constant Angular Acceleration Duration $\simeq$ 4 sec max.

TABLE 2.3-3

CONING - NUMERICAL EVALUATION OF EQUIVALENT DRIFT RATE

INPUT			$\langle \omega_D \rangle$ (meru)
SOURCE	INPUT	MAGNITUDE	
Body Bending (Thrust)	Sinusoidal f = 2HZ	Limit cycle ± 0.05 Degree	65
Slosh Effect (Thrust)	Sinusoidal f = 1/2 HZ	Limit cycle ± 1/2 Degree	1630
Basic Autopilot DEADZONE	Sinusoidal f = 1/20 HZ	Limit Cycle ± 1/2 Degree	163

TABLE 2.3-4

ANISOINERTIA - NUMERICAL EVALUATION OF EQUIVALENT DRIFT RATE

RATE - BOTH AXES			$\langle \omega_D \rangle$ MERU
SOURCE	INPUT	MAGNITUDE (Rad/Sec)	
Maneuvering (Maximum)	Constant	10^{-1}	6.14
Maneuvering (Normal)	Constant	10^{-2}	6.14×10^{-2}
Residual	Constant	10^{-5}	6.14×10^{-8}
Body Bending	Sinusoidal f= 2HZ	1.095×10^{-2}	3.66×10^{-2}
Slosh Effect	Sinusoidal f = 1/2HZ	2.73×10^{-2}	2.28×10^{-1}
Basic Autopilot Dead Zone	Sinusoidal f= 1/20HZ	5.48×10^{-3}	2.28×10^{-3}

TABLE 2.3-5

ANISOELASTICITY - NUMERICAL EVALUATION OF EQUIVALENT DRIFT RATE

ACCELERATION			$\langle \omega_D \rangle$
SOURCE	INPUT	MAGNITUDE g	(meru)
Boost - (Maximum)	Constant	4g	1.28×10^{1}
Boost (Linear Acceleration and RMS Vibration)	Constant and Sinusoidal	5.66g (RSS)	2.56×10^{1}
Maneuvering (Maximum)	Constant	1g	8.0×10^{-1}

2.4 Pendulous Accelerometer Dynamics in a Rotating Frame

The differential equations describing the dynamics of a single-degree-of-freedom pendulum in a rotating system may be derived in the same manner as those of the gyro. The dynamic equation is formulated here for background purposes. Error analysis for representative inputs is not included since it is essentially the same as the gyro analysis in the previous section.

2.4.1 General Equations

The principle of operation is formulated in terms of angular momentum and the equations describing the motion of the pendulum are defined in both case (c) and float (f) coordinate frames. The applied torque $\overline{M}^f$, expressed in the float coordinate frame is:

$$\overline{M}^f = \left(\frac{d\overline{H}^f}{dt}\right)_i \tag{2.4.1}$$

where $\overline{H}^f$ is the float angular momentum in the float coordinate frame. The rate of change of angular momentum is expressed in terms of the Coriolis equation.

$$\overline{M}_f = \left(\frac{d\overline{H}^f}{dt}\right)_f + \overline{W}_{if}{}^f \times \overline{H}^f + \overline{a}_f{}^f \times \overline{P}^f \tag{2.4.2}$$

where

$\overline{W}_{if}{}^f$ is the angular rate of the float with respect to inertial space, i.e.:

$$\overline{W}_{if}^f = \begin{bmatrix} W_{PA} \\ W_{IA} \\ W_{OA} \end{bmatrix}$$

$\overline{P}^f$ is the float pendulosity (mass m displaced by a length l along the pendulous axis) i.e.:

$$\overline{P}^f = \begin{bmatrix} P \\ 0 \\ 0 \end{bmatrix}$$

$\overline{a}^f$ is the acceleration vector of the float, i.e.:

$$\overline{a}^f = \begin{bmatrix} a_{PA} \\ a_{IA} \\ a_{OA} \end{bmatrix}$$

The angular momentum of the float (no spin angular momentum) is

$$\overline{H}^f = \underline{I}\,\overline{W}^f_{if}$$

where

$$\underline{I} = \begin{bmatrix} I_{PA} & 0 & 0 \\ 0 & I_{IA} & 0 \\ 0 & 0 & I_{OA} \end{bmatrix} \qquad (2.4.3)$$

The float axes are defined as pendulous (PA), input (IA), and output axes (OA) and correspond to the principal axes of inertia, I. The case axes are defined as pulse reference (PRA), input reference (IRA), and output reference (ORA).

The angular rate and acceleration of the float may be defined in terms of the case inertial rates ($\overline{W}^c_{ic}$) and acceleration ($\bar{a}^c_{ic}$) and the relative rates between the float and the case $\overline{W}^f_{cf}$. (It is assumed that no relative acceleration between the case and float exists.)

$$\begin{aligned} \overline{W}^f_{if} &= \left[R^f_c\right] \overline{W}^c_{ic} + \overline{W}^f_{cf} \\ \bar{a}^f_{if} &= \left[R^f_c\right] \bar{a}^c_{ic} \end{aligned} \qquad (2.4.4)$$

where:

$$\overline{W}^f_{cf} = \begin{bmatrix} \dot{A}_{PA} \\ \dot{A}_{IA} \\ \dot{A}_{OA} \end{bmatrix}$$

$\left[R^f_c\right]$ is the transform matrix that relates the case coordinate frame to the corresponding float coordinate axes. (Brackets or a bar below the letter is used for matrix representations.)

Torques are generally applied to the float with respect to the case by suspension forces and fluid damping.

$$\overline{M}^f = -\underline{C}\,\overline{W}^f_{cf} - \underline{K}\,\overline{A}^f_{cf} + \overline{M}^f_{TG} \qquad (2.4.5)$$

where

$\underline{C}$ = the damping coefficient matrix,
$\underline{K}$ = the suspension and other elastic restraints,
$\overline{M}^f_{TG}$ = the command or control torques from the instrument torque generator.

2.4.2 Simplified SDF Pendulous Accelerometer Equation

As in the case of the gyro, the equation development may be simplified by assuming that:

1. All internal rotations of the float within the case are about OA; no other relative rotations exist.
2. There are no spring restraints about OA.
3. There is no bearing friction between the float and case.
4. The float structure is perfectly rigid.

Using these assumptions allows one to define $\underline{R}^f_c$ and $\overline{W}^f_{cf}$.

$$\underline{R}^f_c = \begin{bmatrix} \cos\theta & \sin\theta & 0 \\ -\sin\theta & \cos\theta & 0 \\ 0 & 0 & 1 \end{bmatrix} \qquad (2.4.6)$$

$$\overline{W}^f_{cf} = \begin{bmatrix} 0 \\ 0 \\ \dot{\theta} \end{bmatrix}$$

where

$$\dot{\theta} = \dot{A}_{OA}$$

Using (2.4.6) in (2.4.4) and substituting the results in (2.4.2) yields an output axis equation of the form

$$M_{OA} = I_{OA}\,(\dot{W}_{ORA} + \ddot{\theta}) + (I_{IA} - I_{PA})(W_{IRA} - W_{PRA}\,\theta)(W_{PRA} + W_{IRA}\,\theta)$$

$$- P(a_{IRA} - a_{PRA}\,\theta) \qquad (2.4.7)$$

The output axis torques derived from (2.4.5) are

$$M_{OA} = - C_{OA}\dot{\theta} + M_{TG} \qquad (2.4.8)$$

Equating (2.4.8) and (2.4.7) and dropping the θ^2 term (θ is small) yields the SDF pendulous accelerometer output axis equation.

$$I_{OA}\ddot{\theta} + C_{OA}\dot{\theta} = P\,a_{IRA} + M_{TG} - P\,a_{PRA}\,\theta - I_{OA}\dot{W}_{ORA} + (I_{PA} - I_{IA})\left[W_{IRA}\,W_{PRA} + (W_{IRA}^2 - W_{PRA}^2)\,\theta\right] \quad (2.4.9)$$

where

$I_{(\ )}$ = moment of inertia of the float about each of its principal axes (PA, IA and OA)

C_{OA} = the viscous damping coefficient about OA

P = the float pendulosity (ml)

$a_{(\ )}$ = the linear acceleration of the PIP along its respective axes (PRA, IRA, ORA)

$W_{(\ )}$ = the angular velocity of case

θ = the angle about OA of the float with respect to the case.

The terms on the left correspond to the float rotational dynamic response. The first two terms on the right correspond to the desired PIP input axis acceleration response and the measurement control torque. The remaining terms represent the dynamic measurement error sources:

$P\,a_{PRA}\,\theta$ - axis cross coupling

$I_{OA}\,\dot{W}_{ORA}$ - output axis coupling

$(I_{PA} - I_{IA})\left[W_{IRA}\,W_{PRA} + (W_{IRA}^2 - W_{PRA}^2)\,\theta\right]$ - anisoinertia

(Other terms could have been introduced had one considered additional misalignments of the float about the input and pendulous axes. They have been omitted so that a simple representation could be developed that would clearly evidence the nature of the error source terms.)

The output axis coupling term is basic to the nature of the device and cannot be eliminated by design. The axis cross-coupling error can be minimized by torquing control loop design. Similar other misalignment errors may be minimized by suspension and system alignment procedures.

Because of the method of location of the pendulous mass on the float of the 16 PM PIP its anisoinertia coeficient ($I_{IA} - I_{PA}$) is equal to approximately one gm-cm^2. Thus an anisoinertia error does exist. For example, a constant rate of 1/3 radian per second about IRA and PRA would result in an indicated error of 0.11 cm/sec^2. This error does not appear to be significant for an Apollo type mission (reasonably low level angular body modes are assumed). However, in a long burn application (Nerva engine) body bending type angular rate inputs could introduce significant anisoinertia error effects. It would be desirable therefore to consider design of a 16 PM PIP pendulous float that minimizes the ($I_{IA} - I_{PA}$).

2.5 Gyro Pulse-Torque Model and Simulation

2.5.1 Summary

A dynamic digital program for simulation of gyro and control loop was developed. The 18 IRIG gyro and the ternary torque-to-balance parameters were used and actual hardware test conditions were duplicated. Thus, the simulation model allowed investigation of the dynamic character of the gyro and control loop. As such it provided means for a better understanding of the test results. The simulation also allows analysis of parameter variation influences for control loop optimization studies.

The most significant simulation result was the prediction of gyro control-loop-pulse-bursting operation during torque-to-balance rate testing (Section 3.3). The simulations clearly demonstrate that gyro float response limitations cause the ternary torque-to-balance loop to issue pulse bursts in lieu of regularly spaced torquing pulses. For example, for an ideal instrument and control loop subjected to an input rate equal to 20% of the torquing loop-gyro scaled input rate capability one would expect a pulse pattern of one pulse on and four off. The simulation showed that the gyro float lags dominate the dynamic operation and, for a 20% input, a three-on twelve-off pulse pattern resulted at a simulated 9.6 kc sampling (interrogation) rate.

The characteristic grouping of on-and-off torquing pulses was termed pulse-bursting. The average rate measurement over a long period is not affected by pulse bursting; however, it does represent an error source for a high-frequency DDA or whole-number algorithm mechanization. Since the maintenance of the attitude matrix is time dependent and non-commutative, pulse-bursting from all three gyros will result in attitude matrix errors. In other words, at the 20% rate input the pulse-bursting phenomenon represents an effective quantization that is three times larger than the pulse scale factor. Because of these findings development of control-loop techniques to eliminate pulse-bursting and minimize float hang-off (i.e., reduce cross-coupling errors) was initiated. Progress on this development effort is reported in Section 2.6. For the gyro, increasing the damping-to-inertia ratio of the float output axis would have the most effect in reducing pulse-bursting. Discussion of the simulation program and some of the output plots which provide a more detailed appreciation for the dynamics of operation follow.

2.5.2 Loop Model

The digital simulation was mechanized in the MIT MAC language (similar to FORTRAN) for use on the Honeywell 1800 and IBM 360 computer

facility. Fig. 2.5-1A shows a simplified block diagram of the ternary torquing loop and gyro. The basic operational principle is to sample the single-degree-of-freedom gyro's output-axis motion as indicated by its signal generator (SG) and generate a torquing pulse command to the gyro torquer (TG) to return the float to its null position. The operation is called ternary since the indicated motion must exceed some preset level (threshold) before a torquing pulse is issued. Similarly, the polarity of the torquing pulse is dependent upon the sense of the motion. Thus, three torque-command states are evidenced: no torque, plus torque, or minus torque.

The torque commands in the actual hardware are mechanized such that they are fixed in magnitude and width. Thus, each pulse represents a quantized command ($\Delta\theta$) of gyro output-axis motion (or an equivalent measure of input-axis motion). For a constant input rate about the gyro float input axis the ternary control loop would respond with an output torquing pulse train to keep the float output axis at null. The average rate of the pulses would correspond to the input rate. (A detailed description of the torquing-loop electronics configuration is presented in Section 4.5.) The major parameters in the simulation of the torquing loop electronics are: the sampling rates (interrogation rate), the threshold level, the data-processing delay, and the pulse-generator torquing pulse width and magnitude. Interrogation rates of 3200-pps and 9600-pps were investigated. (The SG has a 9600-cps suppressed carrier output, and synchronous sampling at the peak of the carrier frequency is employed in the electronics.) Similarly, the pulse width of the torquing pulse was nominally set to correspond to 3/4 of an interrogation sampling period (i.e. 78 microseconds for 9600-pps interrogation rate). The threshold level is nominally set to correspond to the $\Delta\theta$ increment command of a torquing pulse. This assured that the control loop would not mode (unstable operation resulting from a single torque pulse being capable of driving the float through the threshold and causing opposite polarity torquing pulse).

The gyro model was developed by considering the torques acting on the float. Fig. 2.5-1B illustrates the major torques affecting the output axis. (Mass unbalance, anisoelastic and anisoinertia sources were not considered as they would unduly complicate the simulation and shed little light on the dynamic interaction of the gyro and the control loop.) To properly simulate the gyro dynamics both output- and input-axis equations were mechanized. The equations are listed in in Fig. 2.5-2 (MAC language coding). The pertinent gyro parameters are also tabulated. Note that the second-order derivative of input angle motion in the second equation was omitted. The ratio of input axis

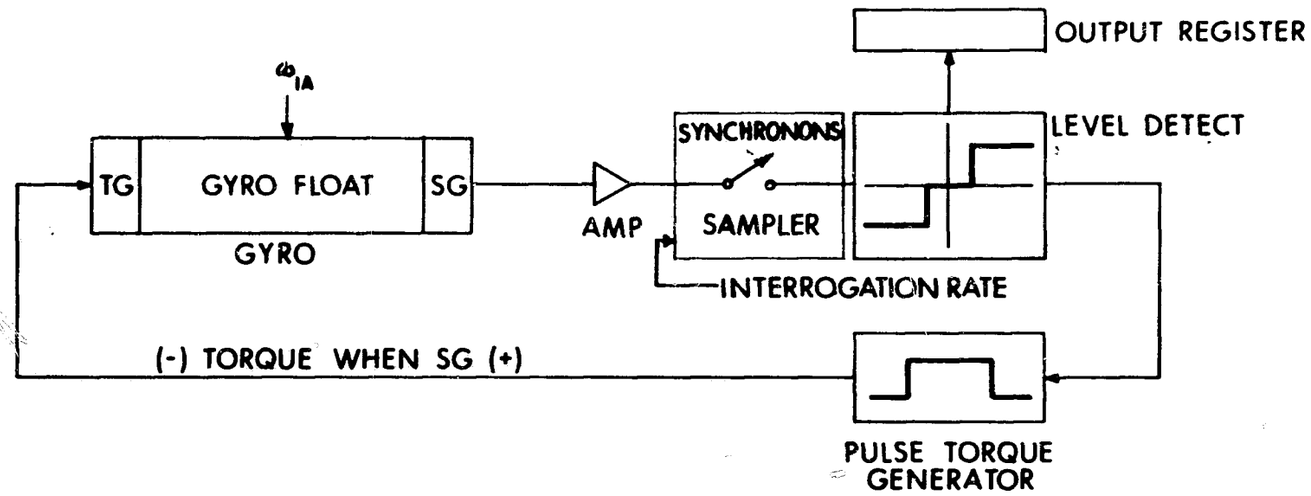

Fig. 2.5-1A Simplified ternary torquing loop.

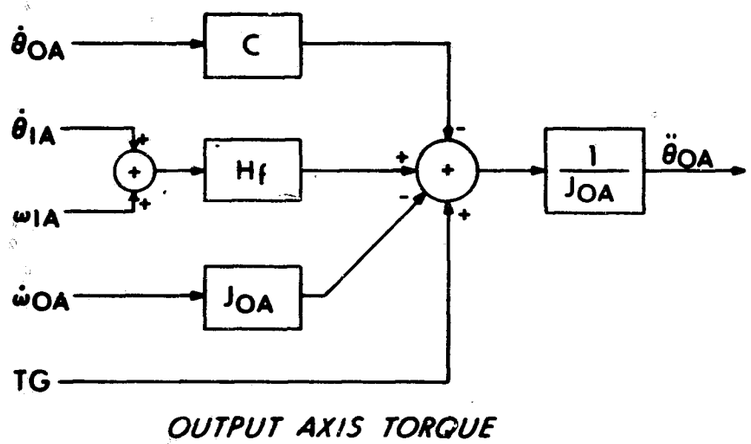

θ_{OA} IS OUTPUT AXIS FLOAT ANGLE

θ_{IA} IS INPUT AXIS FLOAT ANGLE

C IS OUTPUT AXIS DAMPING COEFFICIENT

H_f IS TOTAL FLOAT ANGULAR MOMENTUM

J_{OA} IS OUTPUT AXIS MOMENT OF INERTIA

TG IS TORQUE SUPPLIED BY TORQUE GENERATOR

ω IS ROTATION OF CASE WRT INERTIAL SPACE

Fig. 2.5-1B Gyro float as torque summing device.

```
LOOPS   WIA = WIA, D WOA/ DT = D WOA/ DT , WOA = WOA, WSA = WSA
        D2 AOA/ DT2 = - CG D AOA/ DT + HS ( WIA + D AIA/ DT + AOA WSA ) + MTGA - D WOA/ DT
        D AIA/ DT = - KX AIA + HI ( WOA + D AOA/ DT )
        DIFEQ T, DT
        IF DQ PHASE NZ, GO TO LOOPS
```

WIA	-	RATE WRT INERTIAL SPACE (RAD/SEC) ABOUT	INPUT AXIS - IA
WOA	-		OUTPUT AXIS - OA
WSA	-		SPIN AXIS - SA
AOA	-	OUTPUT AXIS FLOAT ANGLE	RADIANS
AIA	-	INPUT AXIS FLOAT ANGLE	RADIANS
MTGA	-	TORQUE GEN= OUTPUT / JOA	
JOA	-	OUTPUT AXIS FLOAT MOMENT OF INERTIA	
CG	-	C / JOA = 502,000/ 225	
HS	-	H / JOA = 151,000/ 225	
KX	-	SUSPENSION STIFFNESS FOR INPUT AXIS / CIA (KX ≃ 480,000,000/A5,000,000,000)	
CIA	-	DAMPING ABOUT IA ≃ 5×10^9	
HI	-	H / CIA ≃ 151,000 / 5,000,000,000	
D^2X/DT^2	-	SECOND TIME DERIVATIVE OF X	
DX / DT	-	FIRST TIME DERIVATIVE OF X	
DIFEQ	-	MEANS PERFORM GILL INTEGRATION STEP	

Fig. 2.5-2 MAC coding for integration loop.

inertia to damping $(\frac{J_{IA}}{C_{IA}})$ is so much smaller than all other equation coefficients (i.e., 0.2% of HI) that its omission resulted in a negligible error. Further numerical solution of the second term would necessitate multiplying by the inverse ratio (C_{IA}/J_{IA} is approximately $2x10^6$) resulting in solution instabilities. A simplified closed-loop program flow diagram is shown in Fig. 2.5-3.

2.5.3 Closed-Loop Response

The gyro float response to a single torque pulse provided a good deal of insight into the lagged response of closed-loop operation at different sampling rates. As shown in Fig. 2.5-4, only a small percentage of the total float motion to a single fixed-magnitude torquing pulse occurs in the first sampling period. For example, at a 9600-pps interrogation rate the float has only begun to move when the torque pulse is turned off and has gone 11% of its commanded travel when the next torque-loop interrogation sample takes place. At the 3200-pps interrogation rate approximately 34% of the travel has occurred by the time the next sample is made.

Clearly at 9600-pps closed-loop operation an W_{IA} angular rate about the gyro input axis that is in excess of 11% of the torque-loop, full-on, rate-scaling capability will result in some form of multiple torque pulsing. For example, consider an initial condition in which a steady-state W_{IA} was such that the float travel in a sampling period was slightly in excess of 11%. Thus, at sampling time (assume the float crosses over the torquing threshold exactly at a control-loop sampling point) a restraining torque-command pulse is issued. The float operates such that the steady-state input and the pulse command are summed. Thus, at the next sampling interval the float is still outside the threshold and another torque pulse is commanded. (The return travel due to the first torque pulse is only 11% while the travel due to the steady-state input is in excess of 11%.) The operational effect over these two sampling periods has been to command two $\Delta\theta$ increments in response to an input slightly in excess of $\Delta\theta$. For the next few sampling periods the float response to the two successive torque pulses dominate and no further output pulses will occur. Then, dependent upon the threshold cross-over relationship with the sampler, another pulse burst may occur. Thus, the average indicated rate is correct but a pattern of pulse on-and-off bursts may occur.

If the maximum-input-angular-rate capability of the torque loop were set at full-on operation (continuous pulsing) to 15^o/sec, bursting would probably start to occur at somewhat less than 1.65^o/sec and 5.1^o/sec (accounting for additional delays in the control loop) with 9600-pps and 3200-pps interrogation rates respectively. During 18 IRIG unit #411 testing at 9600-pps with this

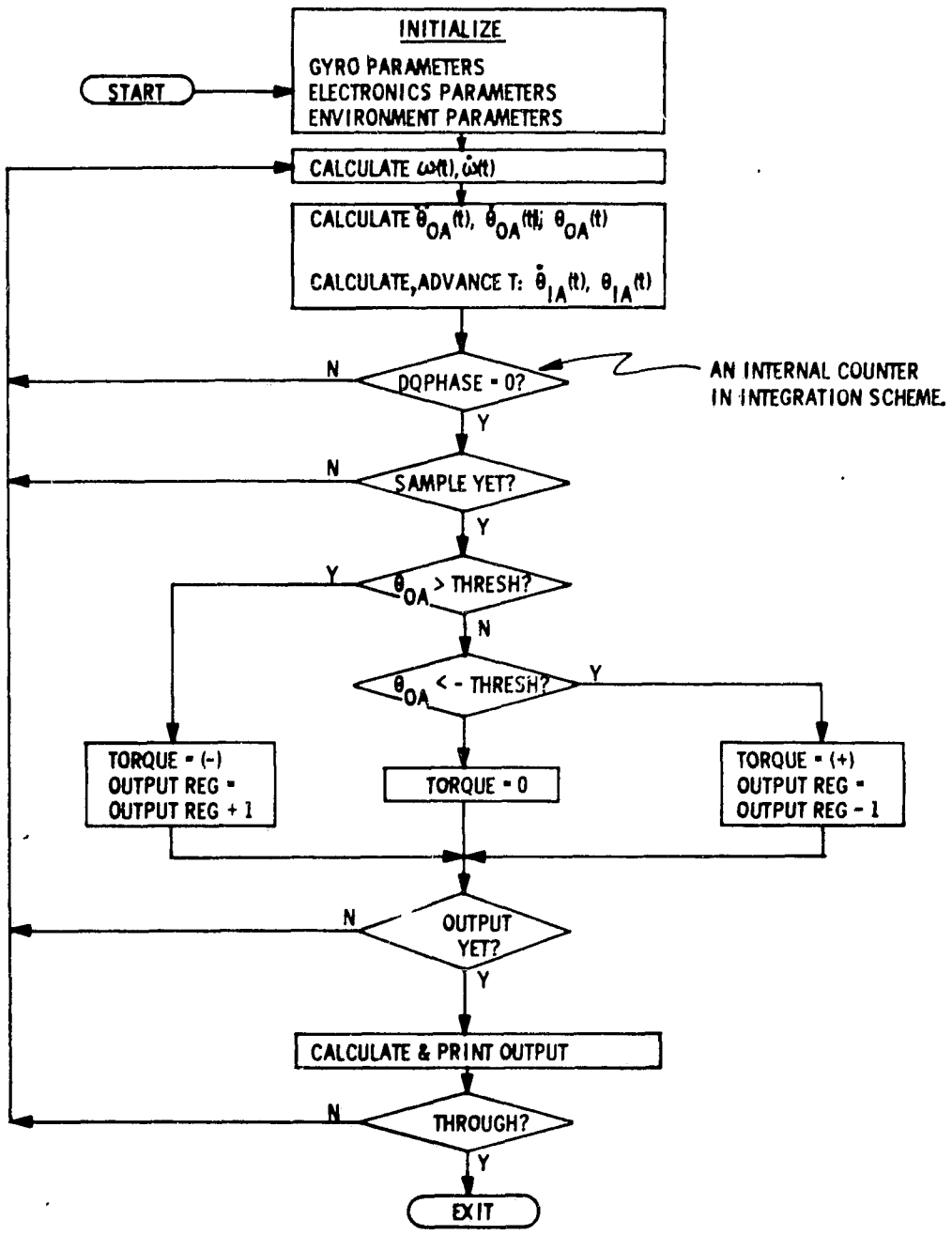

Fig. 2.5-3 Gyroscope loop simulator program.

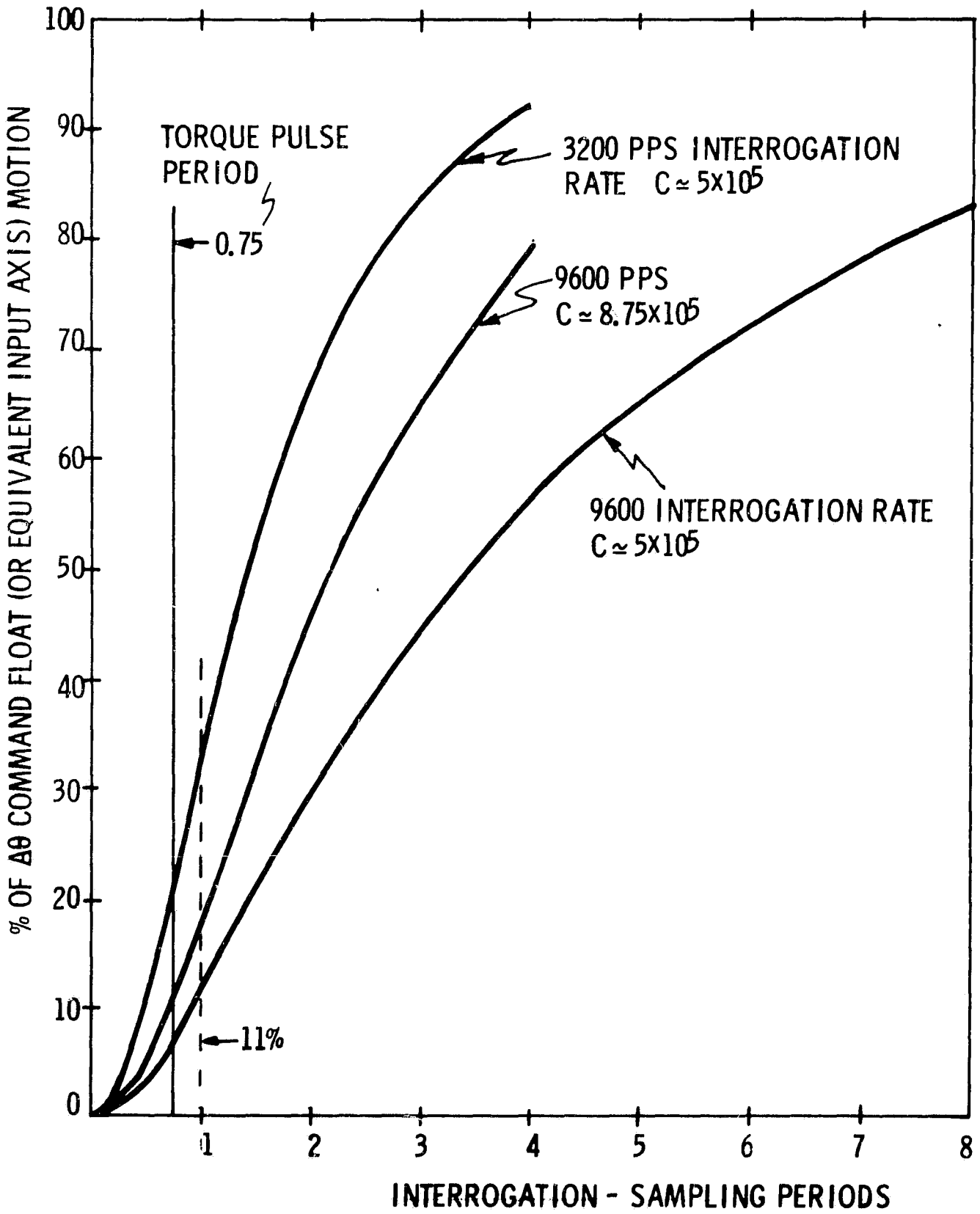

Fig. 2.5-4 Normalized gyro response to a single torque pulse command.

nominal rate scaling, bursting was evidenced at about 1.3°/sec. Fig. 2.5-5 demonstrates a simulation plot of closed-loop operation at a 10K-pps sampling rate with an input angular rate equal to 20% (3°/sec) of the scaled loop capability. The upper curve shows the indicated float input rate relative to the actual input rate. The middle curve shows the torque state with respect to time. Note the steady-state three-pulse-on, twelve-off sampling-period bursting pattern. The lower curve shows the float angle with respect to the torquing threshold. Note the float excursion beyond threshold and its subsequent return after the issuance of three command-torque pulses.

In general, this simulation has provided a valuable tool for the investigation of various gyroscope parameters and torque-loop parameters on closed-loop dynamic operation. For example, Fig. 2.5-6 presents the closed-loop response for a 20% input rate with an increase of the output-axis damping coefficient from 502,000 to 875,000 dyn-cm-sec. Note that in this case a 2-on, 8-off pattern results. Similarly, the single-pulse response shown in Fig. 2.5-4 for this increased damping shows a superior response.

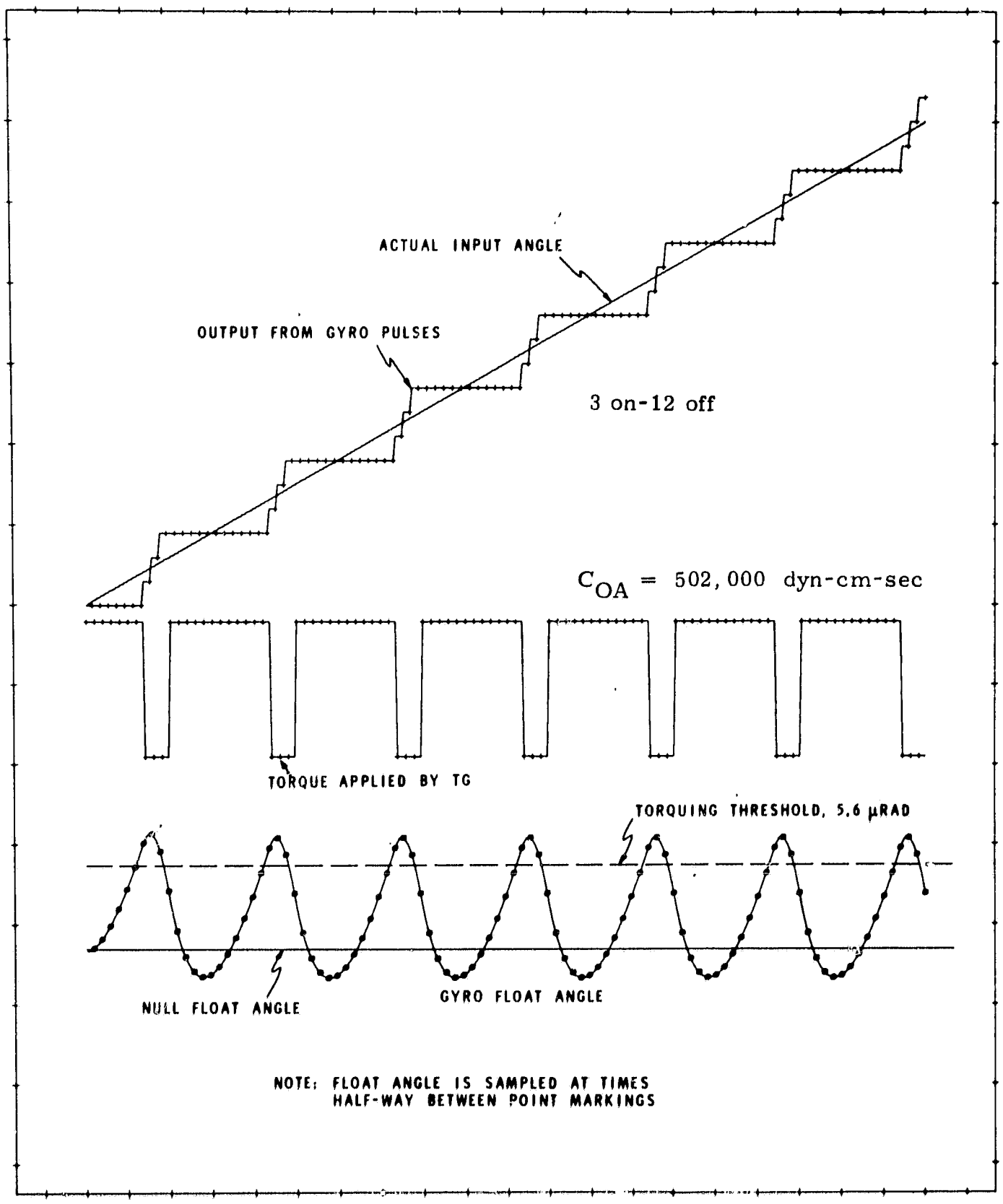

Fig. 2.5-5 "Moding" for constant rate input.

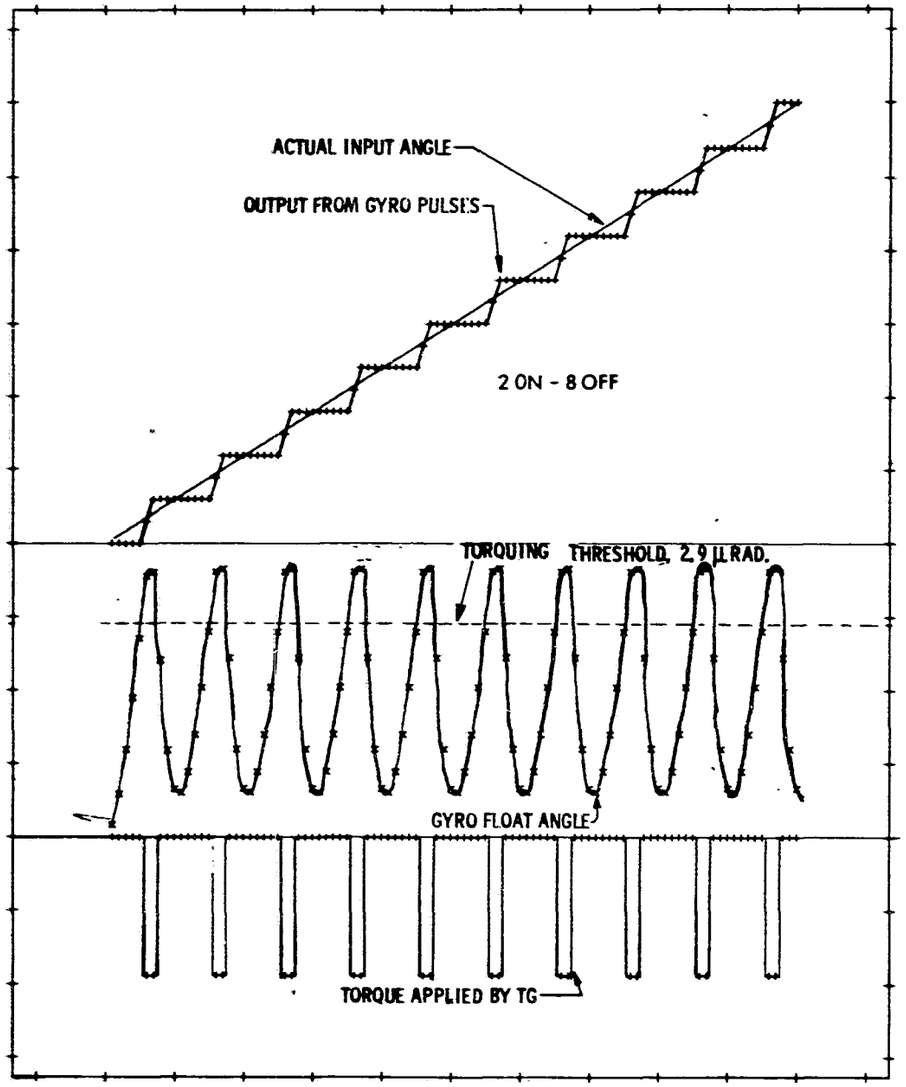

C_{OA} increased from 502,000 to 875,000 dyn-cm-sec

Fig. 2.5-6 "Moding" for constant rate input.

2.6 Improvements in Pulse-Rebalanced Instruments

2.6.1 Introduction

The closing words of Weiner's[20] strapdown survey are a recommendation that someone should solve the "moding" problem of the delta-modulated, or pulse-rebalanced, inertial instrument. Over the last decade considerable study has been directed toward this end and although analytical tools such as describing functions have been improved, only Hayum[21] seems to have formulated a sound basis for synthesizing compensation. His scheme was however described "as an afterthought"[22] and apparently was never developed further. In a master's thesis supported by this contract, Lory[23] presents an analysis which places noise filtering and moding compensation in proper context and develops techniques for synthesizing simple compensation networks (e.g., for the 18 IRIG MOD B). The following descriptive material presents a condensation of the major findings of this thesis. Although the work is applicable to gyroscopes or accelerometers and to ternary or binary interrogate logic, this discussion is specialized to the ternary-torqued gyroscope.

The greatest stumbling block in the design of pulse-rebalance loops is the failure to consider carefully what may legitimately be called an ideal system. For instance, the choice of pulse rebalancing along with quantized, impulsive communication of the output to a digital computer implies that a nonlinear element having jump discontinuities is a necessary and desirable component of the system. Therefore, attempts to "eliminate" the nonlinearity by quasi-linear analysis (describing functions) obscures the ideal solution. Furthermore, without some standard of comparison and an organized approach, one searches for a filter that simultaneously shapes the signal, rejects the noise, and stabilizes the loop. The confused intermingling of specifications precludes successful solution.

2.6.2 The Ideal System

A) System Specification

If we assume, as a specification, that an integrating gyroscope and a periodically-sampled, constant-area pulse-rebalance loop must be used, the simple system shown in Fig. 2.6-1. is a useful idealization. That is, it serves as a standard of comparison for the evaluation and optimization of the actual system. The ideal has no float time constant, no torquer-current rise time,

no noise filter, and, indeed, no noise. Its interrogator and switch (modeled by the step discontinuity, sample, and zero-order hold) have a symmetric, one-step-wide deadband without hysteresis. The deadband is assumed as a system-level specification forbidding a null-input limit cycle. For convenience and without loss of generality, the input and output have been normalized and the loop gain has been associated with the integration.

Now consider the differently arranged but equivalent system of Fig. 2.6-2. By superposition, the integration of the sum of the input and feedback have been replaced by the sum of their integrals. The result is one we could have adopted initially, for we now have an ideal one-step-at-a-time quantizer. But the combination of these is not yet an ideal system. The quantizer acts only on its current input at sample time. Thus, we would better represent the signal in each period if we quantize its value as predicted in the middle of the period. This we can do in our conception of the ideal linear system, and therefore we use the system of Fig. 2.6-3.

B) Modeling the Real System

The selection of a suitable model for the actual system need not be overly sophisticated. Error terms such as output- and spin-axis cross-coupling, anisoinertia and anisoelastic torques, while sources of error, are not of sufficient magnitude to alter the dominant dynamics described by a linearized, single-axis model of the instrument. It is sufficient, at the start, therefore, to take the view that the purpose of the instrument is to measure all other torques about the input axis by proper application of rebalancing torque. Thus the familiar model for a delta-modulated inertial instrument shown in Fig. 2.6-4 will serve. A noise input is assumed, as well as a filter, H(s), for the design of which we must derive some strategy.

C) The Strategy of Solution

Because of its linearity, the model of the actual system can be divided in two, as shown in Fig. 2.6-5, one branch having the torquing commands as the input, the other having all other inputs. The outputs of these two branches add to form the input to the nonlinear interrogate logic. The key innovation necessary is to recognize that, although cascade compensation of the loop is impractical at the input and undesired at the output (for then it would have to appear in both branches), parallel compensation can be applied from the torquer input to add to the signal-generator output. Adding this as the transfer, G(s), and rearranging the diagram to emphasize comparison to the ideal system, one obtains Fig. 2.6-6, which is a graphic guide to the steps necessary to arrive at a solution.

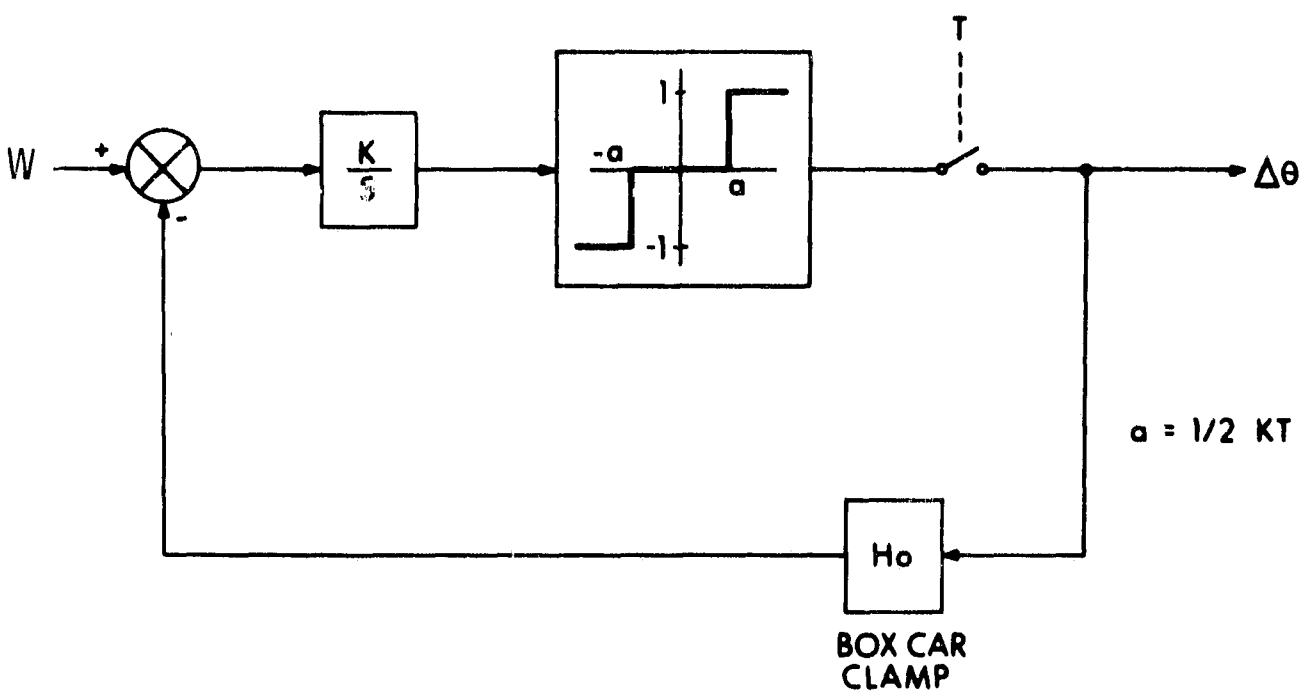

Fig. 2.6-1 Idealized pulse-rebalance loop.

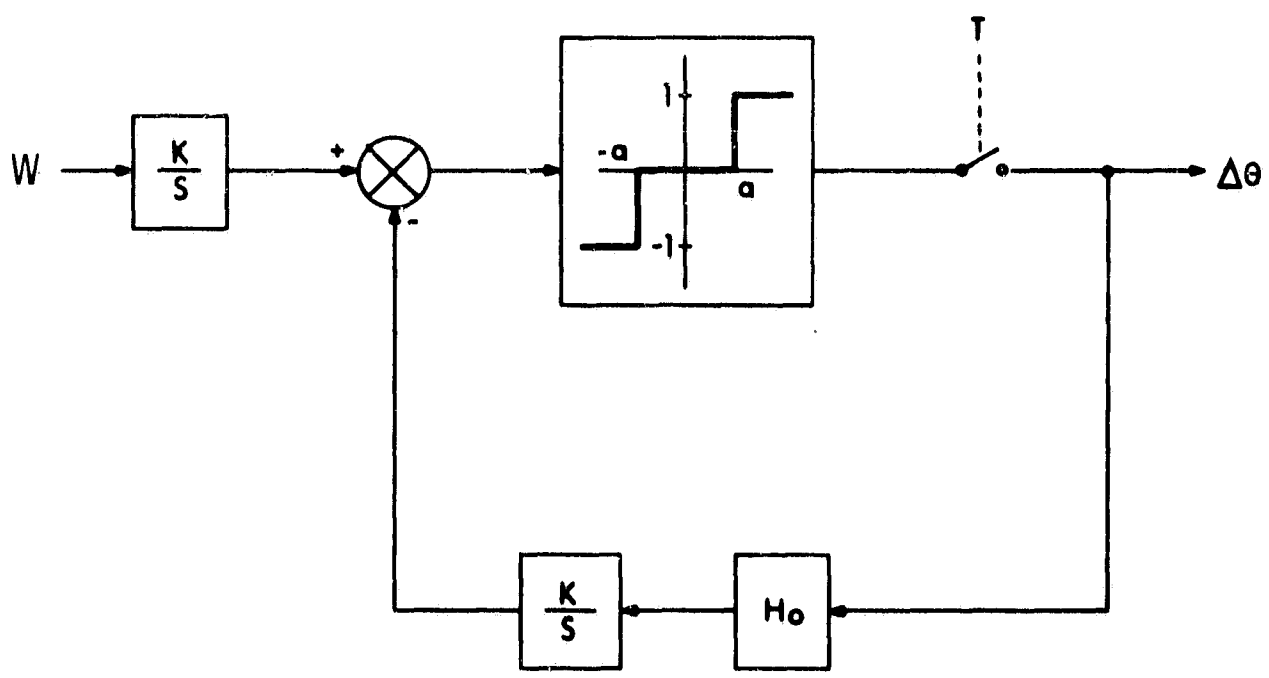

Fig. 2.6-2 Idealized system equivalent to Fig. 2.6-1.

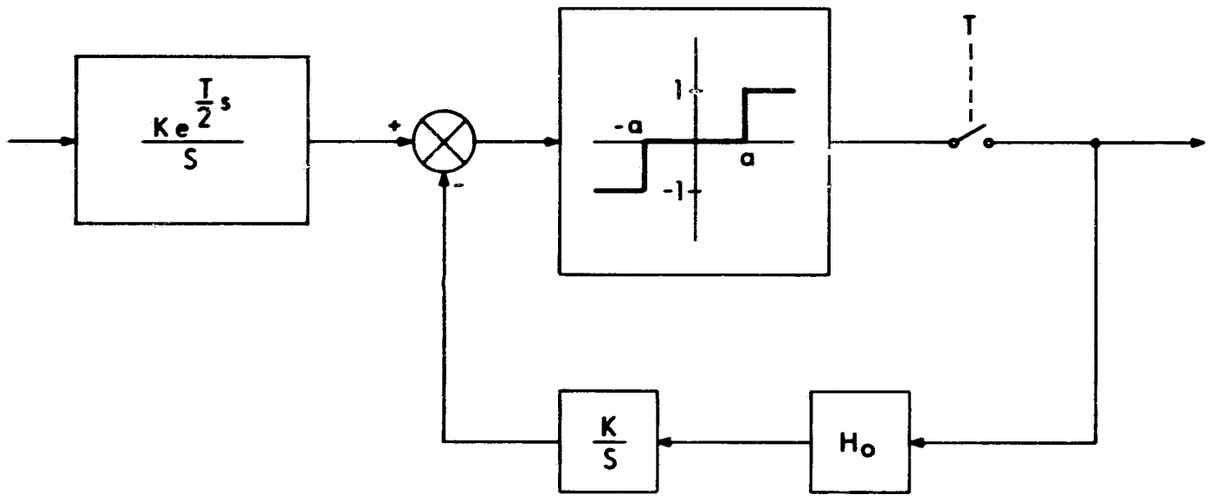

Fig. 2.6-3 Idealized system with one-half clock period prediction added.

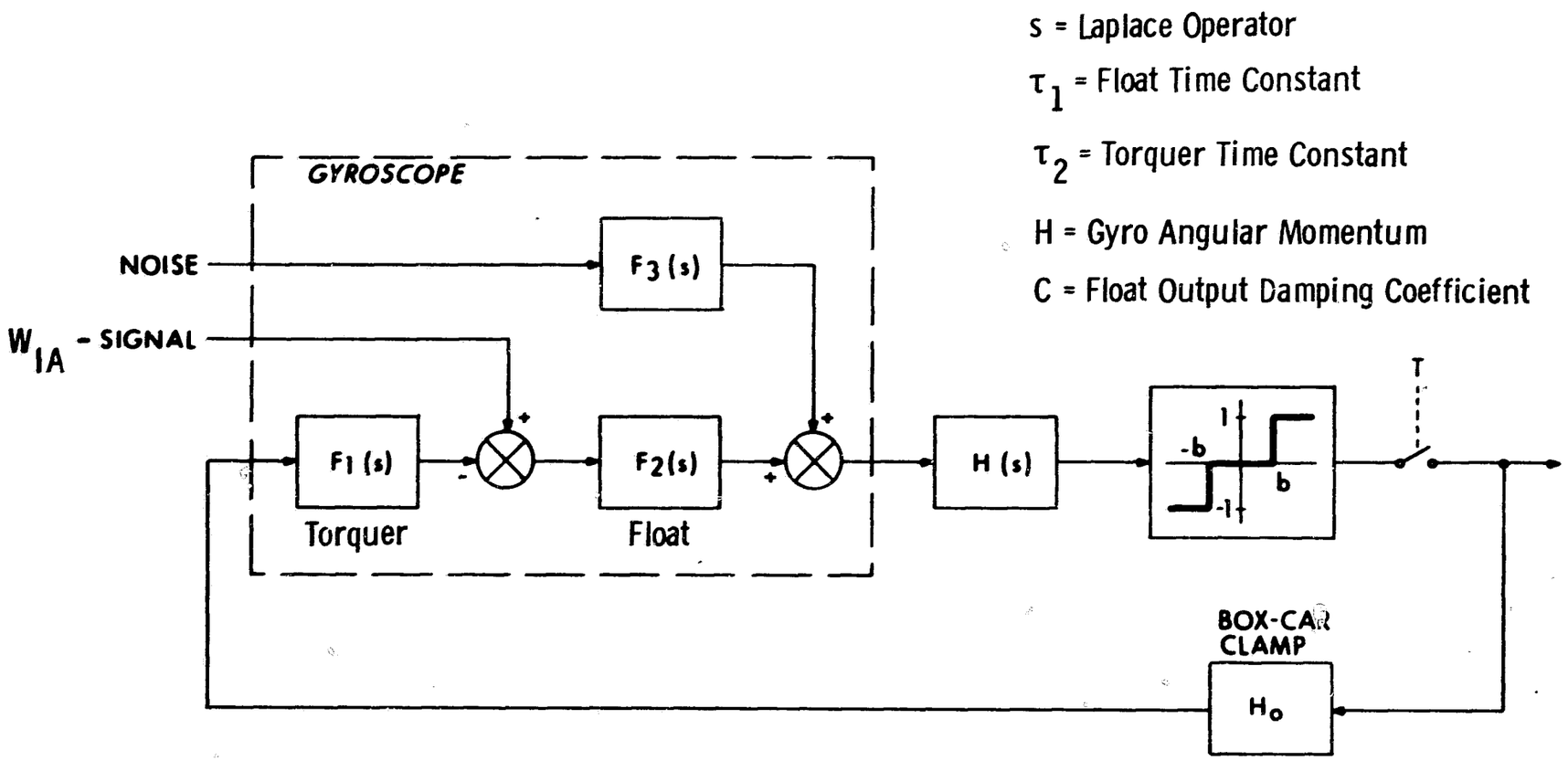

Fig. 2.6-4 **Linearized, single-axis model of a pulse-rebalanced gyroscope.**
(Note normalization of Input and Output)

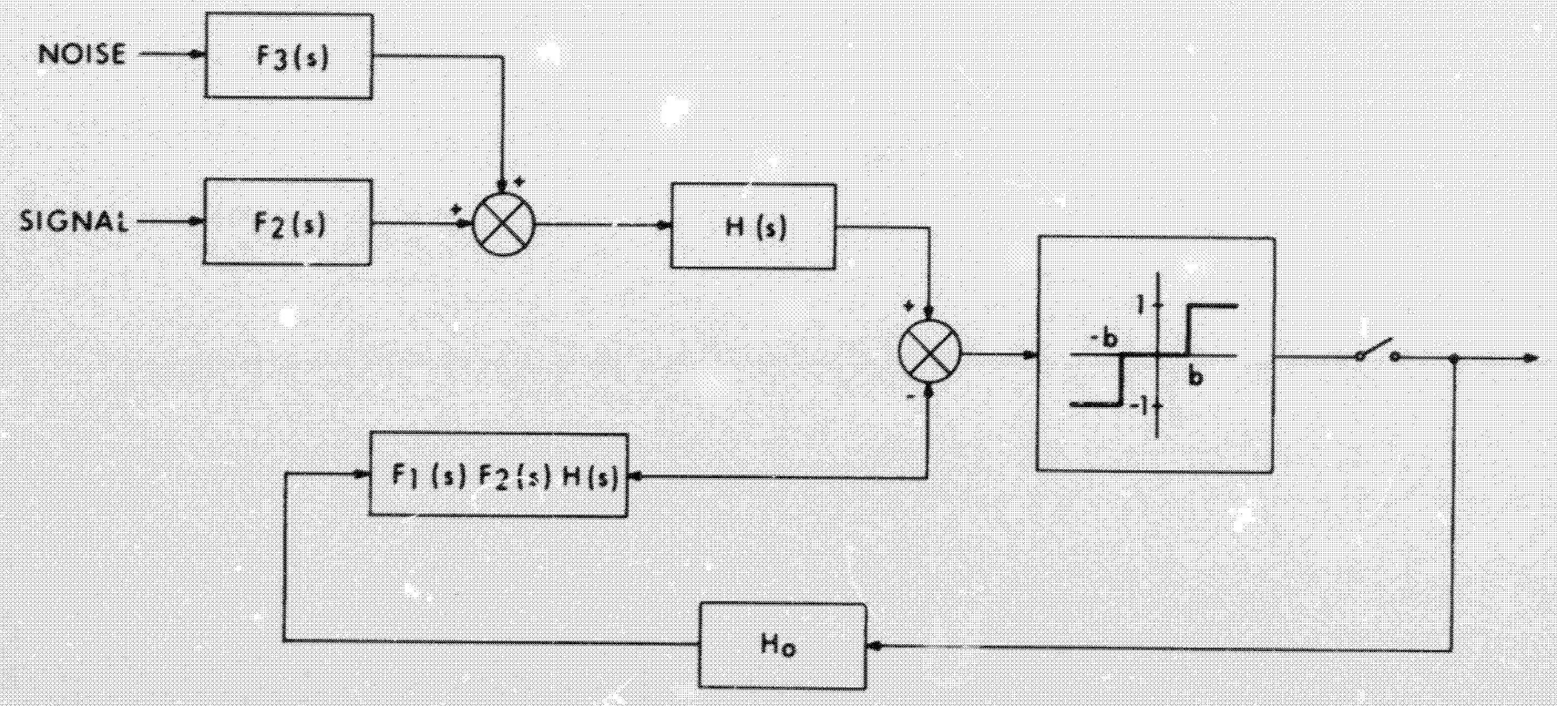

Fig. 2.6-5 Pulse-rebalanced gyroscope model with separate rebalance branch.

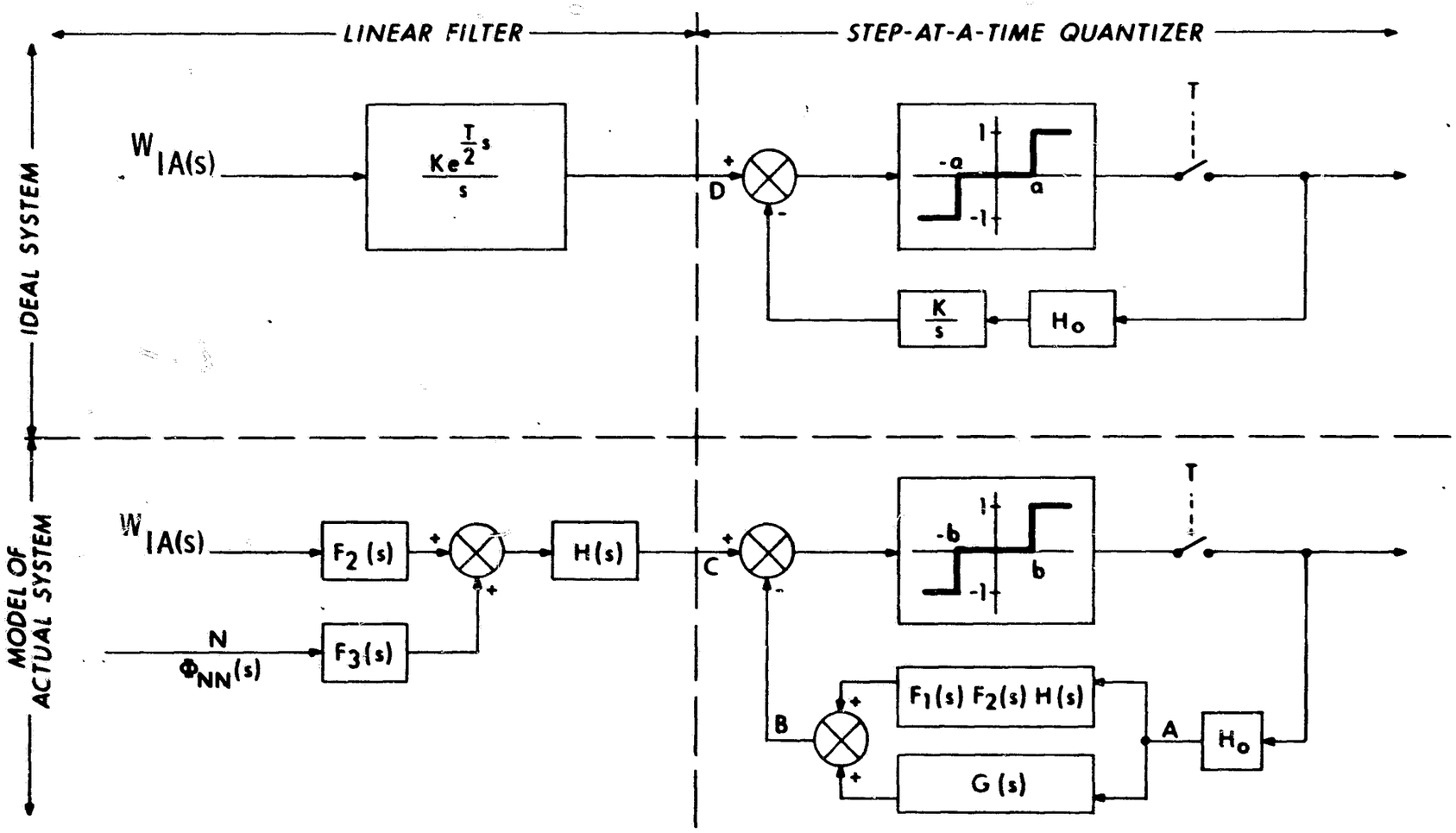

Fig. 2.6-6 Comparison of ideal and actual systems.

These steps are:

1. Formulate the optimum filter problem by choosing a linear filter, H(s), to minimize some function of the error between points C and D.

2. After the filter, H(s), has been chosen, calculate the necessary compensating function, G(s), to match the ideal by.

   a) selecting G(s) so that the overall transfer function from points A to B is K/s, and

   b) setting the trigger level, b, to equal the ideal value, a.

2.6.3 Design of the Compensation

To be able to solve for the ideal compensating transfer function is not enough. Its use in a system is dependent on the relative complexity and reliability of its circuit mechanization. The above theory has been formulated to achieve these objectives, i.e., the invention of a practical compensation mechanization. For example, if we wish to compensate the 18 IRIG MOD B when tested with no output filter, the method below is applicable. The right half of Fig. 2.6-6 shows that proper compensation requires that:

$$F_1(s)\ F_2(s)\ H(s) + G(s) = \frac{K}{s} \qquad (2.6.1)$$

Note that:

$$F_1(s)\ F_2(s) = \frac{K}{s(\tau_1 s + 1)(\tau_2 s + 1)} \qquad (2.6.2)$$

where: τ_1 is the float time constant of 450 microseconds and τ_2 is the torquer-current rise time of 40 microseconds. If we set H(s) to unity the solution for G(s) is:

$$G(s) = \frac{K}{s}\left[1 - \frac{1}{(\tau_1 s + 1)(\tau_2 s + 1)}\right]$$

$$G(s) = K\left[\frac{\tau_1\tau_2 s + (\tau_1 + \tau_2)}{(\tau_1 s + 1)(\tau_2 s + 1)}\right] \qquad (2.6.3)$$

$$G(s) = K(\tau_1 + \tau_2)\left[\frac{\tau s + 1}{(\tau_1 s + 1)(\tau_2 s + 1)}\right]$$

where

$$\tau = \frac{\tau_1 \tau_2}{\tau_1 + \tau_2}$$

But, since $\tau_1 \gg \tau_2$,

$$\tau \approx \tau_2$$

and thus

$$G(s) \approx \frac{K(\tau_1 + \tau_2)}{\tau_1 s + 1} \qquad (2.6.4)$$

Hence, a single-time-constant, R-C network which supplies a bias voltage either to the gyro preamplifier output or to the interrogator thresholds is sufficient to compensate the instrument and eliminate moding in a ternary control loop.

2.6.4 Analog Simulation Results

To illustrate the effectiveness of such simple compensation, an analog simulation of this gyro and rebalance loop was constructed. Even though an output filter having an additional lag of 55 microseconds was added, a single-time-constant compensation was still sufficient, requiring only a slight modification in the gain derived above. Figure 2.6-7 is the response to an initial float displacement of five-pulse quanta with no input and no compensation. The deadzone is plus or minus 3/4 one-pulse weight. Observe that a steady-state limit cycle was established. With the compensation, the response is shown in Fig. 2.6-8. In another test, the deadzone was set to the absolute minimum, plus or minus 1/2 a pulse weight. Then a quite severe ramp to one-half the maximum rebalance rate was applied. The uncompensated response, shown in Fig. 2.6-9, displays a poor initial transient and six-six steady-state moding. The compensated unit responded as in Fig. 2.6-10, with an excellent representation of the ramp and ideal one-on one-off moding to indicate half-rate.

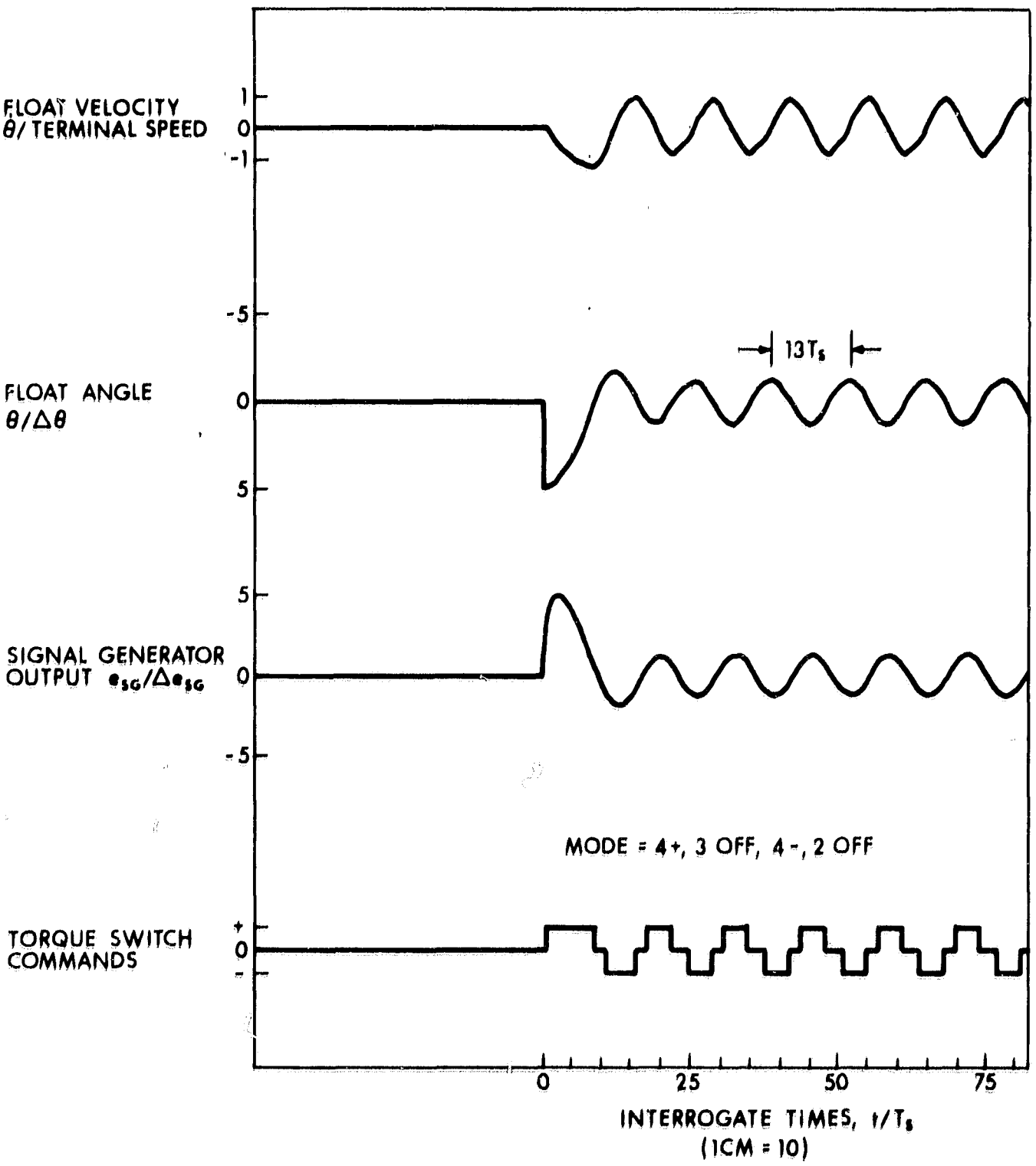

Fig. 2.6-7 Response of uncompensated system to initial condition $\theta = 5\Delta\theta$, DEADBAND = $\pm 3/4\Delta\theta$

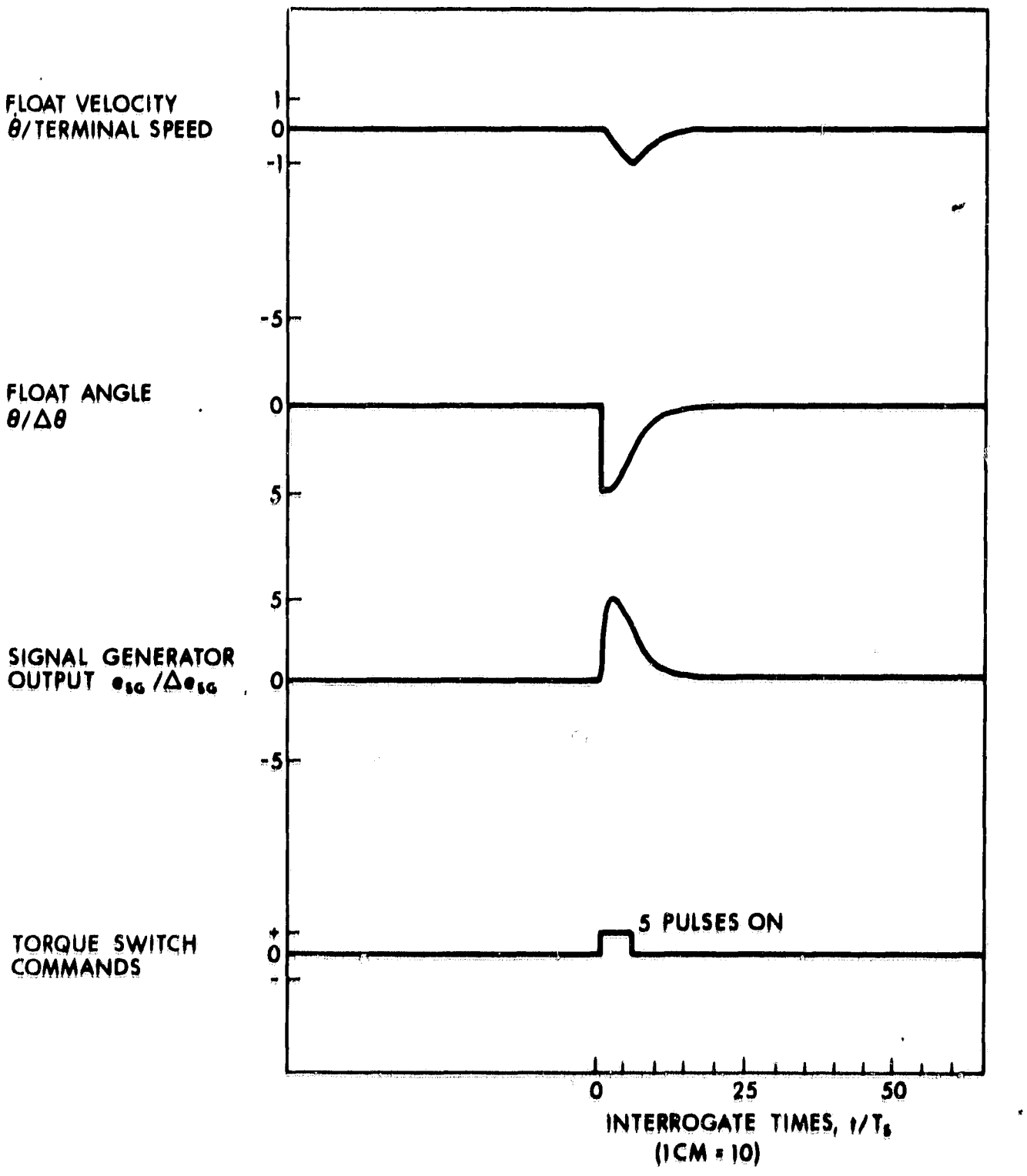

Fig. 2.6-8 Response of compensated system to initial condition $\theta = 5\Delta\theta$, DEADBAND = $\pm 3/4\,\Delta\theta$

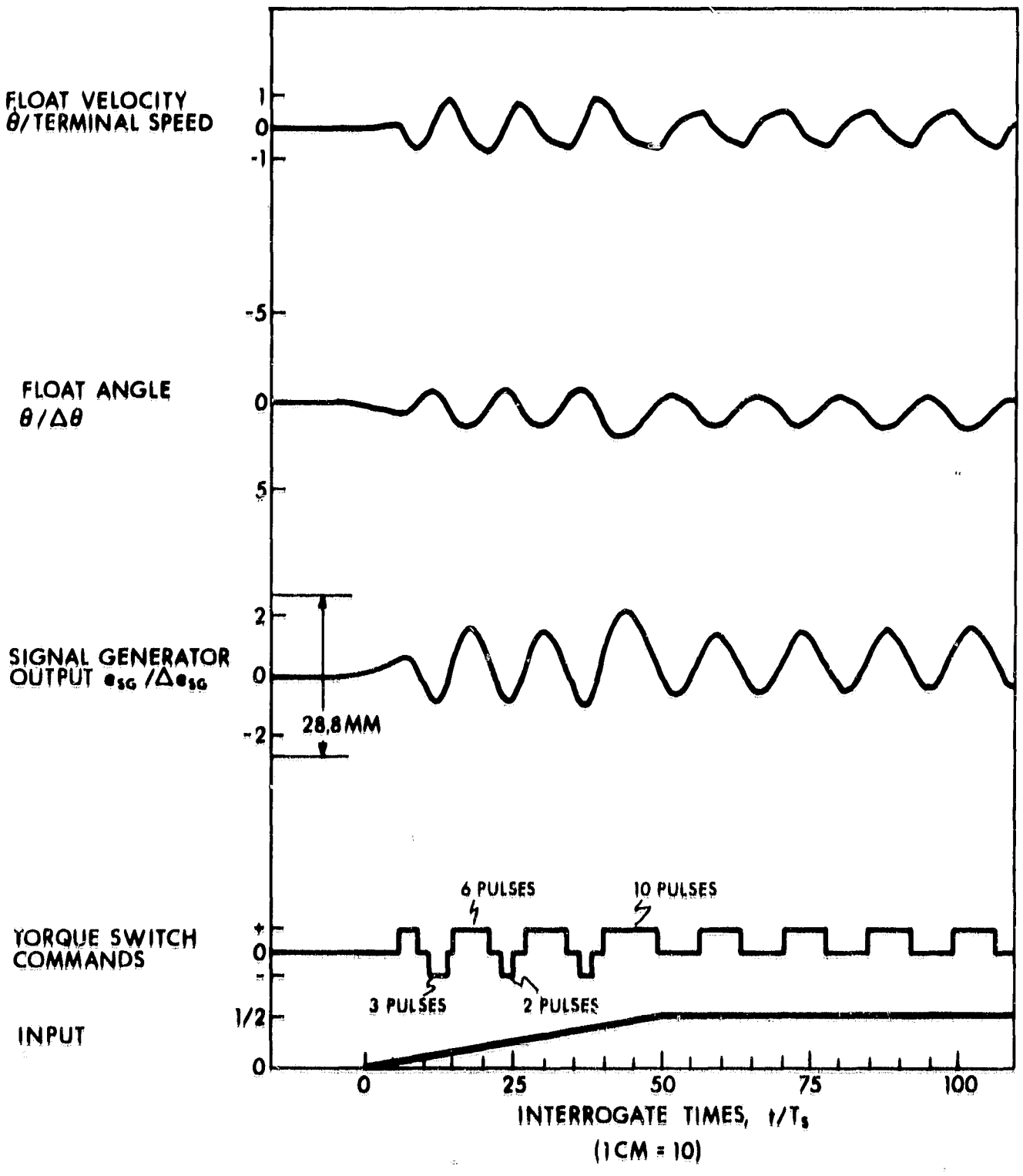

Fig. 2.6-9 Response of uncompensated system to ramp to one-half maximum rate, DEADBAND $= \pm 1/2\Delta\theta$

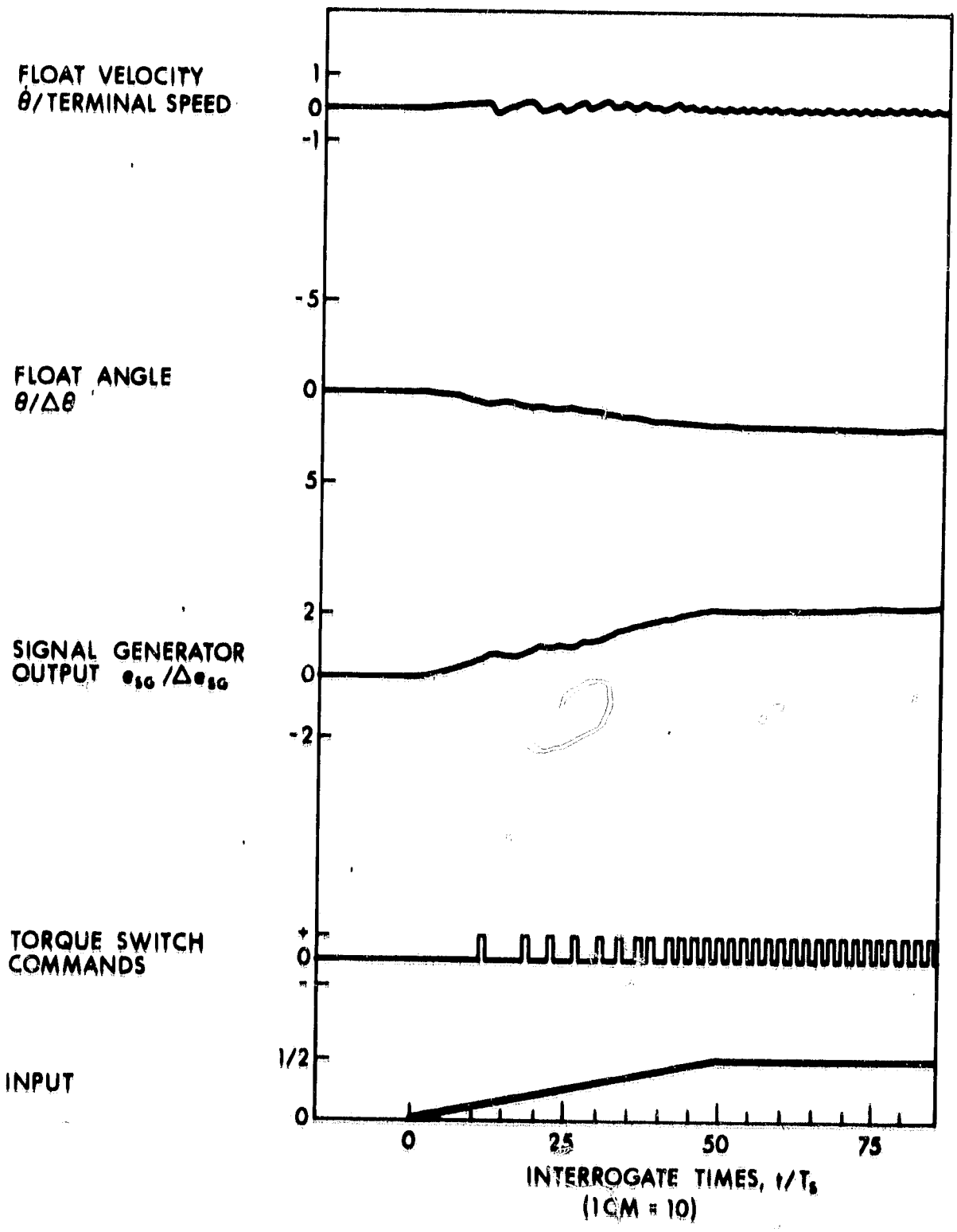

Fig. 2.6-10 Response of compensated system to ramp to one-half maximum rate. DEADBAND = $+1/2\Delta\theta$

3. INERTIAL COMPONENT EVALUATIONS 18 IRIG MOD B AND 16 PM PIP

3.1 Introduction

In addition to consideration of systems configurations and computational techniques it is important to evaluate the basics of instrument performance and reliability. In order to provide a realistic assessment and projection of strapdown systems capabilities, two state-of-the-art inertial grade instrument designs were selected for development study and test evaluations. Evaluation studies were programmed to include both instrument level and integrated Body-Mounted Sensor Package (Chapter IV) testing. The instruments evaluated were the:

1. Size-18-Integrating-Rate-Inertial-Gyro Mod B (18 IRIG MOD B)
2. Size-16-Permanent-Magnet-Pulsed-Integrating-Pendulous Accelerometer (16 PM PIP)

The 18 IRIG MOD B is a single-degree-of-freedom gyroscope that is currently under development at the MIT Instrumentation Laboratory. Apart from reduced size, its gas-bearing wheel package and permanent-magnet torquer are the basic features that distinguish it from the Apollo II gyro. The 18 IRIG MOD B design, however, is specifically oriented towards a strapdown environment application. The torquer, for example, is compatible with input rates of up to one radian per second. Similarly, the suspension design prevents radial side loading for rates somewhat in excess of one radian per second. The gas bearing is considered relative to the objectives of extended operational life that appears warranted for planetary missions of several years duration. Wheel-bearing failure or degradation has accounted for approximately 50% of the Apollo II ball-bearing-gyro failure population.

Continued development of this instrument was funded under the scope of this program. Four units are to be fabricated for evaluation and to support Body-Mounted Sensor Package integrated systems testing. At this reporting date performance data on one unit is available and it is included in this text. Two other units encountered wheel-bearing degradation during preliminary acceptance testing and are under investigation for corrective design action. It is anticipated that all four units will be available by July 1968.

The 16 PM PIP is a single-degree-of-freedom pendulous integrating specific force receiver operated in a closed-loop torque-restrained mode. It represents the next level of maturity in the development cycle of this type of MIT instrument. It is primarily distinguished from its predecessor, the Apollo II 16 PIP, by a permanent-magnet torquer and solid float. Its development was for support of a gimbal Inertial Guidance System and, as such, it is not specifically designed for strapdown

application. It merits consideration in that it represents the current state-of-the-art status for this instrument class and incorporates design features that suggest significant operational and reliability advantages over its predecessor. Among these advantages are the increased stability of the permanent-magnet torquer, the reduced sensitivities to float motion, the absence of radial side loading, and the elimination of hysteresis sensitivites (i.e., gaussing) associated with microsyn torquers. Reliability improvement is projected through the reduced number of parts and their simplified construction features. The solid float and improvements in the case assembly design should eliminate the sealing difficulties that have accounted for over 30% of the Apollo PIP failures.

Four 16 PM PIP's were made available for evaluation testing. One unit, SN-12, was furnished to NASA/MSC.

This chapter is devoted to a description of the test and analysis studies conducted to date on the 18 IRIG MOD B and 16 PM PIP. Physical and operational features are presented and test results are detailed. Descriptions of special test considerations and procedures are included where they provide a fuller appreciation to test results. When applicable, recommendations for design changes to enhance the instruments' suitability in a strapdown application are furnished.

3.2 Evaluation Summary and Recommendations

A brief summary of the evaluation test results on the 18 IRIG MOD B and 16 PM PIP is provided in this section. Their performance and the problems encountered during test are outlined. Design recommendations where applicable are listed. This summary should be viewed as interim in nature, however, since only a limited number of instruments have been available. Similarly, the scope of testing has been curtailed by funding limitations. Vibration, shock, and dynamic-environment testing have not been possible. The detailed test evaluation discussions for each instrument are presented in Section 3.3 and 3.4.

A) 18 IRIG MOD B Test Evaluation Summary & Recommendations

This section briefly summarizes unit 411 evaluation test findings. The coefficient data, presented in (1) below, allow a measure of quality relative to basic inertial component instrument performance. The torquer performance evaluation data in (2) are presented as an index of the instrument's potential suitability for strapdown pulse torque-to-balance operation. Problem areas encountered during test evaluation are outlined in (3) and recommendations for design resolutions are provided when applicable. Design improvements in (4) are then recommended which offer potential performance and utilization advantages for extended mission strapdown applications. (Detailed test evaluation findings, status and problem area discussions are present in Section 3.3)

1. Coefficient Performance

One-sigma drift stability for 21 three-position servo runs.

Bias drift = 3.8* meru (0.057°/hr)

Acceleration Sensitive Terms:

ADSRA (spin reference axis) = 1.3 meru/g (0.0195°/hr-g)
ADIA (input axis) = 1.8 meru/g (0.0245°/hr-g)

Compliance = -0.44 to -1.39 meru/g^2 (0.0066 to 2.09°/hr-g^2)

2. Torquer - Control Loop Performance

a. Pulse torque-to-balance Scale Factor (SF):

Stability - 5 ppm for 13-1/2 hours at 3200-pps interrogation rate,
Linearity - 100 ppm at 3200-pps interrogation rate 2° to 10°/sec input.
(9600-pps interrogation rate SF stability 25 ppm, linearity 200 ppm).

b. Torquer Sensitivites

Temperature - 16 ppm°/F
Axial displacement - less than 50 ppm, 10 g's along output axis
Radial displacement - less than 10 ppm caused by 1/2-radian-per-second rate about the output axis.

The data presented in a. are indicative of the performance consistently obtained. Superior performance was exhibited during a limited number of test runs.

As indicated by the above performance data, the 18 IRIG MOD B has the potential of fulfilling the overall objectives of a strapdown gyroscope for advanced manned missions.

3. Problem Areas and Recommendations

The following problem areas were uncovered during component testing, and design solutions in accordance with the recommendations are in process.

a. Stop-Bias Hysteresis (Section 3.3.5 C1)

Bias changes of up to 10 meru occurred due to the float rotating into the rotational stop caused by magnetic material on the float in the vicinity of the magnet. The recommended solution is the development of a non-magnet torquing coil holder.

*This relatively large bias uncertainty represents the influence of the stop-bias affect. In a 6-day test sequence in which the float was held at a null during test table repositioning the 1 σ , BD = 0.62 meru.

b. Eddy-Current Sensitivities (Section 3.3.5 C2)

SF torquing-rate sensitivity due to induced eddy-current flow in the beryllium coil holder. The eddy-current influence is to cause an effective torquer-coil-inductance resistance change with frequency. A high-resistance, preferably nonmetalic, material is recommended for the coil holder.

c. SG Signal-to-Noise Ratio and Pulse Coupling (Section 3.3.6 & 3.3.10C)

Presence of an 800-cps pickup and 1600-cps side-band carrier modulation limits the ultimate torque-to-balance control-loop sensitivity. The 800-cps pickup and pulse coupling is probably due to internal harness configuration and the side bands result from presence of magnetic connector pins in SG end-housing area. The use of nonmagnetic pins, investigation of an optimum harnessing configuration, and further control-loop development in the areas of noise desensitization and interrogation timing are recommended.

d. Bearing Reliability (Section 3.3.8 & 3.3.10)

To date hard starts have occurred on two units (410B and 412) and high-speed touchdowns have been accidently induced on units 410 and 411. Development of improved bearing-wear surfaces (e.g.: fine-grained hot-pressed alumina) and optimum bearing geometry (higher g and slew capability) is recommended.

4. Desirable Design Improvements

The following are design changes and investigations that are considered desirable for improved strapdown performance and extended mission applications.

a. Torque-Generator Power (Section 3.3.5 A)

Incorporation of higher flux-density magnet assembly would reduce torquer power requirements for a one-radian slew capability by almost 50% and yield a corresponding improvement in electronic design efficiency. Performance improvement in reduced scale-factor difference between cw and ccw torquing would also be achieved.

b. SG-to-TG Alignment (Section 3.3.5 A)

Improved torquer sensitivity to float angle rotation can be achieved by higher-accuracy SG-to-TG alignment coincidence. The ac torquer sensitivity alignment procedure (3.3.5 A) is recommended.

c. Minimization of Gyro Bias Drift (Section 3.3.9)

Matching end-housings and rotor reaction and mechanical torques could yield a desirable reduction in the magnitude of the bias drift terms. Elimination of output-axis acceleration sensitivities by improved flex-lead development would also be advantageous.

d. Reduced Gyro-Float Time Constant (Section 2.5 - 2.6)

Improved gyro bandwidth for optimum control-loop performance would be desirable. The pulse-bursting phenomenon which is due to the large time constant is considered undesirable, especially in a high-speed DDA algorithm implementation. At the 9600-pps interrogation rate, pulse-bursting is evident at all test rates.

e. Wheel-Motor Development (Section 3.3.9)

Studies to reduce wheel power as well as the development of ceramic wheel-motor stator-fabricating techniques are desirable for extended mission considerations.

Finally, it is recommended that continued development and test evaluation of the 18 IRIG MOD B be pursued. In the area of pulse torque-to-balance operation the dynamic and environmental interplay makes parallel development of both the instrument and control-loop characteristics necessary if ultimate strapdown performance objectives are to be achieved. Test-program extension, to include shock and vibration of wheel assemblies to measure the ultimate capability of the bearing design, would be very desirable.

B) 16 PM PIP Test Evaluation Summary & Recommendations

The test evaluation has demonstrated that the PM PIP is a high-performance instrument with the potential of fulfilling the objectives of extended manned missions. The stability of both scale factor and bias under ideal test conditions appear to satisfy the performance objectives of anticipated extended missions when operated at the 3200-pps interrogation rate. Operation at the 9600-pps interrogation rate was poorer, since the interplay between float motion response and noise coupling is more significant at the higher frequency.

Under less-ideal conditions substantial shifts were recorded in the instrument stability measurements. These shifts were at times associated with the double-pulsing phenomenon, though in other instances no explanation was apparent. One probable cause of the shifts is the sensitivity of the entire control loop to noise-coupling between the SG & TG lines. Although the coupling appeared to occur within the instrument harness, the source is associated with the torque-current switching characteristics of the electronics loop. Continued intensive investigation of this noise sensitivity in the development of the electronic control loop is necessary.

As with the Apollo MOD D PIP, stop-bias hysteresis is the primary cause of the bias instability of the PM PIP. Scale-factor changes due to typical on-off operation and to simulated electronics malfunctions have been small.

The anisoelectric term ($I_{PA} - I_{IA}$) is large enough in the present float design to represent an undesirable error source in a strapdown application with sustained angular rates. It is recommended that design studies to reduce the anisoinertia term be initiated. It is further recommended that additional testing be done to evaluate the effects of large current variations, more severe operational malfunctions, vibration, shock, dynamic rates, and high-g inputs. The parallel development of both the instrument and control loop is essential if the ultimate strapdown performance objectives are to be achieved.

3.3 18 Integrating Inertial Gyro MOD B (IRIG MOD B)

3.3.1 Introduction

The 18 IRIG MOD B is a single-degree-of-freedom gyroscope that is currently under development at the MIT Instrumentation Laboratory. Apart from reduced size, its gas-bearing wheel package and permanent-magnet torquer are the basic features that distinguish it from the Apollo II gyro. The 18 IRIG MOD B design, however, is specifically oriented towards a strapdown environment application. The torquer, for example, is compatible with input rates of up to one radian per second. Similarly, the suspension design prevents radial side loading for rates somewhat in excess of one radian per second.

3.3.2 Physical Description

The 18 IRIG MOD B gyro (Fig. 3.3-1) is a single-degree-of-freedom integrating gyro. It has a gas-bearing wheel that rotates at 24,000 rpm and develops an angular momentum of 151,000 gm-cm^2/sec. A 4-pole, 800-cps, 2-phase synchronous motor drives the wheel. The bearing consists of a stabilized journal pressurized by outboard thrust plates. The wheel and motor structure are mounted in a hermetically sealed cylindrical float. The float is pressurized at one atmosphere with neon gas. The float is surrounded by a high-density damping fluid (brominated fluorocarbon), the temperature of which is controlled to maintain the float near neutral buoyance (132°F). Bellows are provided in each end-housing to allow for fluid thermal-expansion changes.

An 8-pole magnetic microsyn suspension is provided at each end of the unit. It stabilizes the (axial and radial) geometrical relationship between the gyro float and case (taper angle of 15° and radial-gap clearance of 0.003 inch). At one end of the case is a signal generator whose output is proportional in magnitude and phase to the angular position of the float about the output axis. It is a 12-pole multiple-E-connected microsyn. Its sensitivity is 20 mv/mr using an 8-volt, 9600-cps excitation source.

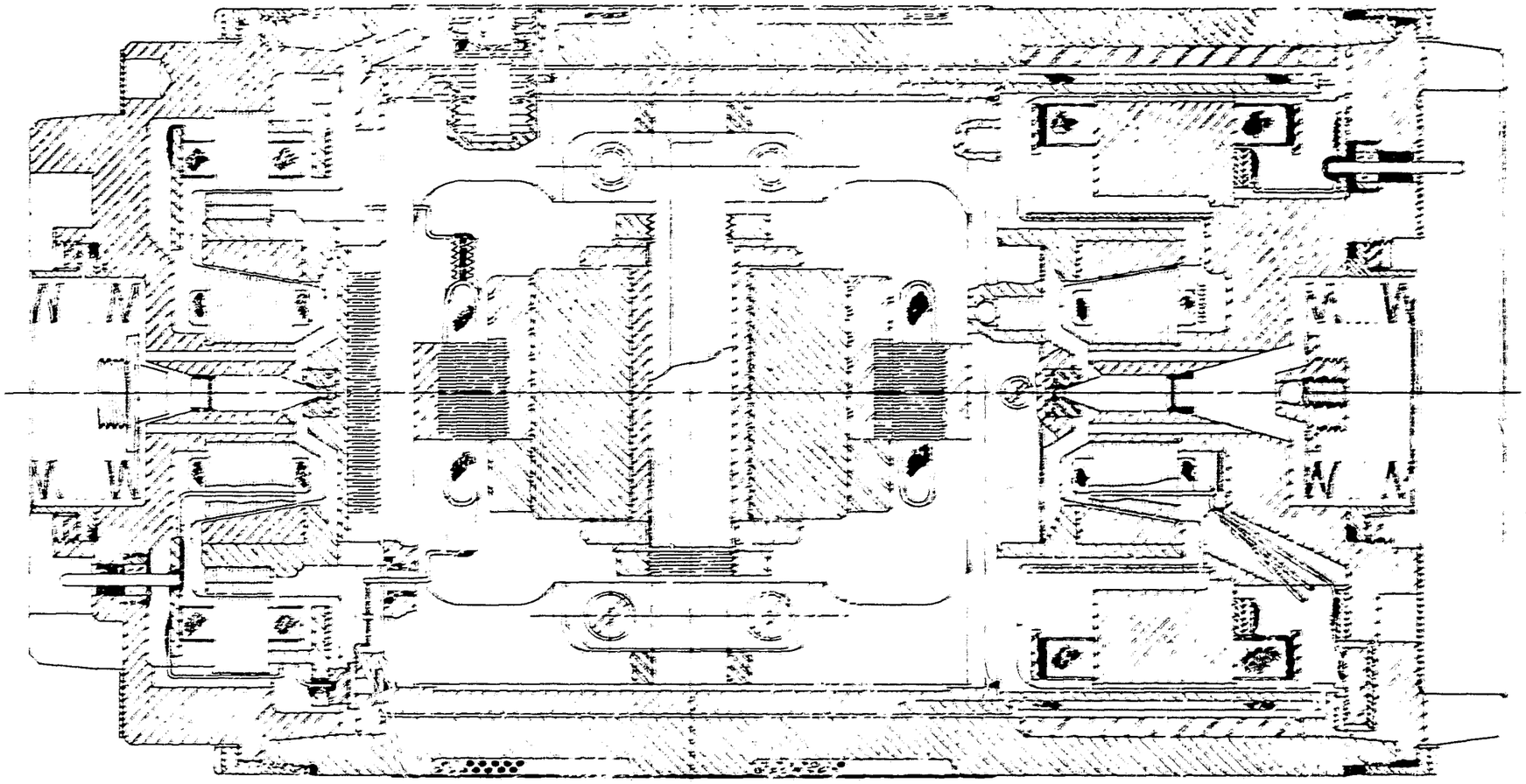

Fig. 3.3-1 18 IRIG MOD B cutaway view.

A permanent-magnet torque generator is at the opposite case end. The permanent-magnet assembly in the 18 IRIG MOD B gyro consists of Alnico V permanent magnet with 8 poles, an armco-iron return path and 8 torquing coils, each having 144 turns. The magnet and return path are located on the gyro-case end-housing. The coil is mounted on a beryllium holder that is attached to the float. The coils are excited through flexible leads. The coils will create a torque on the float about the case output axis that is proportional to the current magnitude. Coils around the magnetic poles are provided to magnetize the permanent magnet. After magnetizing, it is partly demagnetized with an ac voltage. This stabilizes its decay characteristic with time (less than 30 ppm change in torque in 90 days). A magnetic ring located in the end-housing on the side of the magnet provides torquer|scale-factor temperature compensation. The permanent magnet is magnetized after the gyro is assembled to eliminate contamination problems that could occur in assembling a magnetized torquer.

Wrapped around the gyro case are four nickel-wire-wound temperature sensors for temperature control and monitoring. The case is then enclosed in a shroud to provide magnetic shielding and a vacuum envelope to reduce thermal radial gradients. The unit is approximately 2 inches in diameter, 3-7/8 inches long, and weighs 1.15 lb.

Table 3.3-1 represents a survey of operational and control parameters for the 18 IRIG MOD B.

3.3.3 Principles of Operation

The equation of motion for an ideal single-degree-of-freedom gyro is given by

$$I_{OA}\ \ddot{A}_{OA} + C\ \dot{A}_{OA} + KA_{OA} = H\,W_{IA} + M_{TG} + U_T \qquad (3.3.1)$$

where

I_{OA} = moment of inertia of the float about its output axis ($gm\text{-}cm^2$)

A_{OA} = float-to-case angle about the output axis (rad)

C = float damping coefficient about output axis (dyne-cm/rad/sec)

K = elastic spring constant about the output axis (dyne-cm/rad)

TABLE 3.3-1

19 IRIG MOD B NOMINAL PARAMETERS
AND OPERATIONAL FEATURES

Gyro Constants	Units		Symbol
Angular Momentum	0.151×10^6	$\frac{gm\text{-}cm^2}{sec}$	H
Output Axis Damping Coefficient	502,000	dyne-cm-sec	C_{OA}
Output Axis Inertia	225	$gm\text{-}cm^2$	I_{OA}
Float Time Constant	450	μ sec	$t_f = \frac{I_{OA}}{C_{OA}}$
Transfer Function	6	$\frac{millivolts}{milliradian}$	$(\frac{H}{C_{OA}} S_{SG})$
Torquer Rate Scale Factor	1035	$\frac{deg/hr}{ma}$	SF
Torquer Time Constant	55	μ sec	$t_{tg} = \frac{L}{R}$
Anisoinertia Coefficient	9.2	$\frac{deg/hr}{(rad/sec)^2}$	$\frac{I_{SA} - I_{IA}}{H}$
Anisoelastic Coefficient	0.012	$\frac{deg/hr}{g^2}$	K_{IO}
Float Mass Unbalance Uncertainty	0.075	$\frac{deg/hr}{g}$	ADIA ADSRA

TABLE 3.3-1 (CONT'D)

Wheel Bearing Characteristics	Units		Symbols
Speed	24,000	rpm	
Rotor Moment of Inertia	60.5	$gm\text{-}cm^2$	I_{SR}
IA Slew Capability	5	rad/sec	
Motor Excitation	28V, 800-Hz		
Power	11 watts start, 5.2 watts synch		
Run up Time (at 28V)	10	sec	
Float Characteristics			
Moment of Inertia			
OA	225	$gm\text{-}cm^2$	I_{OA}
IA	436	$gm\text{-}cm^2$	I_{IA}
SRA	435	$gm\text{-}cm^2$	I_{SRA}
Float Anisoinertia	$\leq 0.03\ I_{OA}$		
Rotational Stops	±17	mr	
Flotation Temp	132	^oF	
Torque - Characteristics			
Sensitivity	775	dyne-cm/ma	
Magnet Stability	30	ppm/90 days	
Temperature Coefficient	<10	$ppm/^oF$	
Coil Resistance	158	ohms	
Continous power (Negligible thermal unbalance)	0.9	watt	

TABLE 3.3-1 (CONT'D)

Signal Generator Characteristics	Units		Symbols
Excitation	9600 Hz, 8V, 7ma		
Sensitivity	20	mv/mr (about OA)	S_{SG}
Reaction torque	±0.05	dyne-cm	
Secondary Impedance (9600-Hz, 130°F)	194 + j2700		Z_S
Primary Impedance (9600-Hz, 130°F)	115 + j1160		Z_P
Suspension Characteristics			
Excitation	9600-Hz, 8V, .83 watt/suspension end		
Capacitor (working range)	.014 μfd - 45V		
Damping Resistor	7.2 - 9.2	ohms	
Radial Stiffness	8 gms/0.001"		
Peak Radial Force (.0004")	31 (minimum)	gms	
Suspension Recovery	0.001"	radial displacement	
Axial Stiffness	0.64 gm /0.001"		
Reaction Torque	<.6	dyne-cm/ suspension assy.	
Thermal Considerations			
Sensor Resistance 130°F	494 ohms		
Sensor Gradients per sensors	0.00226 ohm /°F		
Storage (Bellows) Range	25 - 190°F		

H = wheel angular momentum (gm-cm^2/sec)

W_{IA} = angular rate of the case about the input axis (rad/sec)

M_{TG} = commanded torque of the torque generator (dyne-cm)

U_T = uncertainty torque acting on the gyro float about the output axis (dyne-cm)

For a unit with a low elastic restraint ($K \approx 0$) and no commanded torque, a constant-input rate, W_{IA}, will cause a constant torque about the gyro-float output axis. The resultant output-axis float rotation corresponds to

$$A_{OA} = \frac{H}{C} \int W_{IA} \qquad (3.3.2)$$

Since the float output angle, A_{OA}, is proportional to the integral of input angular rate, W_{IA}, the gyro is called an integrating gyro.

When the gyro is being command-torqued, the pulse-torque scale factor (defined as an angular motion about the gyro input axis that would yield the same output axis rotation as one pulse of torque) can be calculated from (3.3.1) Under steady-state conditions this equation reduces to

$$M_{TG} = H W_{IA} \qquad (3.3.3)$$

If M_{TG} is a non-time-variant function and t_s is the clock period corresponding to the duration of the control current, the pulse-torque scale factor (SF = the angle about IA resulting from one torque pulse) obtained from (3.3.3) is

$$SF = \frac{A_{IA}}{\text{pulse}} = \frac{M_{TG}\, t_s}{H} \qquad (3.3.4)$$

Counting the quantity of positive (N^+) and Negative (N^-) torquer pulses in a period of time will yield the total input angle charge during that period.

$$A_{IA} = \sum \frac{M_{TG}\, t_s}{H} (N^+ - N^-) \qquad (3.3.5)$$

In addition to the torques resulting from input rates and commands from the torque generator, the gyro experiences torques on its float arising from the non-ideal nature of its physical design. In general, an index of gyro performance is defined as a measure of the uncertainty of these torques. Three significant types of uncommanded torques that act about the gyro-float output axis are:

1. Bias Torques (independent of acceleration input) caused by flex-lead restraints and by magnetic restraints between the gyro float and case due to the suspensions, signal generator, and torque generator. A measure of this torque expressed as an equivalent input-axis rate is termed bias drift, BD.

2. Torques proportional to acceleration input caused by a non-coincidence of the gyro-float center of gravity (cg) and center of buoyancy (cb). The total torque is defined as resulting from specific-force input components acting along the spin axis and the input axis. The cg-cb displacement along the spin axis results in an equivalent input rate that is defined ADIA (drift due to acceleration along the input axis). Similarly, the displacement about the input axis yields an equivalent rate termed ADSRA (drift due to acceleration along the spin reference axis).

3. Torques proportional to the acceleration input squared. These torques are the result of compliance or yielding of the wheel structure. The torque about the gyro output axis due to the compliance effect is given by

$$M_{OA} = m^2 \left[A_S A_I (K_{SS} - K_{II}) - K_{IS} A_S^2 + K_{SI} A_I^2 - K_{IO} A_O A_I + K_{SO} A_O A_S\right] \qquad (3.3.6)$$

where

$A_{S,I,O}$ = the component of acceleration along the spin, input, or output axis, respectively.

m = the mass of the gyro wheel

$K_{i,j}$ = structural compliance resulting in a deflection along the i-axis for a force along the j-axis

Drift performance data for a gyro are taken on an inertially stabilized loop (Fig. 3.3-2). The gyro is mounted on a test table with its input axis parallel to the table axis. The gyro signal-generator output is amplified, then fed to the table servo which operates to rotate the gyro about its input axis. An ideal gyro operating in this type of test loop (servo mode) would maintain its input axis fixed in inertial space. It would sense the component of earth rate along its input axis and rotate the test table at this rate. The table rate for an actual gyro in a servo mode deviates from earth rate due to torques that act about its output axis. These torques are grouped in the following categories: torques that are independent of specific force inputs (acceleration), torques that are proportional to acceleration and to the square of acceleration (compliance). The table rate that is required about the gyro input axis to balance out these torques is the equivalent gyro drift terms (BD, ADIA, ADSRA, etc.). It is convenient to express these terms as a quantity of Earth rate. A meru of drift rate is a thousandth of the rate of rotation of the earth (0.015 degree/hr.)

In an actual system application it is normal practice to compensate for the drift terms. The ultimate instrument performance index is, therefore, the drift-rate stability. The measurement of drift rates is obtained by determining the time for the table to rotate through prescribed angles (generally one degree is used). Thus, the test determines the average drift rate over a period of time.

The three drift terms, BD, ADIA, and ADSRA, can be determined in a servo-mode test by measuring table rate (in a pulse-torque-to-balance-loop output pulses are counted over a period of time) for each of the three gyro positions shown in Fig. 3.3-3. The stability of the individual drift terms is determined by repeated measurements after storage periods or by continuous measurement of table drift rate for extended periods.

3.3.4 Dynamic Errors

In addition to the basic static drift errors, there are dynamic error sources which come into play when one considers a gyro operating in a strap-down environment. They are derived and discussed in a general sense in Chapter 2. Briefly, one error-source group is geometric in nature (coning and output-axis coupling) and would be evidenced even in an ideal instrument. These errors are compensated for in the system application by knowledge of dynamic inputs as measured by the instruments themselves. For example, correction for output-axis coupling can be effected using rate data determined from another instrument (its IA collinear with the OA of the instrument that is being corrected). Other error sources, such as anisoinertia and cross-coupling are due to the departure of the gyro from an ideal instrument, or to the use

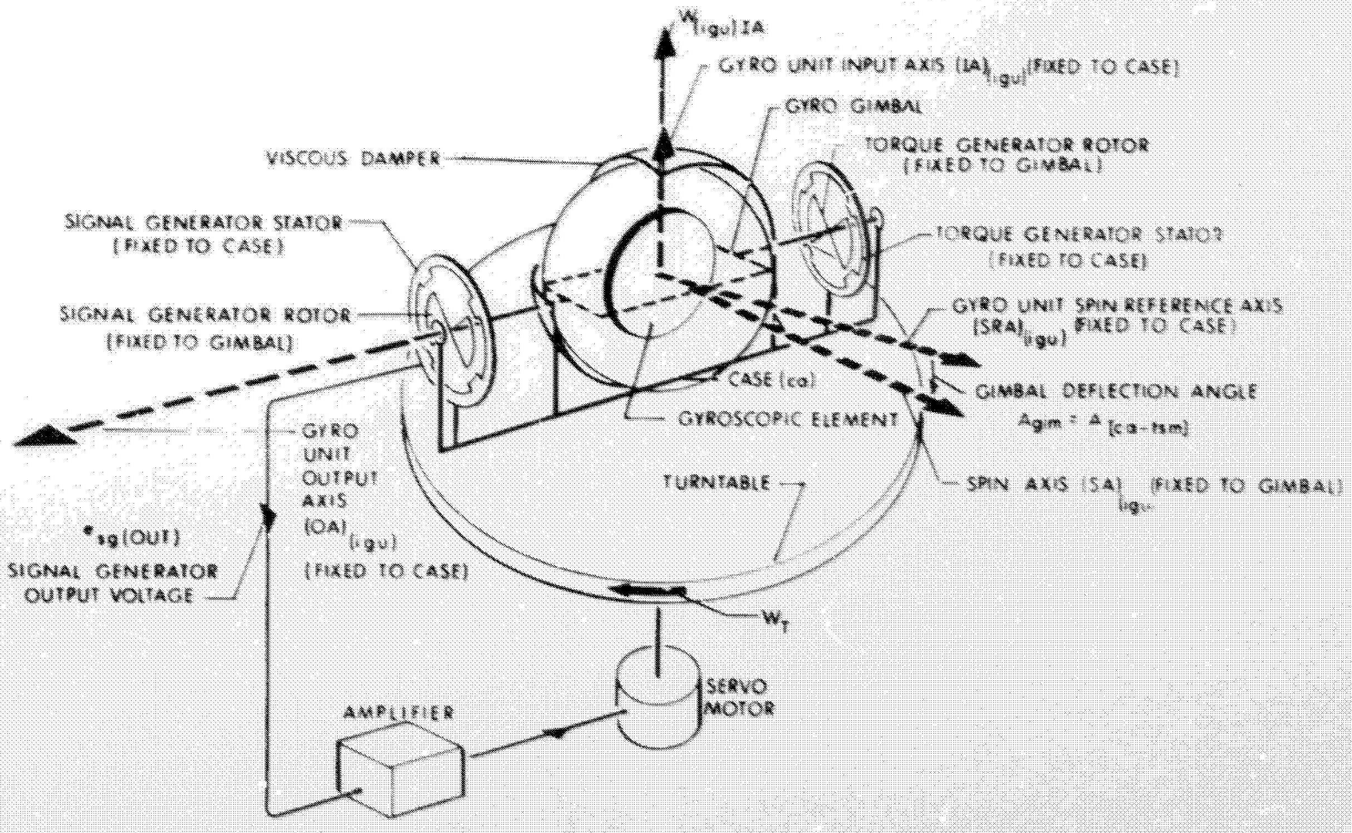

Fig. 3.3-2 A single-degree-of-freedom gyro operating in a single-axis inertially stabilized test control loop.

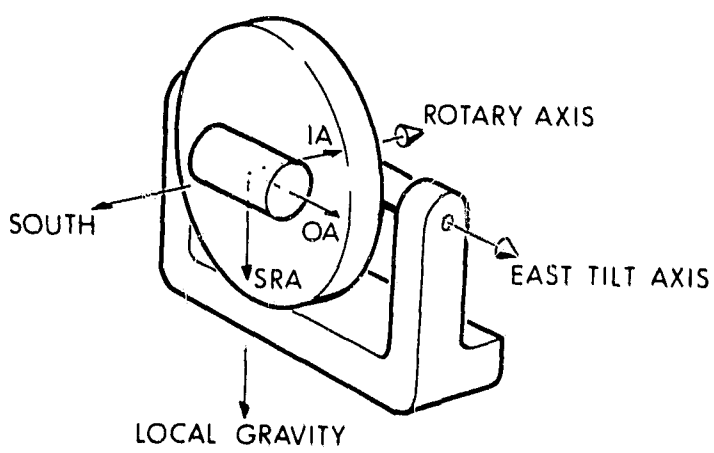

$\omega_T = \omega_{IE_H}$ - BD - ADSRA

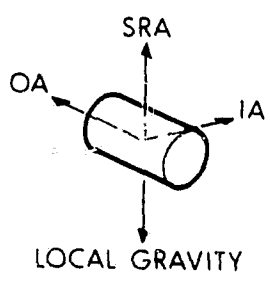

$\omega_T = \omega_{IE_H}$ - BD + ADSRA

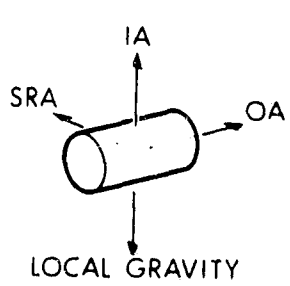

$\omega_T = \omega_{IE_V}$ - BD - ADIA

Fig. 3.3-3 Servo mode gyro drift test positions.

of the gyro in a non-ideal control loop. In stabilized platform applications these various dynamic-error sources are not routinely considered since the platform functions to isolate the instruments from undesired dynamic forcing functions. In a strapdown application the instruments encounter the full dynamic environment and all error sources must be reviewed. The instrument dynamic errors are tabulated below and corresponding average drift terms are calculated for the 18 IRIG MOD B for inputs that are typical of spacecraft dynamics.

1. Output-axis coupling (compensated for)
   Equivalent input-axis drift rate (W_D) due to acceleration of the gyro case about the output axis (steady-state solution):

$$W_D = \frac{I_{OA}}{H} \dot{W}_{OA} \qquad (3.3.7)$$

   W_D = 105 meru for a spacecraft steady-state angular acceleration of 0.005 rad/sec^2.

2. Coning (compensated for in basic algorithm)
   Equivalent input-axis drift due to kinematic rectification of angular sinusoidal vibrations about two gyro axes (SA & OA) which are phase-displaced (δ) from one another:

$$W_D = W_{SA} W_{OA} \pi f \sin \delta \qquad (3.3.8)$$

   f = coning frequency in cps

   W_D = 1630 meru for a limit-cycle angular vibration of 1^o at 1/2 cps, with δ equal to 90^o.

3. Anisoinertia
   Equivalent input-axis drift due to non-equal input- and spin-axis float inertias:

$$W_D = \frac{(I_{SA} - I_{IA})}{H} \left[W_{IA} W_{SA} + (W_{IA}^2 - W_{SA}^2) A_{OA} \right] \qquad (3.3.9)$$

   where A_{OA} represents the float angle offset from the SG Null and is very small in an effective control loop.

   W_D = 6.3 meru max for a 0.1-rad/sec input about IA & SA. with equal to 90^o.

3.3.5 Torque Generator

A) General Discussion

As previously noted, it is the high-rate torque-to-balance capability with minimum adverse performance effects that is the essential requirement for strapdown-gyro utilization. This section discusses some of the overall considerations associated with the torquer and its utilization in a strapdown torque-to-balance control loop. It then reviews torquer sensitivities, problems encountered, and corrective and design improvements anticipated to optimize the design for the strapdown application. These remaining subsections are:

B - Rotational Float-Angle Sensitivity (page 3-22)

C - Magnetic-Material Interaction (page 3-26)

D - Reduction in Torque-Generator Power (page 3-39)

The 18 IRIG employs a permanent-magnet torque 'generator' as opposed to the square-law torquer used in the Apollo Gyro. As such, it is a linear device and (apart from non-ideal features) the magnetic stability and torquer scale-factor errors associated with current-transient rise and decay characteristics are eliminated.

The current (i) through a conductor in the magnet gap field (B) yields a force (F) on the conductor given by

$$\overline{F} = \overline{i} \times \overline{B} \tag{3.3.10}$$

(See Fig. 3.3-4, pictorial of a single pole of the 18 IRIG Torquer.)
This force acting at a distance ($\overline{r}$) from the center of rotation of the float will cause a torque

$$\overline{M} = \overline{F} \times \overline{r} \tag{3.3.11}$$

Reversing the direction of the current flow through the conductor will reverse the direction of torque.

The gyro operates in a closed loop (Fig. 3.3-5) where the torques on the float are restrained by control signals to the torque generator. Any rate about the input axis of the gyro produces a torque about its ouput axis and causes the float to rotate from a null position. The direction and magnitude of the float rotation is sensed by the signal generator. When the SG output voltage reaches a given threshold level, a discriminator provides a positive-or-negative set signal, depending on the polarity of the SG output voltage. These set signals are interrogated at a given clock frequency to switch a control current of fixed amplitude and duration into the positive or negative direction of the torque-

generator winding torque. A detailed description of the electronic test loop that was used in this evaluation and its parameters is provided in Chapter 4. Theoretical aspects of pulse-torque-restrained instrument servo loops are included in Chapter 2.

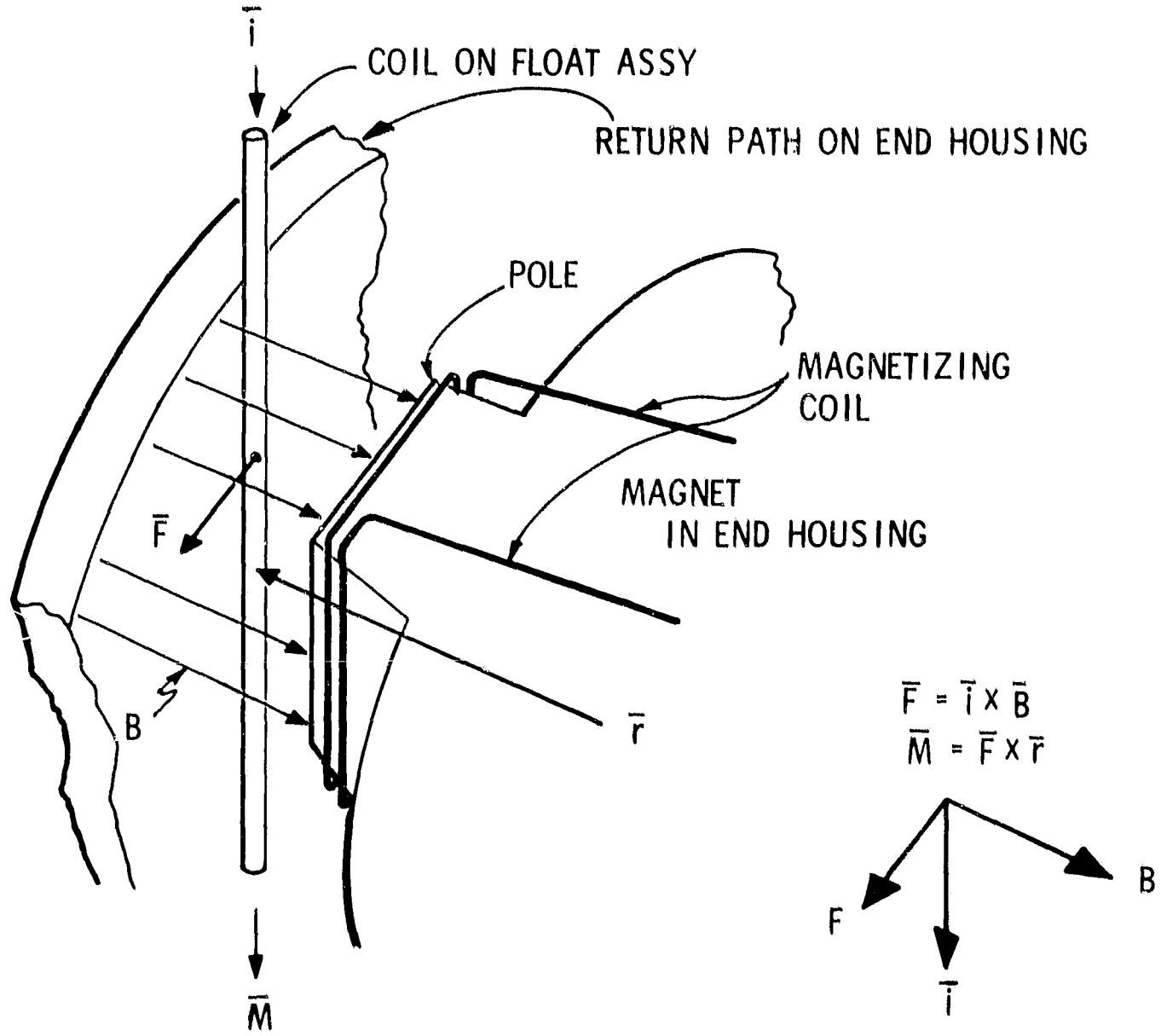

Fig. 3.3-4 Perspective view of single pole section of permanent magnet torquer.

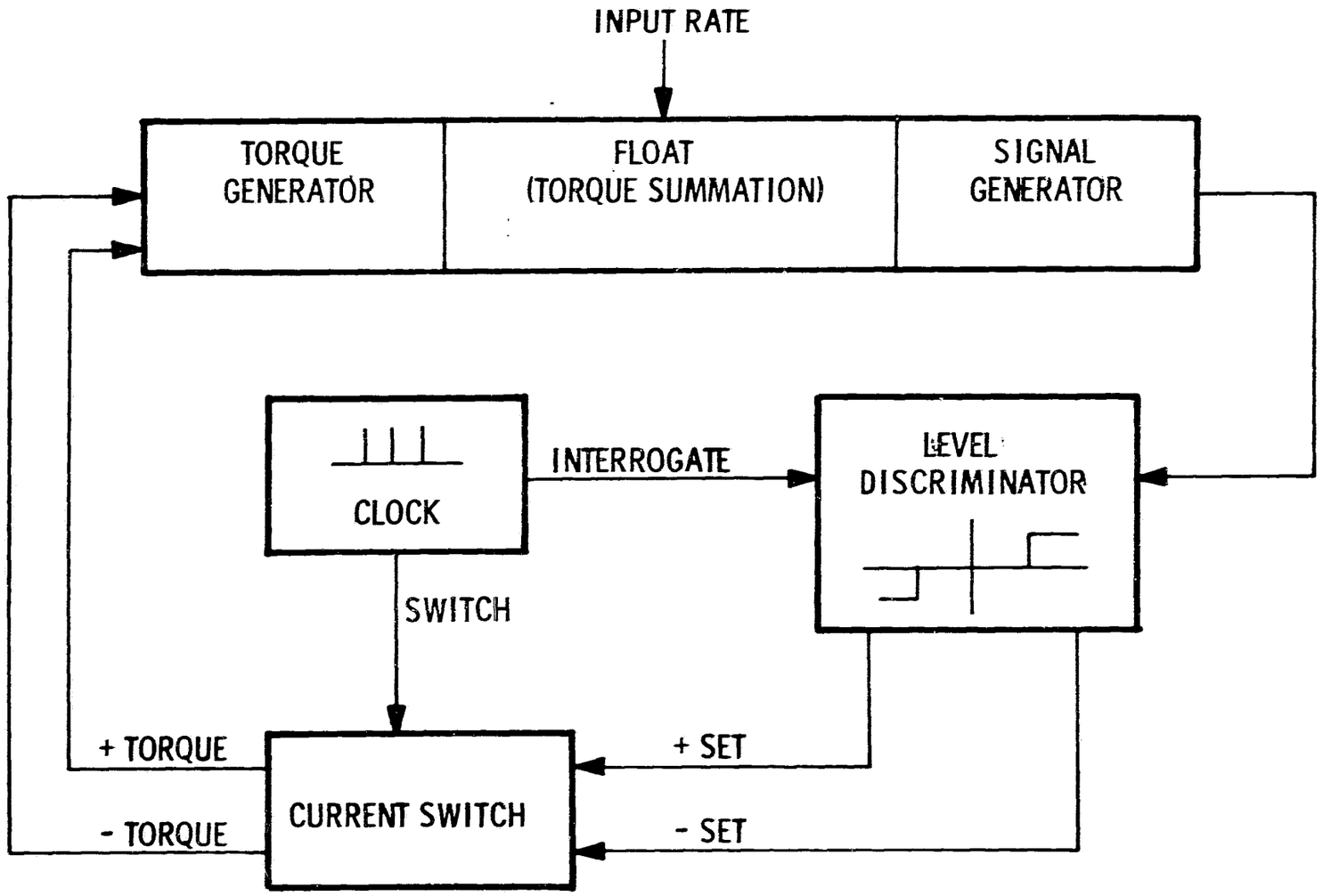

Fig. 3.3-5 Block diagram-18 IRIG closed loop.

The quality of torque pulses is a very important consideration since each pulse is used by the strapdown algorithm as a corresponding measure of gyro input rate.

For the control-loop mechanization, the principal error source is inaccuracies in the torquer pulse area. For a torque pulse of 75-ma amplitude and 300-microseconds width , a scale factor error of one ppm corresponds to a current amplitude variation of 75×10^{-6} ma or a pulse width change of 3×10^{-10} second. Methods of maintaining this type of control are discussed in the torquing electronics discussion of Chapter 4, Section 4.5.6.

With respect to the torquer, a variety of sensitivities associated with the torquer-assembly geometry and materials as well as environmental inputs to the gyro must be considered. Some of the sensitivities that are briefly described here and then developed in detail in subsequent sections are:

1. Gyro Rotational Float Angle,
2. Float Radial and Axial Positions,
3. Magnetic Material Interaction,
4. Thermal inputs.

With respect to the geometry of the torquer, scalefactor (torque sensitivity) changes occur for different float rotational angles (coil-magnet pole orientation). In the torque-to-balance operational mode the float angle is maintained within the threshold level (quantization) of the ternary control loop which is centered about the SG null. Sensitivity changes can be minimized by reducing misalignments between the SG null position and the TG maximum sensitivity position. Beyond this provision the design itself must allow operation in the ternary deadzone region without exhibiting appreciable torquer sensitivity changes. Further, a desirable performance objective is to hold the sensitivity uncertainties due to this effect to 2 ppm.

Float radial displacement occurs due to an angular rate about the gyro output axis. This rate operating on the angular momentum of the wheel causes a torque about the input axis. This torque is resisted by the magnetic suspension. The suspension must be adequate to prevent radial displacement to a jewel extreme under angular rates of up to 1 rad/sec (the maximum rate for which system performance is specified). In addition, a torquer sensitivity resulting from the radial float motion due to the rate about OA should be less than 25 ppm for rates up to 1 rad/sec.

Linear acceleration input will cause radial and axial displacements that are proportional to the difference between the operating and the unit flotation temperature. Under 10 g's of linear acceleration and a 2°F error from flotation temperature, the axial or radial displacement that could result should cause changes in torquer sensitivity of less than 50 ppm.

Magnetic material interaction on the assembly can adversly influence instrument-torquer sensitivity and basic performance stability. For example, any magnetic material on the float that is in the vicinity of the magnet can interact to yield torque uncertainties in the BD drift terms. It would be desirable to assure that such influences would account for less than 0.2-meru BD uncertainty. Similarly, magnetic influences in the torquer assembly can contribute to errors in scale-factor linearity and stability. A desirable design objective would correspond to total SF linearity over the .001-to-0.4 rad/sec of 50-ppm. From 0.4-to-1 rad/sec 100 ppm linearity would appear to be adequate. SF stability of 20 ppm would represent a reasonable performance objective.

Temperature sensitivity represents a trade-off between temperature control-loop capabilities and internal magnet compensation technique complexities. Temperature control to within $\pm$ 0.1^{o}F is attainable and a torquer sensitivity of 10 ppm per ^{o}F appears to be a reasonable objective.

Rotational, axial, radial and thermal sensitivity evaluation testing is presented in Section 3.3.10. The measured sensitivities were previously presented in the summary (Section 3.2). The remaining discussion in this section provides a theoretical background for some of the sensitivity factors, details known problem areas and their solutions or tentative solutions, and identifies proposed TG improvements.

B) Rotational Float-Angle Sensitivity

In an actual instrument the torque generated differs when the same current is applied in opposite directions through the torquer coil. The torque difference may be explained by noting that the SG null position and the TG maximum torque-sensitivity positions are not perfectly coincident. Thus, if the gyro is operated with the float at its SG null, the torquer is not necessarily at its optimum position with respect to the magnet. Figure 3.3-6 illustrates this condition. A single coil is shown relative to a two-pole magnet. The plane of the coil makes an angle θ with the plane of the permanent magnet. For the direction of current in the coil as shown, the mmf of the permanent magnet (fm) is decreased by a component of the coil mmf of magnitude (f_{TC} sin θ). If the coil current is reversed, the component of mmf of the torquer coil f_{TC} adds to the permanent-magnet field by the component (f_{TC} sin θ). This results in a torque difference between cw and ccw torquing that is proportional to the angle between the plane of the permanent magnetic and coil (θ). For θ equal to zero, the cw and ccw torquer scale factors would be equal. In the gyro this effect will cause a ΔSF change proportion to unit float angle about

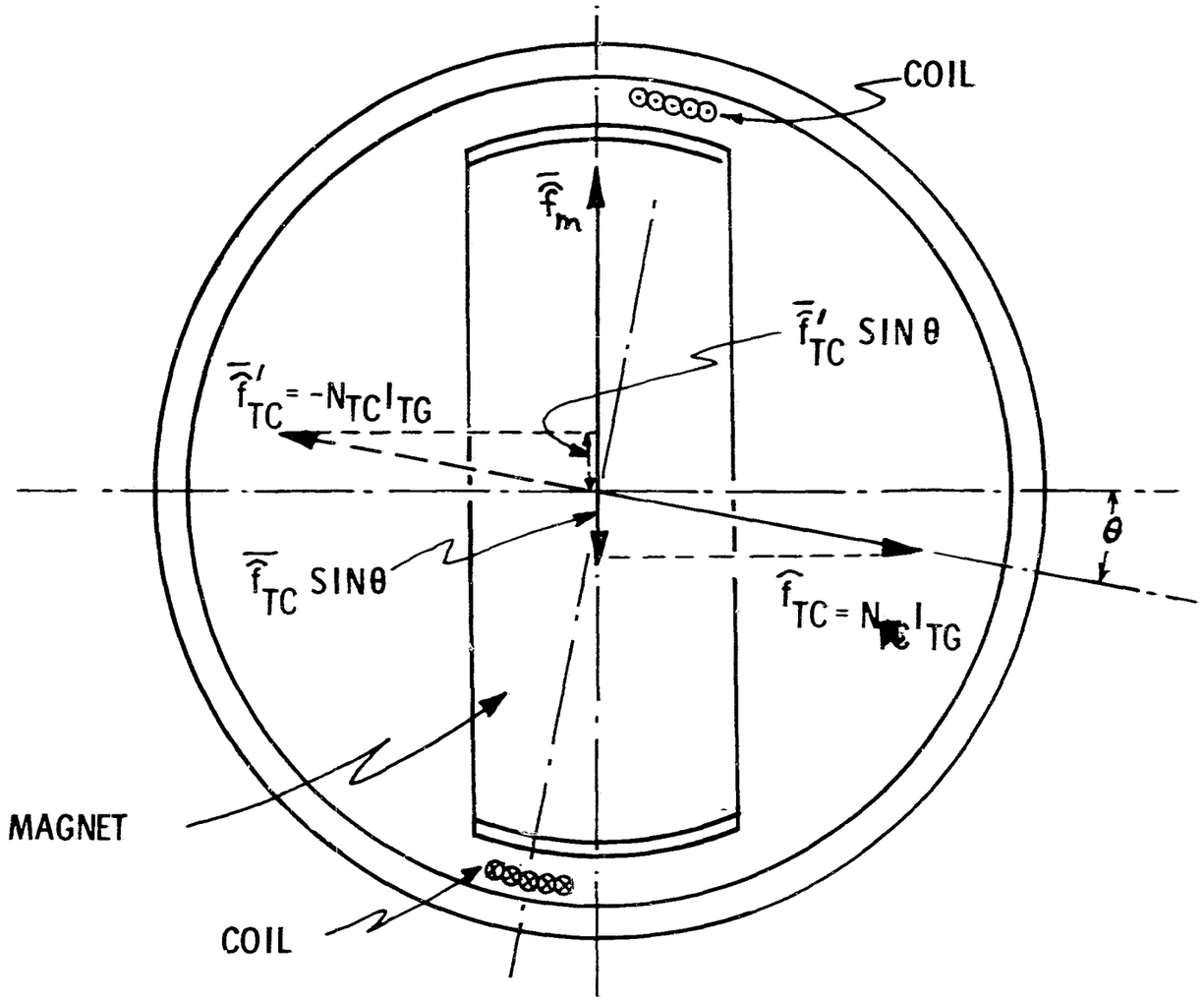

Fig. 3.3-6 Torquer coil reaction effect for 2 pole PM torque generator.

the output axis. This difference between positive and negative scale factor, called ΔSF, is given by the following relationship:

$$\Delta SF = \frac{N_{TC}\ I_{TG}\ \theta}{F_M} \qquad (3.3.12)$$

where

N_{TC} = torquer coil turns

I_{TG} = torquer current (ma)

F_M = permanent-magnet mmf (ma-turns)

θ = angular misalignment between torquing coil and permanent-magnet pole (radians)

Similarly, if an ac current is fed to the coil, an output torque will result that is proportional to the angle θ and the magnitude of the current. This ac torquer sensitivity can be used in the assembly of the instrument to minimize the cw and ccw torquing scale-factor difference.

For example, during testing of the end-housing, the torquing coils may be excited with an alternating current and the magnet mechanically rotated until the ac torque produced reduces to zero. In this position an output signal is observed at the magnetizing windings on the magnet and its magnitude and phase are recorded. Then, during the dry centering phase of gyro assembly, the magnet end-housing is rotated so that the same magnitude and phase are observed when the signal generator is at its null position. The use of this procedure should result in a reduction of the misalignment angle between the SG and TG. Techniques that are currently used allow θ to equal one milliradian maximum; the use of this technique could reduce θ by an order of magnitude.

Early in the program, large torquer sensitivities with changes in rotational, radial, and axial float motion were evidenced. The problem was traced to the magnet casting. It was found that the casting could not be fabricated to accurately locate the maximum flux density at the center of each mechanical pole. A composite magnet structure was then developed. Figure 3.3-7 shows the composite and cast magnet designs with illustrative flux patterns. The composite structure consists of a ring upon which salient poles are accurately fixtured and adhesively attached.

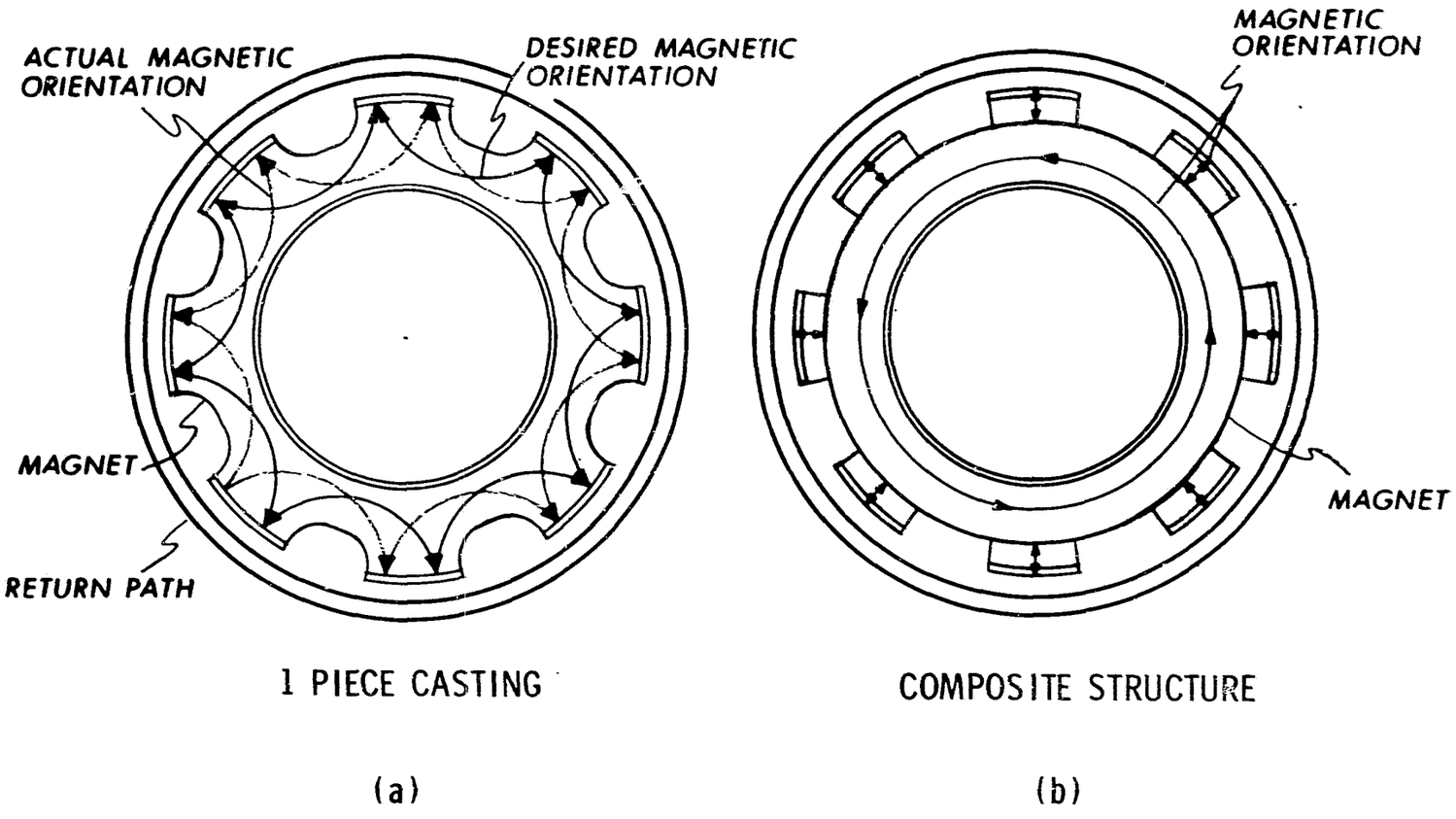

Fig. 3.3-7 Magnet assembly-8 PMT 1.730-1B.

Figure 3.3-8 shows the distribution of gap flux density in relation to the mechanical pole center for a composite and cast magnet assembly. Noté the steep distribution and offset in the cast design as opposed to the almost flat distribution of the composite structure.

A typical average torque generator scale factor variation with the float angular displacement from its electrical null position is shown in Fig. 3.3-9.

Scale-factor radial-position sensitivity is shown in Fig. 3.3-10. In this curve scale factor is shown with the rotors displaced radially about IA & SA from the stator center. SF is measured for each of these displacements.

These figures clearly illustrate the marked scale-factor sensitivity improvements of the composite magnet.

C) Magnetic-Material Interaction

Three basic magnetic-material interaction problems have been discovered in the 18 IRIG evaluation. They are:

Magnet Stator - suspension rotor coupling;
Stop-Bias Hysteresis;
Eddy-Current Sensitivities.

The stop-bias and eddy-current sensitivities are problems which have been uncovered during the current development period and are discussed in some detail. The magnet-suspension rotor problem was observed as marked increases in bias torques quite early in development and was corrected by inserting a sleeve of magnetic material between the magnet stator and suspension rotor. The sleeve shunts coupling flux.

1) Stop-Bias Hysteresis

Stop-bias hysteresis appeared uniquely while testing unit #0411. Prior to torquer magnetization the unit demonstrated excellent performance repeatability when tested in the three-position servo mode. Subsequent to magnetization the unit exhibited a bias shift of approximately 0.1 dyne-cm (Fig. 3.3-11) which appeared as an independent drift rate (ID) term. In addition after magnetization bias stability was erratic (5 - 10 meru). It was found, however, that stable NBD performance data was obtained if the float was held at null when the test table was rotated to the various positions during a servo test, (i.e., float was not allowed to rotate). These test results indicated that the instrument exhibited a stop-bias hysteresis.

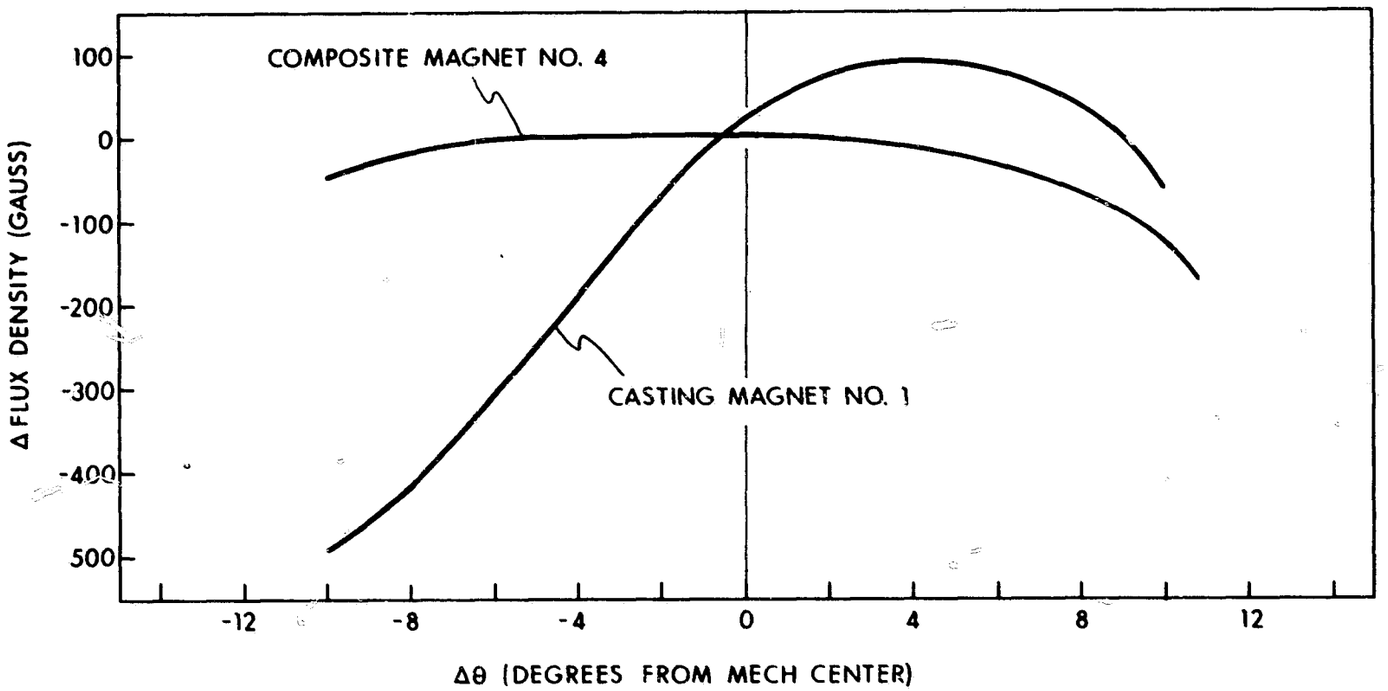

Fig. 3.3-8 Air gap flux density vs magnet pole angle.

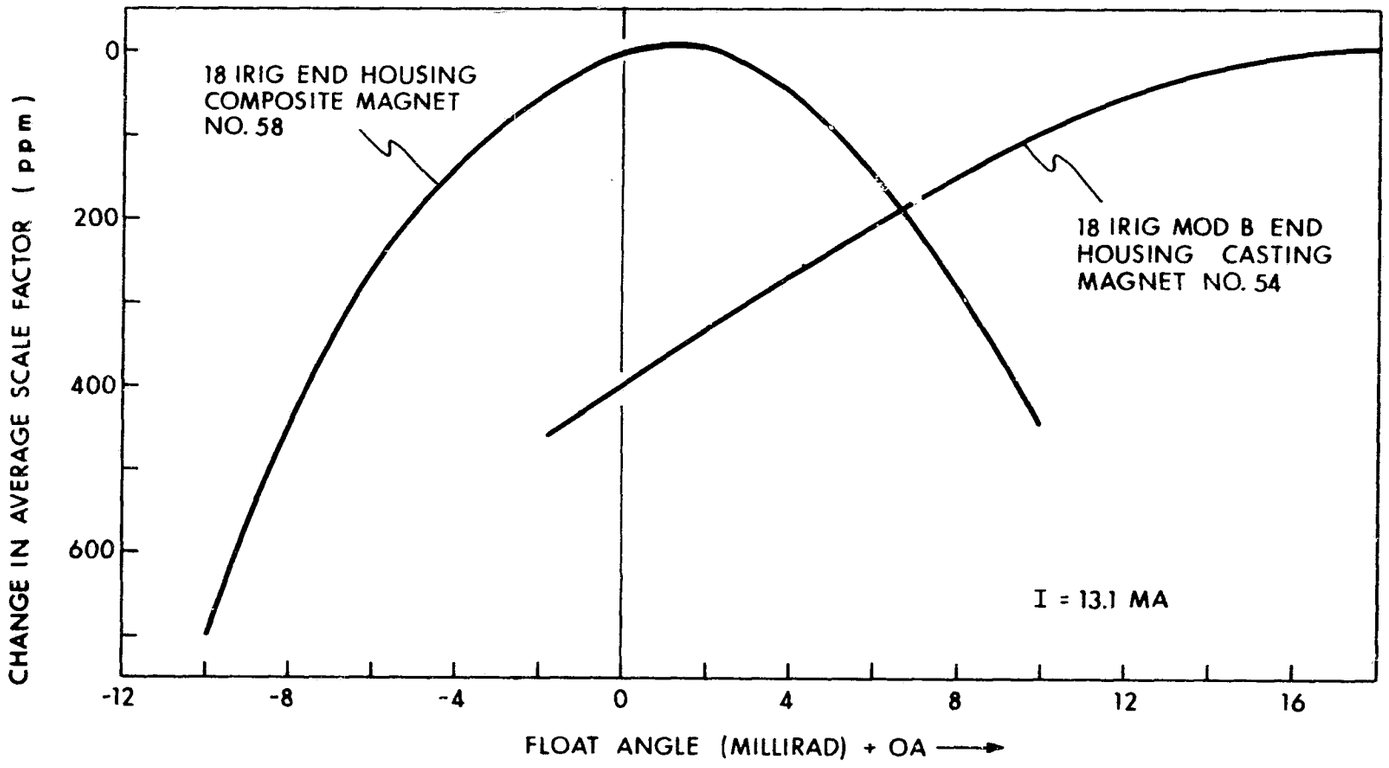

Fig. 3.3-9 TG scale factor sensitivity vs float angle.

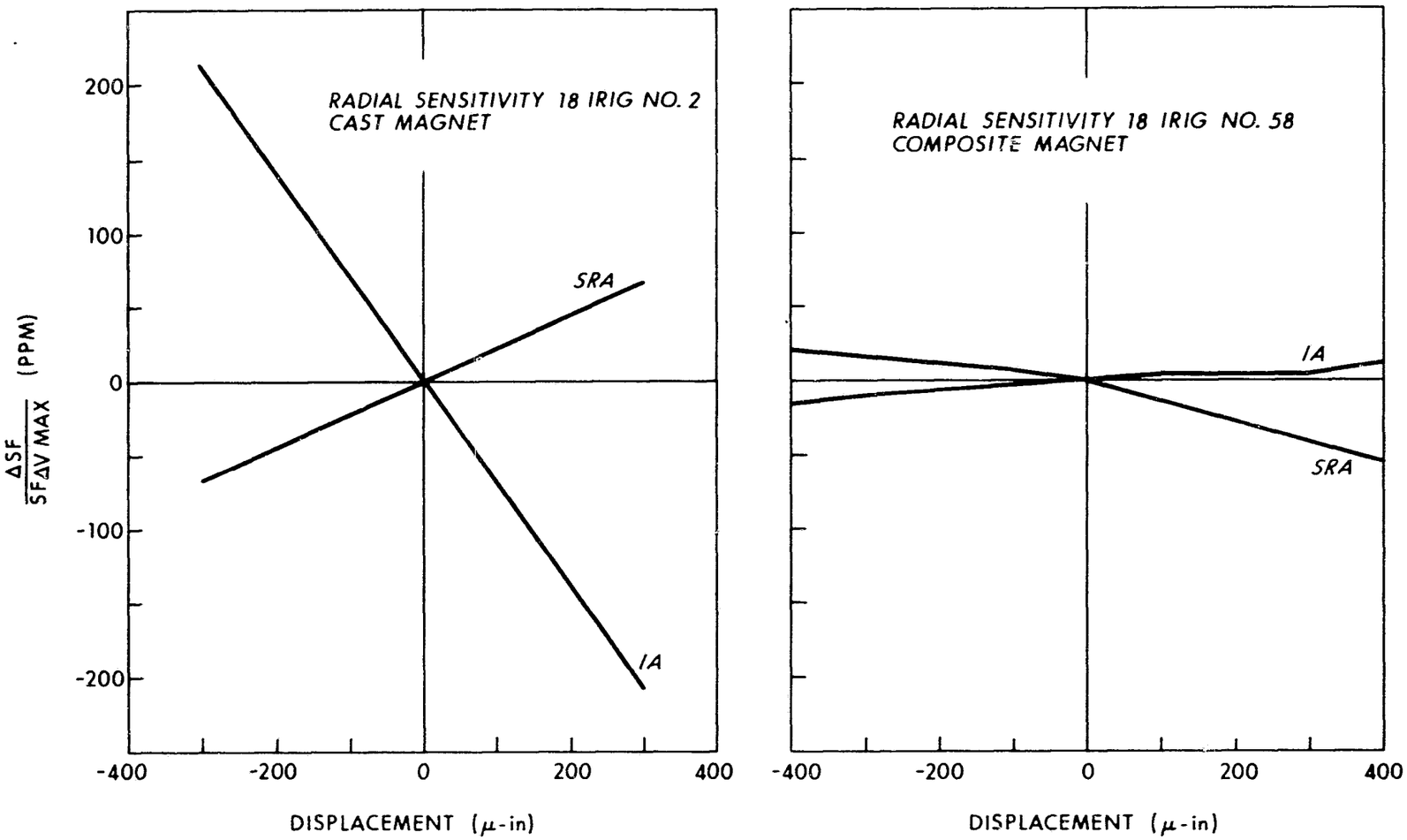

Fig. 3.3-10 Scale factor-radial sensitivity.

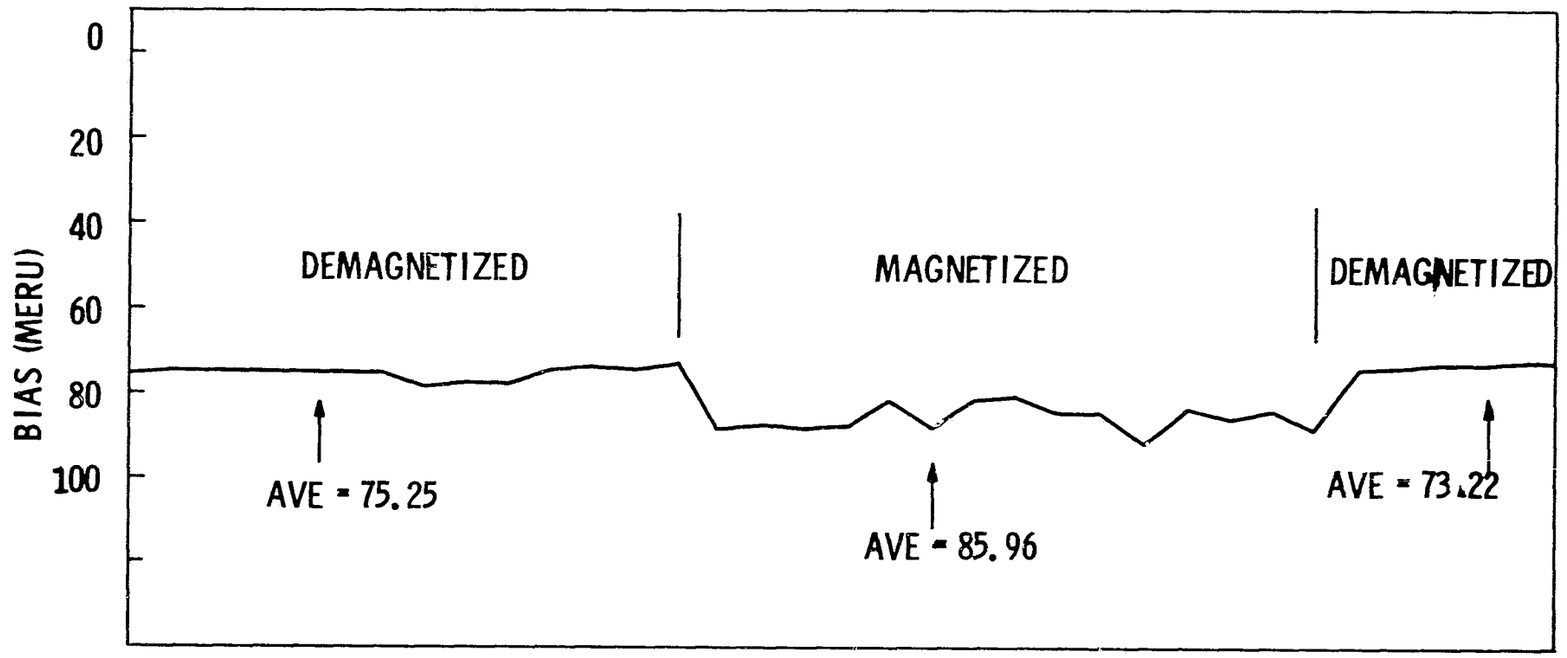

Fig. 3.3-11 Bias stability across PM magnetization 18 IRIG MOD B #411.

Stop-bias hysteresis is the term that is used to describe instrument-bias sensitivities that result when magnetic materials are present on the float in the vicinity of the permanent magnet. With the magnet energized, and the test servo-loop closed, these magnetic particles assume a domain orientation that stays fixed until conditions are changed. When the table is repositioned, the servo loop is opened, float motion towards a stop occurs (the gyro is not held at SG null) and the magnetic particles assume a new random domain orientation. This causes a change in the total reaction torque on the float. Reaction torque variations resulting from rotational float angle changes are illustrated in Fig. 3.3-12. When the servo loop is kept closed during the gyro test position changes, float motion and thus these reaction torque changes are minimized, and repeatable data is obtained. Tests conducted on 18 PIRIG's (the ball bearing predecessor of the 18 MOD B IRIG) also detected stop-bias hysteres.

To isolate the source of this magnetic effect, all torquing-coil holders and coil assemblies not already mounted on floats were subjected to test on a precision gas-bearing table. In all cases reaction torque sensitivities with position were observed; however, their magnitude was considerably less than that seen in unit #0411. The principal cause appeared to be associated with the coil-holder material iron content. The holder is fabricated from I-400-grade beryllium. Investigation revealed that this grade of beryllium has an allowable iron content of 0.5% maximum. S-350 in a new Brush Beryllium alloy was investigated; reportedly its physical qualities are the same as I-400 but maximum allowable iron current is reduced to 0.25%. A coil support of this material was fabricated recently. It is anticipated that this material change will reduce the plus-to-minus stop-bias difference to about a meru. This is an interim fix only, and ultimately we propose to replace the beryllium coil holder with a completely nonmagnetic material.

It is interesting to note that a similar experience occurred with an accelerometer which employs a potted torquing-coil assembly. Similar erratic performance were observed and, in this case, traced to magnetic particles dispersed throughout the potting compound. It was discovered that these particles were introduced during the manufacture and processing of the compound filler material. Although the 18 MOD B torquing coil assembly is not potted, the flex-lead attachment pins are fastened in place using a filled adhesive (Bacon Ind. LCA-9) and the major float joints (one of which is adjacent to the torquing coil) are

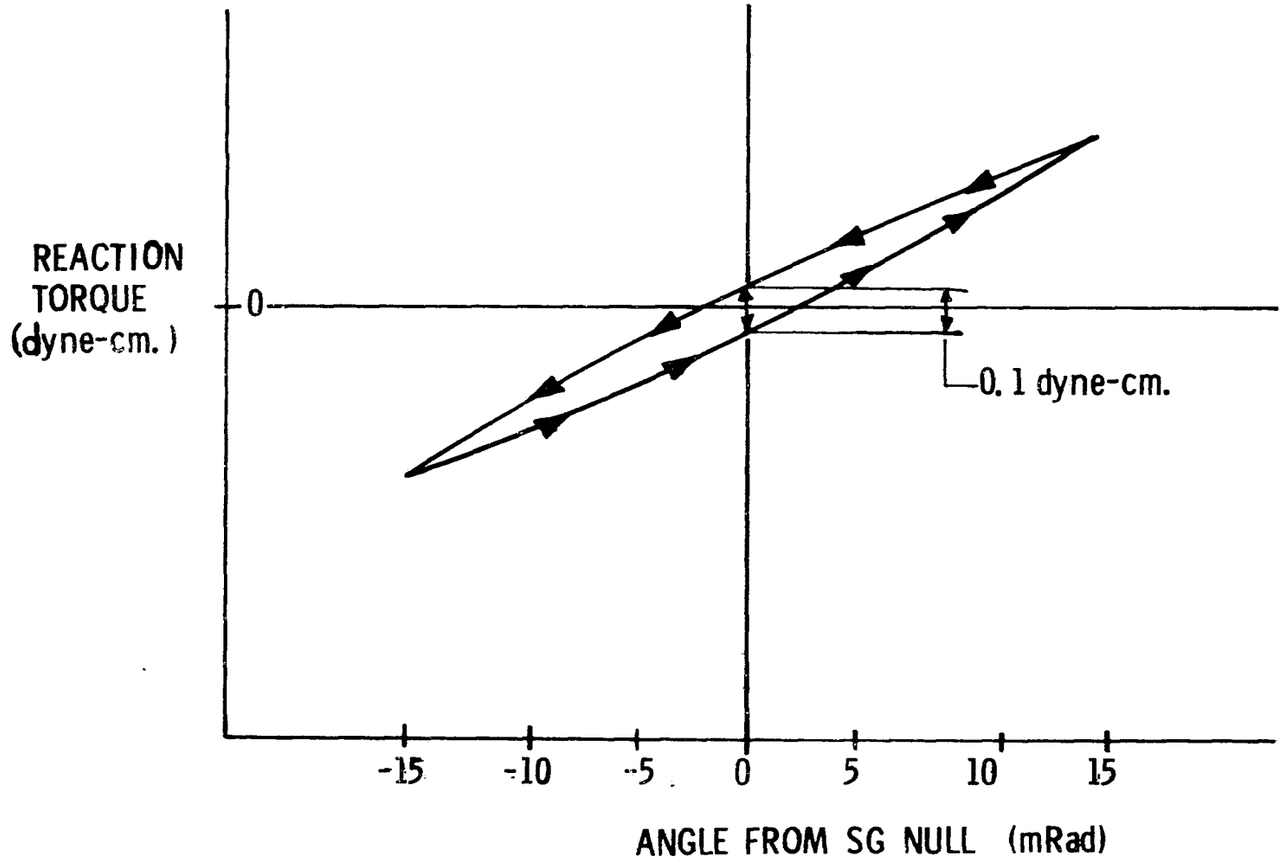

Fig. 3.3-12 Torque vs angle, stop bias reaction torque variation with float angle.

sealed using this same LCA-9 adhesive. A nonmagnetic version of this adhesive has been purchased and is presently being evaluated. As a further precaution, all torquing-coil assemblies not already complete will use coils wound with OFHC copper wire which is drawn through nonmetallic dies.

2) Eddy-Current Sensitivity

Since the torquer is used in a pulse rebalance type of control loop in which the pulse rate is a function of the input, a considerable amount of testing was done by the Electromagnetics Engineering Section to determine the effects of varying frequencies on the torquer-assembly's operation. An inductance and resistance sensitivity with frequency was discovered (Fig. 3.3-13). The same data was taken using a titanium support with a solid- and a laminated-magnet return path (Fig. 3.3-14) and indicated the marked decrease in frequency sensitivity. The difference in frequency response for a beryllium torquing-coil support and one made from a nonmetallic material (Bacon Ind. P-20 potting compound) with both a laminated and solid return path is shown in Fig. 3.3-15. (These tests were on a different size holder.)

In addition to the inductance and resistance tests described above, tests with a constant alternating current applied to the torquing coil were conducted. The net reaction torque was measured for different frequencies at several magnet-coil rotational angles. For the beryllium coil support the test showed a change in reaction torque with frequency for identical angle orientations (Fig. 3.3 - 16). In contrast, similar tests with a titanium coil support (solid and laminated return paths) showed a marked reduction in reaction torque with frequency dependence (Fig. 3.3 - 17). The nonlinearities are directly attributable to the magnitude of eddy currents induced in the coil holder and magnet return paths. A major electrical difference in the holder materials is that beryllium is a fairly good electrical conductor (4.3 microhm-cm while titanium is not (176 microhm-cm).

Both of the effects described influence the scaling characteristics of the torque-to-balance loop. For the ternary-control loop pulse torquing is used and the rate and molding pattern are a function of the applied angular input rate (Section 2.5). The frequency content of the torquing current is therefore directly related to the input rate and thus the result is a scale factor nonlinearity. The inductance and resistance changes directly influence the performance of the torque current magnitude control loop (Section 4.5) which is band-width limited. The reaction torque tests indicate a measure of the direct influence of eddy currents on the torquer sensitity.

It is evident from Fig. 3.3-13 through 3.3-16 that the beryllium is not an ideal selection for a torque-coil support for a gyro used in a srapdown pulse-torque-to-balance loop. The influence of current frequency components on the torque-generator control loop scaling was further illustrated during pulse-

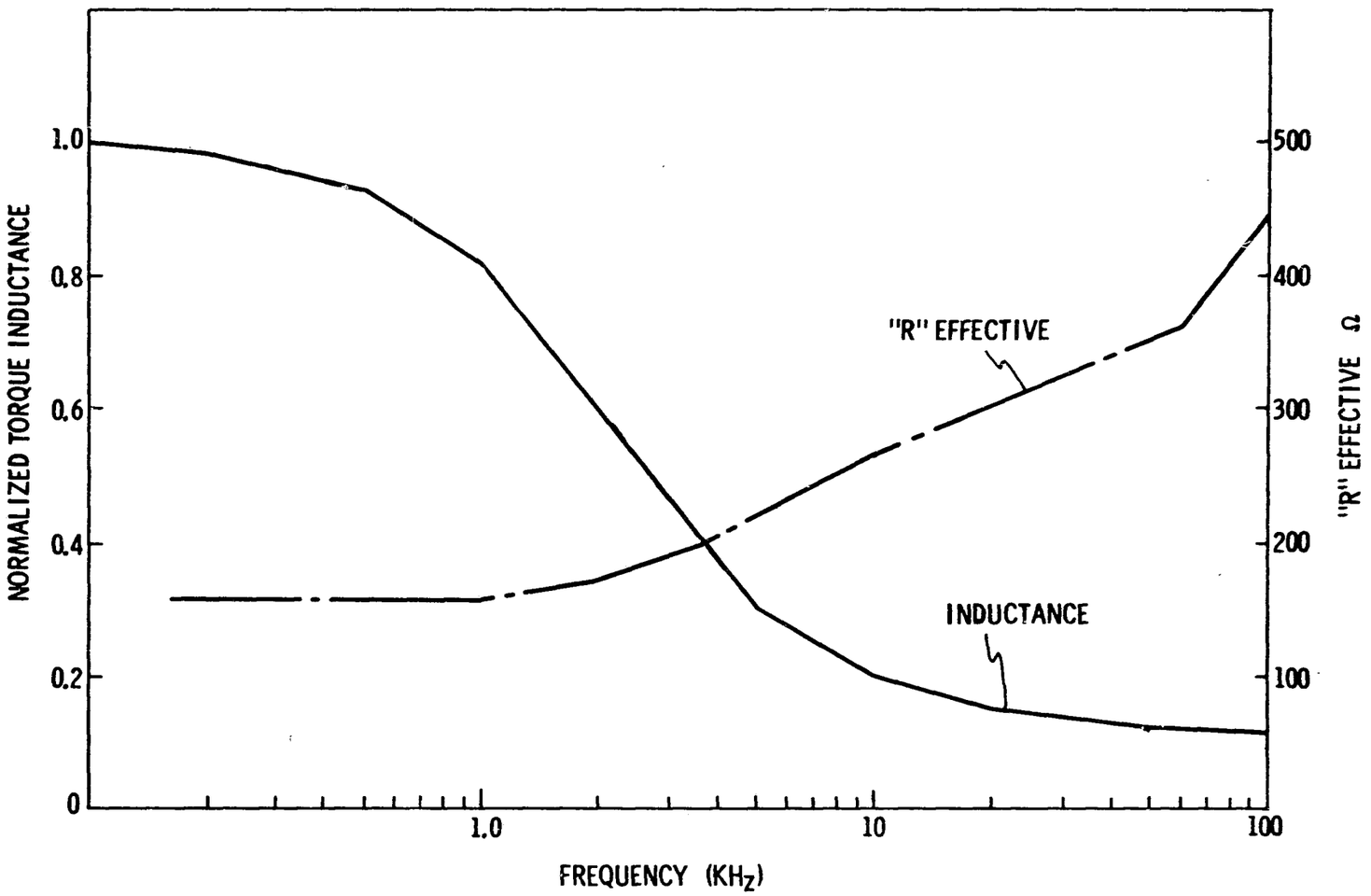

Fig. 3.3-13 Resistance vs frequency 8 PMT 1.73-2A (18 IRIG MOD B).

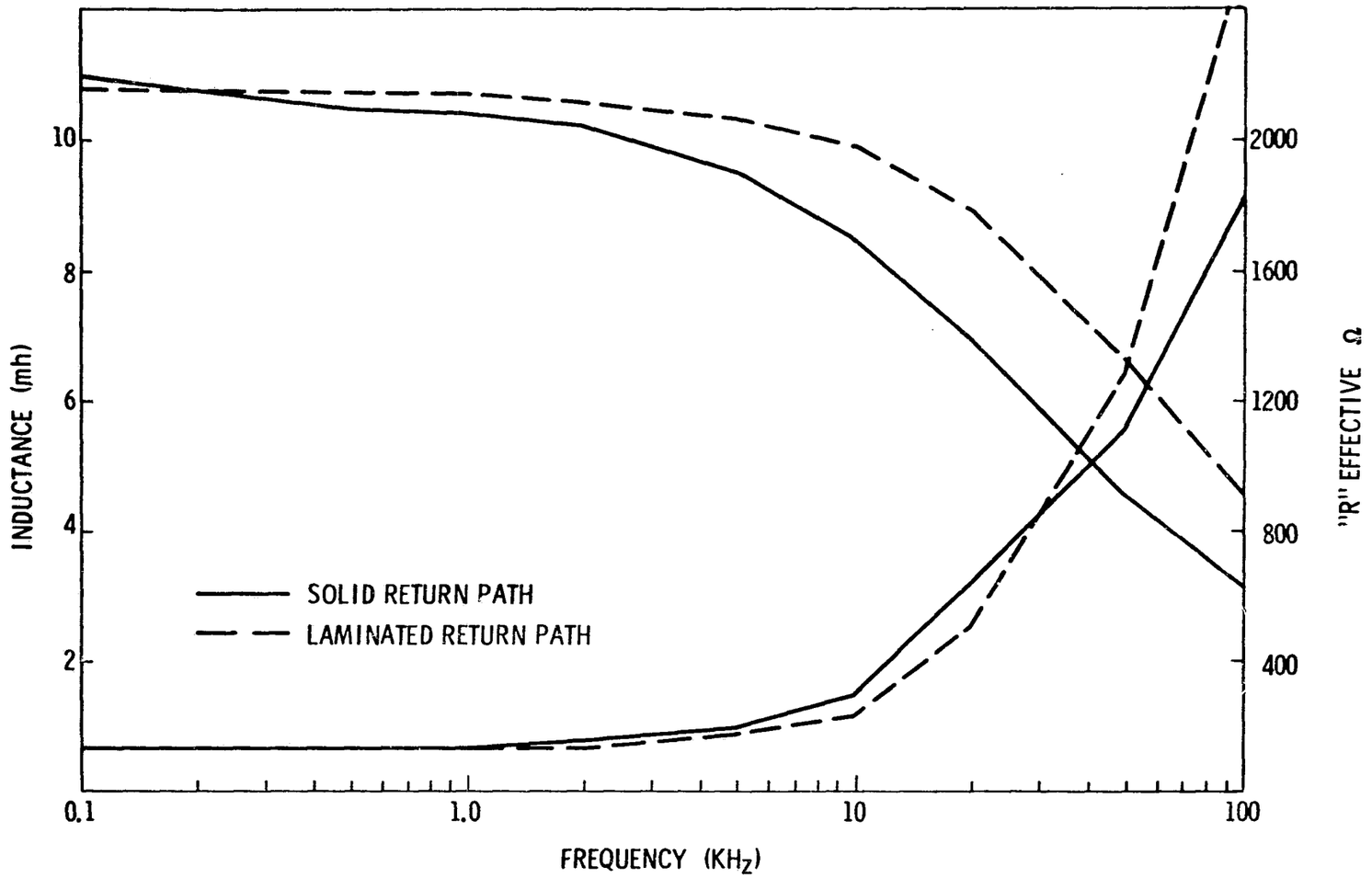

Fig. 3.3-14 Normalized frequency sensitivity-titanium coil holder.

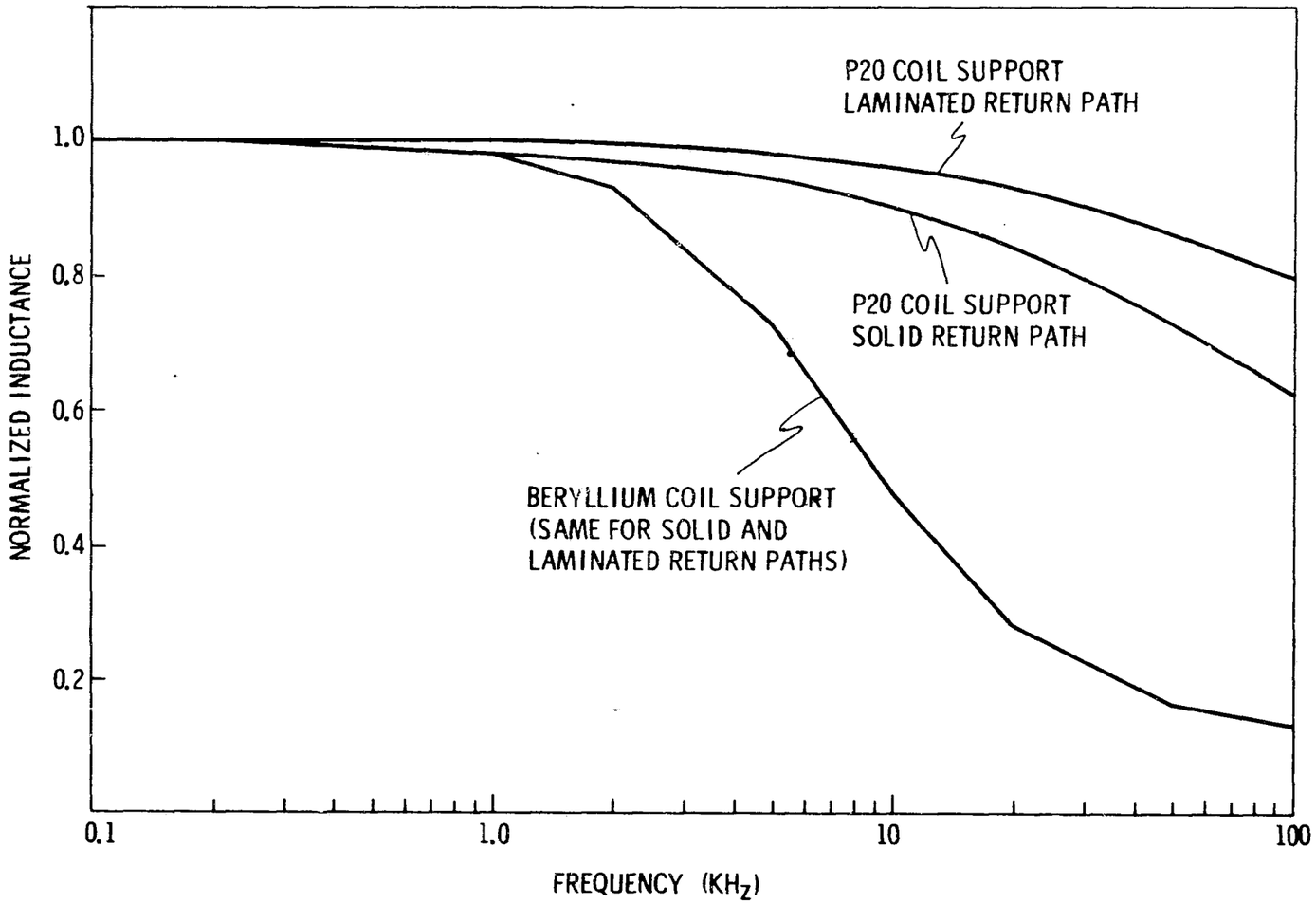

Fig. 3.3-15 Normalized frequency sensitivity-plastic vs beryllium coil holder.

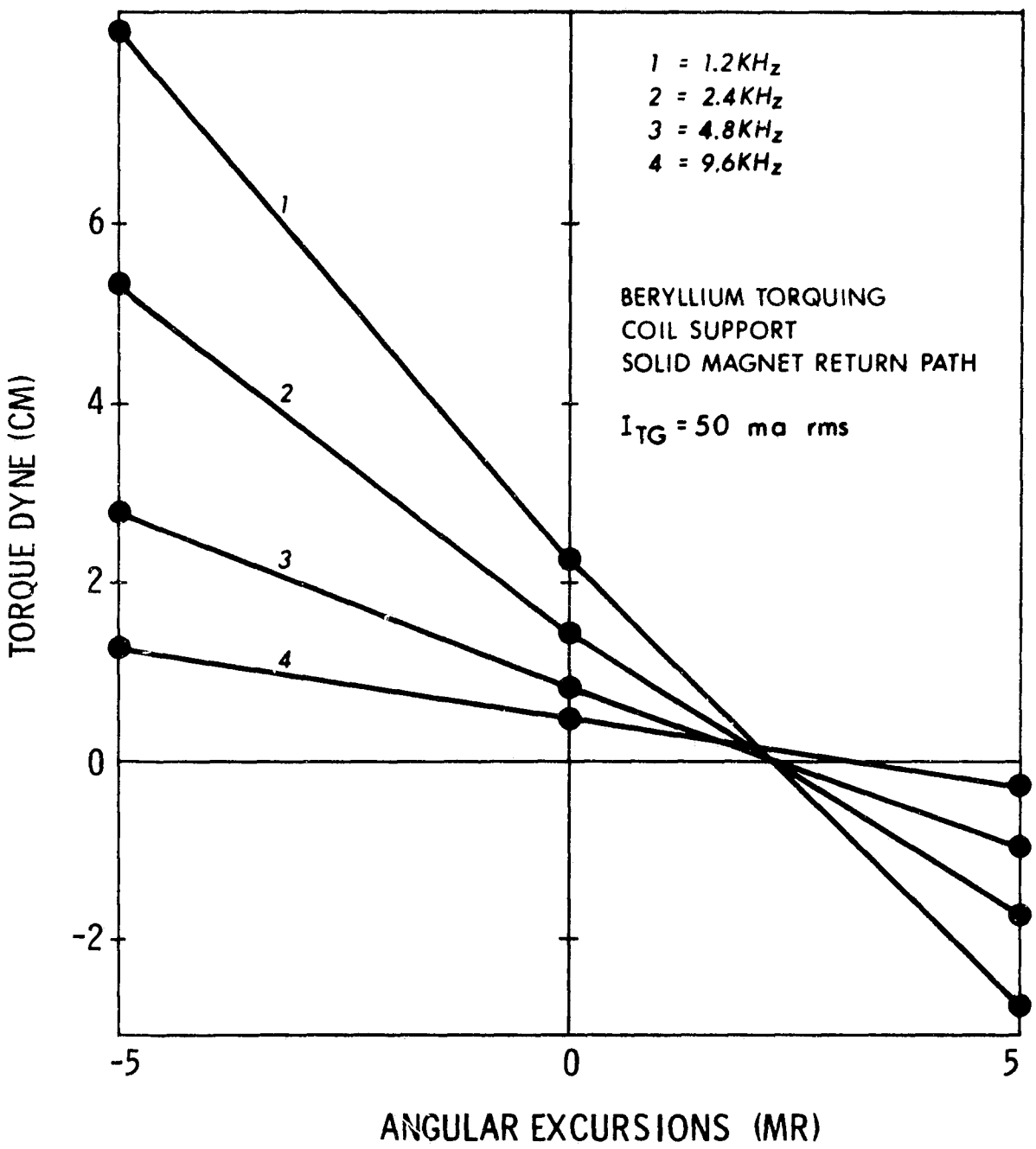

Fig. 3.3-16 Reaction torque vs angle and frequency.

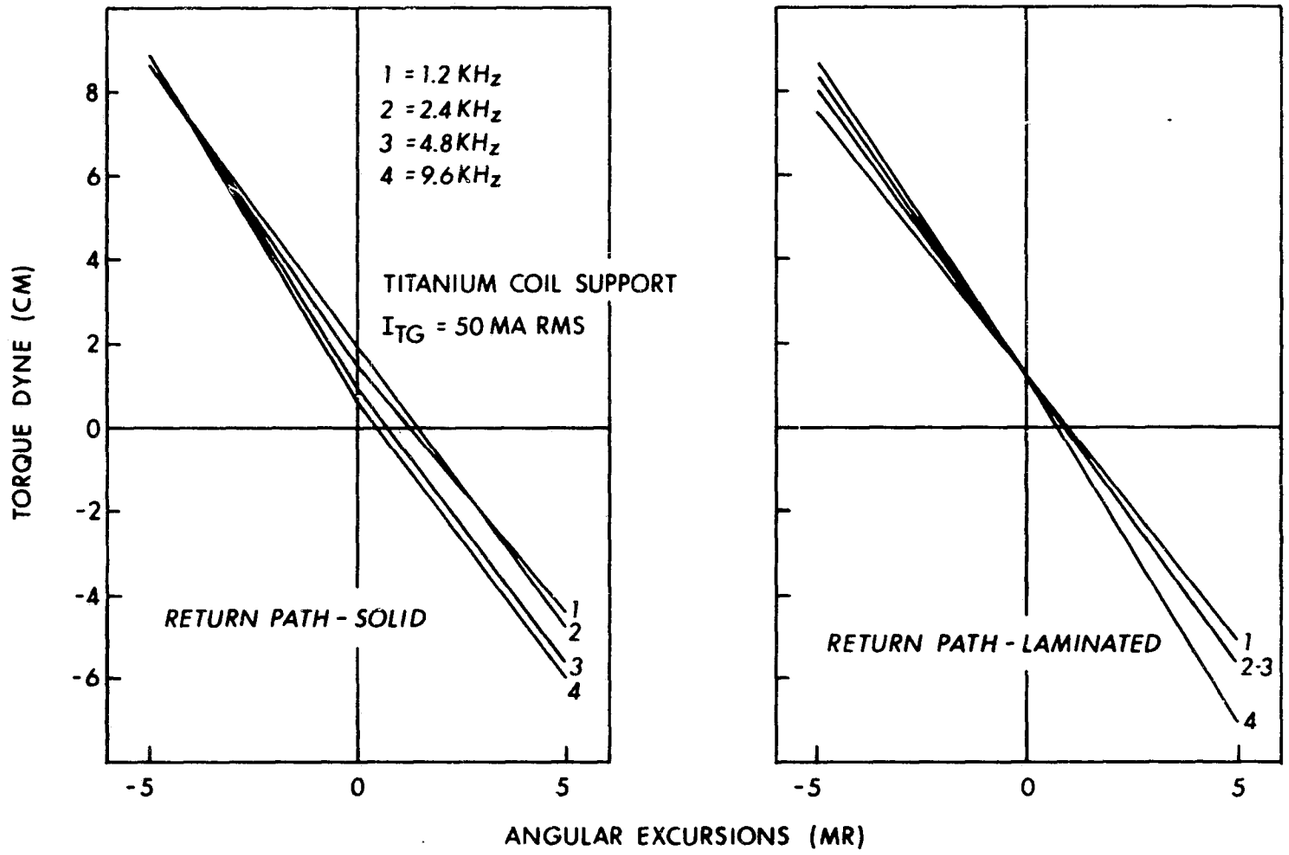

Fig. 3.3-17 Reaction torque vs angle & frequency.

torquing tests on unit #411. Superior scale factor linearity and stability were obtained with a 234 μ sec current pulse as opposed to a 78 μ sec pulse width (tested at input angular table rates of 2^{o} to 12^{o}/second).

Some investigations have been conducted for alternate materials to be used in the manufacture of torquing-coil supports. From the figures shown it is apparent that, to minimize the eddy-current effects, a nonconductive material would be best. Supports can be made of a variety of plastic compounds to satisfy this requirement, but plastics in general are dimensionally less stable than most metals. Since the coil support is mounted directly on the float member, which requires high mass stability, the use of plastics will necessitate detailed analysis.

From the standpoint of dimensional stability most ceramics are ideal but, because of the very thin-wall sections of the holder, manufacturing a ceramic support is a problem. Further, if a gyro gimbal redesign is to be avoided, the material density is an important consideration since end-to-end float balance would be affected.

Other materials which should be considered are composites(fibers of boron, sapphire, graphite held in softer supporting matrices).

D) Reduction in Torque-Generator Power

As noted previously the 18 IRIG MOD B's torque-generator capability to cope with high-input rates is its essential strapdown feature. In the present design status, however, a one-radian capability can be accommodated for relatively short periods due to the magnitude of the current required(approximately 190 ma; coil resistance is 158 ohms normal). Thus, approximately 5.7 watts thermal input of this magnitude will result in both a thermal-gradient unbalance (affecting basic gyro drift performance)and scale-factor uncertainties. Electronic design is also complicated by the need to develop current switches and a dc precision-current regulating loop that are required to operate at a relatively high current level (power dissipation in the electronics also represents an operational penalty).

Studies to see if an increase in the torquer flux density could be obtained with the same mechanical design constraints of the present assembly were conducted. It was discovered that the flux density could be significantly increased by changing the material used for the composite magnet pole pieces. The original design used Alnico V for both the ring and poles. The use of Alnico IX for the pole pieces appeared to provide a better magnetic-material match for the magnetizing-coil geometry and yielded almost a 50% increase in the coil gap flux density.

Table 3.3-2 compares the original design to the Alnico IX configuration for the same torquing coil. In addition to reduced power operation, another advantage resulting from a higher flux density is a reduction in the scale-factor difference between cw and ccw torquing (ref. Eq. 3.3.12).

TABLE 3.3-2

TORQUER PARAMETERS	CONSTRUCTION	
	Alnico V Ring Alnico V Poles .069" gap	Alnico V Ring Alnico IX Poles .069" gap
Flux Density (B_g) Stabilized	1,600 gauss	2,380
Generator Sensitivity (S_{tg})	775 $\frac{\text{dyne-cm}}{\text{ma}}$	1,150
Power at 150,000 dyne-cm (one rad/sec)	5.7 watts	2.59
Scale Factor Difference at 1 rad/sec (ΔSF)	110 PPM/mr	50 PPM/mr

3.3.6 Signal-Generator Noise

Early in the sequence of system pulse-torque testing, erratic performance indicative of the presence of a high noise level was encountered. Closed-loop testing was being conducted with a scale factor of 6 seconds of arc (rotation about the input axis) per torque pulse. This corresponds to setting of the electronic torque command threshold to approximately 180 microvolts. The noise was directly traced to output of the signal-generator secondary. The output of the signal generator was monitored on a broad-band frequency analyzer and a spectrum of magnitudes at the various frequencies is tabulated in Table 3.3-3. The major noise component was pickup from the wheelpower lines (140 microvolts at 800 cps) and a band-pass filter (9600 cps ± 3 KC) was incorporated into the gyro preamplifier. A wide-band filter is used so that affects on the loop dynamics are minimized. The spectral output of the SG band-pass amplifier normalized to correspond to an equivalent SG signal at null is shown for comparison in the second column of Table 3.3-3.

As indicated by the table, the amplifier eliminated the large undesirable 800-cps signal, and reasonable performance was attainable with a 6-arc-second torquing quantization. Consideration of finer quantization (1 to 3 seconds of arc) levels may be desirable for optimization of attitude matrix algorithm performance. This would necessitate operating with signal levels as low as 30 microvolts. At this level the noise coupling observed at side-band frequencies of the SG 9600-cps carrier would also become undesirable.

The dominant modulation side band frequencies that were observed at the SG null position were ± 400 cps, ± 800 cps, and ± 1600 cps. The appearance of a 9600 cps ± 400 cps modulation is expected as it corresponds to the 400 rps wheel speed. The mechanism for the 800 and 1600 cps was not clear since modulation of this could not be attributed to harness pickup, etc. Further, if a 30 microvolt torquing threshold were set, the 8-15 microvolt magnitude of the ± 1600 cps (corresponding to second harmonic of wheel-voltage excitation) would be intolerable.

A magnetic-coupling phenomenon was suspected and the Electromagnetic Engineering Section conducted a detailed investigation. It was determined that the connector pins located near the suspension gap were magnetic (COVAR, a nickel-iron alloy, is used because of its thermal match with the glass seal on the end-housing) and acted as a bridge for the suspension flux to couple into the SG (illustrated in Fig. 3.3-18). The figure shows flux cutting across the connector and into the SG. When the motor current flows through the connector, it creates a flux which modulates the suspension flux leakage into the SG. The 800 cps motor current saturates the connector twice in each cycle and, therefore, the dominant modulation is seen as a second-harmonic (9600 ± 1600) side-band.

TABLE 3.3-3

SG SECONDARY NOISE

No Filter		Band-Pass Amplifier
Frequency (cps)	Amplitude (microvolts)	Amplitude (microvolts)
800	140	.2
4000	6	--
8000 (9600-1600)	15	8
8800	4	5.5
9200 (9600-400)	1	3
9600 (quadrature)	13	8.5
10,000 (9600+400)	1	3
10,400 (9600+800)	2.5	3.5
11,200 (9600 + 1600)	11	8.5
19.200	40	.6

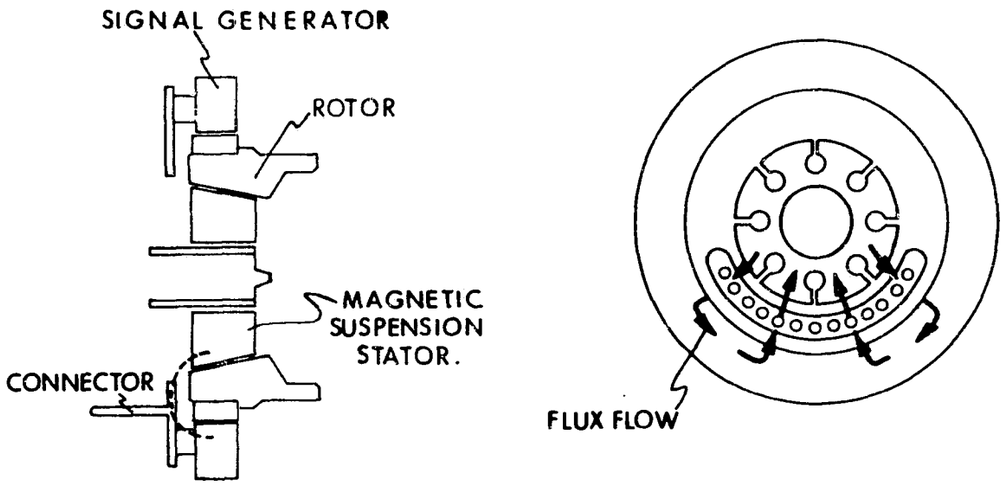

Fig. 3.3-18 Signal generator magnetic modulation.

As a result of this finding follow-on 18 IRIG units will incorporate nonmagnetic connector pins.

3.3.7 Gas-Bearing Design Consideration

A) Rate Slew Capabilities & Compliance

Apollo experience has shown that a significant percentage of gyro failures have been attributable to the wheel ball bearing wear. The use of a gas bearing offers the potential of extended operational life that is required for missions of several years duration. The gas bearing, however, is subject to a potential wheel-touchdown catastrophic failure precipitated by environmental inputs. This factor was clearly evidenced by the failure of the first developmental gyro, delivered to test in October 1966, which failed due to a high-speed touchdown 1/2 hour after it was turned on. Subsequent to this failure, design investigation to increase the slew capability to 5 radian/sec was initiated. This design capability was achieved by reducing the bearing radial and axial clearances, and changing the float gas from helium to neon.

Figure 3.3-19 presents a comparison of the original and the current design parameters. Note that not only was the slew capability increased but also that the compliance term was significantly reduced. However, the use of neon increased the wheel power by approximately 16% (Fig. 3.3-20) and the dimensional changes resulted in a two-fold increase in mechanical power requirements.

Unit #411 wheel incorporated all of the noted design parameter changes and was tested to rates of 9 rad/sec without bottoming.*

To determine the effect of dimension tolerances on the gas-bearing slew-rate capability and compliance a computer parameter-variation study was conducted. The results showed the marked influence of axial and radial clearances on compliance and slew-rate capability, Fig. 3.3-21 and 3.3-22 respectively. Variation of groove depth, groove land-to-width ratio, and gas pressure on compliance did not appear to be significant.

B) Start-Stops

Experience in early wheel-qualification testing indicated that a design change was desirable to minimize bearing-wear problems during starts and

---

*On 19 December 1967, after approximately 4 months of testing, a connector on the Gertz gas-bearing test table was accidently removed during rate torque linearity testing on unit #411. The table accelerated to in excess of 12 rad/sec, resulting in a bearing touchdown and failure.

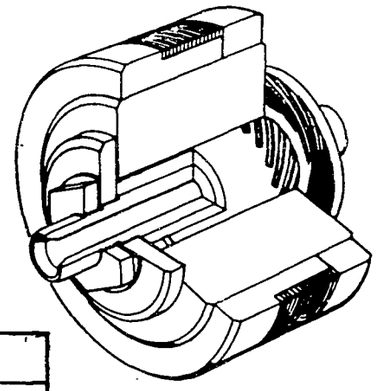

DESIGN PARAMETERS	CASE A	CASE B
BEARING CHARACTERISTICS	24000 RPM	24000 RPM
AXIAL CLEARANCE - μ in.	69	40
RADIAL CLEARANCE - μ in.	90	40
AXIAL COMPLIANCE - μ in/lb.	14.5	1.8
RADIAL COMPLIANCE - μ in/lb.	12.1	1.6
ATTITUDE ANGLE - degrees	24.9	12
WEIGHT OF ROTATING ELEMENT - gm	57.4	58.0
ANGULAR MOMENTUM - gm-cm^2/sec	0.151×10^6	0.151×10^6
POWER		
MECHANICAL - dyne-cm	2600	4850
watts	0.65	1.22
ELECTRICAL - watts	3.3 @ 21.5 V	5.2 @ 28V
COMPLIANCE TORQUE (T_0) - meru/g^2	8.5	0.8
MAXIMUM ANGULAR INPUT RATE		
ABOUT 1A - rad/sec	1.9	5.0

CASE A: ORIGINAL DESIGN PARAMETERS.

CASE B: REVISED DESIGN PARAMETERS INCORPORATED IN CURRENT 18 IRIG MOD B BUILD

Fig. 3.3-19 18 IRIG MOD B gas bearing wheel assembly.

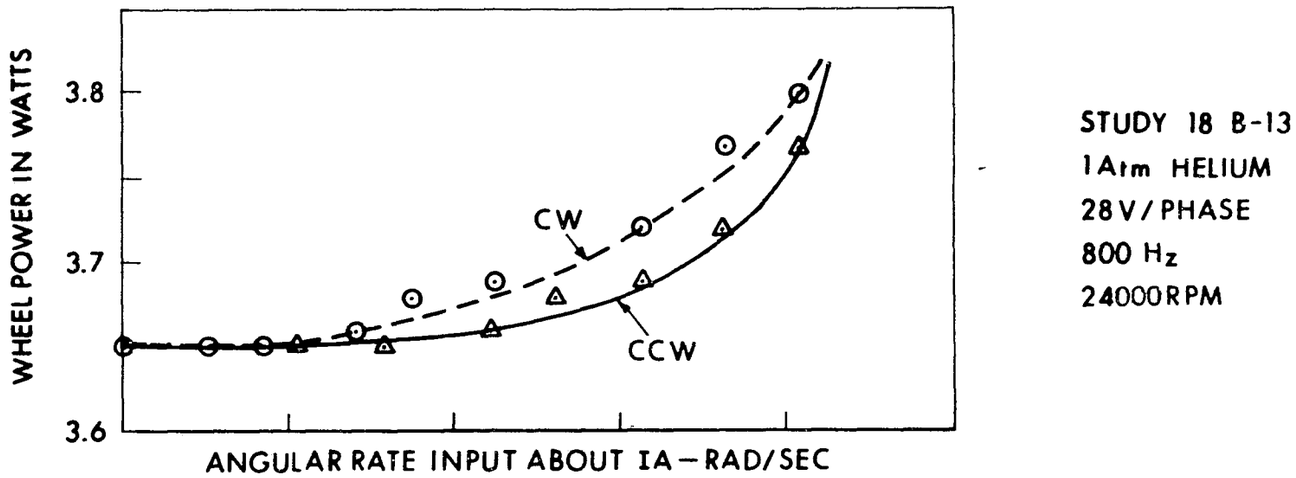

STUDY 18 B-13
1 Atm HELIUM
28 V/PHASE
800 H_z
24000 RPM

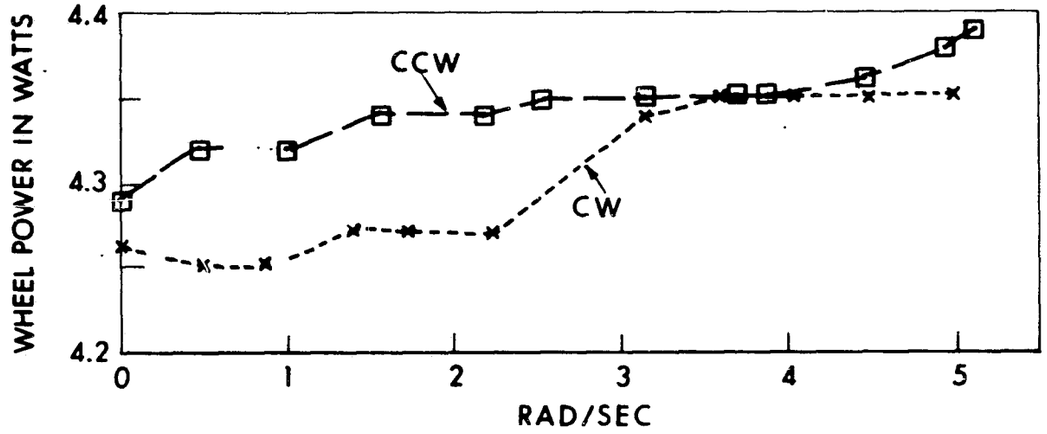

STUDY 18 B-13
1 Atm NEON
28 V/PHASE
800 H_z
24000 RPM

Fig. 3.3-20 18 IRIG MOD B slew rate tests, case B, design parameters.

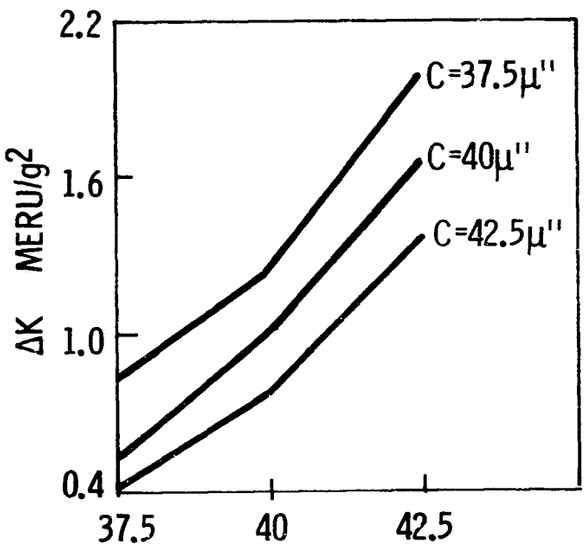

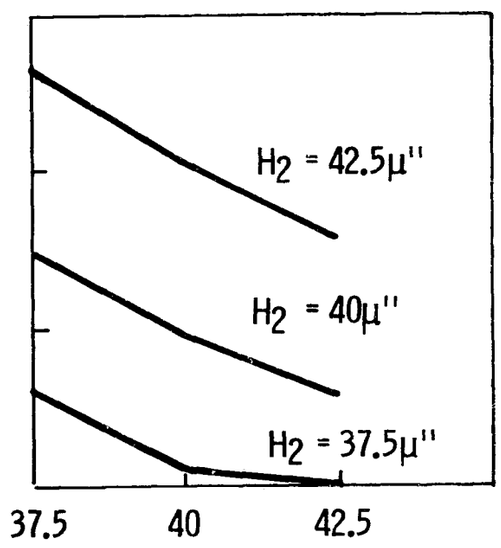

LEGEND: C- RADIAL CLEARANCE
H_2- AXIAL CLEARANCE

Fig. 3.3-21 18 IRIG MOD B, effect of clearance on ΔK (helium atmosphere).

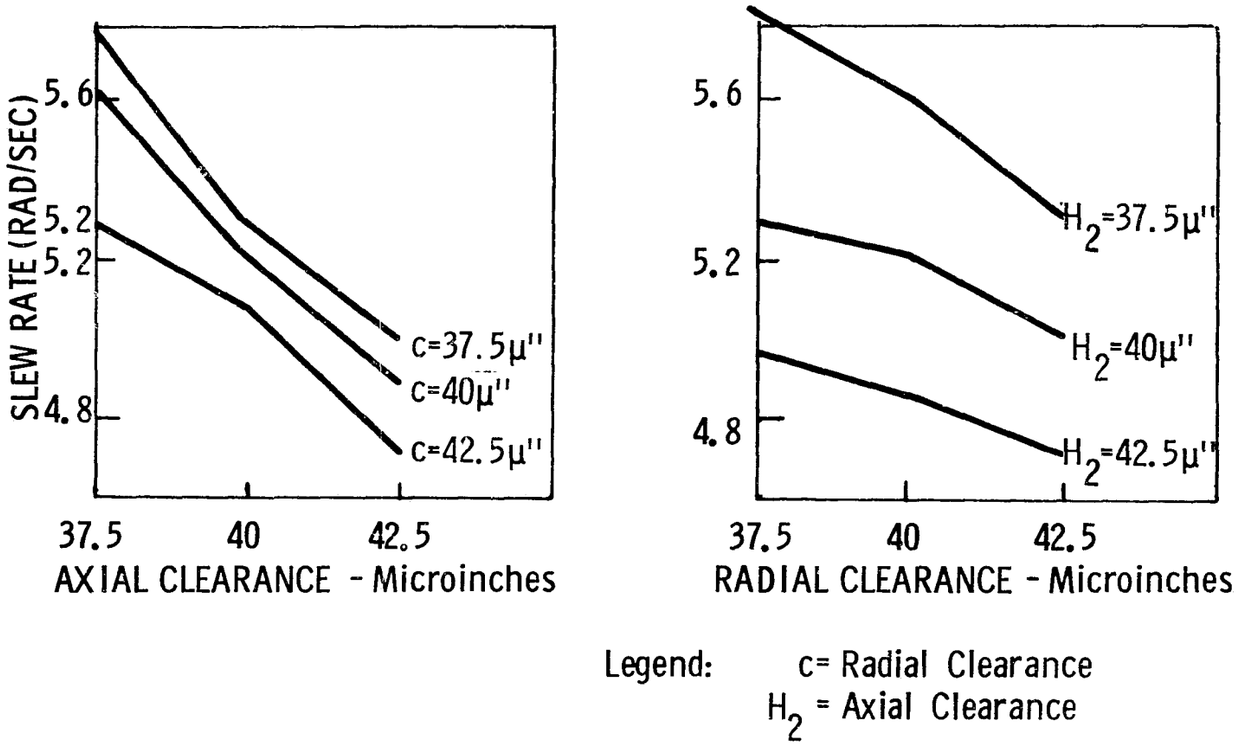

Fig. 3.3-22 Effect of clearance on slew rate capability (helium atmosphere).

stops. An improvement incorporated has been to crown the wheel thrust plates so that the wheel hub contacts the thrust plates at a point of minimum radius.

Each wheel assembly is subjected to a minimum of 1000 starts and stops in each of the critical three positions. (IA vertical and SRA up and down.) This procedure attempts to screen failures in the wheel assembly stage (burn-in period) rather than after the float or gyro assembly, with attendant increased cost and schedule delays.

During test it was observed that the originally-projected 24-volt pull-in wheel excitation voltage could not be assured. It was determined that at this level the available motor torque was marginally close to the required pull-in torque. Rather than considering redevelopment of the motor it was judged more suitable to design the wheel power supply to assure an excitation of 28 volts, which is still well below the motor saturation level.

C) Maximum Gas-Bearing Load-Carrying Capability

Recent advances in the analysis of the grooved thrust bearing have also been incorporated into the later gyros in the 18 MOD B program. This is basically an adjustment in groove depth which has resulted in extending the thrust capacity of the bearing. Work which continues on other programs indicates that further optimization may be improved by using this technology.

D) Journal-Bearing Environmental Testing

A maximum $\hat{g}$ test run on the journal bearing of an 18 IRIG MOD B wheel over the frequency range 50-2000 Hz indicated a capability in excess of 40 $\hat{g}$. In the vicinity of half-speed whirl frequency (i.e., 200 Hz), however, the level reduces to 21 $\hat{g}$.

3.3.8 Gas-Bearing Reliability

Experience has shown that, for a ball-bearing wheel, indications of impending failure are evidenced by one or all of the following:

1) Mass instability of the wheel package along the spin axis,
2) Change in time for the wheel to decelerate to 1/4-speed or stand-still after the wheel voltage has been turned off,
3) Stability of the power required to run the motor, and
4) Stability of the bearing-retainer frequency evidenced on the signal-generator secondary.

With respect to the gas bearing, insufficient data is available to allow development of a failure-prediction technique. Two failure modes have been experienced for gas-bearing gyros. They are:

1) A rate input such that a wheel touchdown occurs during operation and a permanent instantaneous failure results with essentially no warning.

2) Increase in starting voltage occuring over a length of time and eventually the wheel will not start within the range of voltages that can safely be applied. Temperature cycling of the unit at times allows the unit to be restarted.

The first failure mode is an environment hazard and only preventative techniques or a further extension of the rate slew capabilities constitute reasonable solutions.

The second mode may be amenable to impending bearing-failure prediction. A history of the voltage level required for pull-in and the pull-in time may be significant. A wheel-speed indication is present in the modulation of the SG signal output. This signal may be of value in monitoring and developing a failure criterion.

Tests run on a 25 IRIG MOD 3 gas bearing shown in Fig. 3.3-23 illustrate the relationship between SG frequency and (wheel power supply) voltage change. The wheel voltage was decreased while the unit was operating in sync and the corresponding change in wheel speed is shown.

To assure reliable gas-bearing operation, it is essential that the gyro be able to withstand, with an adequate factor of safety, the system environmental inputs of angular rates, vibration, and shock. Tests can then be instituted to determine the adequacy of the design for the application. Tests on 25 IRIG MOD 3 by FBM personnel have demonstrated increased vibration and shock capability by changing the thrust-plate groove depth and pressurizing the float with as much as 3 atmospheres of helium. The penalty for these types of design changes is increased running wheel power.

Increased reliability of the bearing surfaces may be achievable by material and surface-finish changes. Effort is presently under way to have the gas-bearing surfaces manufactured from a fine-grained hot-pressed alumina. The one-micron-or-less grain size of this material (as compared to grain size of ten-to-forty microns in other commercial aluminas) shows promise of better surface finishes with a lesser tendency for crystal pullout to occur (one cause of stop-start generated debris).

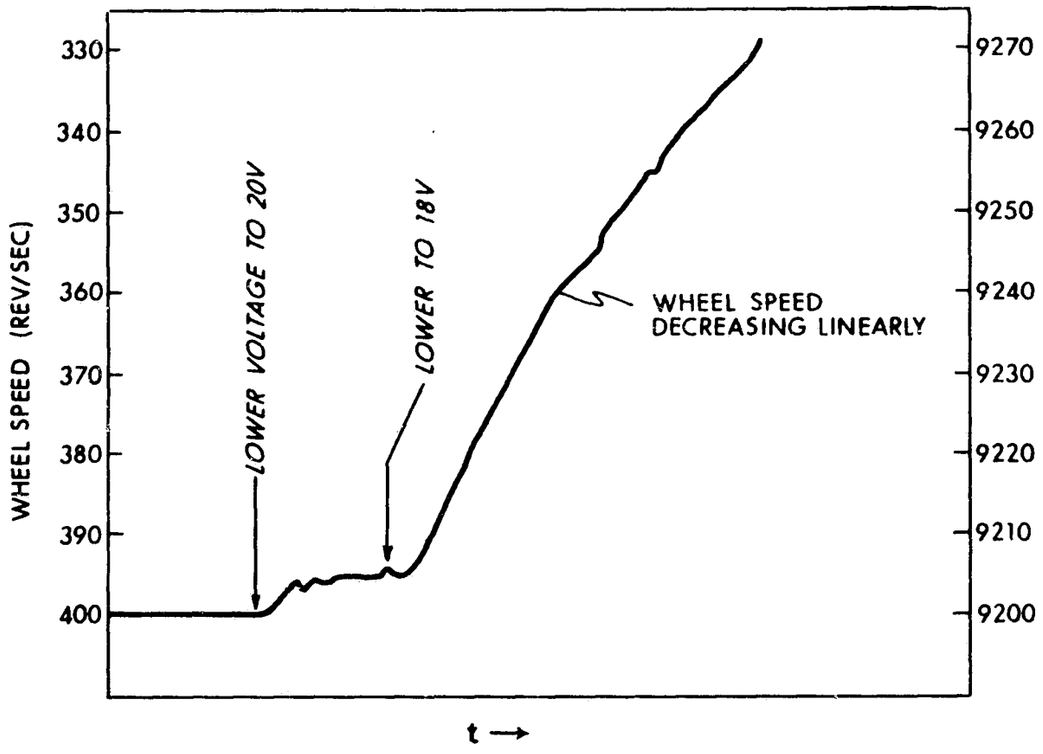

Fig. 3 3-23 Wheelspeed & SG frequency vs wheel voltage changes.

The lack of test data and reliability information for the gas bearing wheel assembly makes reliability and failure-mode testing an important investigation area.

3.3.9 Other Design Improvement Activity

A) Development work is being conducted within the FBM/IC group in the application of ceramic fabrication techniques to the wheel-motor stator. Ceramic bonding of the laminations and vacuum depositing ceramics about the assembly after the coil has been mounted offer the following possible improvements:

1) Improved mass stability,

2) Lower stator-surface vapor pressure and a reduction in possible contaminants internal to the float that may be ingested into the gas bearing.

Although supported by separate funding, these techniques are directly applicable to the stators used in this program.

B) Minimization Gyro Bias Drift

To minimize the amount of bias torque about the output axis (bias torque = current-sensitive torque and mechanical torque) the reaction torque of end-housings is measured with various rotor assemblies. Then pairs of end-housing assemblies and rotor combinations are selected and assigned to specific units such that the measured reaction torques tend to cancel when the unit is assembled.

In a related area investigatory work is being done with aluminum flex leads. Since the density of aluminum (2.77 grams/cc) is very close to the density of the damping fluid (2.390 grams/cc at 130°F) the aluminum flex leads would be very nearly floated. Because of this, difference in bias torque which appears from the OA-up and OA-down test runs would be virtually eliminated.

3.3.10 Gyro-Evaluation Testing

A) General

Testing performed on the 18 IRIG MOD B have generally had the following test sequence:

1) Functionals (centering), floatation, and transfer

2) Servo-mode temperature-drift sensitivity (120-140°F)

3) Cool-down drift sensitivity

4) Torquer magnetization retest centering, float freedom and servo-mode test, torquer sensitivity

5) Shroud seal-cool-down testing

6) Performance testing: servo mode, compliance, wheel power, pulse torquing

During the test sequence special tests were performed when anomalies in data appeared.

B) Component-Area Evaluation-Test Findings and Status

Five units were tested in the component area. Unit #410 was delivered to component test on 10-06-66. While the unit was being initially aligned on the test table, the wheel had a high-speed touchdown and subsequent failure. This wheel was operated at 48,000 rpm. The remaining 4 units were run at 24,000 rpm. The unit #410 was recycled for a new wheel and redesignated as #410A.

Unit #410A

The unit was in test from 24 March to 14 April 1967. It was delivered to Apollo systems 14 April and returned 14 July following delivery of Unit #0411 to the systems group.

Servo data were erratic and, to determine if contamination was the cause, float-freedom tests were performed at its axial extremes as well as its centered position. It was found that data taken with the float displaced toward the SG had no large torque changes. It was generally concluded that there was a contaminating particle in the instrument TG end. Long-term servo-mode and IA-vertical tests with the float axially displaced toward the SG appeared to confirm this.

The unit was delivered to the systems group for gyro-electronics check-out. It was recommended that all testing be done with the float axially displaced toward the SG.

Subsequent teardown to the float level on this unit when it was returned was inconclusive.

Unit #411

This unit was in test from 16 May to 29 June 1967 and was delivered to Systems on 29 June.

Run-to-run servo data repeatability was poor following initial torquer magnetization. The torquer was demagnetized and servo data were retaken and good repeatability was attainable.

Further testing revealed that the run-to-run variations in drift rate with the torquer magnetized was caused by opening the servo loop. This allowed the unit to drift to the OA stops.

Stop-bias-hysteresis testing was then conducted and the unit drift sensitivity to excursions of the float from the null position was confirmed. (Reference Stop-Bias discussion, Section 3.3.5 C.) Figure 3.3-24 shows typical bias shifts obtained with different changes in the float excursion.

A sampling of servo-test performance that was obtained with the gyro servo-loop closed (OA held at a null) during table position is shown in Fig. 3.3-25.

Long-term IA-vertical servo runs were made. A deviation curve for two consecutive 36-hour runs is shown in Fig. 3.3-26. Note that the RMS and average deviations are -0.14 and-0.28 meru respectively.

A cross compliance(K_{IO}) of -0.44 meru/g^2 was obtained in a long-term IA-horizontal servo test run. This is compared to -1.39 determined from a test run by statistical averaging (lower confidence level).

Unit #410 B

Unit #410 A was returned from systems for teardown to the float. After reassembly it was redesignated unit #410B. This unit was tested from 30 August to 27 October 1967. It was furnished to systems for continued electronic checkout on 27 October.

Performance appeared to be very satisfactory and no measurable evidence of stop-bias hysteresis was detected. Following a wheel rundown the wheel could not be restarted in either SRA-horizontal or vertical orientations. After overnight storage at temperature, restart was attempted and then retried at 137°F. A restart was achieved with 400-ma/phase current (as opposed to 280-ma/phase nominal). An ADIA shift of -325 meru had also occured. Subsequent testing included run-up and run-down at various unit orientations, cooldown across servo testing and rebalancing with no further start difficulty. Performance had deteriorated slightly but was still reasonably good (ΔBD = 0.1 meru, ΔADSRA = 2, ΔADIA = 4.5 meru over four servos runs). The unit was furnished to systems to be used for continued electronic checkout. Because of its wheel history, however, it is suspect and is not considered a delivered instrument.

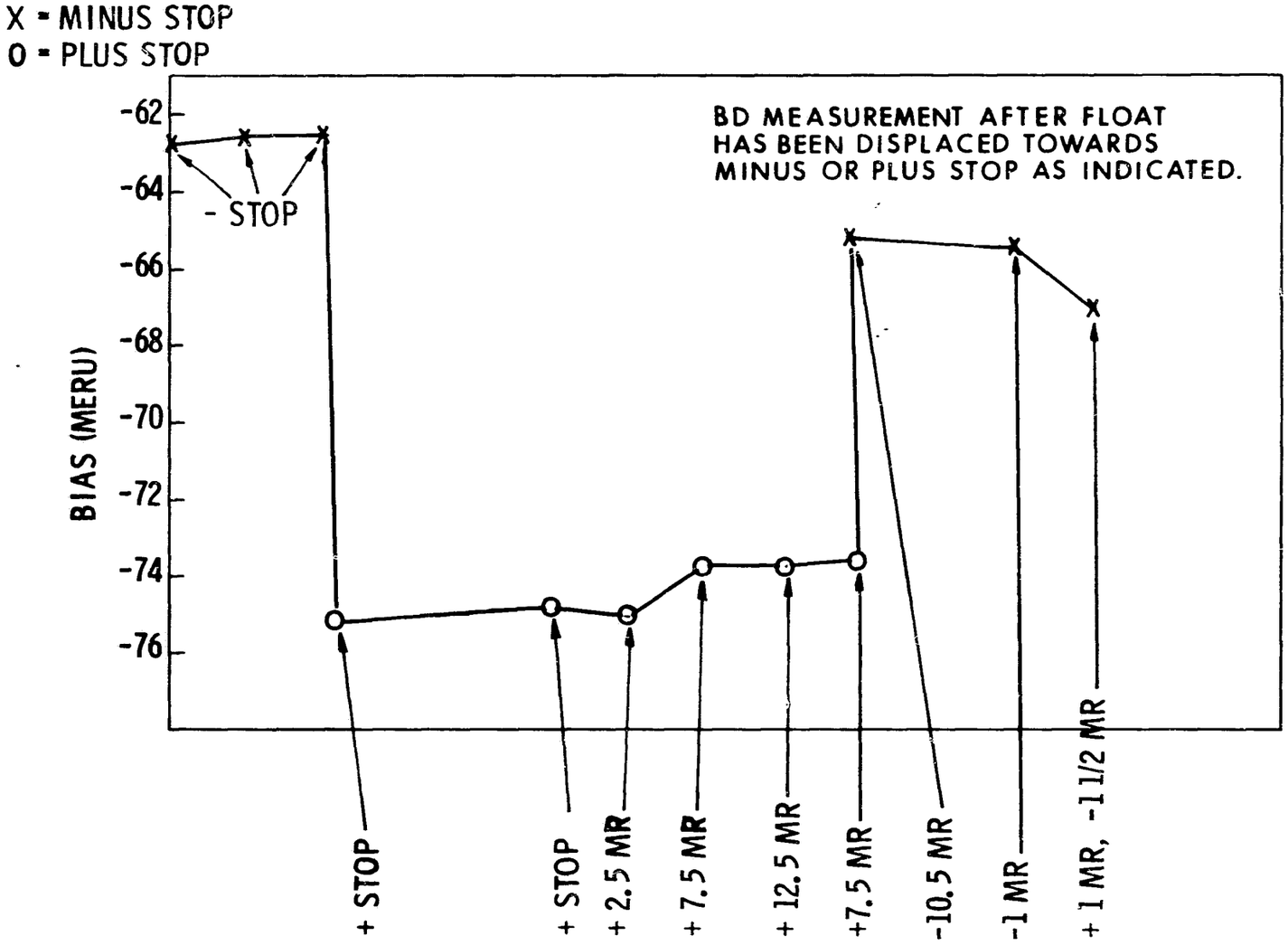

Fig. 3.3-24 Stop bias hysteresis, 18 IRIG MOD B #411.

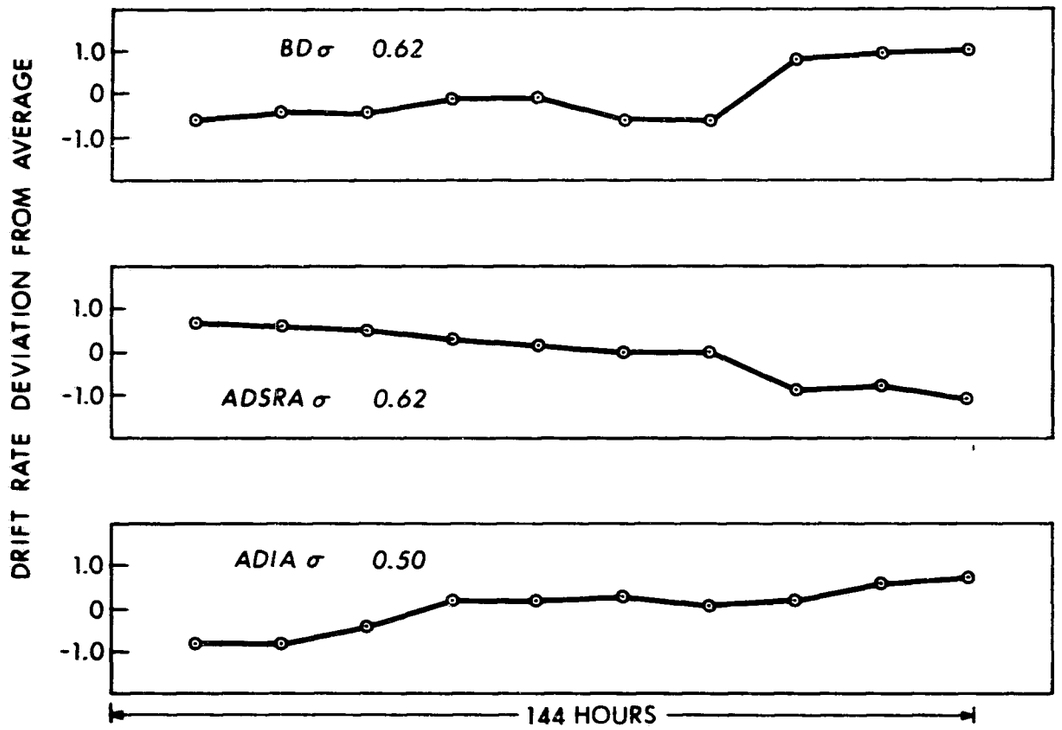

Fig. 3.3-25 Servo performance tests, six day period.

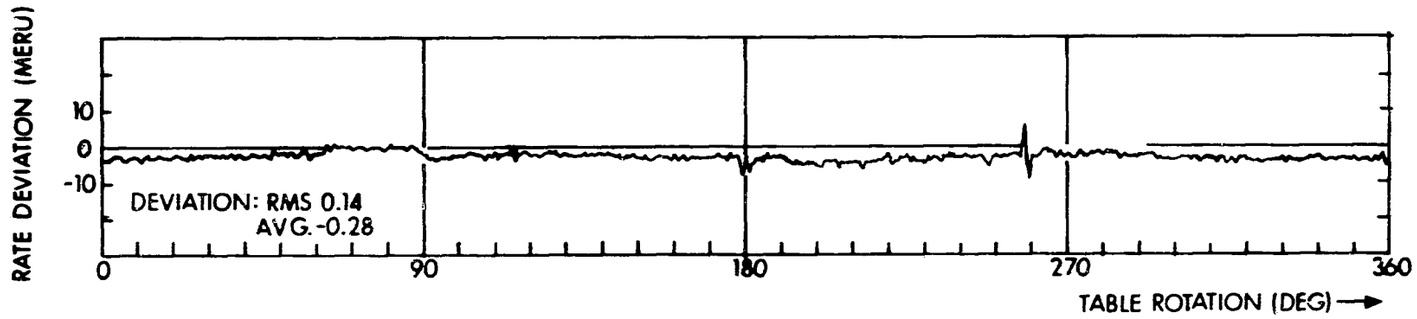

Fig. 3.3-26 Table rate deviation, 2 consecutive 36 hr IA vertical servo runs (unit #411, 7/10/67).

Unit #412

This unit was in test from 31 October to 30 November 1967. Hard-start difficulties were encountered (required 45V/phase after cooldown and the minimum start voltage had increased from 15 to 28 volts), and the unit was returned for teardown to the wheel assembly for further analysis. Inspection did not reveal a visible cause although debris in the +SRA thrust plate was suspected from analysis of the test data. The wheel was cleaned, reassembled, and retested. Wheel retest with over 1000 start-stops has been conducted with no difficulties encountered.

Reassembly of the gyro is expected to begin in mid-January and the gyro will be redesignated Unit #412A.

Unit #413

Assembly has been completed, preliminary tests began on 11 January 1968. Initial performance data are satisfactory.

C) System Test - Torquer Evaluations

System test evaluations on unit #411 were oriented towards defining torquer sensitivities. The initial phase of the investigations were conducted with precise dc current level inputs and were intended to define a base line for sensitivities with respect to float angle, radial and axial displacement, and temperature. The second phase was testing in a ternary pulse-torque-to-balance control loop. The objective here was to evaluate the adaptability of the instrument to the strapdown application. In these tests scale-factor stability and linearity with various test rates and torquing parameters were investigated. All tests were conducted on a precision air-bearing test table which could be operated in either a gyro servo-mode or could be driven at precise-angular input rates (15°/hr to 600°/sec). The test area is shown in Fig. 3.3-27. (Photographs of 18 IRIG unit #411 installed in system alignment hardware are shown in Fig. 4.3-7, 4.3-8, and 4.3-9.) In all test setups a band-pass pre-amplifier mounted close to the gyro test block was used to provide noise and 800cps wheel power filtering. (See Section (3.3.6)).

1) Torquer Sensitivity with Float Angle

Figure 3.3-28 shows difference in cw and ccw torquer sensitivity with float angle. This test was run using dc current levels of 10, 30 and 60 ma applied to the torquer with the test table operating in a servo mode. Table rates were determined using the table inductosyn readout. The 60-ma level corresponds approximately to the current level used for the pulse-torque-to-balance mode of operation. At 60 ma, the difference between cw and ccw scale factor changes by less than

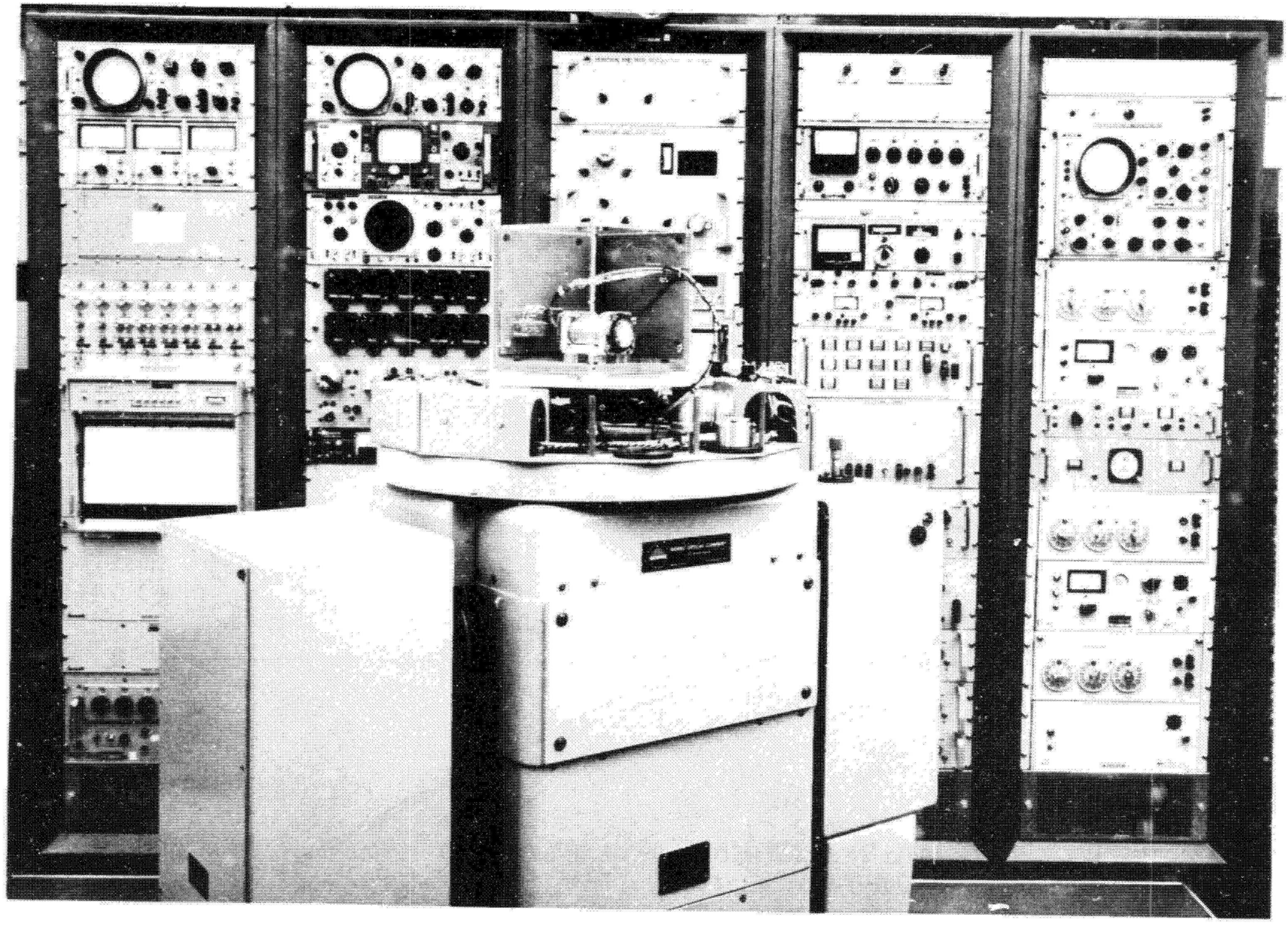

Fig. 3.3-27 Gyro test area.

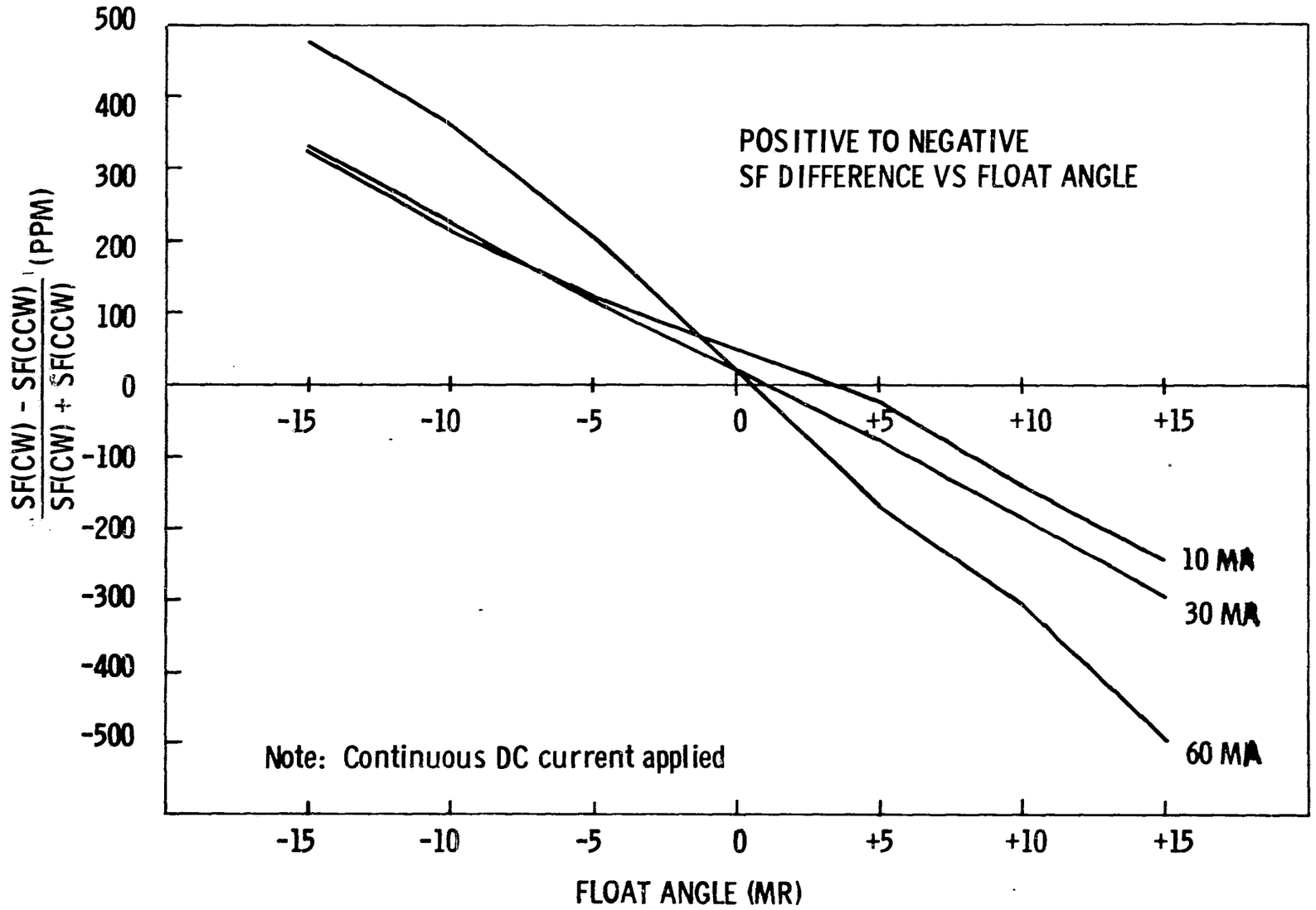

Fig. 3.3-28 Unit 0411, 18 MOD B.

40 ppm/milliradian.

The average cw and ccw torquer-sensitivity change is shown in Fig. 3.3-29. Note that the point of maximum torque corresponds to approximately +5 milliradians (mr) of float angle measured via the SG. As discussed in Section 3.3.5B, the optimum alignment corresponds to one in which the SG null is coincident to the TG maximum-torque position. It would appear that SG-to-TG misalignment was on the order of 5 milliradians (use of the alternating current alignment procedure, Section 3.3.5B, should improve the alignment accuracy). For unit #411 the average scale-factor sensitivity near the SG null at the 60-ma current level corresponds to 60 ppm/mr

2. Temperature Sensitivity

The temperature sensitivity of the torquer is shown in Fig. 3.3-30. A temperature-compensation ring which acts as a magnetic shunt is selected and installed during torquer assembly. Its temperature coefficient is matched to achieve a design objective of 10 ppm/^{o}F torquer SF sensitivity. The tests on Unit #411 indicate a sensitivity of 16 ppm/^{o}F. Since thermal control to within 0.1^{o}F is anticipated, scale-factor variations due to this influence were not a problem.

3. Radial Sensitivity

Average scale-factor sensitivity to radial displacement along IA and SRA are shown in Fig. 3.3-31. The sensitivity is less than 10 ppm for a radial displacement of 400 microinches. A rate about the gyro output axis of more than 1/2-rad/sec would be needed to cause radial displacements of this magnitude.

4. Axial Sensitivity

Figure 3.3-32 shows the torquer sensitivity change with axial displacement. The sensitivity changed by less than 50 ppm for displacement of 250 microinches. This axial displacement would occur for a 2-1/2^{o}F. floatation error and 10 g's acting along the output axis.

5. Torque-to-Balance Testing

a) Test Electronics

The instrument was tested employing a ternary-pulse-restrained torque-to-balance control loop. "Ternary" is used in the sense there are three distinct torquing states: positive, negative, or zero torque. The simplified mechanical switching schematic,

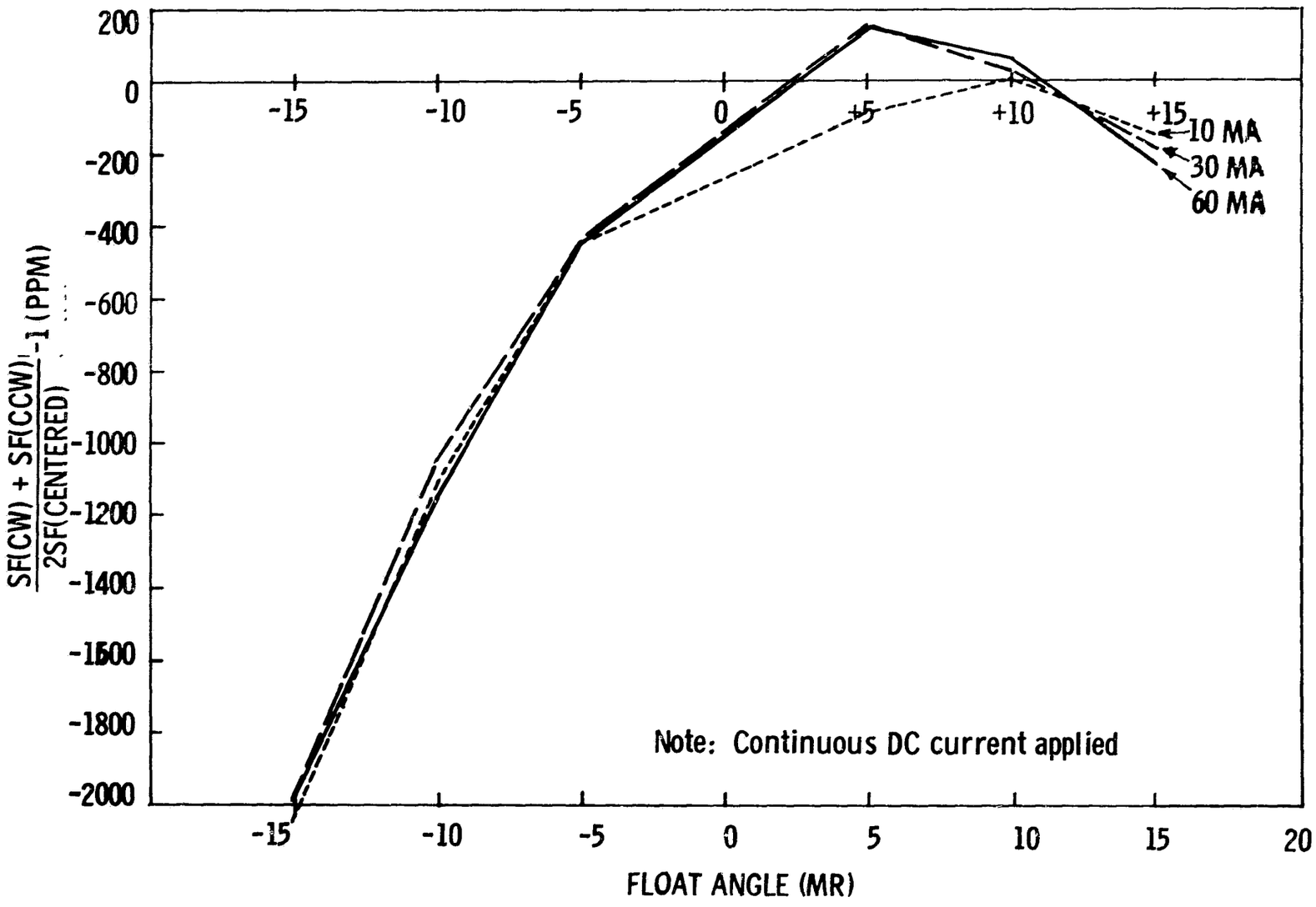

Fig. 3.3-29 Unit 0411, 18 MOD B, scale factor vs float angle.

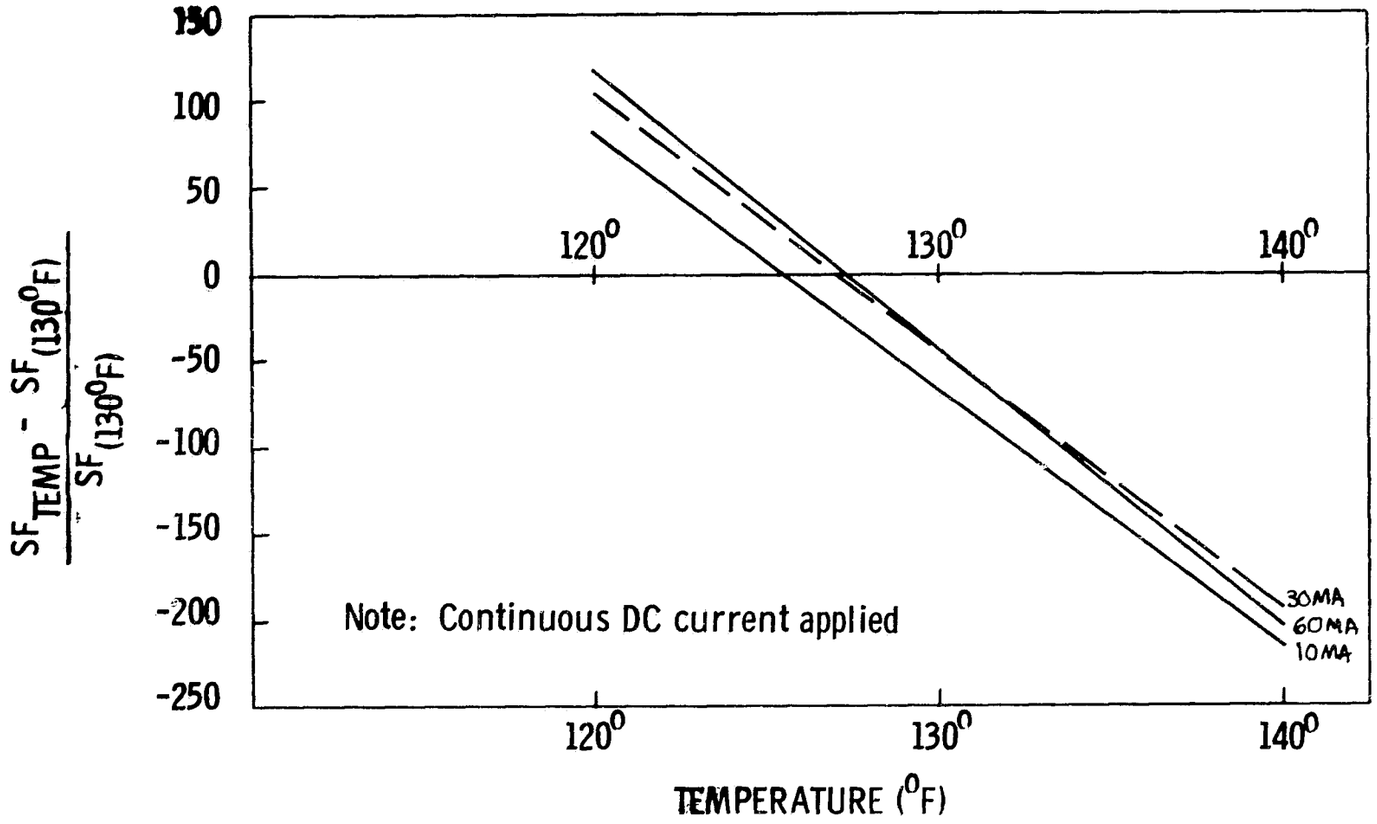

Fig. 3.3-30 Unit 0411, 18 MOD B, scale factor vs temperature.

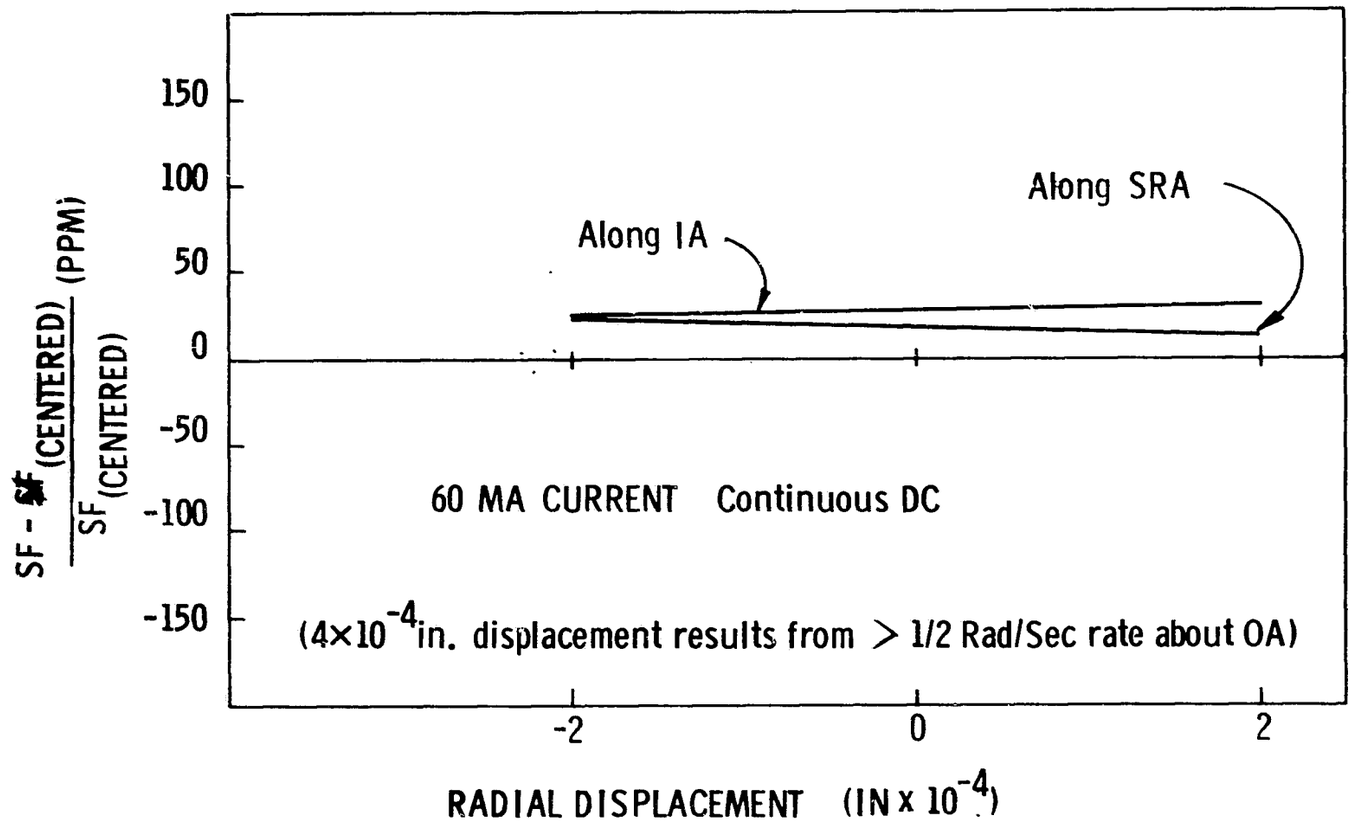

Fig. 3.3-31 Unit 0411, 18 MOD B, scale factor vs radial displacement.

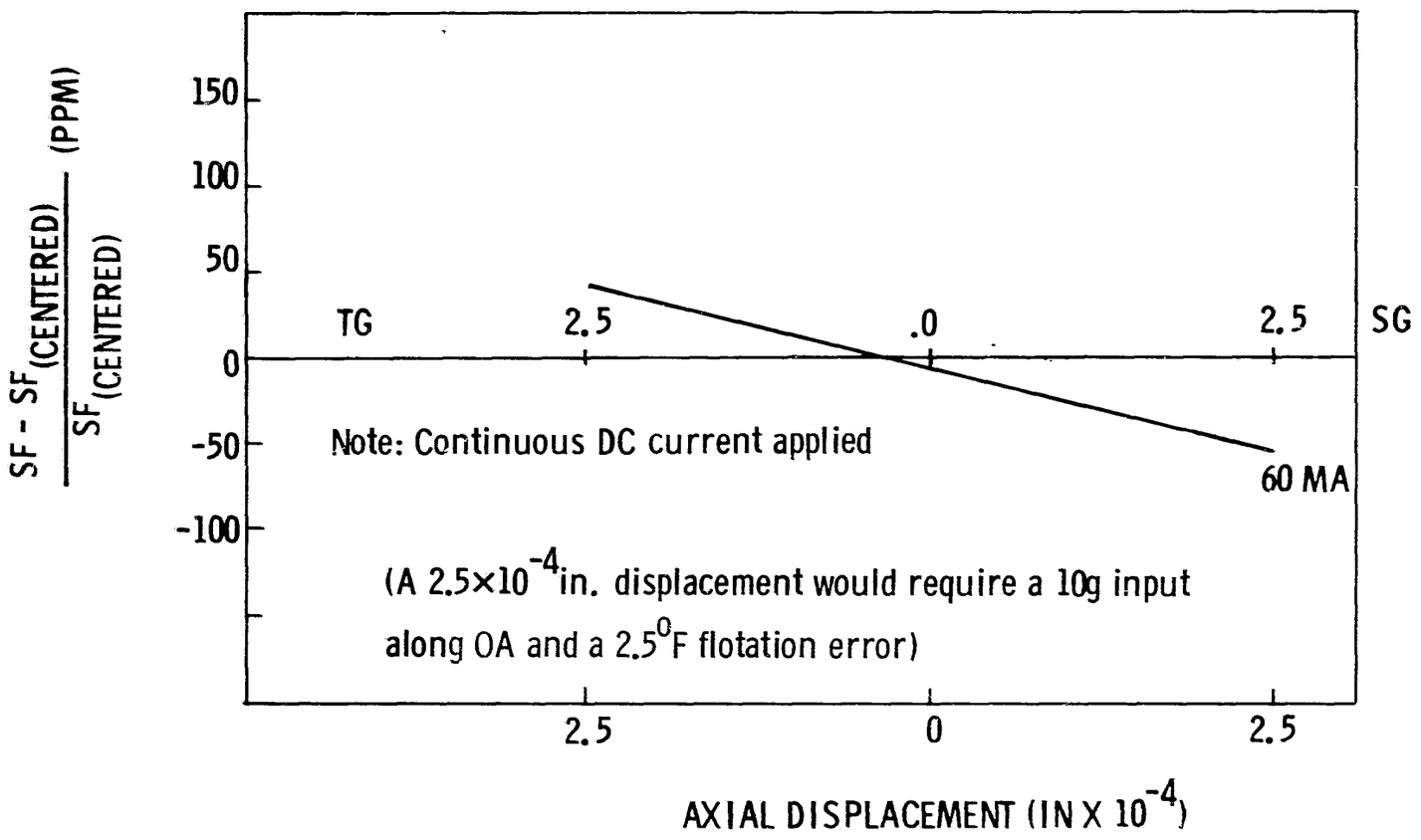

Fig. 3.3-32 Unit 0411, 18 MOD B, scale factor vs axial displacement.

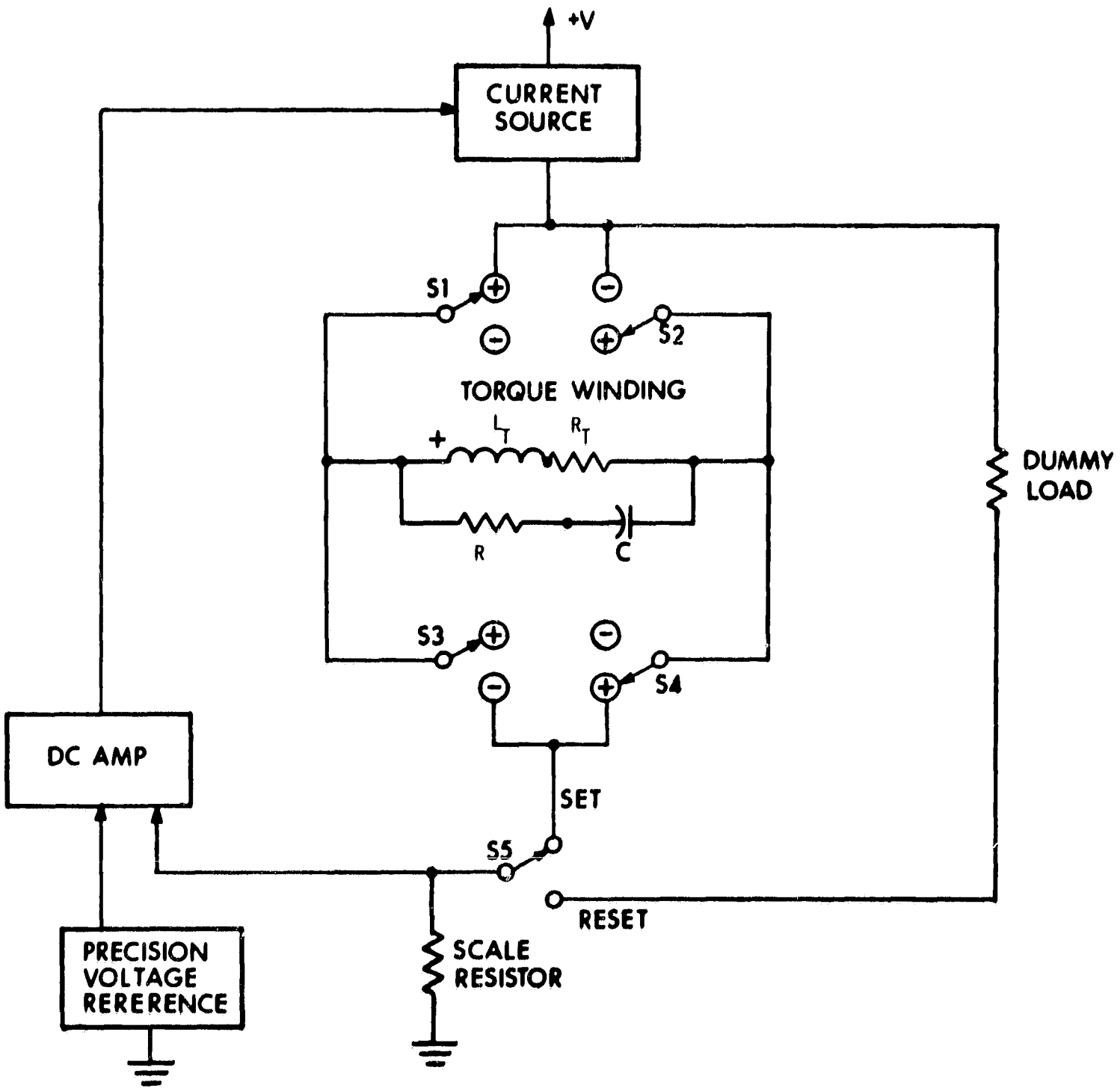

Fig. 3.3-33 **Ternary pulse torque switching.**

Fig. 3.3-33, (semiconductor switches are actually used) helps illustrate ternary control and some of the subtleties of the test electronics. The switch status is shown in the zero-torque mode, positive-torque polarity. Note the torquing polarity is set by an "H" switch (switches S_1, S_2, S_3, and S_4 function as a double-pole-double-throw switch) that feeds current into the plus-or-minus direction of the torquer winding. Switch S_5 operates so that current flows through either a dummy load or the torquer winding.

The dummy load is a resistively wound heater (approximately the same resistance as the torquer winding) located on the TG end of the gyro. Thus, S_5 not only turns on the command torquing (set position) but also is mechanized to maintain a thermal balance in the reset position. In addition, regardless of the torque command state, approximately the same current is fed into the scale-factor resistor. The scale-factor voltage is compared with a precision-voltage reference in the input stage of a high-gain dc amplifier. The amplifier is part of the dc control loop that maintains a precise fixed-current level. Note also that an R-C compensation network is connected across the torquer. It functions to tune the torquer so that the load seen by the switches and current source is purely resistive.

The turn-on and turn-off of torque (operation of S_5) can occur only at specific switch set-and-reset-pulse times respectively. For the electronic test configuration that was used, a switch set-and-reset pulse is issued in each (interrogation) clock cycle. The reset pulse precedes the switch pulse so that S5 is operated such that a torque-off command exists in each clock cycle. Thus, current is applied to the torquer as pulses and even for maximum commanded torque a short off-period exists in every clock interrogation interval. The average applied restraining force for a given measurement period is, therefore, a function of the number of torque pulses applied during the measurement period. The resultant loop operation is such that an equivalent torquing pulse rate exists for each constant level of applied input rate. For an ideal permanent-magnet torquer, however, the rate pulses applied to the torque winding have no effect on the amount of torque derived from each pulse or the float response to each pulse. As noted previously in Eq. 3.3.4,

each torque pulse represents an equivalent increment of indicated angle change. By definition, the torque pulses are termed $\Delta\theta$ pulses. They are represented in the control-loop mechanization by another pulse that is issued either on the $[+\Delta\theta]$ or $[-\Delta\theta]$ line for a torquing pulse that results in response to an applied angular rate along the positive or negative sense of the instrument input axis respectively.

b) Test Setup

A block diagram illustrating the functional elements of the control loop and various test monitor and support equipment are shown in Fig. 3.3-34. The general test technique used for both SF stability and linearity testing is to set the table controls to desired rate, set the test-counter preset section to accumulate a number of $\Delta\theta_T$ pulses from the table inductosyn, and route the gyro $\Delta\theta$ pulses to the counter accumulator. The counter preset section controls the input gate to the accumulator so that when the desired number of $\Delta\theta_T$ pulses are received the count of gyro pulse increments is stopped. The result accumulator count (N) represents an exact measure of the gyro output $\Delta\theta$ pulses for a preset number of table increments (X).

Within this test setup, the test uncertainties result from both the instrument and test equipment.

The test equipment may introduce uncertainties due to their inability to maintain a constant instrument environment (i. e., temperature control, wheel and microsyn excitation, power-supply noise, and line-voltage regulation). Torquer temperature sensitivity of 16 ppm/^{o}F was determined (Fig. 3.3-11), and test temperature control loop maintained control to within $\pm$ 0.1^{o}F. Variations in microsyn and wheel excitation can cause bias changes due to microsyn reaction-torque and thermal-gradient variations respectively. Microsyn excitation was maintained within 0.1%. Variations in the dc or ac power can directly influence the torque-to-balance control loop. The control loop itself incorporates a pre-regulator to minimize ripple and noise to its power supply. The basic dc test-rack power supply is regulated to within 0.01%. In general, it was determined that laboratory line-transient filtering by the test-console power supplies was adequate to assure no influence on the test runs. All power supplies and the pulse-torque electronics were synchronized by a test clock and scaler (1.382 megacycles, stability of 1 part in 10^8 per day).

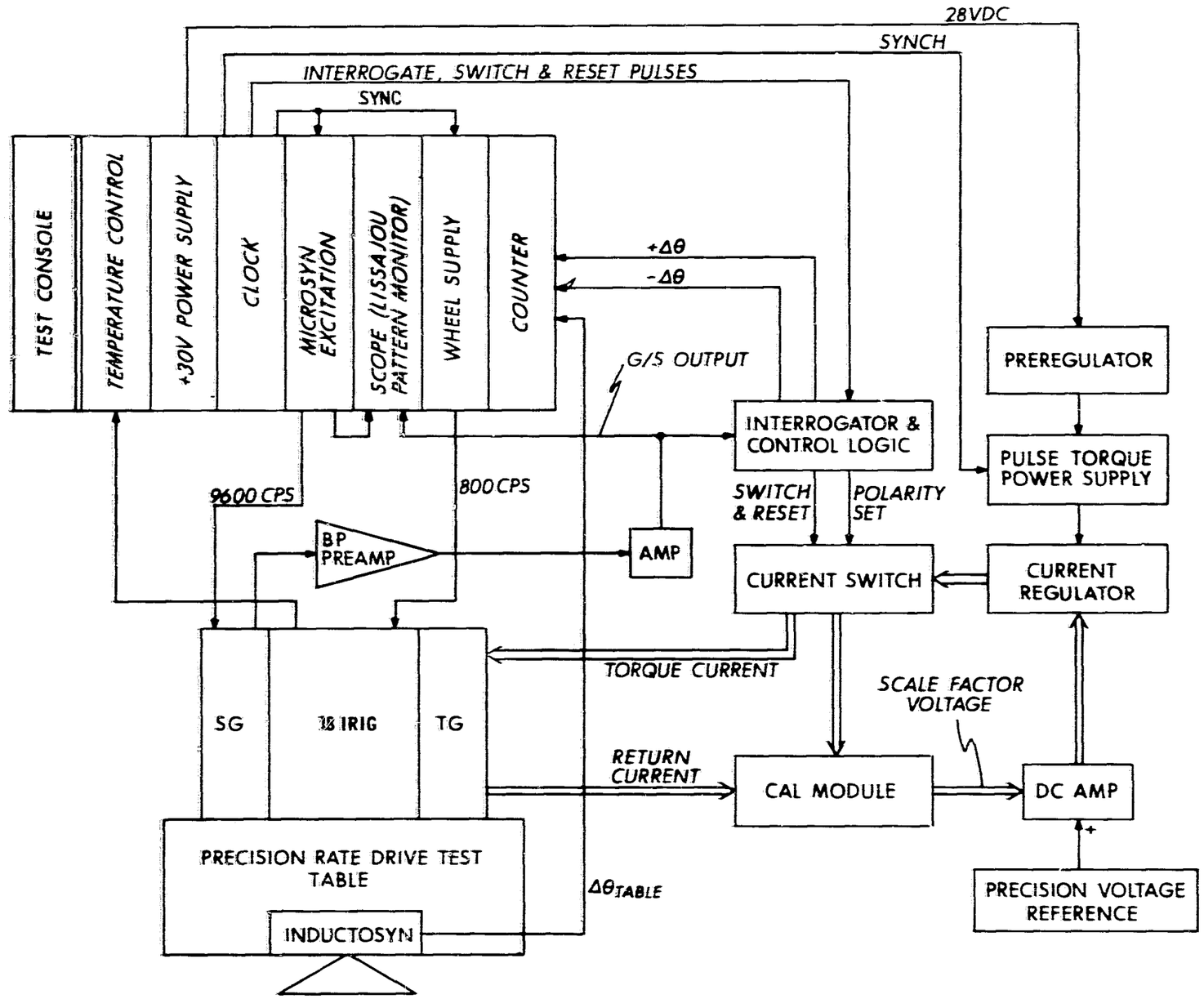

Fig. 3.3-34 Gyro in pulse torquing electronic test setup.

Another factor in test accuracy is the basic test resolution. In the procedure of counting $\Delta\theta$ and $\Delta\theta_T$ gyro and table pulses outlined previously, the effect of small table-rate variations between test runs or printouts is eliminated by using a measure of table angular motion as the precision input (± 1/3 arc-second point-to-point accuracy). The gyro resolution accuracy may influence stability because of the time relationship of a single gyro pulse count relative to the total table-count preset control. To minimize this influence, in excess of a million pulses are counted for each stability measurement run.

Variations in gyro drift during test will also influence scale-factor stability and linearity. This measurement error is inversely proportional to the input rate during the test. If the drift uncertainty is one meru and the torque-to-balance input-table test rate was only 1000 meru, the influence of the drift-time uncertainty can be equivalent to an indicated SF stability of 1000 ppm. Servo-mode drift tests showed BD and ADIA stability on unit #411 to be better than 1 meru (Fig. 3.3-25) when the float excursion was controlled about the SG null. Thus, table test rates for stability runs were set in excess of 1000 earth rates (15×10^3 deg/hr) to assure that SF-stability uncertainty effects due to drift variation were less than 1 ppm. The minimum table rate used for scale-factor linearity runs was 3.6×10^3 deg/hr (1^o/sec).

As noted previously a preamplifier with a band-pass filter for noise-pickup attenuation was mounted on the table with the gyro. A grounding and shielding mechanization was developed to minimize noise and special care was exercised in routing the signals through the table slip-ring assembly. Good noise rejection was achieved through the use of the amplifier (Section 3.3.6); however, both 1600-cps wheel modulation and noise coupling between the TG and SG at torquing-current switching times was observed. (The SG harness runs along the gyro shroud and is connected to external connector pins at the TG end.) The magnitude of the switching spike was considerably larger than the SG signal-level change corresponding to float motion that would result from a torque pulse.

c) Multiple Pulsing

The presence of noise on the SG lines appeared to contribute substantially to shifts in instrument-stability measurements. One probable cause of shifts during closed-loop pulse-torque-to-balance operation was multiple-pulsing. The term multiple-pulsing is used to describe the occurance of a burst of several $\Delta\theta$ torquing pulses of the same polarity during tests at constant-input rates.

As discussed in Section 2.5, the 18 IRIG gyro float dynamics (time constant) cause the torque-to-balance loop to pulse-burst (9600-pps)interrogation rate for input rates in excess of 1.5 degrees per second. The computer simulation described in Chapter 2 predicted pulse-bursting of 3-torquing-pulses-on and 12-off for an input rate of 3^{o}/sec (9600-pps operation). In tests on unit 411, a 3-on, 12-off busting pattern was observed in the region of 2.8^{o}/sec. (The difference may be accounted for by the variation between nominal and actual instrument parameters.)

At low rates the multiple-pulsing appeared to be noise-induced and normally took the form of a "Double-Pulsing" phenomenon. Double-pulsing is explained in detail in Section 3.4.7. Briefly, an additional erroneous pulse of the same polarity would occur immediately following a normal torque command. The additional pulse does not drive the float through the electronics ternary-control dead-zone but does represent a source of measurement error. Figure 3.3-35 helps demonstrate double-pulsing. The figure is a reproduction of a phase-demodulated recording of unit 411's SG output signal taken with earth rate as the basic test input.

The unit is in a pulse-torque-to-balance control-loop mode operating at a 9600-pps interrogation rate. The scale factor is equivalent to approximately 7.7 seconds of arc per pulse. For the earth-rate input this should correspond to approximately two pulses a second.

The spikes shown on the figure correspond to the recorder-demodulator's response to the switching-signal noise coupling of the torquing pulse. The actual float motion is represented by

(Input- EARTHRATE plus NBD & ADIA)
(Torque loop -9600 pps interrogation rate, $\Delta\theta \simeq 7.7$ sec)

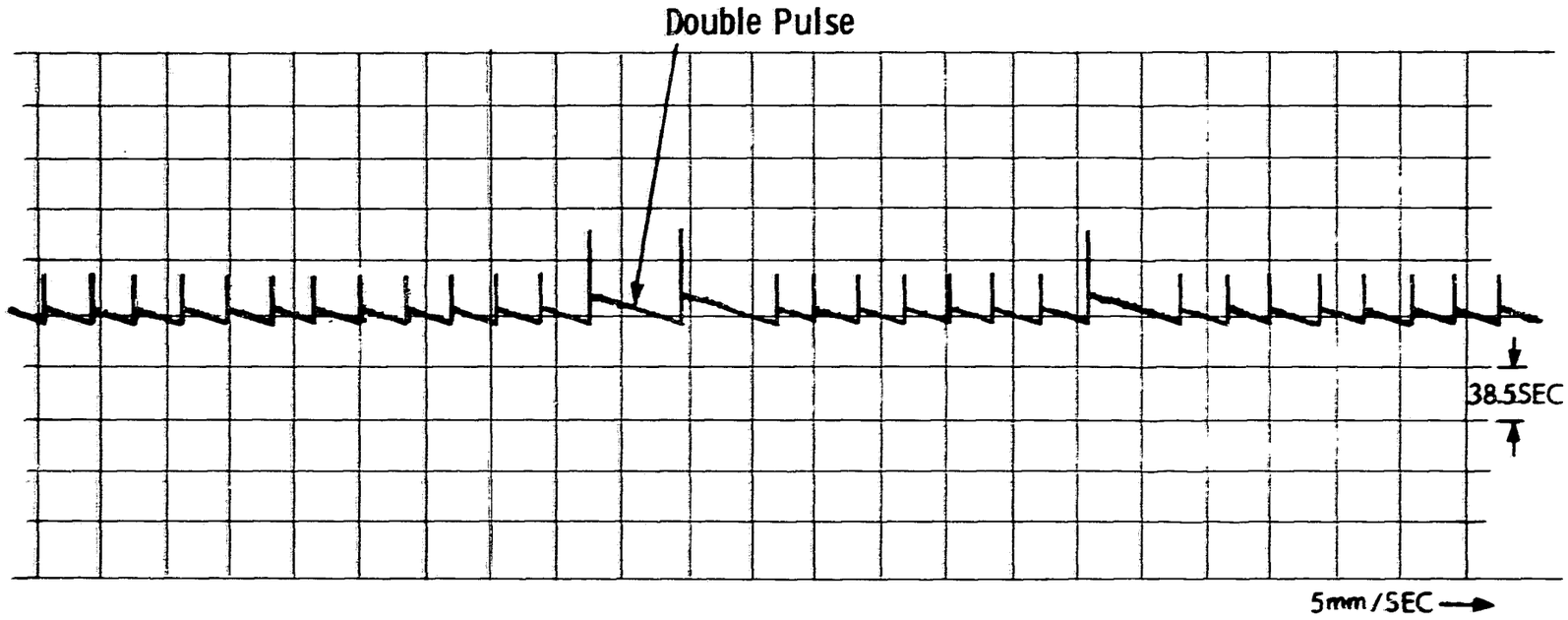

Fig. 3.3-35 SG output vs time.

the saw-tooth curve. As shown, the torquing pulse drives the float towards the SG null (approximately a $\Delta\theta$ increment). The float then drifts out to the minus-polarity torquing threshold in response to the earth-rate input. At an earth-rate input, float-dynamic considerations can not account for pulse-bursting. As shown, the double-pulsing occurred randomly. It would appear that the double-pulsing is precipitated by the presence of noise at the SG output. The influence of double-pulsing on measurement stability for the PIP is presented in Appendix B. The same general considerations are applicable to gyro measurements.

d) Pulse-Torque Test Results

The frequency sensitivity of the torque resulting from the coil-holder eddy-current effects, (discussed in Section 3.3.5 combine with multiple-pulsing effects to yield varying degrees of measurement and performance instabilities. These are evidenced during pulse-torque-to-balance scale-factor stability and linearity testing. As discussed previously, both multiple-pulsing and eddy-current frequency sensitivities are more pronounced at higher control-loop interrogation rates. Thus, superior stability and linearity was always exhibited at 3200-pps as opposed to operation at 9600-pps. Figure 3.3-36 shows a 13-hour scale-factor stability run on unit 411 at a 3200-pps interrogation rate. A total excursion of 5ppm was obtained. The best 9600-cps interrogation stability test run is shown in Fig. 3.3-37.
In this case the total excursion is on the order of 15 ppm with peaks of 25 ppm.

Torque-to-balance scale-factor linearity test results at 3200- and 9600-pps interrogation rates are shown in Fig. 3.3-38 and 3.3-39 respectively. Again, the 3200-pps interrogation rate operation is considerably better. During testing, however, it was observed that improved performance could be obtained by using an additional R-C tuning network across the torque-coil winding. In theory only a single R-C network should be necessary to account for the torquer-coil time constant (L/R).

The additional benefits derived from the use of dual tuning are probably explained by the coil-holder eddy-current effects. For example, in Fig. 3.3-13 the normalized inductance and resistance of the torquing-coil was shown to have varied with frequency. The dual-network time constants taken individually were 116 microseconds and 6 microseconds; together they yield a more complex function which probably approximates the variations of the coil and holder more closely. The left-hand side in each of the test figures (3.3-38 and -39) shows the measured scale-factor linearity variation for a single R-C tuning network. The right-hand side shows the test results with dual tuning. Note the improvements in scale-factor linearity and the marked reduction in the difference between the CW and CCW scale factors. With dual tuning, scale-factor linearity on the order of 100ppm and 200 ppm appeared to be consistently obtainable at 3200-pps and 9600-pps interrogation rates respectively for an input range of 1 to 10^{o}/ sec .

RATE DRIVE 12 °/SEC CCW
SF = 15 SEC/PULSE, 3200 pps INTERROGATE RATE
σ = 1.6 ppm
July 26, 1967

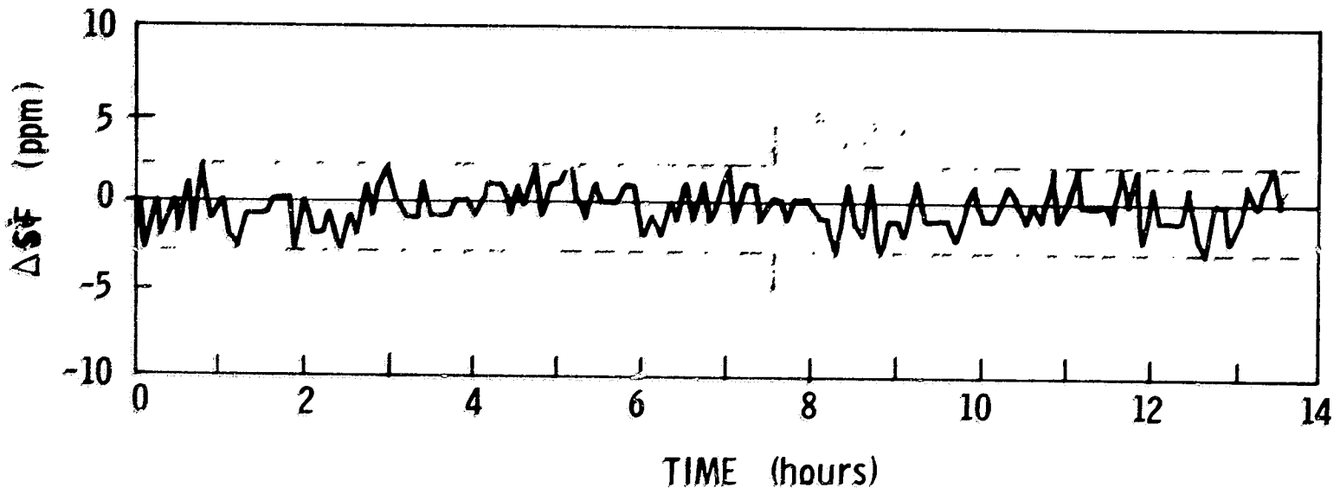

Fig. 3.3-36 Pulse torque SF stability, 18 IRIG MOD B #411.

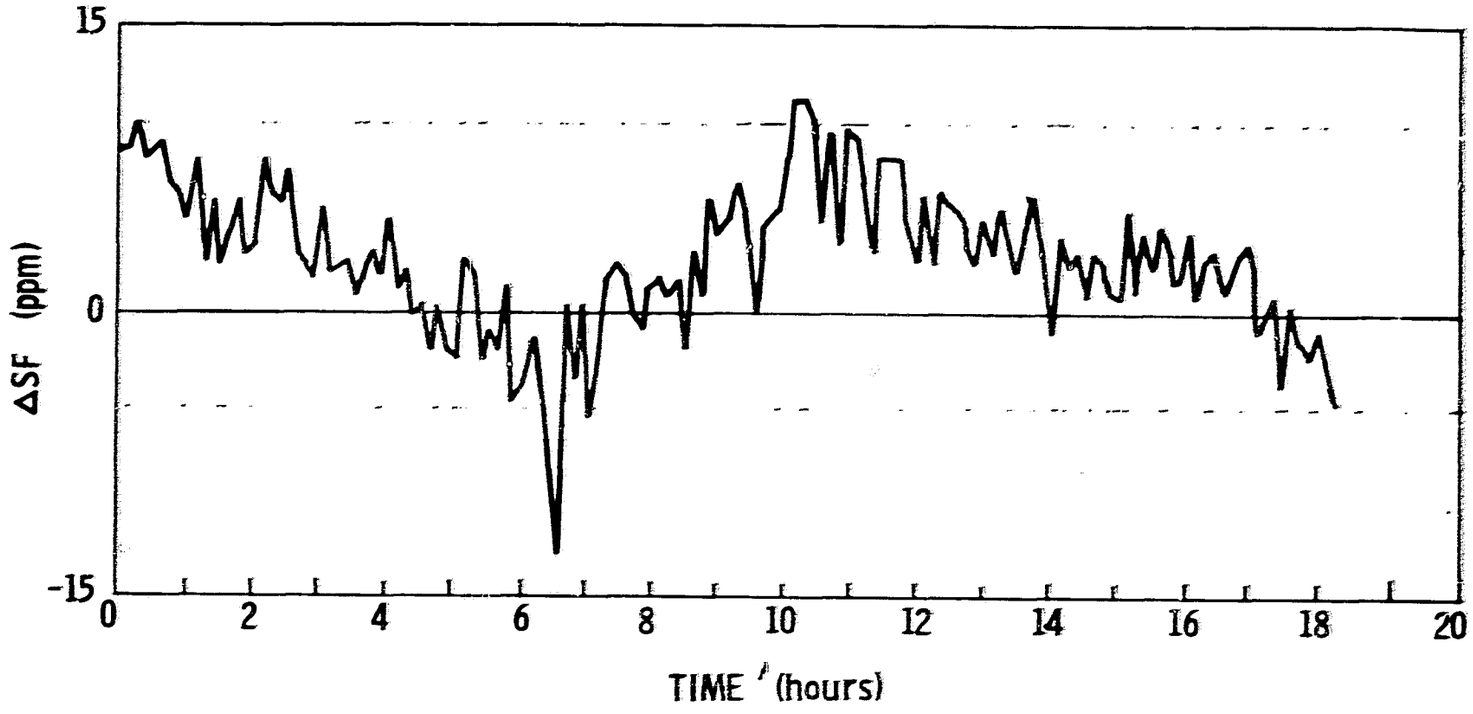

Fig. 3.3-37 Pulse torque SF stability, 18 IRIG MOD B #411.

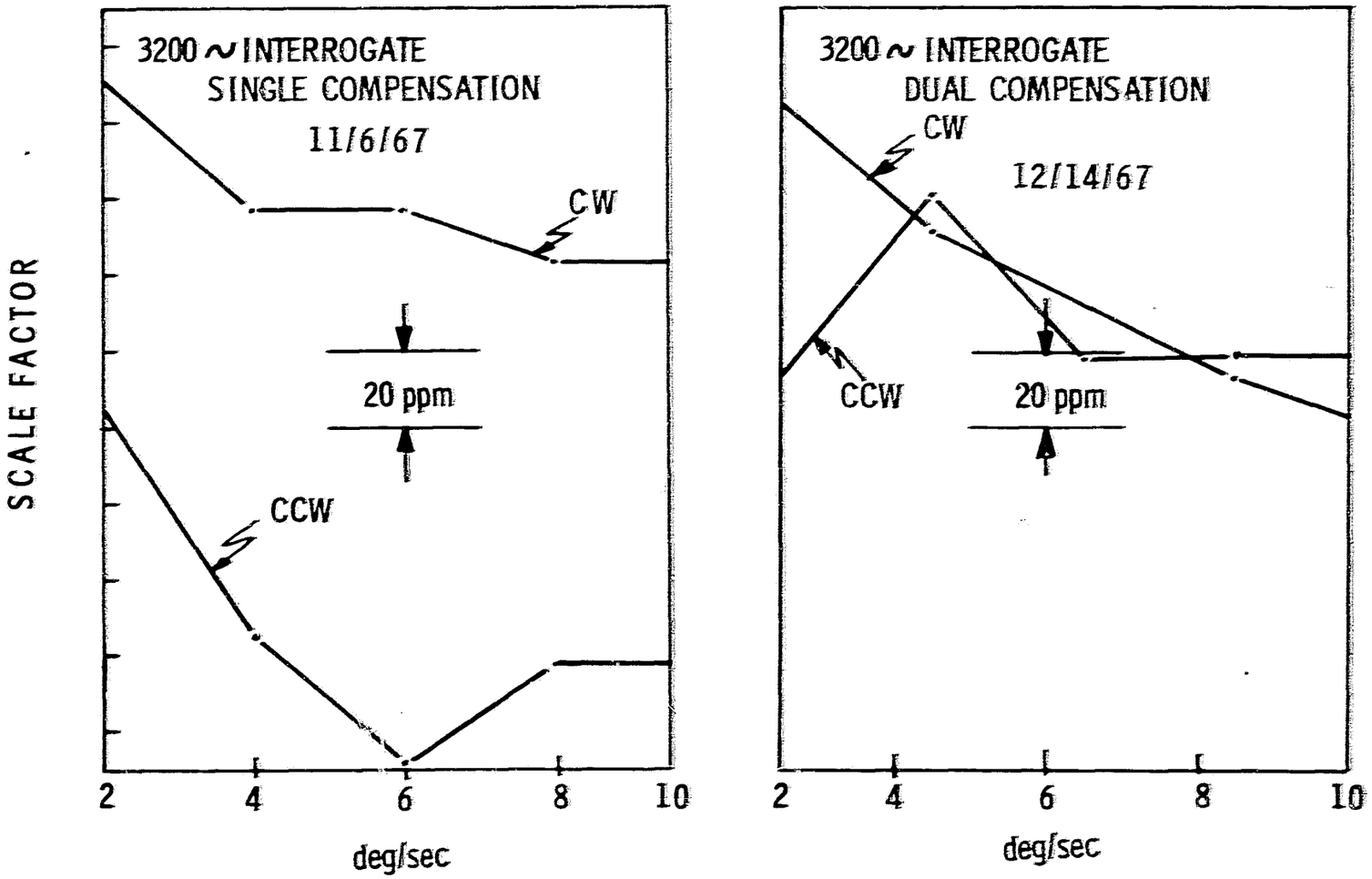

Fig. 3.3-38 Scale factor linearity, unit 411.

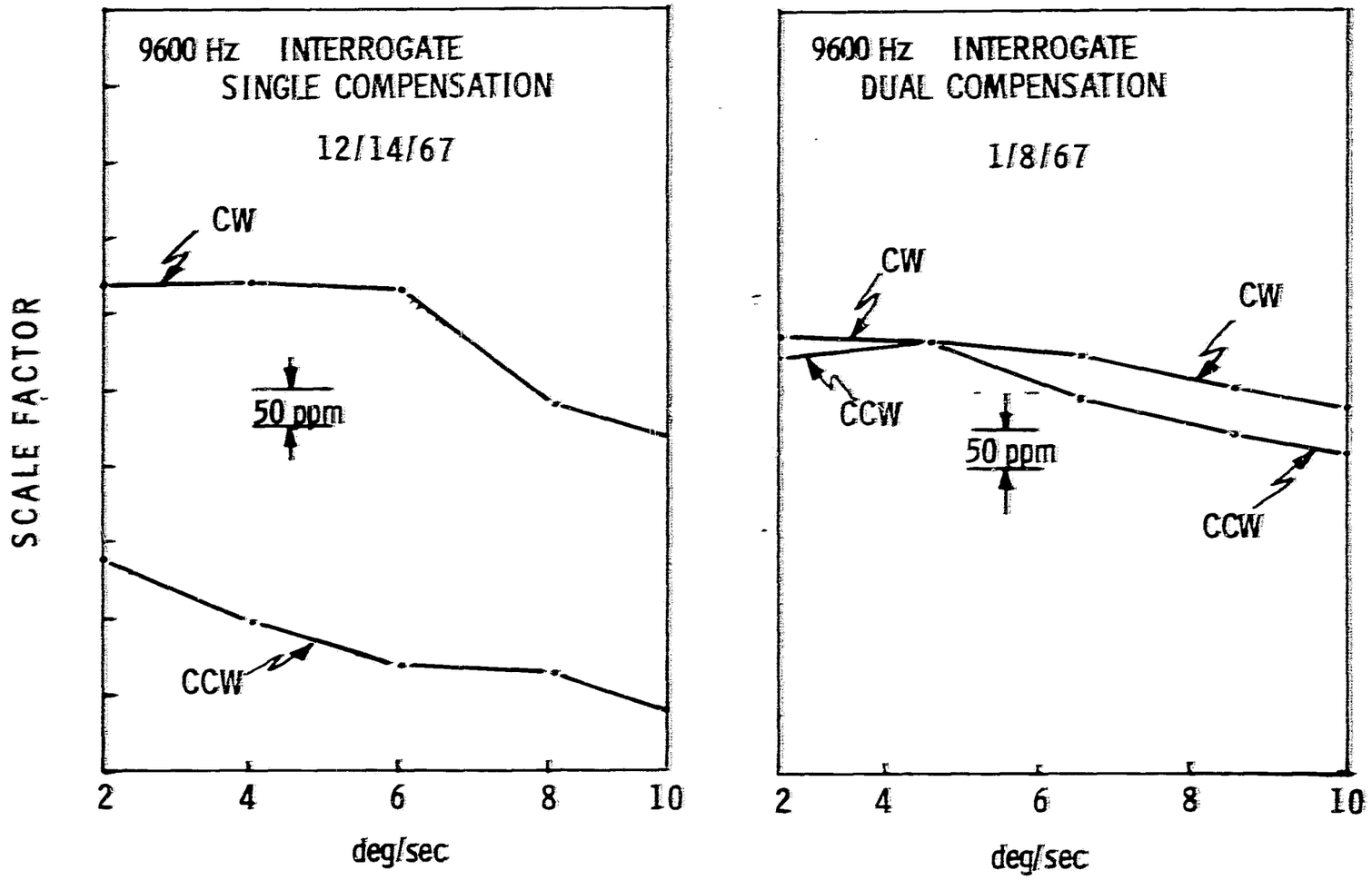

Fig. 3.3-39 Scale factor linearity, unit 411.

3.4 16 Permanent-Magnet-Pulsed-Integrating Pendulous Accelerometer (16 PM PIP)

3.4.1 Introduction

The 16 PM PIP is a single-degree-of-freedom integrating specific force receiver. The PIP consists of a cylindrical body (float) that is suspended in a state of neutral buoyancy within a cylindrical case by a dense, highly viscous fluid. The float has freedom of rotation about its longitudinal axis (output axis) and the mass on the float offset from the axis provides specific force measurement sensitivity. In addition to buoyancy support, the fluid provides rotational motion damping. Rotation of the float resulting from specific force applied to the pendulous mass is sensed by a signal generator (SG), a linear angle-to-voltage generator located at one end of the instrument case. Restraining torques about the output axis may be applied to the float by a torque generator (TG), a linear current-torque transducer, located at the opposite end of the case. In addition to the fluid buoyand support the float is actively supported and centered radially and axially by a microsyn (variable reluctance transducer) at each end of the case.

3.4.2 Physical Description

Physically, the PM PIP is defined by three basic assemblies: the float, an SG end-housing and a TG end-housing. The SG and TG end-housings assemble about the float to form a hermetically-sealed case. The unit is then housed in a magnetic shroud that also serves as a thermal insulator. Wrapped around the case are four temperature sensors that are used for temperature control and monitoring.

Float:

The float is a solid cylinder of beryllium. Embedded in the float cylinder is the pendulous mass that includes a projection which also serves as the mechanical stop for rotational motion. Blind holes are located along the axial center of each end of the float to align with the ball pivots in each

PAGES 3-80
PAGE 3-81
PAGE 3-82

WERE REMOVED FROM THIS DOCUMENT PER INSTRUCTIONS.

end-housing. The pivots and holes serve as a mechanical bearing for the PIP when power is off and assure that the float does not settle beyond the radial and axial pull-in capabilities of the microsyn suspension. When the power is on, the microsyn operates such that the float is suspended about the pivot. The suspension rotors are ferrite and are located at each end of the float. The inner diameter is tapered to provide axial magnetic support. A four-pole ferrite rotor located on one end of the float mates with the stator in the end housing to form PIP E-type microsyn SG. The TG rotor is an encapsulated assembly of eight air-core coils mounted to the opposite end of the float. The coils are oriented rotationally to match the eight-pole permanent-magnetic located in the TG end-housing. Current is brought into the torquer coils through two flex leads and the torque produced by the TG is proportional to the applied current. There are two axial through-holes in the float, symmetrically located with respect to the pendulous axis. Tubular slugs are placed in the holes for flotation and end-to-end balance adjustment. The holes also allow fluid flow for more rapid axial centering, fifteen minutes maximum compared to two hours for the Apollo PIP. (Scale-factor linearity is influenced by TG-rotor axial and radial motion.)

SG End-Housing Assembly:

The SG end-housing assembly contains a tapered eight-pole magnetic suspension stator and a twelve-pole E-type microsyn stator concentrically mounted in a one-piece beryllium end-housing and encapsulated with an epoxy compound. A ball pivot is located at the inside center of the end-housing and mates with the float.

TG End-Housing Assembly:

The TG end-housing assembly contains a tapered eight-pole magnetic suspension stator, an eight-pole permanent-magnet torque generator stator, and an Armco magnetic ingot-iron-cylinder (acting as a return path for the permanent-magnet stator) mounted concentrically in a one-piece beryllium end-housing. The permanent magnet stator is made of Alnico V and is an assembly of a ring structure with poles that are adhesively attached.

Mounted on the stator are the eight magnet energizing coils, the temperature compensator ring, and the coil printed-circuit ring. This assembly is also encapsulated in epoxy compound.

3.4.3 Theory of Operation

The 16 PM PIP operates on a closed-loop principle (see Fig. 3.4-3), where the torques on the float are restrained by torque generator control signals.

Any component of acceleration along the input axis of the PIP produces a torque about the output axis, and causes the float to rotate from a null position. The direction and magnitude of the float rotation is sensed by the signal generator. When the SG output voltage reaches a given threshold level, a discriminator provides a positive-or-negative set signal, depending on the polarity of the SG output voltage. These set signals are interrogated at a given clock frequency to switch a control current of fixed amplitude and duration into the positive or negative direction of the torque generator winding. The polarity of the torque is set to oppose or restrain the sensed input torque. A detailed description of the electronic test loop that was used in this evaluation and its parameters is provided in Chapter 4. Theoretical aspects of pulse-torque-restrained instrument servo loops are included in Chapter 2.

The float acts as a torque-summing member (neglecting any inaccuracy torques) and the torques acting on the float can be expressed as:

$$I_{OA}\frac{d^2\theta}{dt^2} + C\frac{d\theta}{dt} + m\ell a_{in} \pm M_{(tg)} = 0 \qquad (3.4.1)$$

where

$I_{OA}\frac{d^2\theta}{dt}$ = the torque due to inertia of the float

I_{OA} = moment of inertia of the float about OA

θ = angle of rotation of the float about OA

$C\frac{d\theta}{dt}$ = the viscous damping torque about OA

C = damping coefficient

$m\ell a_{in}$ = input acceleration torque

$m\ell$ = pendulosity of float

a_{in} = component of acceleration input along IA

$M_{(tg)}$ = restraining torque provided by the torque generator for a fixed current amplitude

Integrating (3.4.1):

$$I_{OA}\frac{d\theta}{dt} + C\theta = m\ell V_{in} + \int_0^t \pm M_{(tg)}dt \qquad (3.4.2)$$

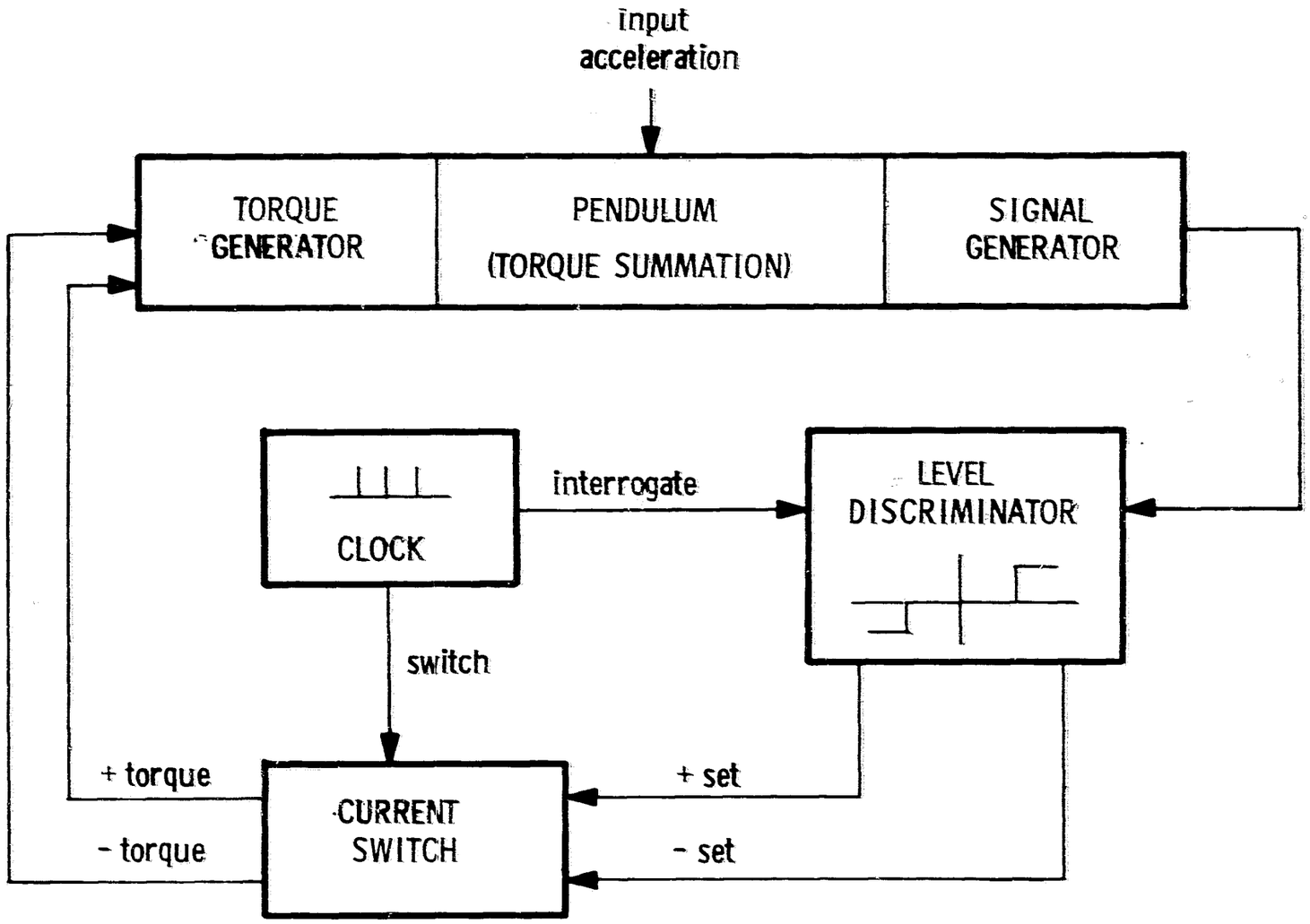

Fig. 3.4-3 Block diagram 16 PM PIP closed loop.

where:

$$V_{in} = \text{component of velocity along IA} \qquad (3.4.3)$$

The θ and $\dot{\theta}$ terms on the left-hand side of equation (3.4.2) represent the dynamic storage characteristics of the instrument. For steady-state conditions, the control-loop functions to keep the float at the null position; the average storage term is, therefore, negligible with respect to a measurement period. Thus, in the steady-state the torquer output is seen to balance the specific-force input and the indicated velocity is:

$$V_{in} = \frac{1}{m\ell} \int_o^t \pm M_{tg}\, dt \qquad (3.4.4)$$

Since the feedback current to the torque generator is controlled and measured over discrete integral intervals determined by the clock frequency, (3.4.4) may be expressed in the following form:

$$V_{in} = \frac{1}{m\ell} \left[\int_o^{ts} \pm M_{tg}\, dt \pm \int_{ts}^{2t_s} \pm M_{tg}\, dt \; . \; . \; . \right] \qquad (3.4.5)$$

where

$t_{(s)}$ = is the clock period, corresponding to the duration of the control current

Thus, if $M_{(tg)}$ is a non-time-variant function, the indicated velocity measurement for an integral number of sampling periods is:

$$V_{ind} = \sum \frac{M_{tg} ts}{m\ell} (N^+ - N^-) \qquad (3.4.6)$$

As indicated in (3.4.5), the velocity measurement may be expressed in a quantized form. It can be computed, therefore, by counting the clock periods corresponding to positive or negative torque in a test period and multiplying by a constant. The constant may be termed the instrument scale factor and represents an increment of velocity (ΔV) measurement.

Thus

$$V_{(tc)} = (\Delta V) \sum N^+ - N^- \qquad (3.4.7)$$

where $\Delta V = M_{(tg)} t_s / ml$ (3.4.8)

$V_{(tc)}$ = indicated velocity input in a test period

N^+ = number of sampling intervals of positive torque in a given computational period

N^- = number of sampling intervals of negative torque in a given computational period

t_c = the test observation period

The torquing constant (M_{tg}) for a permanent-magnet air-coil torquer is basically linear. The magnetic stability problems experienced with square-law electromagnetic torquers and the scale-factor errors due to torque-current transient rise and decay characteristics are eliminated.

3.4.4 Test Program

A test plan was formulated to allow a fine-grain investigation of the instrument's suitability for use in a strapdown configuration. In addition, tests were defined to uncover any PM PIP sensitivities that could result in adverse performance in a system-level operational environment.

In general, test evaluation program sought to answer the following questions:

a) What is the limit of the PM PIP's capability?
b) How is this capability affected by operation of the instrument in a system environment?
c) How does noise on the SG and torquer lines affect loop operation and stability?
d) What results are obtained by interrogating at different frequencies?
e) What cross-coupling errors are associated with use of a PM PIP in a strapdown environment?

The test effort was divided into two main areas. The first was to set up a PM PIP in an optimum manner, keeping all environments as ideal as possible, in order to ascertain the PM PIP's performance limits. The second phase was to subject the PIP to a range of operational environments which would be present within a system configuration and to evaluate the resulting degradation in the PIPA performance. In addition, problems peculiar to the use of such an instrument in a strapdown environment were also to be investigated.

3.4.5 Test Setup

The PM PIP was tested employing a "ternary" pulse-restrained torque-to-balance control loop. The torque loop is essentially identical to the one described in Section 3.3. This description has been modified as applicable and provided for completeness. "Ternary" is used in the sense that there are three distinct torquing states: positive, negative, or zero torque. The simplified mechanical-switching schematic, Fig. 3.4-4, (semi-conductor switches are actually used) helps illustrate ternary control and some of the subleties of the test electronics. The switch status is shown in the zero-torque mode, positive-torque polarity.

Note the torquing polarity is set by an "H" switch (switches S_1, S_2, S_3, and S_4 function as a double-pole, double-throw switch) that feeds current into the plus or minus direction of the torquer winding. Switch S_5 operates so that current flows through either a dummy load or the torquer winding.

The dummy load is a resistively wound heater (approximately the same resistance as the torquer winding) located on the TG end of the PIP. Thus, S_5 not only turns on the command torquing (set position) but is also mechanized to maintain a thermal balance in the reset position. In addition, regardless of the torque-command state, approximately the same current is fed into scale-factor resistor. The scale-factor voltage is compared with a precision-voltage reference in the input stage of a high-gain dc amplifier. The amplifier is part of the dc control loop that maintains a precise fixed-current level. Note also that an R-C compensation network is connected across the torquer. It functions to tune the torquer so that the load seen by the switches and current source is purely resistive.

The turn-on and turn-off of torque (operation of S_5) can occur only at specific switch (set) and reset pulse times respectively. For the electronic test configuration that was used, a switch set-and-reset pulse is issued in each (interrogation) clock cycle. The reset pulse precedes the switch pulse so that S5 is operated such that a torque-off command exists in each clock cycle. Thus, current is applied to the torquer as pulses and, even at maximum commanded torque, a short off period exists in every clock-interrogation interval. The average applied restraining force for a given measurement period is, therefore, a function of the number of torque pulses applied during the measurement period. The resultant loop operation is such that an equivalent torquing pulse rate exists for each constant level of applied specific force. For an ideal permanent-magnet torquer, however, the pulse rate applied to the torque winding has no affect on the amount of

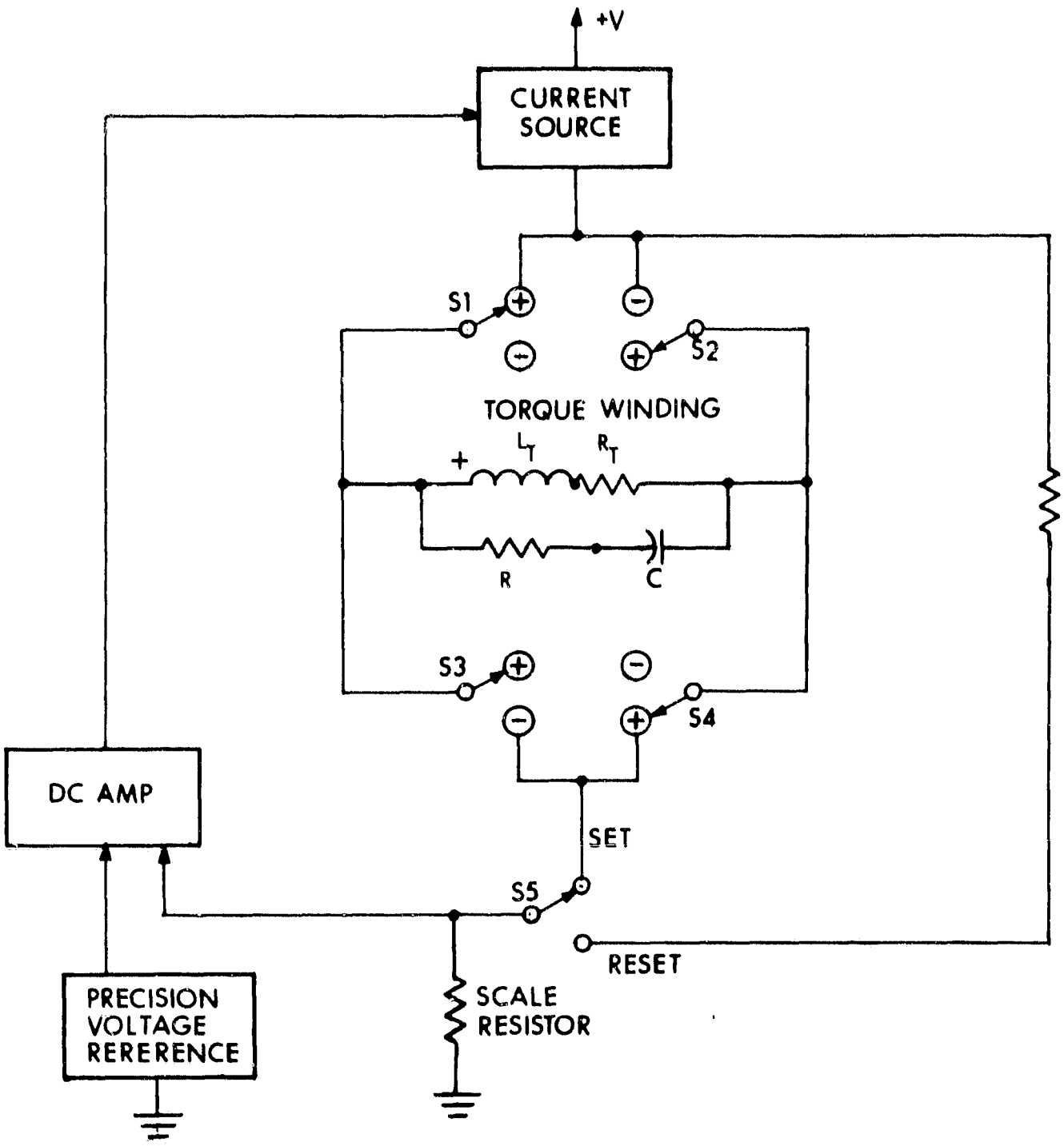

Fig. 3.4-4 Ternary pulse torque switching.

torque derived from each pulse or the float response to each pulse. As noted previously in (3.4.7), each torque pulse represents an equivalent increment of indicated velocity change. By definition, the torque pulses are termed $+\Delta V$ or $-\Delta V$ pulses. This terminology is in keeping with vector convention and is represented in the control-loop mechanization by a pulse that is issued either on the $(+\Delta V)$ or $(-\Delta V)$ line for a torquing pulse that results in response to an applied specific force along the positive or negative sense of the instrument input axis, respectively.

A block diagram illustrating the functional elements of the control loop and various test monitor and support equipment is shown in Fig. 3.4-5. Figures 3.4-6 and 3.4-7 are photographs of the PM PIP laboratory area and test configuration.

In order to determine the instrument's capability accurately, the test conditions and setup were precisely defined and controlled. For example, the interconnection of electronics and test equipment was carefully developed to assure that noise on the SG and torquer lines would be kept to an absolute minimum. To eliminate ground-loop problems a single-point grounding scheme was employed. Signal and power grounds were completely isolated and then interconnected at a single ground-point tied to the external bus. Lead lengths were minimized and critical signal lines were shielded to assure a minimum of pickup. The result was an exceptionally clean SG monitor (better than a 40-dB signal-to-noise ratio) and excellent dc-loop-current stability (less than 5 parts per million). (The measurement of current-loop stability was limited by test equipment capabilities.)

In addition, it was determined that pre-regulator and power supply filtering of laboratory line transients (induced by power load changes) was adequate to assure no effects on PIP performance. Sensitivity of electronic-loop scale-factor control to laboratory temperature environment was observed and room temperature ($72^{\circ} \pm 2^{\circ}$F) was controlled to assure optimum performance.

In the interconnection scheme, noise coupling between the torquer and signal generator was observed at current-switching times. The transient magnitude measured at the SG was generally in excess of twice the magnitude of the selected interrogation detection level (6-8 sec of float rotation). Major portions of the coupling were traced to the instrument harness, unshielded from the base of the instrument where the leads emanate to its connector. On one test unit, SG-lead shielding was added and the noise was reduced (approximately 50%), but could not be eliminated. Some noise coupling may be magnetically induced within the body of the unit. However, unlike the

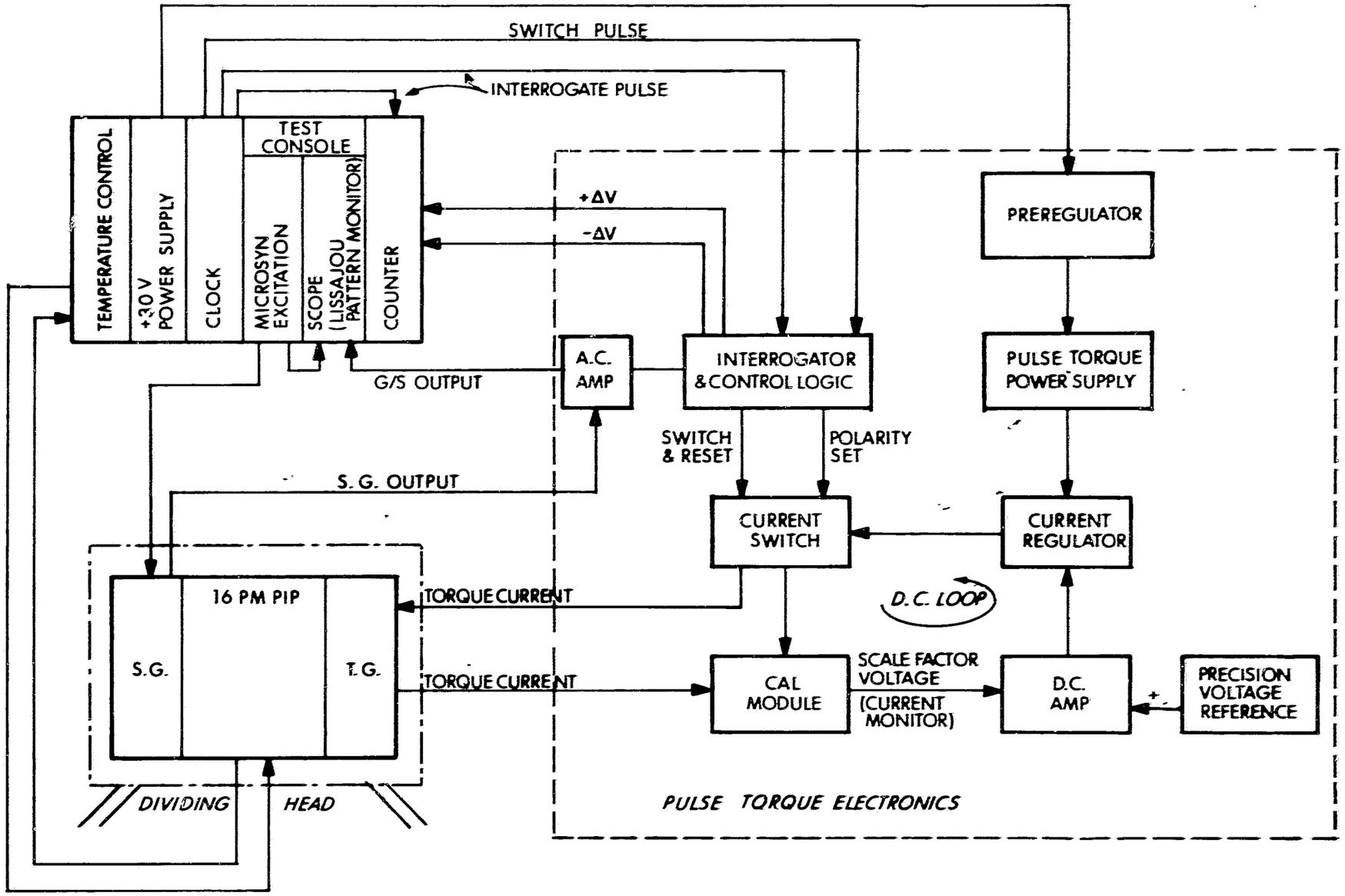

Fig. 3.4-5 Block diagram - PIP, pulse torque electronics and test equipment.

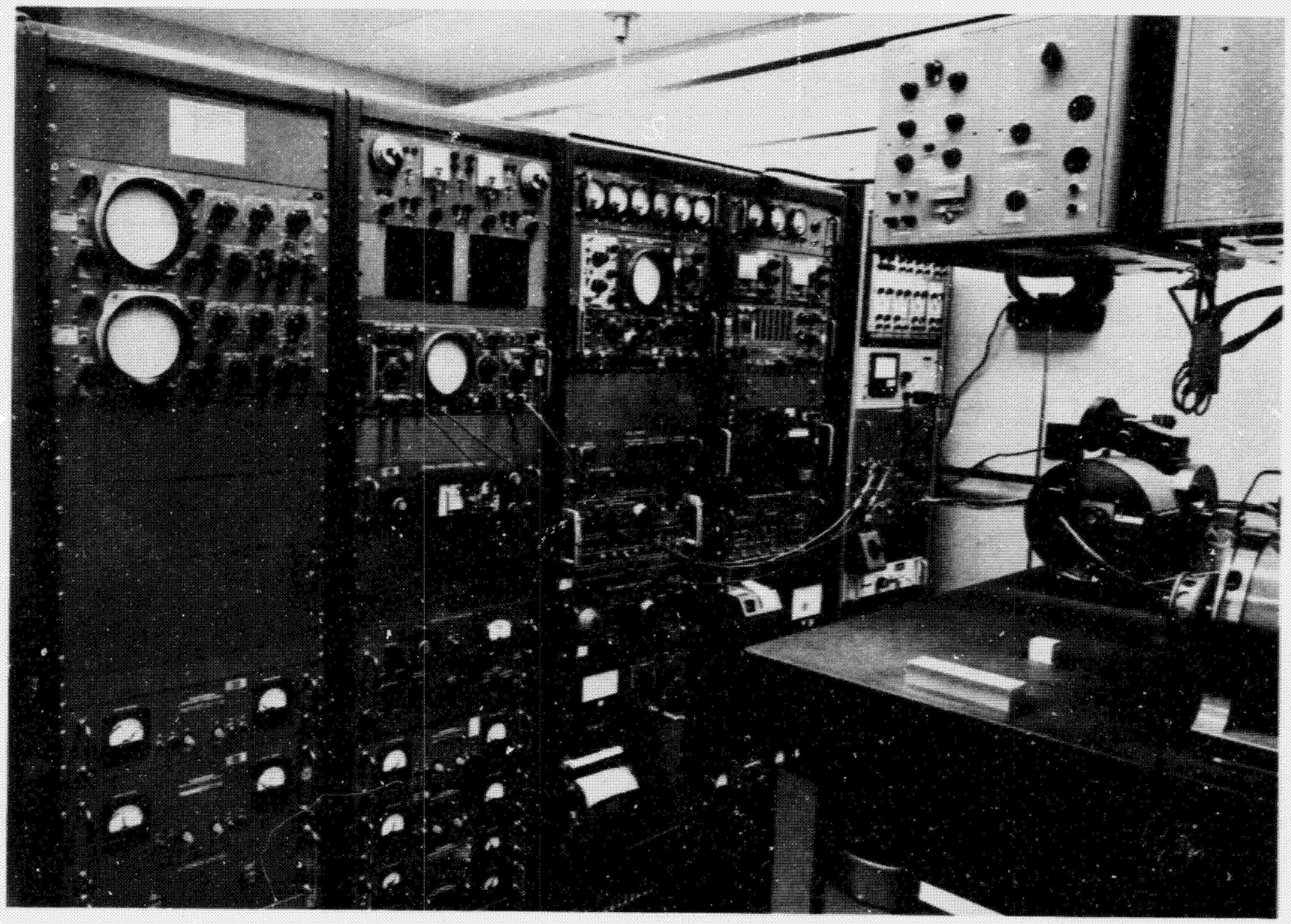

Fig. 3.4-6 PM PIP laboratory area.

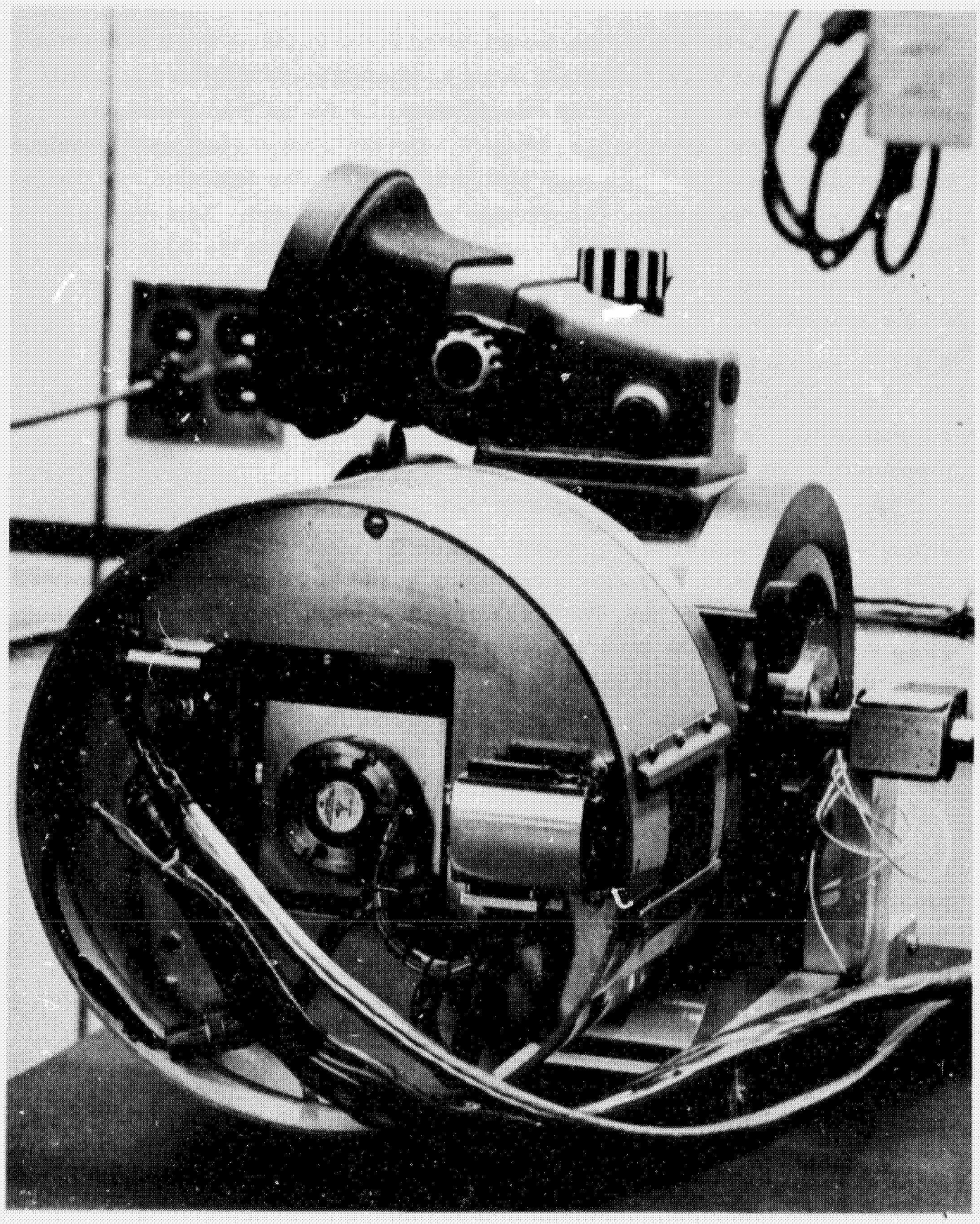

Fig. 3.4-7 Close-up of PM PIP and test fixture.

Apollo PIP, magnetic shields are incorporated in the instrument. It is doubtful that any significant noise reductions would be attainable from further magnetic shielding improvements. Further investigation of optimum lead placement and shielding might prove more productive. Development of electronic techniques to desensitize the control loop from switching noise is also desirable. A change in the test-loop mechanization is currently being implemented. This change reverses the timing sequence of the control-loop logic so that the SG voltage-level detection and interrogation occurs prior to any current changes in the torque generator.

3.4.6 Scale Factor and Bias Stability

Detailed tests were conducted on two instruments, units 9 and 14. A discussion of the test equations and technique as well as the test results are presented in this section.

The accelerometers' performance characteristics that were most critically evaluated are the instrument bias and scale factor stability. The scale factor (SF) was defined in (3.4.7) and corresponds to an equivalent indicated velocity measurement increment, ΔV. The bias term, A_b, results from torques acting along the pendulous input axis. These torques arise from non-ideal geometric aspects of the physical instrument (i.e., suspension and SG reaction torques). The bias torque is generally expressed as an equivalent acceleration of the pendulous mass. For a given instrument the indicated velocity change differs from the true velocity change by the time integral of the bias.

Guidance system performance is governed in large measure by the accuracy of the measured velocity change. For each system, therefore, it is common practice to determine each accelerometer's scale factor and bias to calibrate the system accordingly. Ultimate system performance is then dependant upon one's ability to define the instrument's scale factor and bias. Techniques may be developed to minimize errors in the test measurement of these parameters so that the uncertainties correspond to the basic stability of the instrument and control loop.

Stability test data are presented for both instruments in Figs. 3.4-8, -9, -10. This performance represents the probable limit for the instrument and electronics design. The data were obtained under well-controlled laboratory environment and test conditions. Some of the special setup considerations, as well as the noise coupling and thermal sensitivity problems that hindered obtaining consistent data of this caliber, were described in the

PM PIP #9 10 AP 67

1g INPUT 3200 CPS INTERROGATION RATE

PREST = 30,00 ΔV's

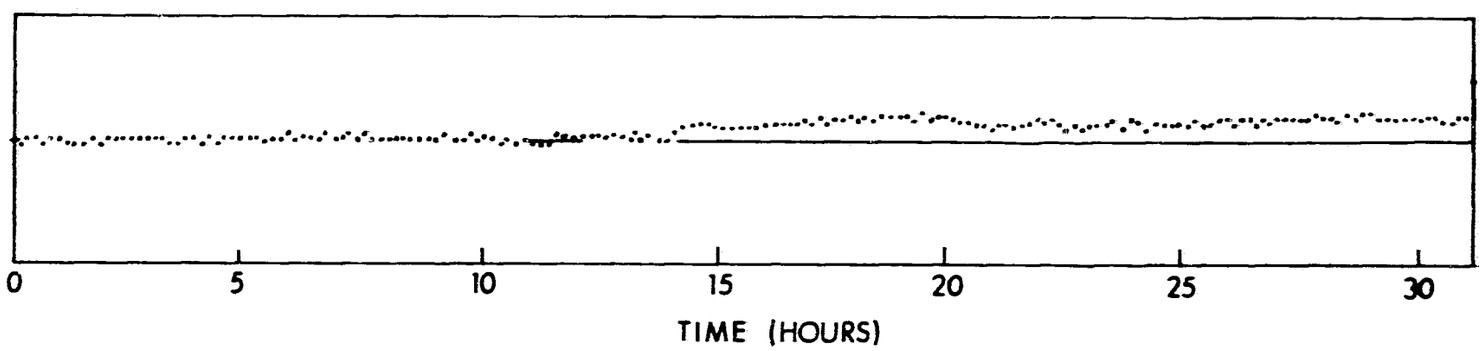

Fig. 3.4-8 PIP scale factor stability vs time.

PM PIP #14

1g INPUT 3200 CPS INTERROGATION RATE

PRESET ≡ 112,530 ΔV's

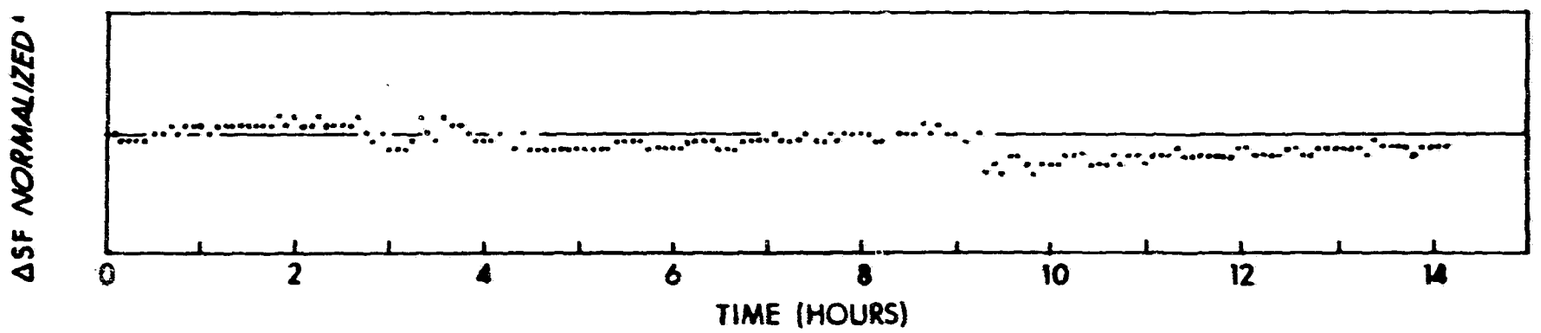

Fig. 3.4-9 PIP average scale factor stability vs time.

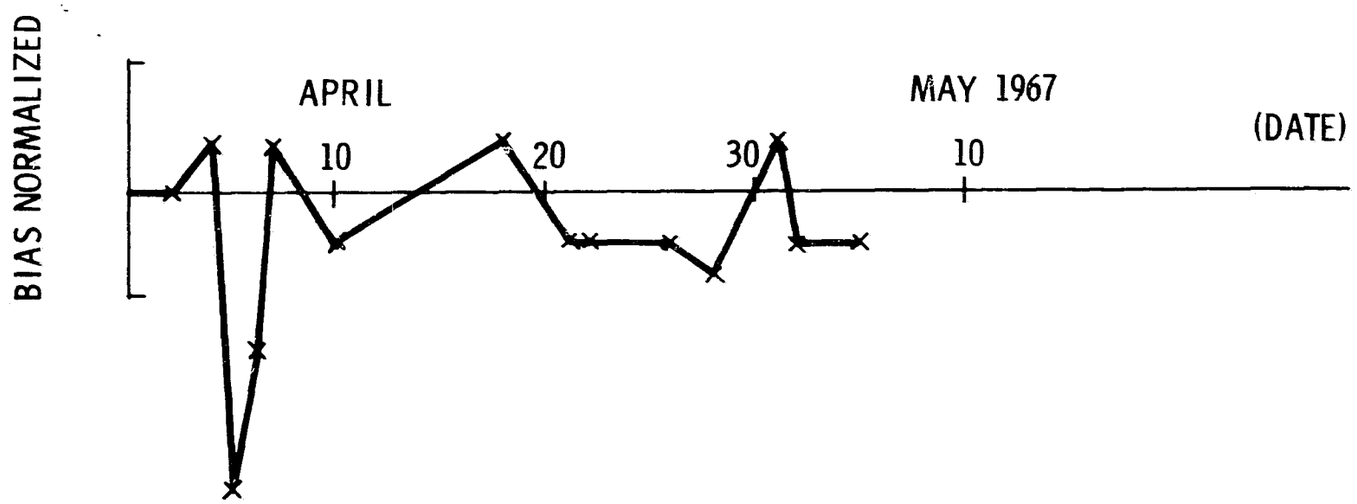

Fig. 3.4-10 Bias stability vs time, PM PIP #9 (9600 pps interrogation rate)

previous section. Repeatable data of this quality were attainable, however, through the implementation of standardized procedures and vigorous attention to all test-technique details.

A fuller appreciation of the measurement accuracy and the meaning of the test data is attained by considering some details of testing and the associated data-reduction derivations. Fundamental to accelerometer testing is the orientation of the instrument with respect to the local gravity vector. With the instrument input axis aligned for a positive one-g input, the relationship between the time (τ_1) to accumulate a selected number of corresponding +ΔV pulses is:

$$\frac{X\,(SF_1)}{\tau_1} = g + A_b \qquad (3.4.9)$$

where

X equals the number +ΔV pulses selected,

SF_1 is the positive scale-factor constant corresponding to the magnitude of the incremental velocity represented by each +ΔV pulse for +IA alignment with the g vector. (See equation and the discussion in the previous section.)

A_b is the true PIP bias expressed in the same dimensions as the gravity term, "g"; it is the bias term which exists at both open- and closed-loop operation when the instrument is at a null.

Recall that the test time (τ_1) can be related directly to the number of clock cycles (interrogator pulses) that occur during the accumulation of X ΔV's

$$\frac{N_1}{F} = \tau_1 \qquad (3.4.10)$$

where:

F = the clock interrogation frequency

N_1 = the number of interrogation pulses during the count interval of X-positive ΔV's.

Assuming a 3200-cps interrogation rate (used for test results shown) and substituting (3.4.10) into (3.4.9)

$$\frac{3200\,(SF_1)\,X}{N_1} = g + A_b \qquad (3.4.11)$$

In general, instrument nonlinearities exist that yield a scale-factor difference between positively- and negatively-applied torque pulses (discussed in detail in Section 3.3). Thus if the instrument input axis were aligned in a negative sense with respect to the local "g" vector, and if X number of ΔV counts were accumulated, the following relationship would result:

$$\frac{-3200\ (SF_2)\ X}{N_2} = (-g + A_b) \qquad (3.4.12)$$

In this case

X equals the number of $-\Delta V$ pulses selected

SF_2 is the negative scale factor constant represented by each $-\Delta V$ pulse for a -IA alignment with the g vector

N_2 is the number of interrogation pulses during the count interval of X $-\Delta V$ pulses.

By manipulating (3.4.11) and (3 4.12) to solve for SF_1 and SF_2 and then by adding, the resultant solution allows representation of the average scale factor (SF_{avg}) in the form:

$$SF_{avg} = \frac{SF_1 + SF_2}{2} = \frac{g}{6400}\ \frac{(N_1 + N_2)}{X} + \frac{A_b}{6400}\ \frac{N_1 - N_2}{X} \qquad (3.4.13)$$

For a precision instrument such as the PM PIP the bias value is very small (less than 0.2-dyn-cm torque) compared to the specified test input and, similarly, the scale-factor difference should not yield a significant difference in interrogator pulse counts. The average scale factor may be approximated, therefore, to a very accurate degree by

$$SF_{avg} = \frac{g}{6400}\ \frac{N_1 + N_2}{X} \qquad (3.4.14)$$

For example, if we assume relatively large values of bias and scale-factor differences, A_b equal to 0.02% of g, and the interrogator count differed by 1%, the percentage error in a SF_{avg} determination using (3.4.14) would correspond to two parts per million.

Another test derivation is obtained by adding (3.4.11) and (3.4.12)

$$2A_b = 3200\left[SF_1\ \frac{X}{N_1} - SF_2\ \frac{X}{N_2}\right] \qquad (3.4.15)$$

The right-hand side of the above equation can be manipulated to obtain

$$2A_b = 3200 \left[\frac{SF_1 + SF_2}{2} \left(\frac{X}{N_1} - \frac{X}{N_2} \right) + \frac{SF_1 - SF_2}{2} \left(\frac{X}{N_1} + \frac{X}{N_2} \right) \right] \qquad (3.4.16)$$

Because $\frac{SF_1 + SF_2}{2}$ is the average scale factor and $(SF_1 - SF_2)$ represents the difference in scale factor (ΔSF), (3.4.16) may be rewritten in the following form

$$A_b = 1600 \left[SF_{avg} \left(\frac{X}{N_1} - \frac{X}{N_2} \right) + \frac{\Delta SF}{2} \left(\frac{X}{N_1} + \frac{X}{N_2} \right) \right] \qquad (3.4.17)$$

Now, substituting (3.4.14) into (3.4.17) and combining fractions

i.e.: $\left(\frac{1}{N_1} - \frac{1}{N_2} \right) = \frac{N_2 - N_1}{N_1 + N_2}$, etc.) we obtain:

$$A_b = 1600 \left[\frac{g}{6400} \frac{(N_1 + N_2)(N_2 - N_1)}{N_1 N_2} + \frac{\Delta SF}{2} \left(\frac{N_1 + N_2}{N_1 N_2} \right) X \right] \qquad (3.4.18)$$

Additional simplifications can be obtained by introducing the relationship

$$N_{avg} = \frac{N_1 + N_2}{2} \qquad (3.4.19)$$

where

$$N_1 = N_{avg} + \delta$$

$$N_2 = N_{avg} - \delta$$

substituting in (3.4.18)

$$A_b = 1600 \left[\frac{2g\ N_{avg}\ \delta}{6400(N_{avg}^2 - \delta^2)} + \frac{\Delta SF\ N_{avg} X}{N_{avg}^2 - \delta^2} \right] \qquad (3.4.20)$$

dividing numerator and denominator by N_{avg}^2

$$Ab = 1600 \left[\frac{2g\ \delta / N_{avg}}{6400 \left[1 - \left(\frac{\delta}{N_{avg}} \right)^2 \right]} + \frac{\Delta SF\ X / N_{avg}}{1 - \left(\frac{\delta}{N_{avg}} \right)^2} \right] \qquad (3.4.21)$$

Since N_1 and N_2 will always be within a few hundred parts per million, the term $\left(\frac{\delta}{N_{avg}}\right)^2$ can be considered negligible and (3.4.21) reduces to

$$A_b = g\left[\frac{N_1 - N_2}{N_1 + N_2}\right] + \Delta SF\left[\frac{X}{\frac{N_1 + N_2}{2}}\right]1600 \qquad (3.4.22)$$

Referring back to (3.4.14) we note that:

$$\frac{X}{N_1 + N_2} = \frac{g}{6400\ SF_{avg}} \qquad (3.4.23)$$

Substituting (3.4.23) into (3.4.22), we obtain:

$$A_b = g\left[\left(\frac{N_1 - N_2}{N_1 + N_2}\right) + \frac{\Delta SF}{2SF_{avg}}\right] \qquad (3.4.24)$$

A_b in (3.4.24) represents the bias measurement determined from a +one g and -one g count. This may be defined as the "count bias" and is exactly equal to the true bias if the scale factor difference is zero.

One should note that (3.4.24) and (3.4.14) were derived for a ±one g count. They would be applicable for other test orientations if g sin θ were substituted in the equation and θ were restricted such that g sin $\theta \gg$ ab (i.e., $N_1 - N_2 \ll N_{avg}$). With this restriction count bias determinations will differ from the true bias by a constant.

We may determine the instruments true bias with a precision dividing head (optigon B) that is used to accurately orient the instrument to obtain an absolute signal generator null. The bias determined in this manner is referred to as the null bias, a_b. At the null orientation the relationship between the bias and the angle between the sensitive input axis and the local gravity vector is shown in equation (3.4.25).

$$a_b + m\ell g \sin\theta = 0 \qquad (3.4.25)$$

The magnitude of a_b determined from the null bias tests may then be used in (3.4.22) or (3.4.24) to obtain the ± scale factor or scale-factor linearity ($\Delta SF/SF$), respectively.

Since the position of the sensitive axis of the instrument with respect to the dividing-head readout scale zero may differ by some small consistent

angle, two orientation readings are used for each null bias determination. Input axis orientation pairs (R_1 & R_2 or R_1' & R_2') for which null readings may be obtained (dependent upon the sense of the bias) are shown in Fig. 3.4-11.

The "R" corresponds to the optigon B scale reading. For the case illustrated R_1-R_2 and R_1'-R_2' correspond to a negative and positive bias respectively. For the test setup the magnitude of θ is then:

$$|\theta| = \frac{(R_2 - R_1) \pm 180^\circ}{2} \qquad (3.4.26)$$

The maximum error in the R_2-R_1 with the optigon B used in testing is approximately 7 seconds of arc (consisting of 4-second scale error and a 3-second operator repeatability error). The head error is essentially constant for a specific test setup. Bias stability measurement uncertainty is, therefore, governed by operator repeatability errors and at a maximum corresponds to 1.5 arc seconds in the determination of θ. The error determination of the absolute null bias, however, will also influence the error in determination of the scale-factor difference (ΔSF) in (3.4.23). For example, a 3.5-arc-second uncertainty in null bias determination corresponds to approximately a 36-ppm error in the determination of ΔSF in an instrument scaled for 18g capability at a 3200-cps interrogation rate.

From 16 PM PIP test observations it would appear that the Apollo PIP dividing head readout accuracy limitations can introduce a significant uncertainty in the determination of the PM PIP's absolute performance characteristics. System application requirements that necessitate the ultimate knowledge of the instruments performance potential will necessitate an improved orientation readout capability (resolution of 0.25 arc seconds with a maximum run-out accuracy of 2 arc seconds would, for example, reduce performance measurement uncertainties by three).

3.4.7 Moding and Double-Pulsing

As previously noted in the "Test Setup" discussion, noise coupling between the torquer and signal generator lines was observed and could not be completely eliminated. During closed-loop pulse-torque-to-balance operation, coupling tended to cause a "double-pulsing" or "moding" phenomena.

Double-pulsing is the term used to describe operation in which, following a normal torque command, an additional erroneous pulse of the same polarity would occur. Stable ternary operation is retained, however, since the discriminator (zero-torque region) dead zone was set sufficiently wide so that the additional pulse did not drive the float through the dead zone to the opposite

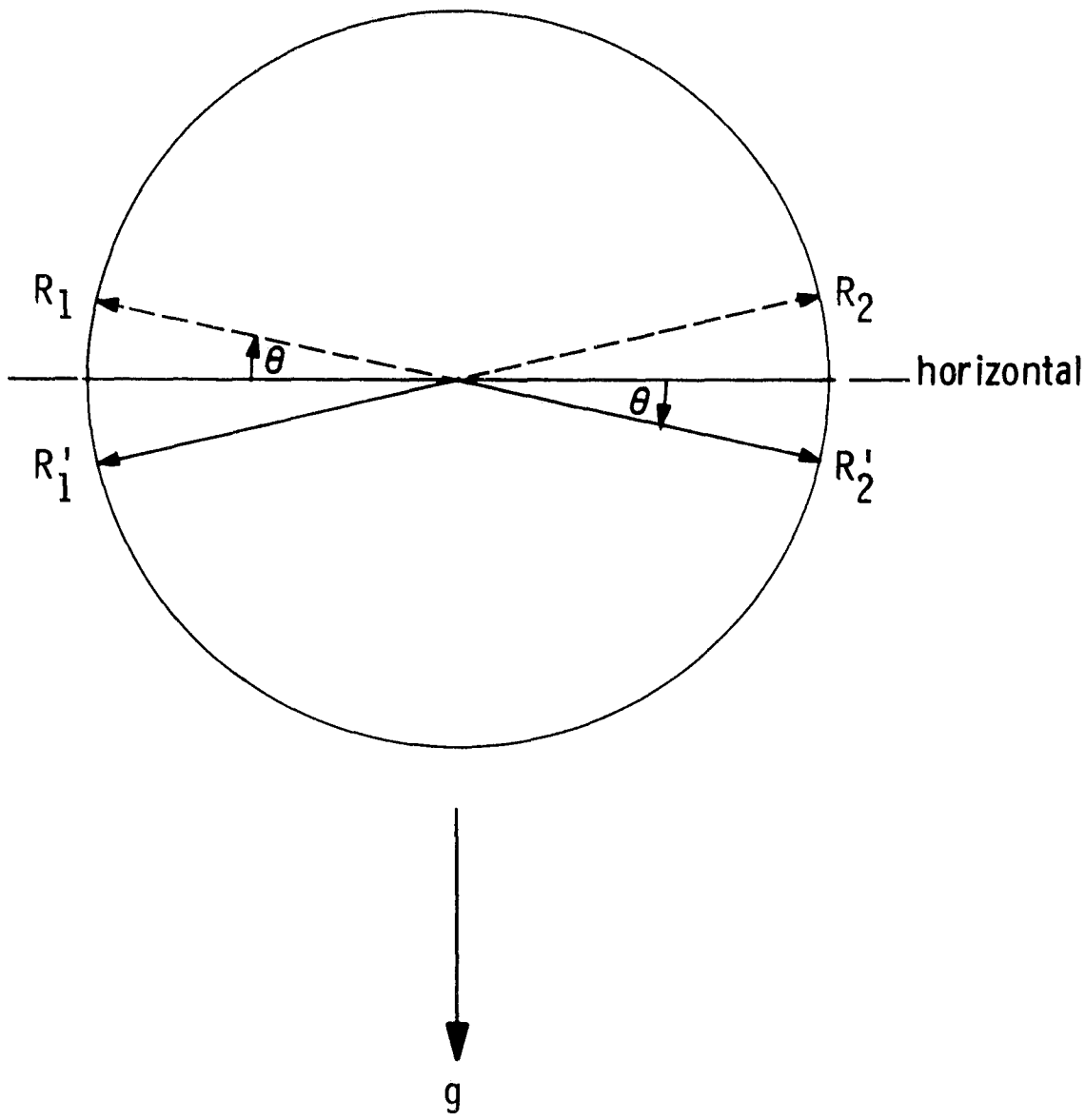

Fig. 3.4-11 Bias measurements - input axis orientations.

polarity torquing threshhold. Figure 3.4-12A attempts to illustrate the double-pulsing phenomenon. For this illustration it is assumed that a sizable amount of the float rotational response to a torque pulse occurs before the next interrogator pulse (this is essentially true for a 3200-cps interrogation rate). Figure 3.4-12B shows the float motion and corresponding output for some fixed input A_{in} (less than the restraining loop torque capability). We observe that some steady-state float offset from null occurs which is proportional to the ratio of the input pendulous torque to the total full-on torque command capability. In Fig. 3.4-12B we observe that, for the same input (in this case equal to approximately 50% of the instrument capability), the float tends to return to the same offset position. At the next interrogation time, however, the presence of noise (due to the previous torque current pulse) causes an additional pulse command to be triggered and, similarly, additional float motion. If one were to count interrogation pulses N_1 (3.4.14) for a preset ΔV pulses, dependent on the test-setup initial starting point, variations in the interrogation pulse count would occur. These counts would then be used to determine the average scale factor for each test run and a corresponding change would be obtained. Thus, erroneous scale-factor stability data would be generated.

In actual operation, possibility of three distinct interrogator counts could be accumulated for a given number of ΔV's. The particular count obtained is dependent on the test synchronization of the interrogation pulse count in relation to the ΔV pulse train. A detailed quantitative derivation of the count instability in relation to double-pulsing is presented in Appendix B of this chapter.

When the ternary control-loop zero-torque-command dead zone is too small to accomodate the float rotation due to an additional torque pulse, "Moding" results. Dependent upon the test input and the loop parameters the additional torque pulse caused by noise coupling may drive the float through the dead zone and trigger the opposite polarity torque command. Binary type operation may result in intermittent or continuous 1:1, 2:3, etc., moding. Since, for a specific test condition, only a single-polarity ΔV is used for the preset counter gate control and the occurance of moding results in an abrupt shift in the interrogator count, moding can be eliminated by increasing the control loop dead zone. This, however, results in a system inaccuracy due to the increased float velocity storage.

3.4.8 Frequency of Interrogation

In the strapdown application, the velocities measured in the body frame must be transformed through the attitude matrix in the computer into the inertial frame. Because of the time-varying nature of the attitude matrix and the

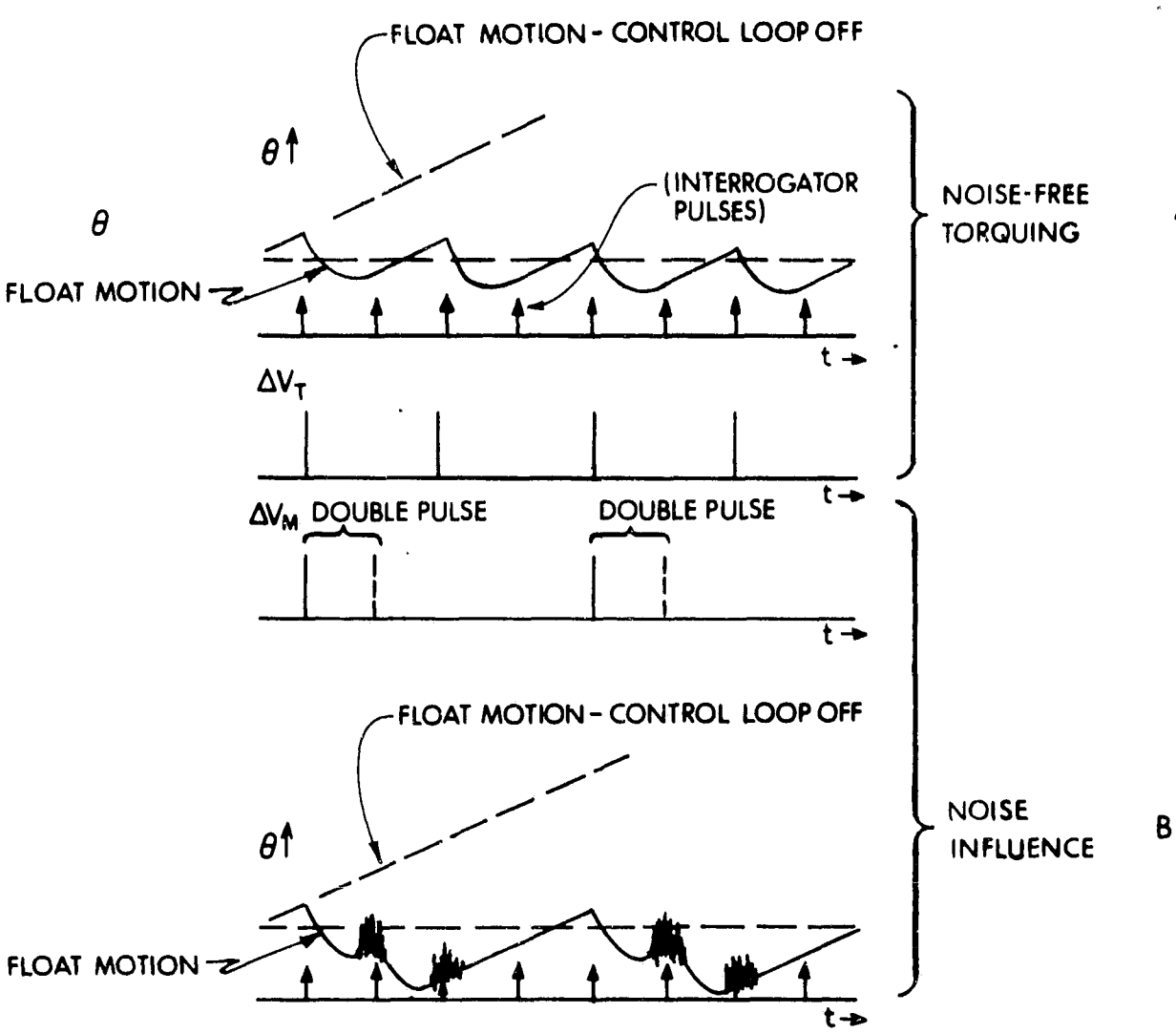

Fig. 3.4-12 Double pulsing.

iterative characteristics of the numerical transformation, consideration of smaller velocity increments would appear desirable for improved system performance. For the same instrument range capability, increasing the interrogation rate of the pulse torque-to-balance control test-loop results in correspondingly smaller torque pulse widths and, therefore, in finer velocity quantization. Since the test loop operates on an error detection at the peak of the SG carrier signal, only integer ratios of interrogator to carrier frequency are possible.

The previous test results were obtained with a 3200-cps interrogation rate which, for an 18g capability, corresponds to approximately a 5.5-cm/sec-per-pulse scale factor. Experimental tests were conducted using both 4800- and 9600-cps interrogation rates with corresponding scale factors of 3.6- and 1.8-cm/sec pulse, respectively. In the 3200-cps 1-g tests the double-pulsing could be eliminated; however, at 4800-cps, test conditions could not be obtained for which double-pulsing did not occur occasionally. At 9600-cps, random double-pulsing was always evidenced. The increased noise sensitivity at higher interrogation rates results from the instrument float response limitations. As discussed in Chapter 2, the float rotational response to a torque pulse is primarily limited by its time constant. If the torque pulse width is set approximately equal to the time interval between interrogation pulses, for a 3200-cps interrogation rate, over 80% of the total float rotational travel will have occurred for a single torque pulse before the next interrogation pulse. At 9600-cps, however, only approximately 55% of the total travel will have occurred. Thus, in the dynamic 1-g, 9600-cps test, more noise susceptibility exists since a prior torque-pulse command does yield as large a voltage margin between the torquing threshold level and the SG output signal.

A SF stability run taken at 9600-cps interrogation frequency conditions under test conditions in which a minimum of double-pulsing occurred is shown in Fig. 3.4-13. Note that poorer stability performance was obtained when compared to a 3200-cps test run (Fig. 3.4-8). The difference in performance probably stems from both the double-pulsing phenomenon as well as an increased scale-factor sensitivity to torque pulse width stability at the higher interrogation frequency.

A control-loop design change to reduce noise coupling effects and minimize, if not eliminate, multiple pulsing is under development. Further investigation into the instrument harnessing design would also be advisable. As for the need for higher interrogation rates, this determination is primarily influenced by mission objectives and the computational errors associated with the coordinate transformation processing. It would be desirable to extend the integrated

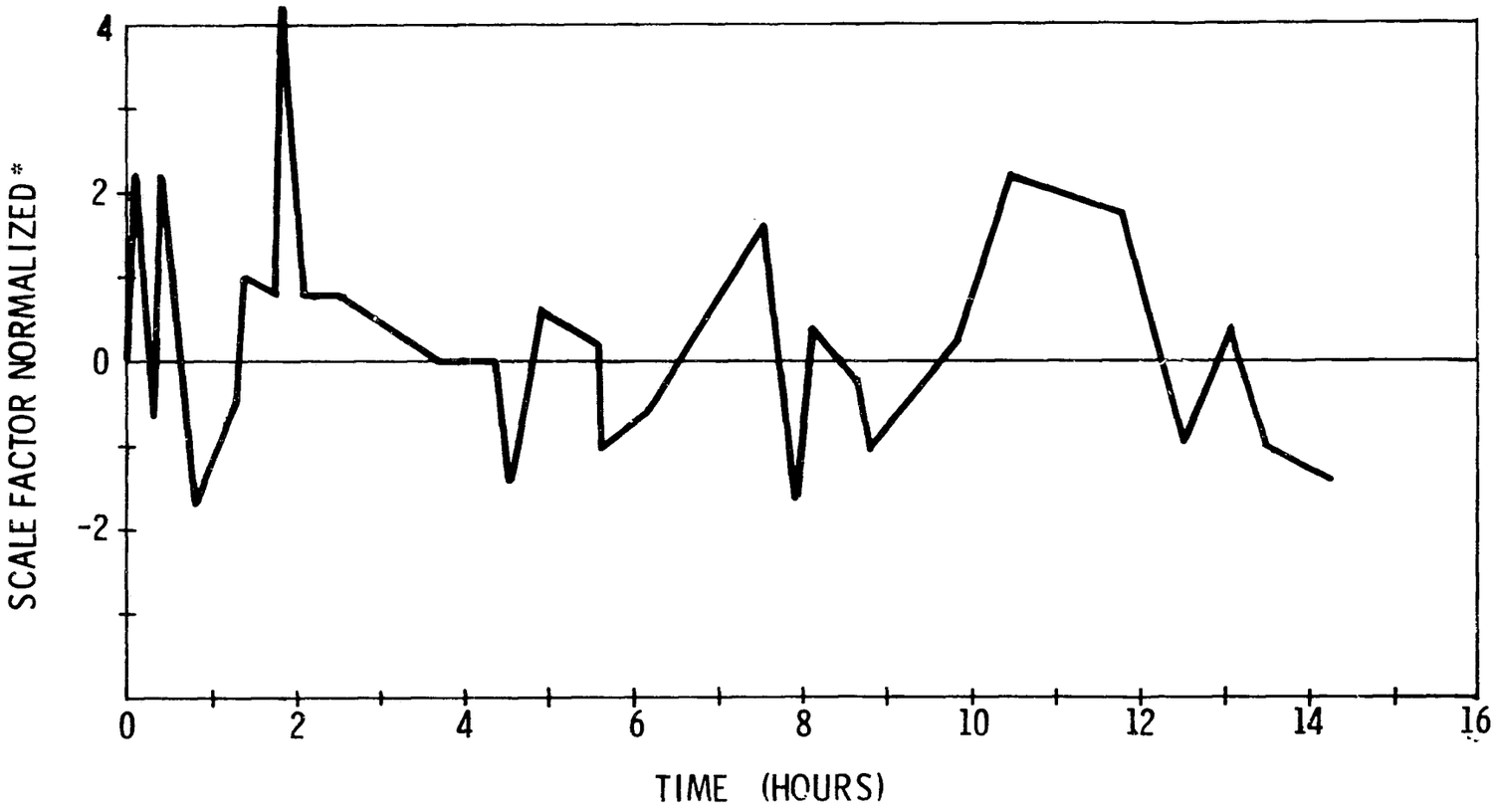

Fig. 3.4-13 Stability run, PM PIP #14, 9600 Hz, September 1967.

attitude algorithm and gyro test package study to investigate their interplay with accelerometer performance and data processing.

3.4.9 Sensitivity Testing

PM #9 was subjected to a limited number of tests to determine scale factor and bias sensitivities to turn-on and turn-off sequences and to typical malfunctions.

Figure 3.4-14A shows the results of a stop-bias hysteresis test. This test is used to determine peak-to-peak bias variations resulting from excursions of the float into the plus and minus rotary stops. The test had little affect on scale factor. The affect on bias is attributable to a change in the magnetic state of the suspension rotor due to rotation through the magnetic field produced by the suspension coils. The null and one g bias numbers shifted equal amounts, indicating that the scale factor difference remained constant during the course of the test.

Figure 3.4-14C shows the affects on bias due to turning off the 27V to the current switch, the 4V excitation to the suspension and SG microsyn, and the 30V main power to the Pulse Torquer Power Supply.

Figure 3.4-14B also shows the affects of torquing the float alternately into the plus and minus stops. Here, as in the case of the stop-bias hysteresis test, the only affect seen is the change in bias due to the rotation of the float into the stop.

Affects due to changes in 4V excitation and quadrature were also investigated. The scale factor was found to vary 2 ppm per 1% change in excitation near the normal operating point. Quadrature changes had no affect unless very high levels were reached (approximately 5V p-p).

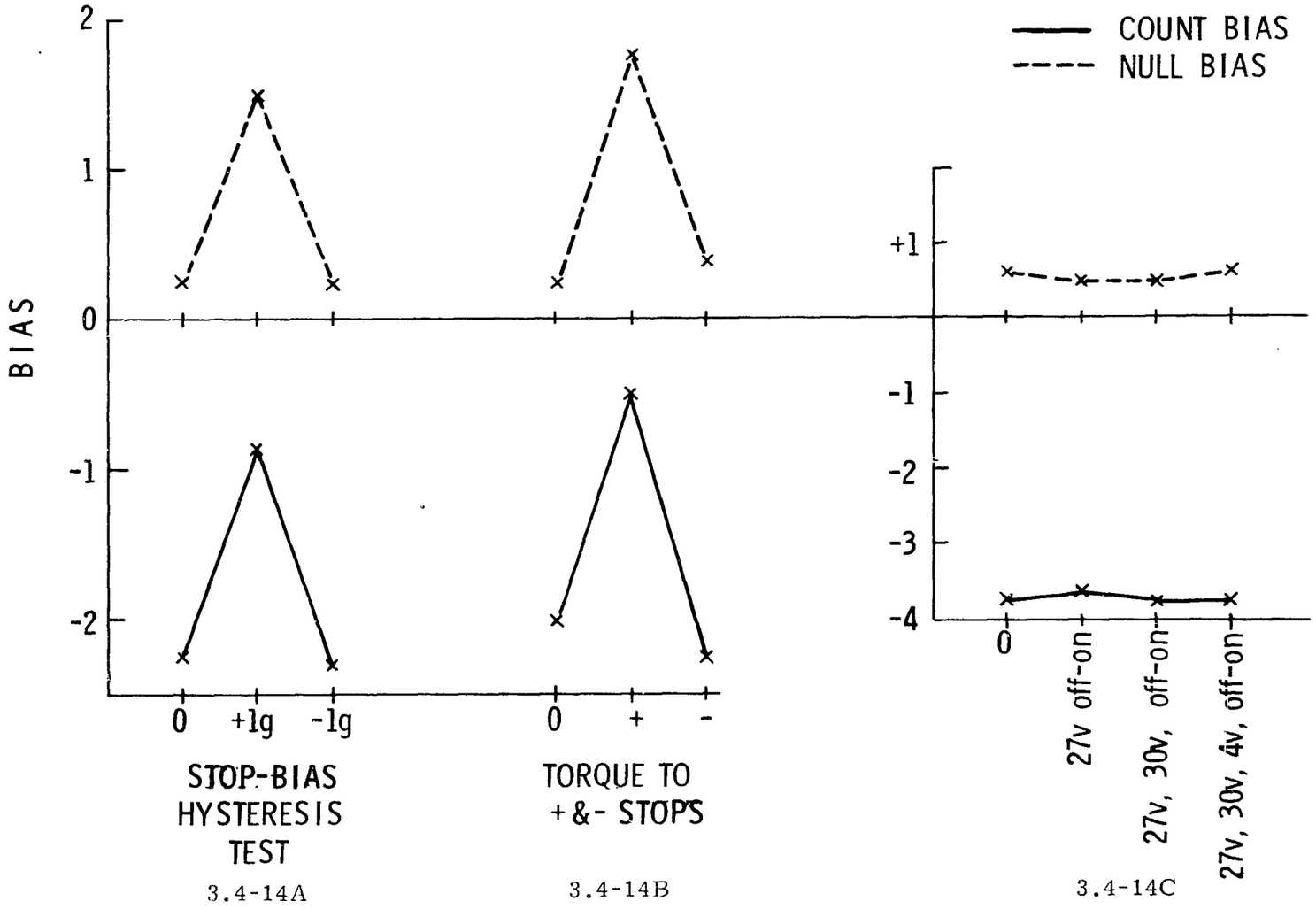

Fig. 3.4-14 Bias variations vs test sequence PM PIP #9, July 1967.

4 BODY MOUNTED TEST PACKAGE AND REAL-TIME ALGORITHM TEST AND EVALUATION

4.1 Introduction

The objective of this test evaluation program is to define the operational capabilities and limitations of strapdown system performance and thereby provide a basis for development of a body-mounted system configuration for advanced manned missions.

Clearly, to achieve the evaluation objective, the basic test tools (hardware and software) and a test sensor package with support electronics must be developed. The sensor package should incorporate state-of-the-art instruments and the electronics should allow a flexible investigation of different quantized torque rebalance levels and sampling rates. Similarly, a real-time computational facility and sensor package interface should be devised to allow investigation of a variety of algorithms at various computational update rates. Within the framework of these activities, support equipment must be mechanized to allow both precision static and dynamic inputs and to provide detailed component performance and environment monitoring.

The major activity through this reporting point, therefore, has been devoted to the development of hardware, facilities and test plans to fulfill the test evaluation objectives. For the most part, the design and fabrication effort has been completed and the total facility and test package integration is in its early stages of checkout. Because of funding limitations, the initial development effort was restricted to a gyro sensor package and attitude algorithm evaluation. Provisions for the addition of accelerometers were included, however. The initial stages of sensor performance testing should commence shortly, pending availability of gyros. Facility capabilities for 0.3-rad/sec multi-axis slew rates and up to 10 cps-10 arc-min peak-to-peak oscillatory inputs are operational. Real-time computational test programs for both 1st and 3rd order quaternion attitude algorithms have been defined and will undergo preliminary test verification.

The major sections of this chapter describe the following areas:

1. Design and Development of a Body-Mounted Inertial Sensor Test Package,
2. The design features of the pulse torque control loop and power supply electronics,

3. Development of Real-Time-Algorithm Computational Capabilities for Integrated System Testing,

4. Static and Dynamic Sensor Package and Integrated Test Concepts and Procedure Development,

5. Design and Development of Strapdown Sensor Package Ground Support Equipment.

4.2 Summary

The following is a brief summary of salient features of the body-mounted test package and real-time test facility (see Figs. 4.2-1, -2).

A) Gyro Package Assembly

The gyro package contains three 18-IRIG MOD B gyros, each mounted in an adjustable alignment mount assembly. Each gyro axis compliment includes an individual temperature controller, SG preamplifier, quadrature trim-potentiometer and magnetic suspension hardware. These components are mounted on an aluminum frame whose form factor allows it to be substituted for an Apollo IMU inner gimbal for special dynamic tests. An optical reference cube is mounted on the frame and used both as a reference to which the gyros are aligned and as a means of aligning the test package to the test table.

The frame is attached to a 4-axis test table via a high thermal resistance, adjustable alignment plate. Frame temperature is precisely maintained by a heat exchanger mounted adjacent to the thermal shroud enclosing the system. A thermostat located on the frame controls the flow of liquid coolant through three parallel coolant passages on the frame.

B) Support Electronics Console (SEC)

The circuitry housed in this console fulfill the electronic functions associated with basic self-contained system operations.

The major elements are:

a) Three-axes of ternary pulse-torque rebalance loops. Each loop has a variable torque rate capability (a submultiple of 9600 Hz). The present maximum torque rate is 0.3 rad/sec.

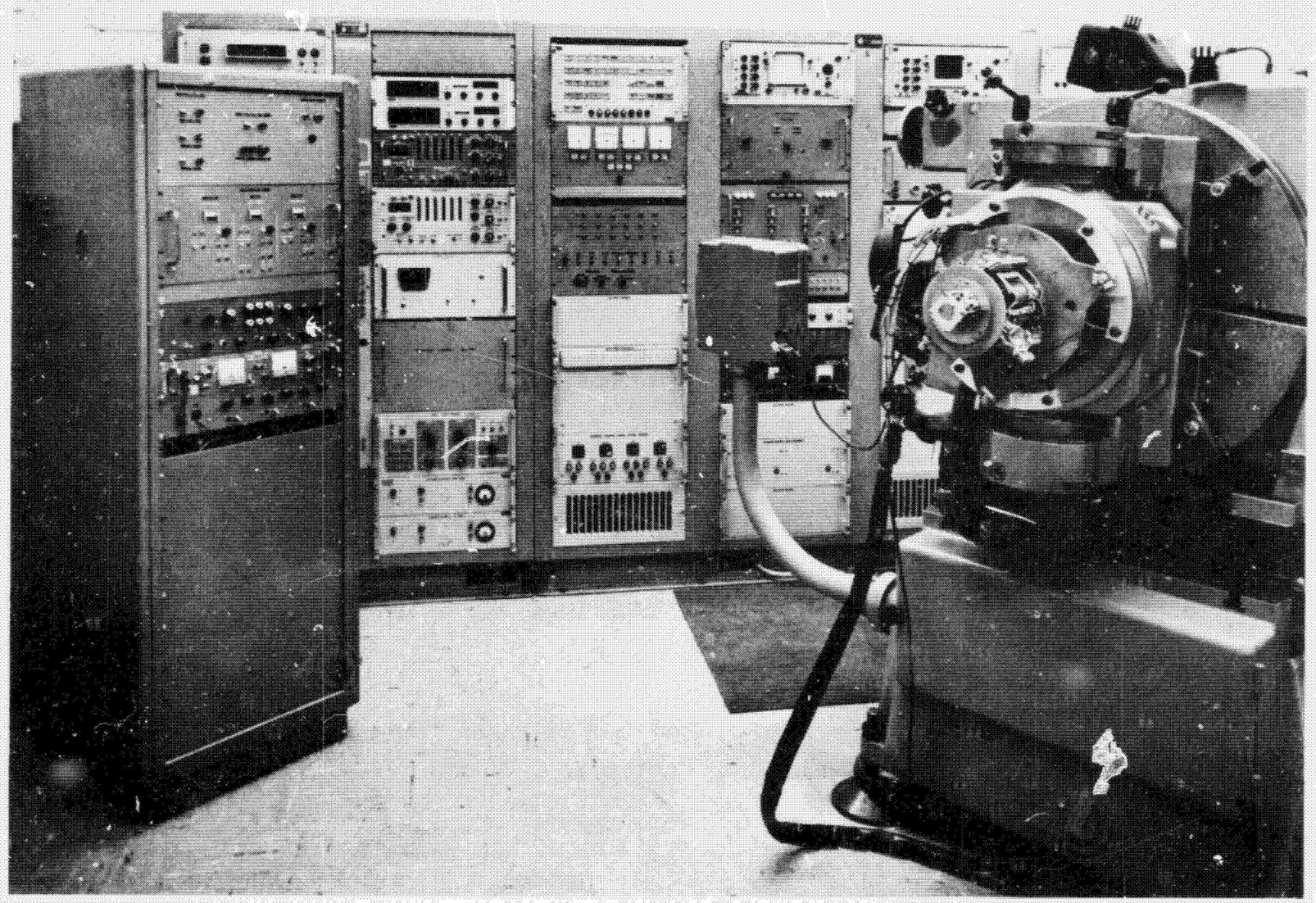

Fig. 4.2-1 Body-mounted real-time test facility.

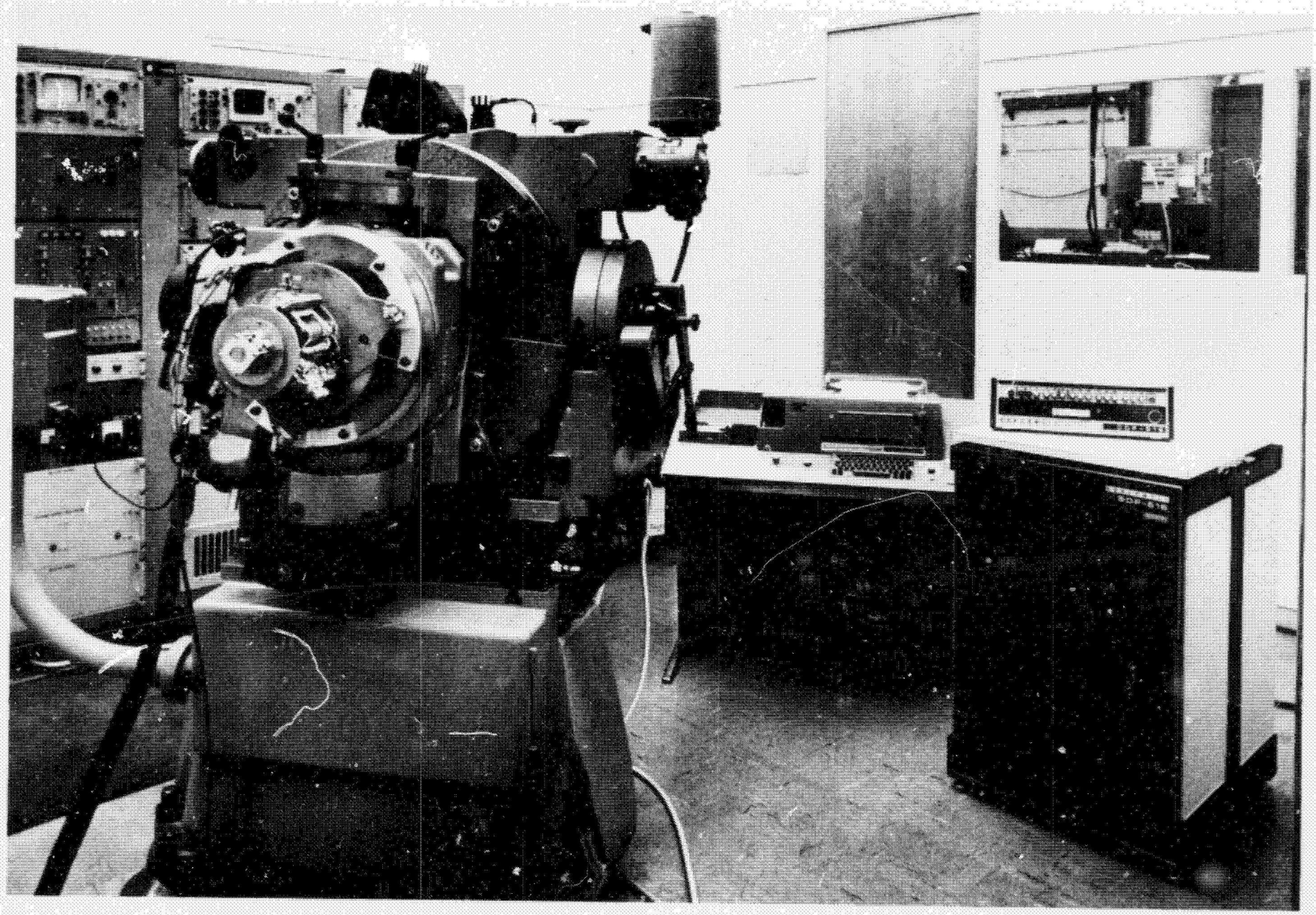

Fig. 4.2-2 Body-mounted real-time test facility.

b) 800-Hz gyro wheel supply

c) 9600-Hz Ducosyn excitation supply

d) ± 15-Vdc Power Supply for the individual gyro temperature controllers.

In addition, a Manual dc Torque circuit is included for use in gyro IA misalignment angle determinations.

C) Precise Test Input Table

A four-axis table configuration with positioning accuracies up to 2 arc-seconds is utilized for both static and limited dynamic testing. Constant rates to 1.0 rad/sec and oscillatory frequencies up to 10 Hz can be utilized about two of the four table axes.

D) 3-Axis Dynamic Test Inputs

Use of the gyro package frame in a modified Apollo gimbal system will allow 3-axis rate and oscillatory drive capabilities for extreme environmental testing.

E) Real-Time Algorithm Computation

A Honeywell DDP-516 Computer with an 8K word memory and a 0.96-μsec memory cycle time is interfaced with a gyro-torque pulse accumulator. This system will be used for both gyro parameter evaluation and for integrated real-time attitude-transformation algorithm testing. Both high-order whole number type algorithms and a simulated DDA processing will be programmed and evaluated.

F) Ground Support Equipment (GSE)

The GSE performs the following functions:

a) Gyro Package mode control; i.e.; standby, wheels-on and pulse torque loop moding. Safety interlocks for proper gyro temperatures and excitation voltages are included.

b) Signal Monitoring - gyro and frame temperatures, critical pulse torque voltages, clock frequencies and gyro error signals.

c) Pulse Torque ($\Delta\theta$) Data Acquisition - preset counters, timers, storage registers, printers and tape punch are all utilized to obtain gyro pulse counts and timing required for instrument level data performance analysis.

G) Optical Alignment References

An azimuth heading accurate to 5 $\widehat{sec}$ is provided by a permanently mounted porro prism. Fixed targets consisting of Davidson 2" aperture autocollimators will be mounted along an east and north line, respectively. These targets will be used in conjunction with the porro prism for gyro package alignment.

4.3 Test Package and Supporting Hardware

4.3.1 General Considerations

The developmental gyro test package consists of three frame mounted 18-IRIG MOD B gyros with their alignment hardware and associated electronics (Figs. 4.3-1 and 4.3-2).

The 18 IRIG MOD B is a single-degree-of-freedom integrating rate gyro. It has been specifically developed for strapdown applications and has a permanent magnet torquer that is sized to be compatible with input rates of up to one radian per second. A complete description of instruments' design details, performance parameters and data is included in Chapter 3, Section 3.

The frame form factor has been designed to allow it to replace the stable member of a prototype Block II Apollo gimbal system. This provision was made so that body-mounted test evaluations could be conducted with extremely high simultaneous three-axis slew and oscillatory inputs. The gimbal system control electronics will be modified so that they can be externally positioned for various test sequences (dynamic inputs up to 50 cps with one degree excursion are anticipated). This gimbal system adaption provides an ideal multi-degree-of-freedom test table configuration, i.e.: low-noise slip rings assemblies, multispeed resolver readouts, and a controlled thermal environment.

For basic high accuracy position and rate inputs, consistent with component performance determination and typical mission altitude maneuver rates, a four-axis test table will be used (Fig. 4.3-3). The table configuration consists of a 16", two-degree-of-freedom precision control table mounted on a larger 32" two-degree-of-freedom table. Both table rotary axes are equipped with variable rate drives. As shown in Fig. 4.3-4 the frame mounts on a titanium plate, which in turn is mounted to the 16" table via 3 leveling adjustments.

4.3.2 The Frame and Fixtures

A reference alignment cube is mounted on top of the frame. The cube faces representing the X, Y, and Z triad are orthogonal within 1 arc-second. The leveling provisions on the titanium mounting plate are provided to allow precise alignment of the top cube face with respect to rotational rate input vector of the lower table rotary axis. The gyro input axes are aligned with respect to the appropriate cube

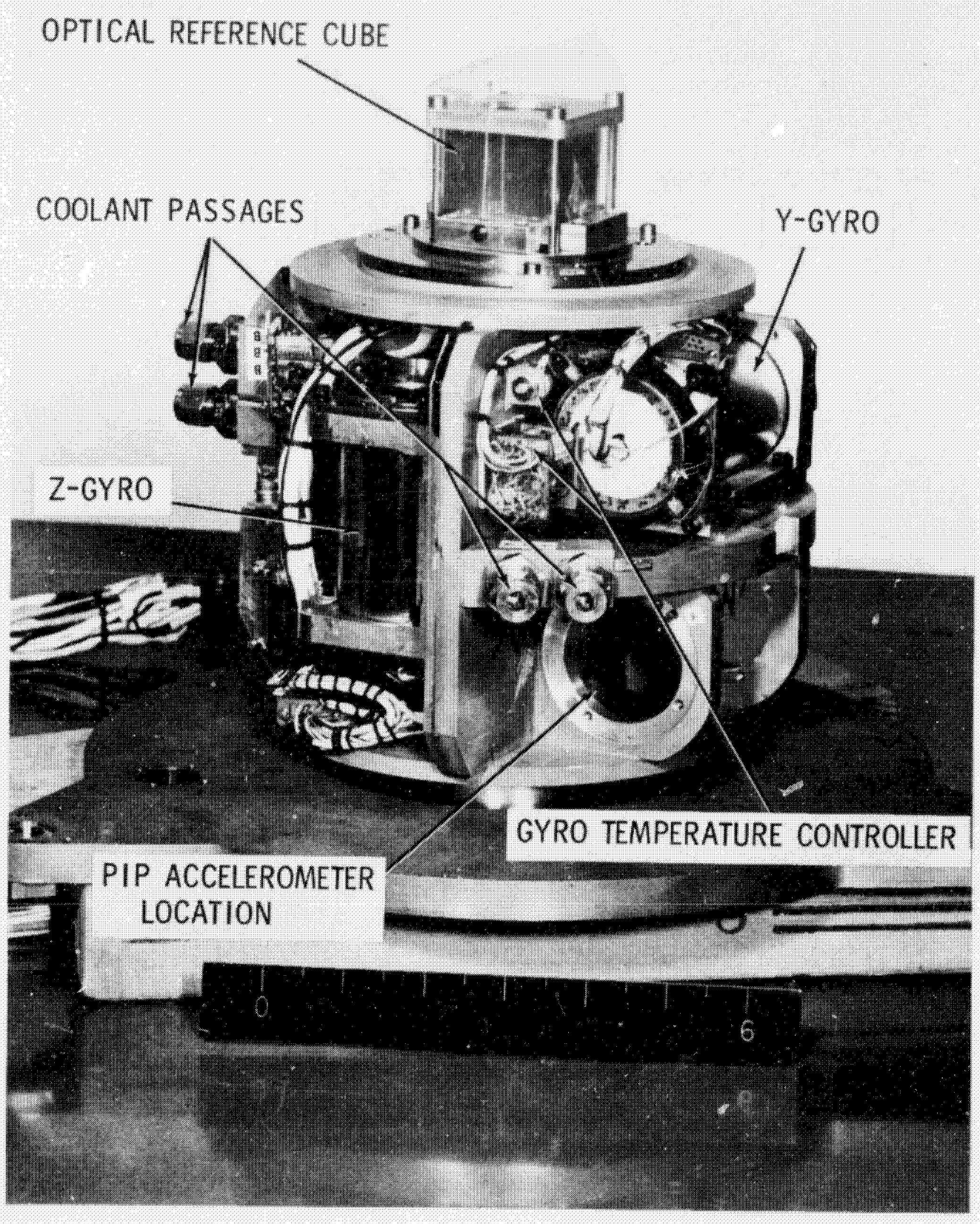

Fig. 4.3-1 Gyro test package, Y and Z gyro view.

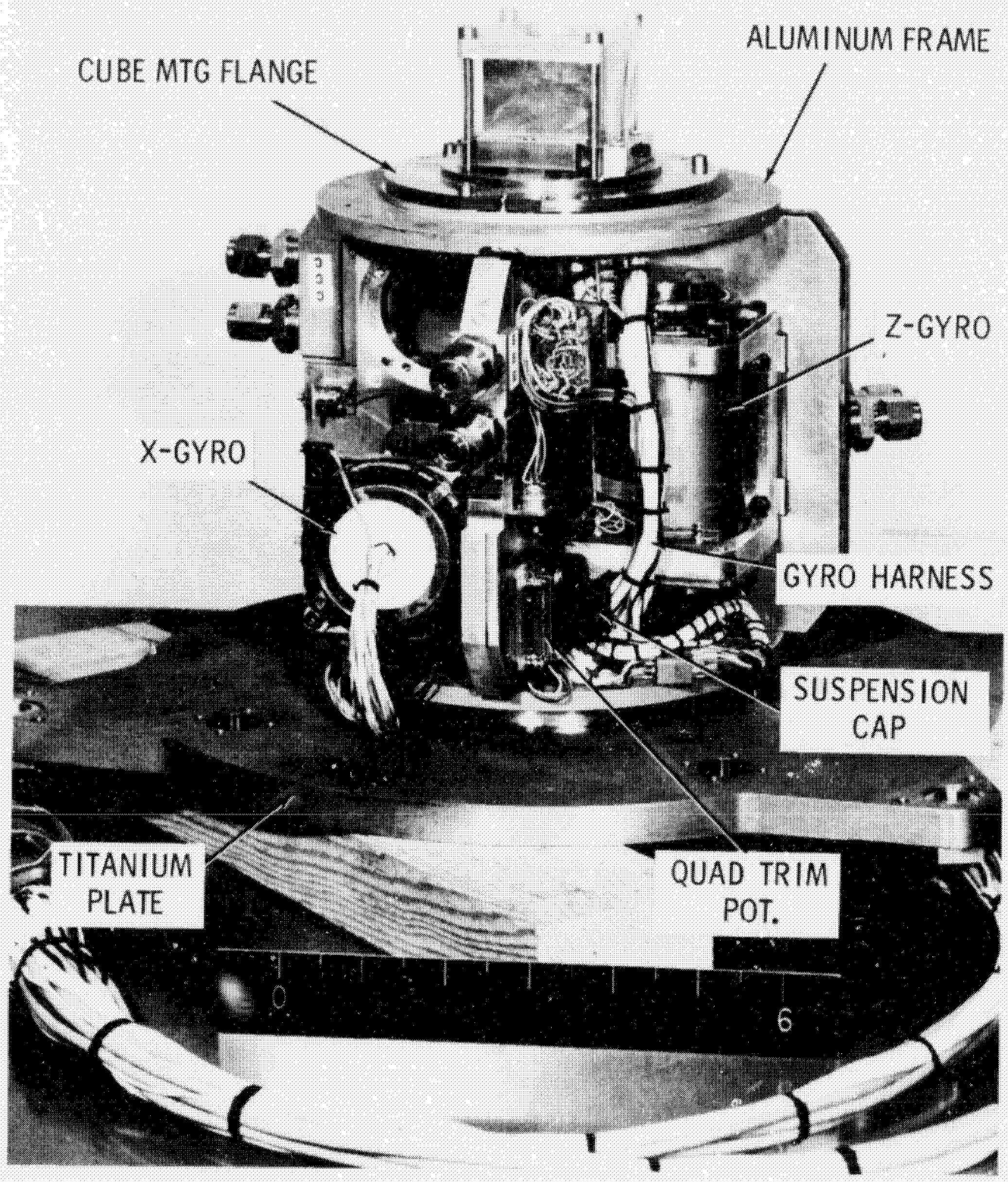

Fig. 4.3-2 Gyro test package, X and Z gyro view.

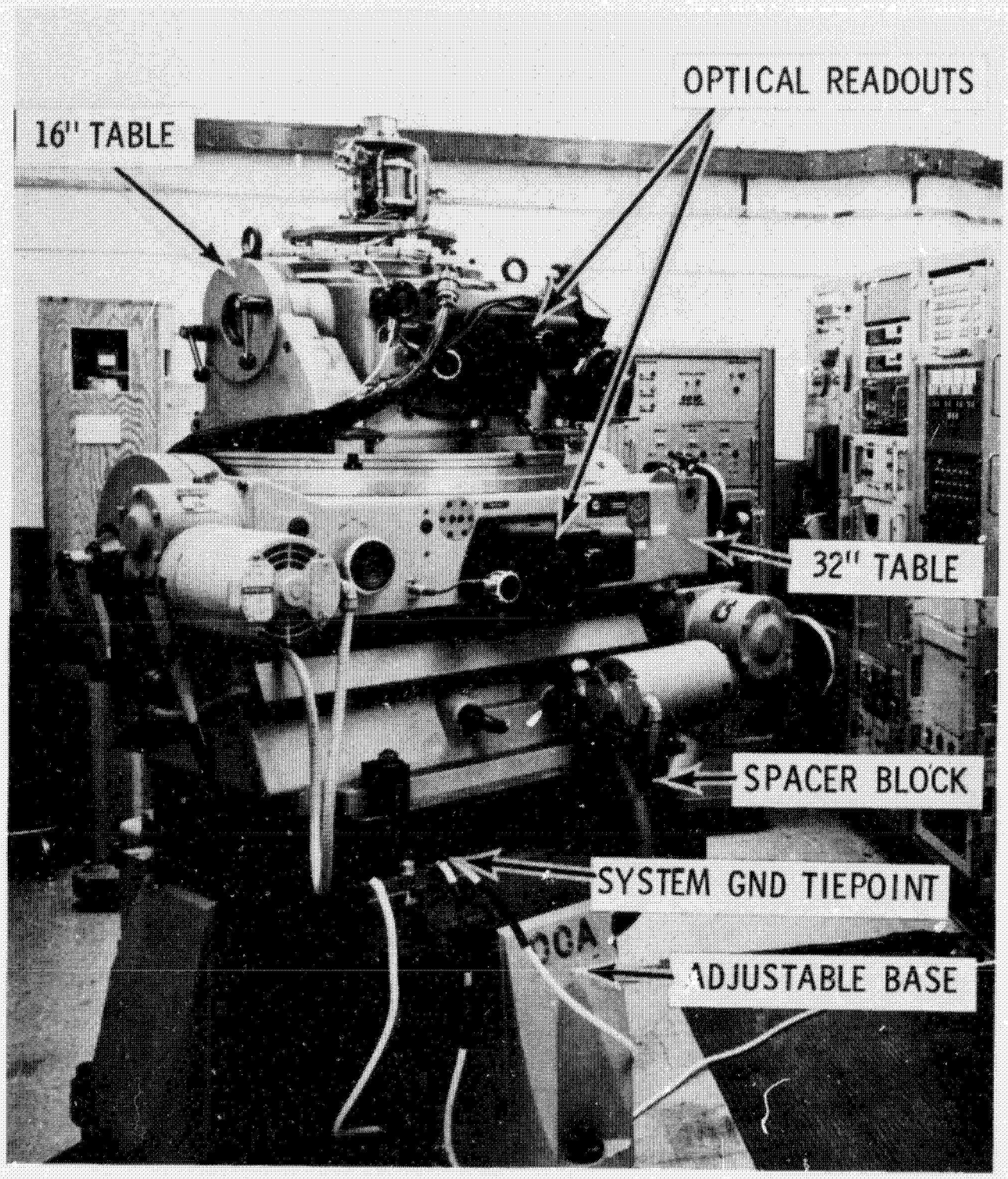

Fig. 4.3-3 4-axis test table.

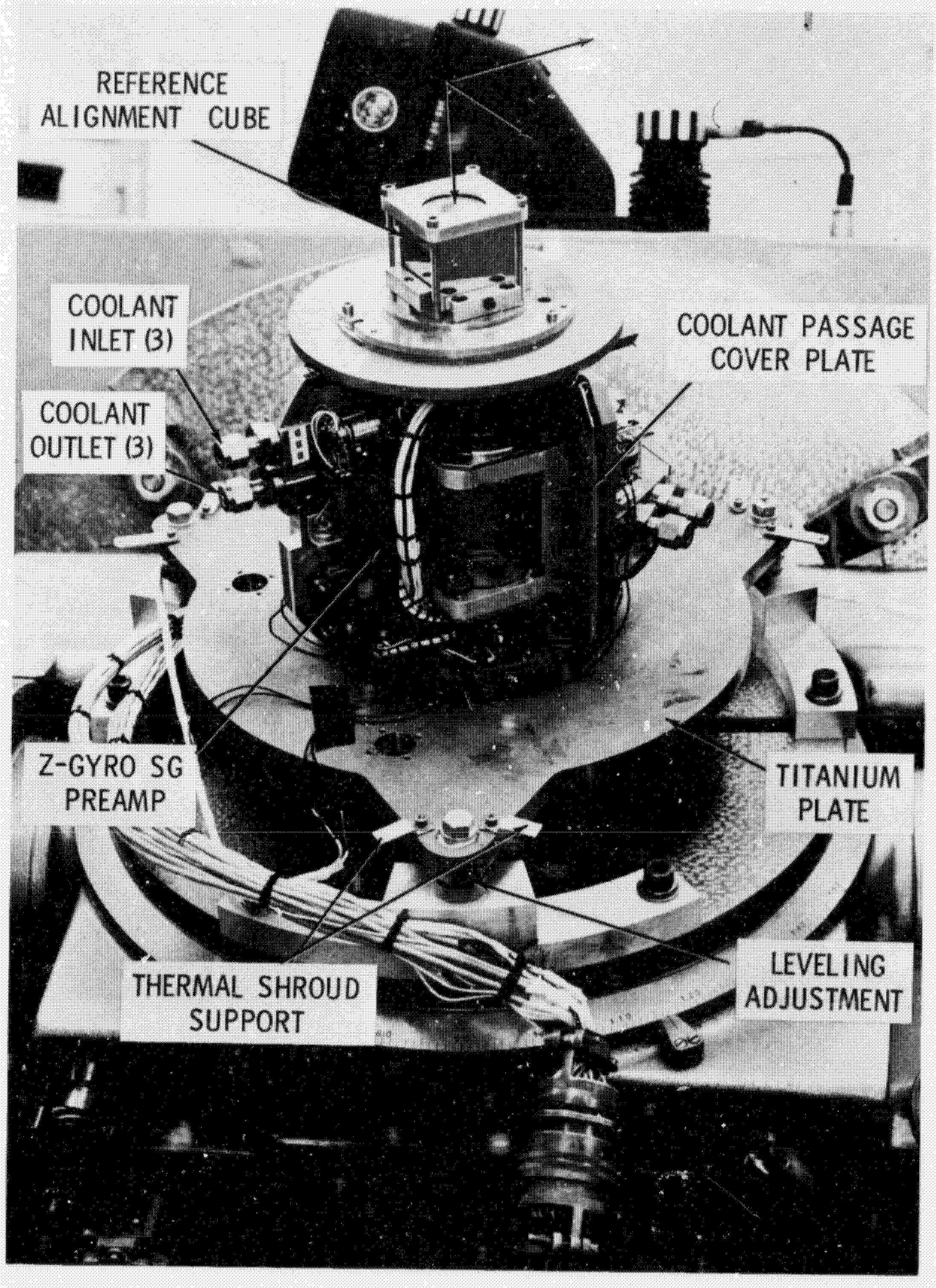

Fig. 4.3-4 Gyro test package mounted to 16" table via alignment plate.

faces. The cube surfaces then serve to define the absolute reference orientation of the test package relative to azimuth and local vertical, as defined by a facility porro prism and reference autocollimators.

The frame is made of aluminum; it incorporates integral coolant passages through which water glycol is circulated for instrument thermal environment control. Figure 4.3-5 is a photo of the frame that was taken prior to final machining and bonding (i.e.: insertion of cover plates over the coolant passages). Note the coolant intake and return passages parallel each other so that thermal gradients across the frame are minimized. The view shown in Fig. 4.3-5 is identical to the frame view shown in Fig. 4.3-4. Note the cover plates on both sides and the coolant line connectors. The connectors are installed on the blocks where the passages terminate as shown on the left-hand side of Fig. 4.3-5. Similarly, 4 mounting pads (Fig. 4.3-5) are provided for each gyro alignment fixture. They are precision ground to form a flat surface. The three sets of pads form a triad of planes that have been machined so that their tolerances with respect to the cube faces are within the adjustment ranges of the alignment rings. The surface orientations of each pad set has been accurately measured with respect to the reference cube faces. Figure 4.3-6 shows the misalignment of the mounting-pad normals with respect to the alignment cube reference normals. Each gyro is prealigned in its alignment fixture to account for these fixed angular misalignments.

4.3.3 Gyro Normalization

The alignment fixture (shown in Fig. 4.3-7) allows freedom of adjustment of the gyro input axis about the output and spin reference axes. The alignment about OA and SRA is achieved by means of two independent adjustment mechanisms on the alignment fixture. Adjustment of IA about OA is achieved by rotating the plate that the TG gyro end is mounted to with respect to the alignment assembly frame (Fig. 4.3-6). This is accomplished by the operation of two conical screws that are operated against tapered surfaces on the mounting plate. Adjustment about SRA is achieved by rotation of an eccentric ring located on the end-mount clamp. The gyro mounts in the clamp on a spherical seat which functions to avoid generating bending stresses along the axial length of the gyro due to the rotation of the eccentric ring. The range of adjustment capability is 7 min of arc and 32 min of arc of IA about SRA on OA, respectively. The measured adjustment sensitivities are approximately 1.3 arc seconds of rotation of IA rotation about OA for degree of rotation of the conical screws, and 2.6 arc-seconds of rotation of IA about SRA per degree of rotation of the eccentric ring. The experimental test objectives are to align each IA within 10 arc-seconds of its corresponding reference cube surfaces. In addition to the alignment features, heaters for thermal control are integrally wound about each of the fixture's gyro end mount alignment clamping rings.

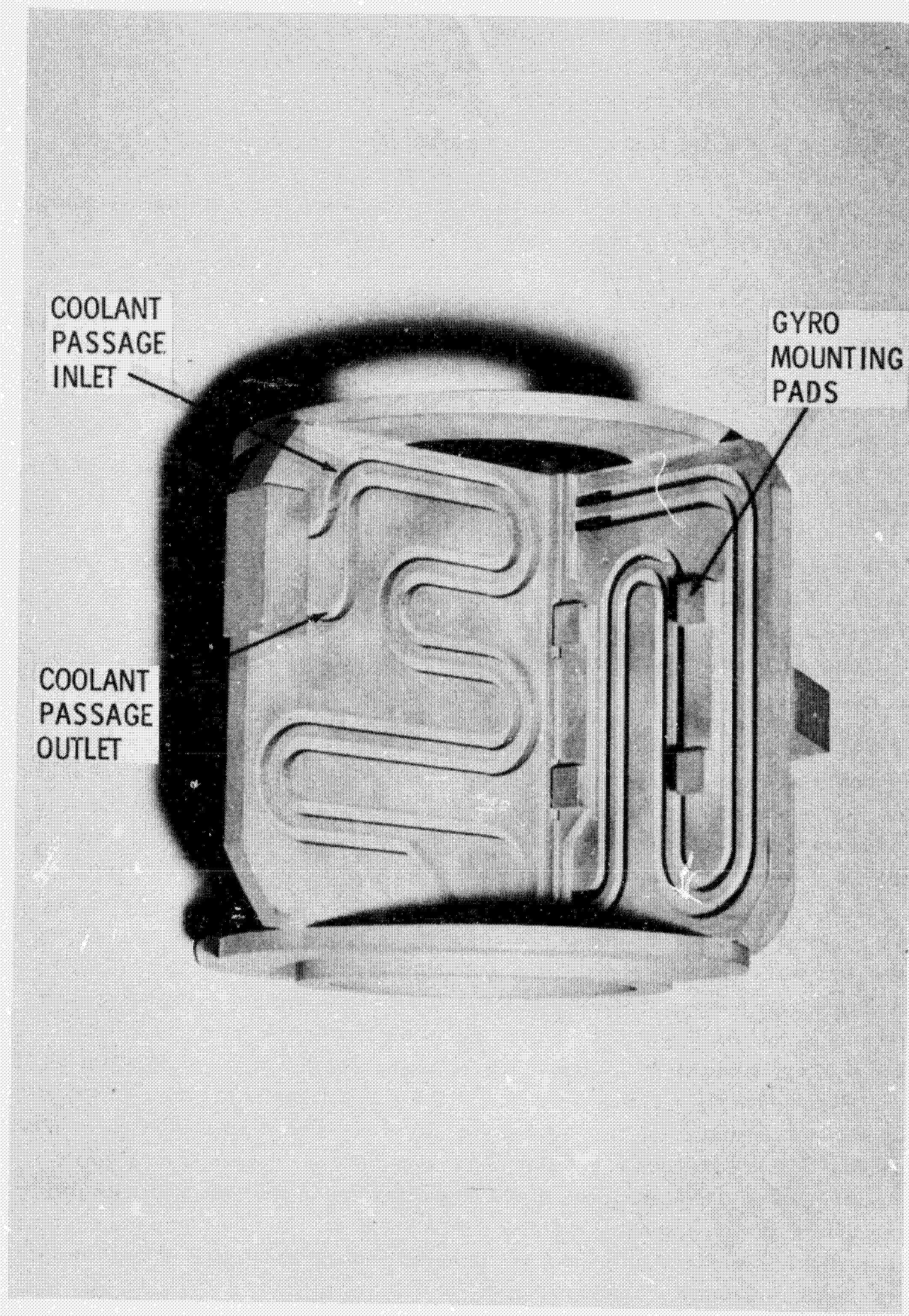

Fig. 4.3-5 Frame prior to final machining.

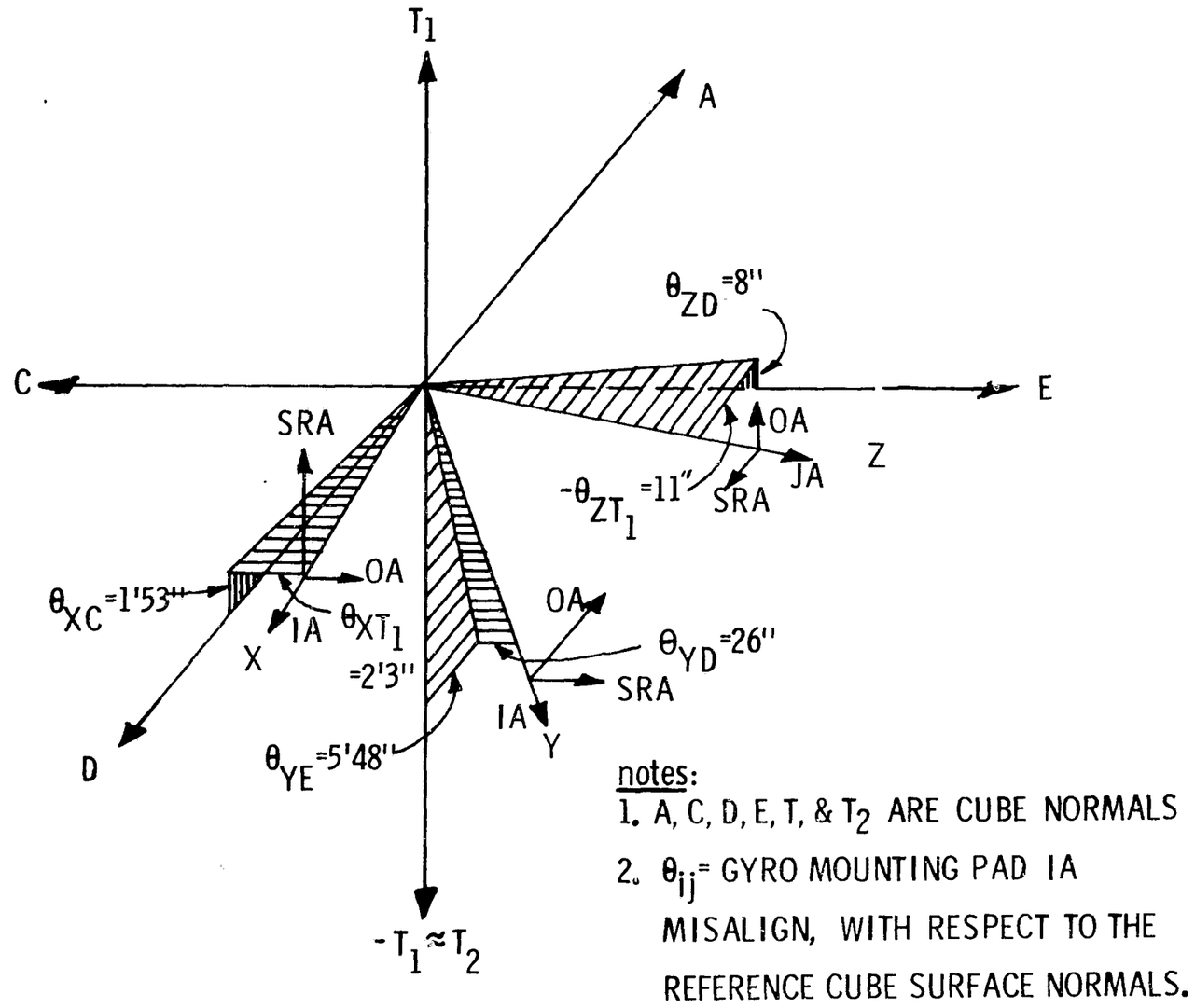

Fig. 4.3-6 Gyro mounting flat misalignment angles wrt reference cure.

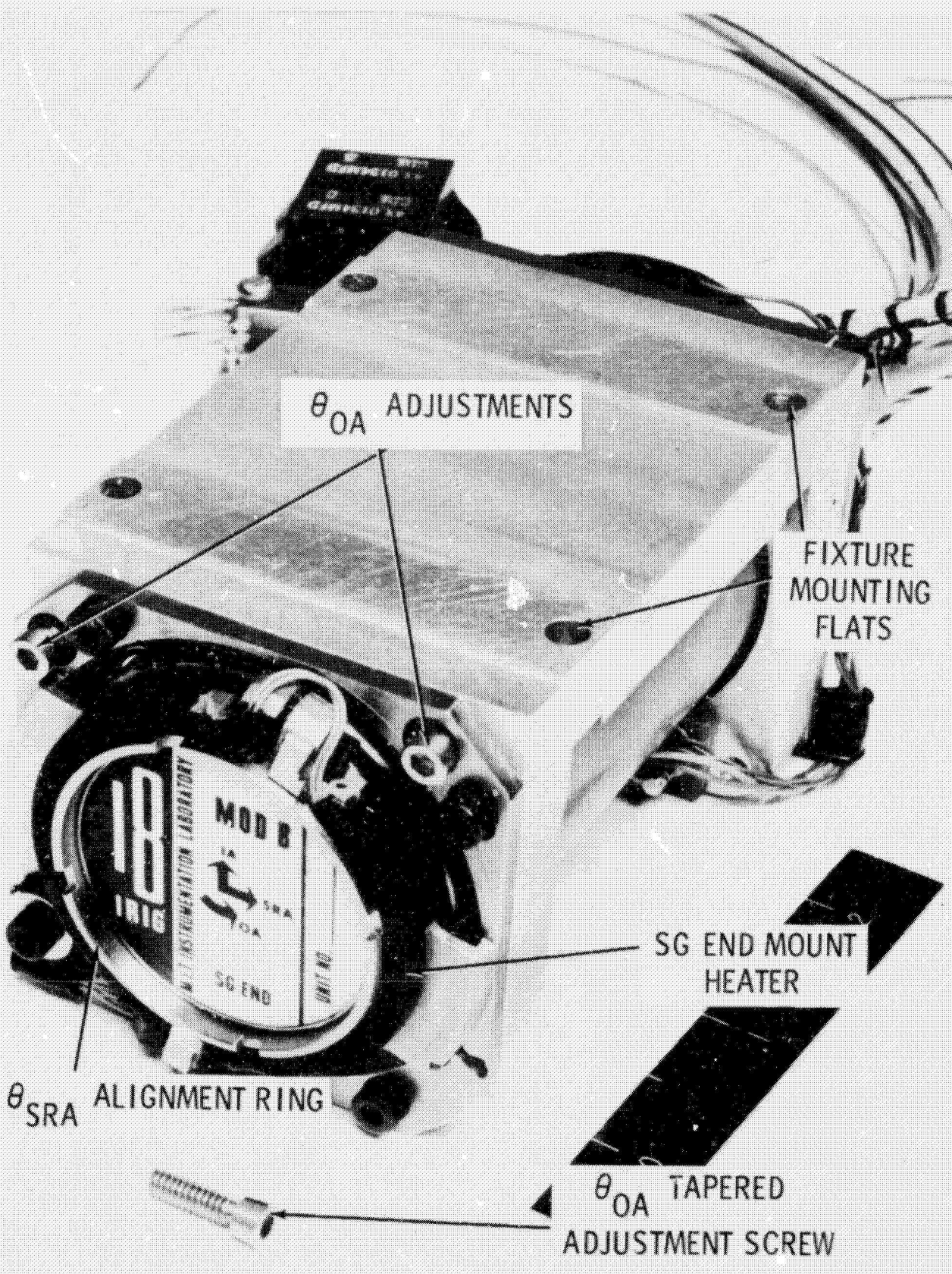

Fig. 4.3-7 Gyro alignment fixture, front view.

As shown in Figs. 4.3-8 and 4.3-9 integral to each gyro harness is a complete set of normalizing electronics which include: a signal generator pre-amplifier, magnetic suspension capacitor modules and quadrature adjustment components. The gyro,therefore, is normalized and aligned in its system level configuration at a component prealignment level. The advantage of this normalized configuration is uniformity of test setup and the assured validity of data correlation between system and component test runs.

The preamplifier is a differential amplifier for common mode rejection qualities with a gain of approximately 100 (adjustable) at 9600 Hz. It includes a bandwidth filtering provision for noise rejection of spurious wheel power signal pickup and their harmonics. The amplifier input connects directly to the gyro SG secondary and its output is transformer coupled to the pulse-torque electronics located in the Support Electronics Console (SEC). The primary function of the amplifier is to assure that a high level signal is transferred across the package interface so that environment noise influences on the pulse-restrained loop performance are minimized. A ducosyn 3.5:1 stepdown transformer located on the frame provides 8-Vrms 9600-Hz excitation to the gyro ducosyns. Voltage stability is maintained by feedback from the transformer secondary to the source supply located in the SEC.

4.3.4 Thermal Design

Individual temperature controllers for each gyro are mounted on the frame. A proportional dc controller was selected in lieu of a more efficient pulse-width-type control to minimize the package electronic noise environment. The controller employs a balanced bridge sensor circuit in which two of the elements are the sensors located in the 18 Gyro. The controller design will maintain control temperature to $\pm 0.01^{\circ}F$. Each controller is sized to provide a maximum of 26 watts control power. A unique feature of the controller is the use of two integrated circuit amplifiers. The controller preamplifier employs a Fairchild A726 preamplifier followed by a A709. The use of the A726 which has self-contained substrate temperature control minimizes the equivalent input stage drift to less than one microvolt per $^{\circ}C$. A schematic of the controller is shown in Fig. 4.3-10.

A cooling technique has been designed for the test package that allows development of variable thermal resistance concepts. This investigation was undertaken with the objective of minimizing the electrical power used by the temperature control system during an extended mission. For example, in the Apollo system, approximately 20 watts are required in standby operation to maintain the components near their operational temperature. The standby phase represents the major portion of the mission time.

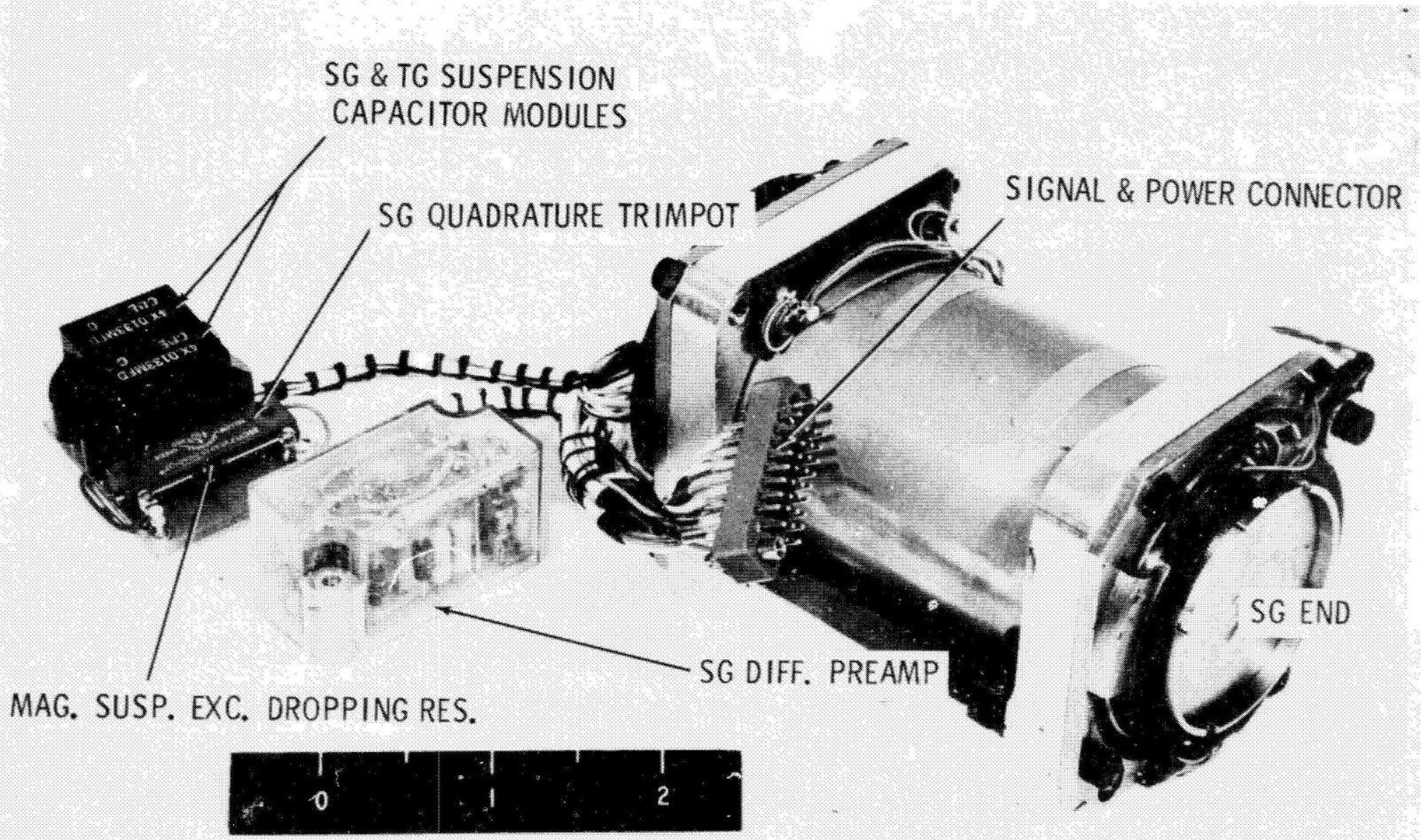

Fig. 4.3-8 18 IRIG MOD B gyro in alignment fixture with integral normalizing electronics (SG end view).

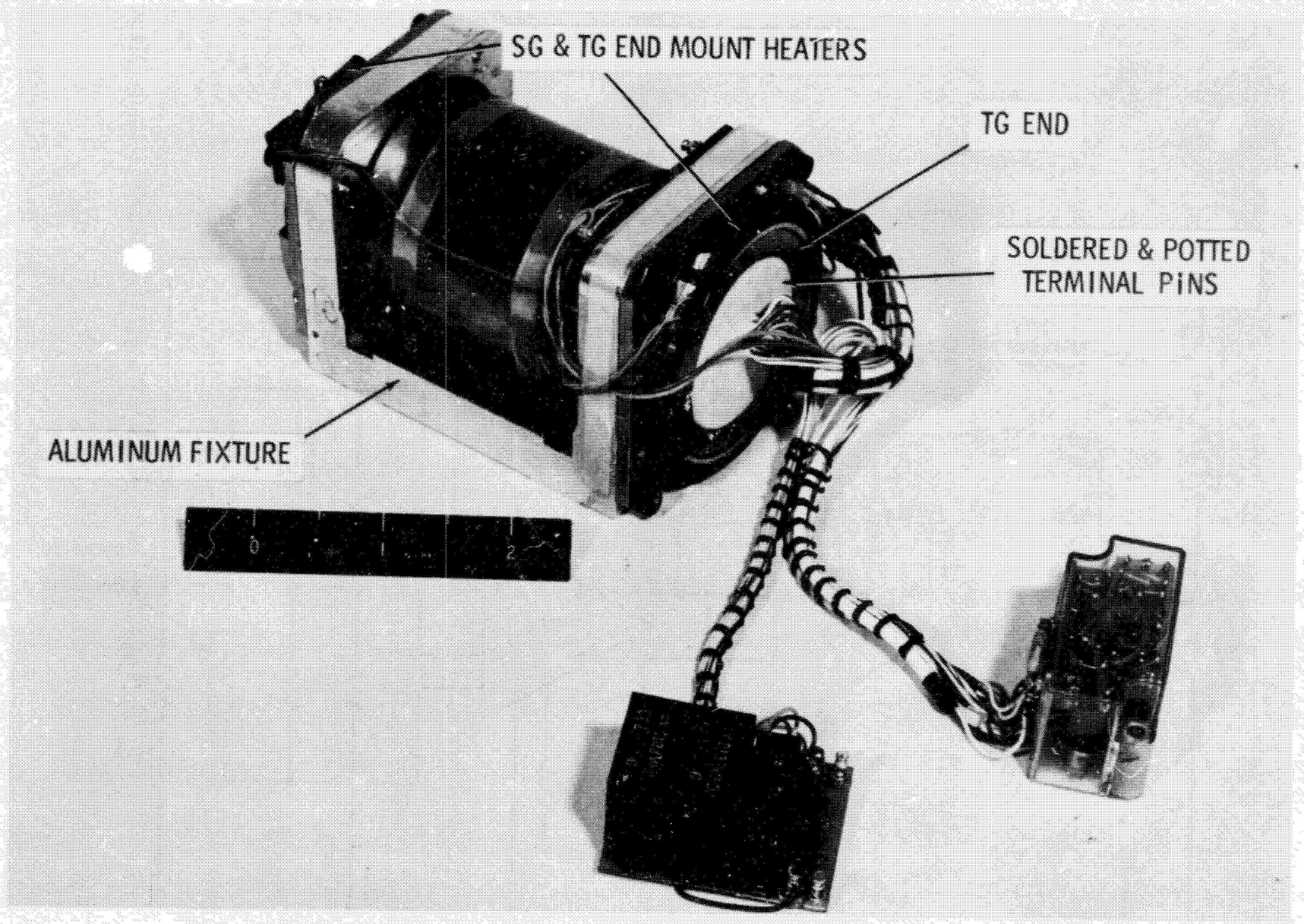

Fig. 4.3-9 18 IRIG MOD B gyro in alignment fixture with integral normalizing electronics (TG end view).

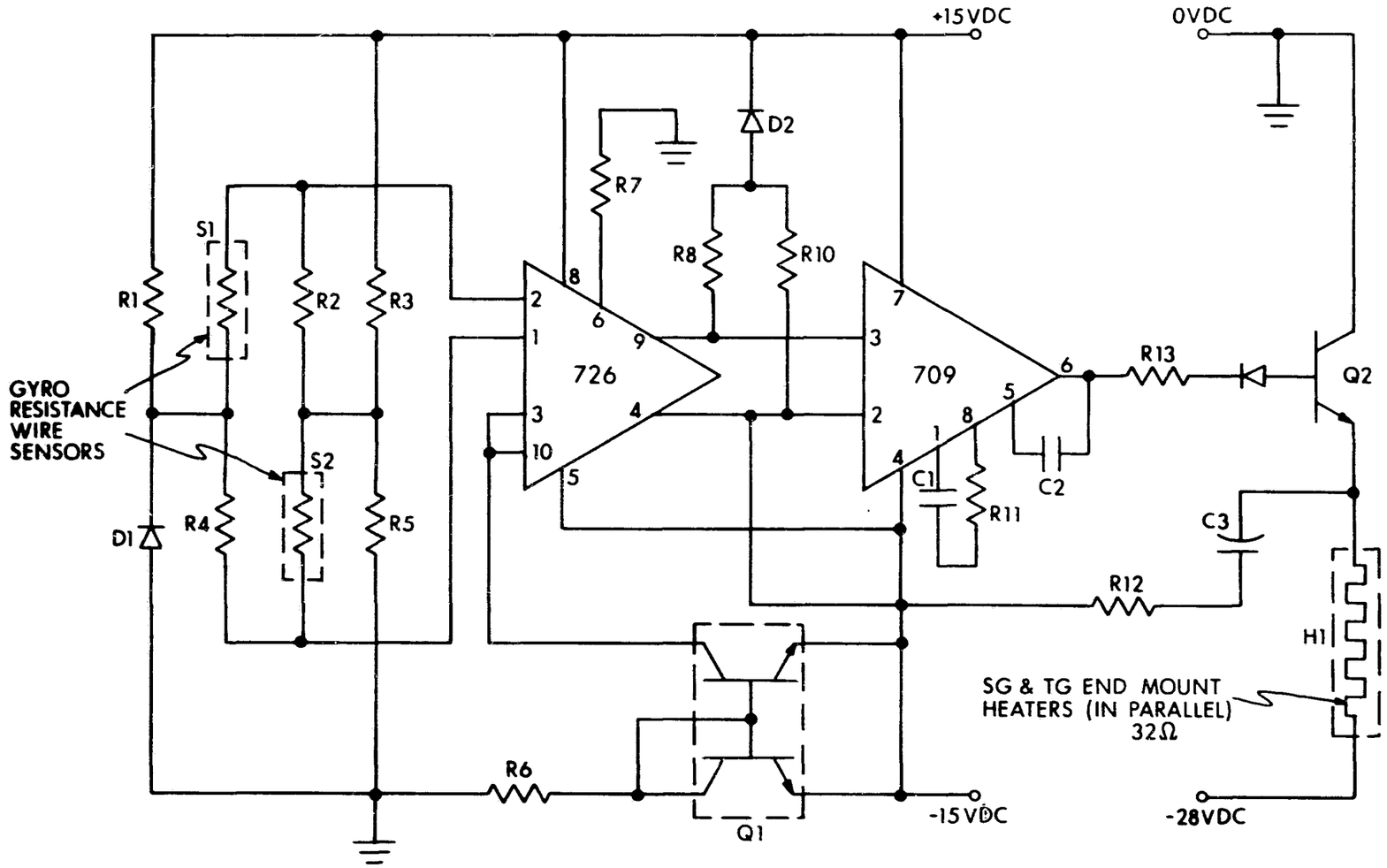

Fig. 4.3-10 Gyro frame mounted proportional temperature controller.

The concept is to vary the thermal resistance from the platform to the heatsink depending on the enviornment and system mode. The result would be that in standby, a high thermal resistance would minimize the power required to keep the platform at temperature. Similarly, in operate (instruments, wheel power, and associated electronics powered) the thermal resistance is adjusted such that only excess heat is removed. The direct gyro heater control power is minimized, therefore, since the platform is at a temperature that is only slightly lower than that of the instrument control point.

A block diagram of the configuration developed for the test package is shown in Fig. 4.3-11; photographs of the completed assembly are shown in Figs. 4.3-12 and 4.3-13. Note that the coolant loop varies the thermal resistance by adjustment of coolant mass flow through the frame's integral coolant passages. In general, the total temperature control loop consists of both the liquid coolant loop and the individual instrument temperature controllers.

The coolant loop serves to regulate the amount of heat which is transferred from the platform to the heatsink. It consists of the following:

1. a pump for coolant circulation,
2. a thermally-operated three-way valve for coolant flow direction,
3. a reservoir and expansion bellows
4. a heatsink which consists of a liquid to liquid heat exchanger. One side of it is utilized by the self-contained coolant loop, the other side interfaces with the coolant supply or a forced-air heat exchanger which couples to the heatsink. This provision was made to facilitate dynamic testing on the test table. (Universal coolant couplings to allow coolant flow to the test package during table rotational tests are avoided.), and
5. a valve mode controller which is operated by a mercury thermostat on the platform.

In the operate mode, the heat is removed by the coolant mass flow through the platform to a coolant bypass valve. A mercury thermostat senses and controls the platform at a constant temperature. From the valve, the coolant has two paths, one which is a bypass and the other through the heat exchanger. Both of these lines are united again at the reservoir and the coolant is pumped back through the frame. Depending on the environment, the coolant bypass valve will switch the flow such that only the excess heat is transferred to the exchanger so that a minimum amount of control power will be required at the gyro.

CONCEPT: Control the Thermal Resistance from the Platform to the Heat Sink Based on Environment & System Mode.

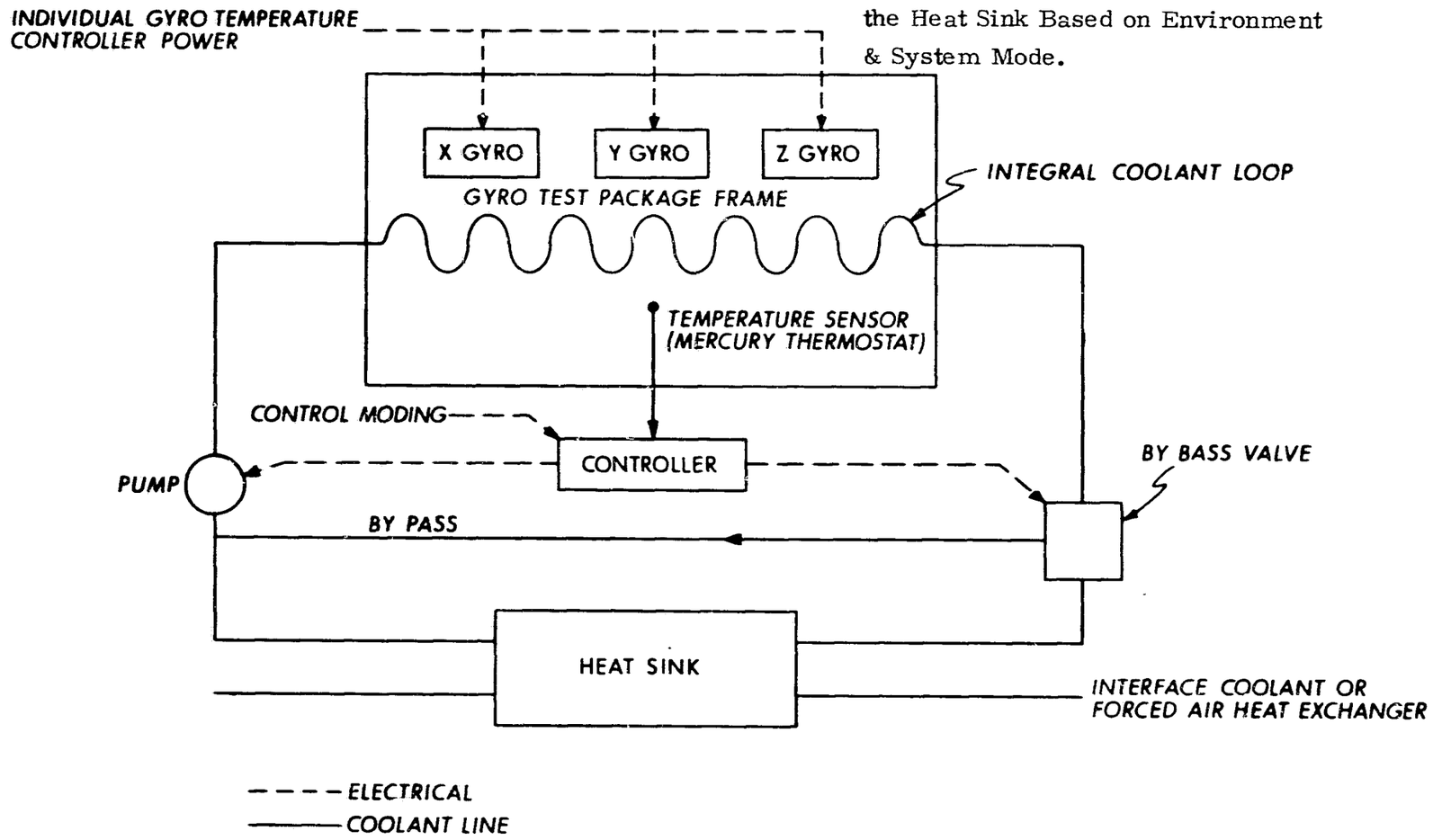

Fig. 4.3-11 Variable thermal resistance.

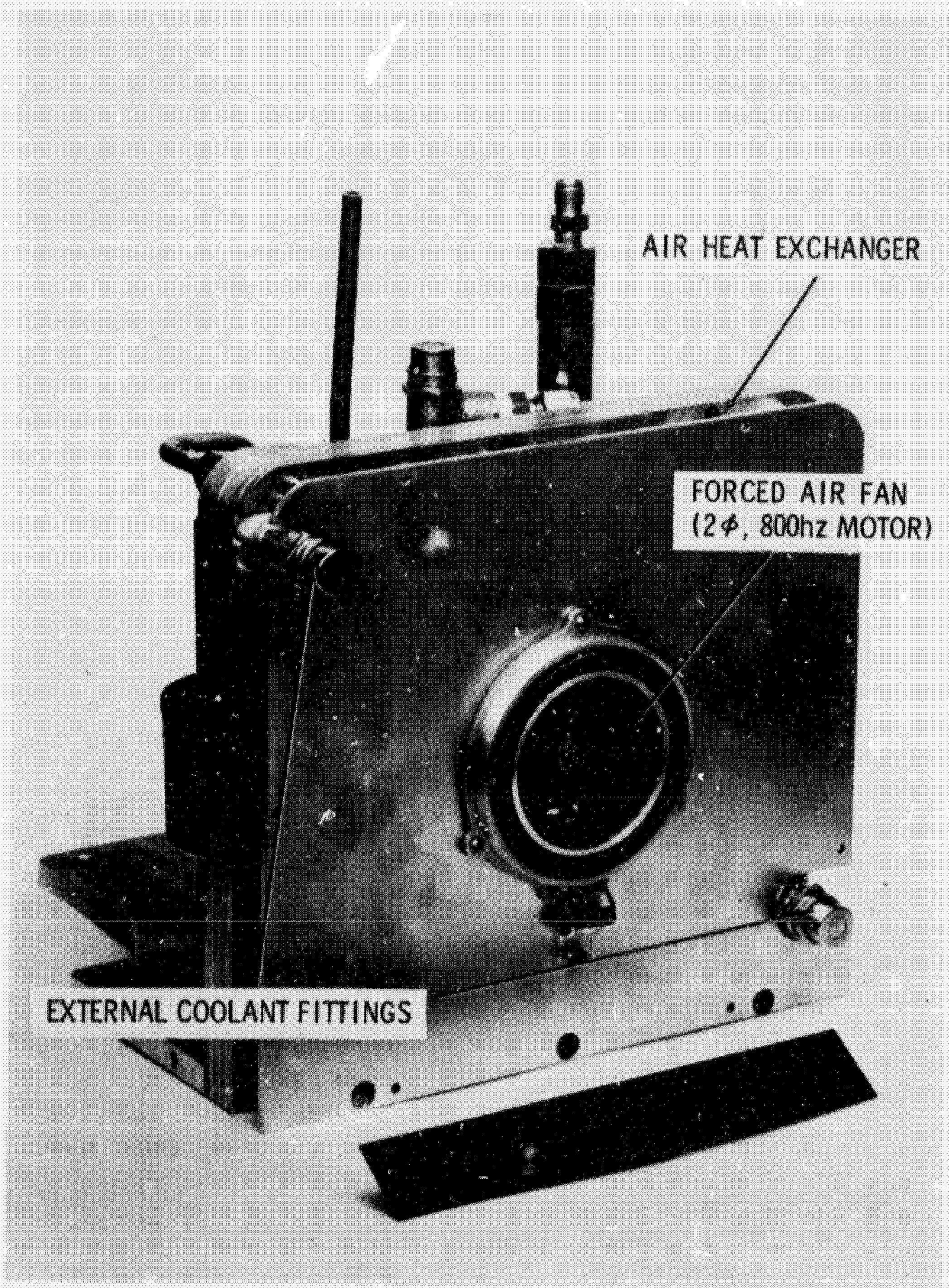

Fig. 4.3-12 Frame variable coolant controller (front view).

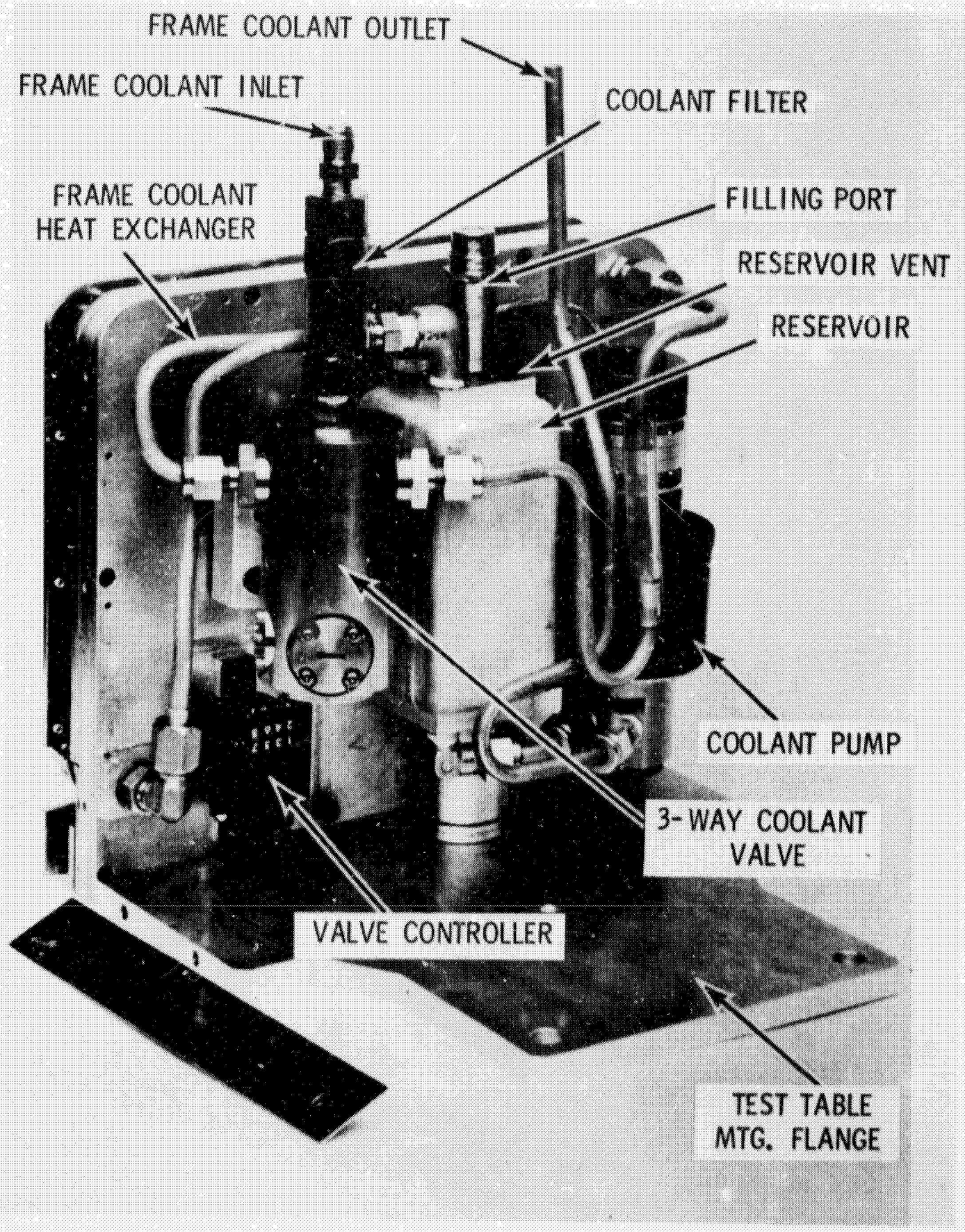

Fig. 4.3-13 Frame variable coolant controller (rear view).

In the standby mode, the pump and bypass valve will normally be off in order to conserve power. But, if the platform temperature were to rise above the standby control point (i.e., ambient becomes hotter than the platform), the pump and valve will become operational.

A thermal shroud was designed to isolate the gyro test package from the laboratory environment during testing on the rate drive table. The thermal shroud assembly consists of a polished stainless steel dome and bottom cover; both are lined with one inch of closed-cell foam insulation. The shroud creates high thermal resistance and permits the variable thermal resistance coolant loop to effectively control the frame temperature. Figure 4.3-14 is a pictorial schematic illustrating the overall coolant loop, test package, shroud, etc. A photograph of the hardware mounted on the test table is shown in Fig. 4.3-15; Fig. 4.3-16 shows a cut-away of the assembled shroud, mounting plate, and test package.

Test evaluation of the thermal shroud insulating characteristics was undertaken at room conditions and an overall thermal resistance of $4^{o}F/W$ from the frame to the base mounts was determined. A thermal resistance of $4.3^{o}F/W$ was obtained when the frame was removed from the base mount. This indicates a very high thermal resistance, more than $50^{o}F/W$, from the mounting base. Most of the heat flow is across the thermal shroud.

A system of this size with its constraints (i.e., mirror viewing ports) presents a problem using standard thermal insulating techniques (i.e.: the more insulation, the larger the overall shroud size). In order to achieve higher thermal resistances, a "super insulation" would have to be used (i.e., vacuum shroud). This method has been suggested and is incorporated into gyro module concept presented in Chapter 1.

4.3.5 Facility Features

Facility Alignment References are required to accurately define the orientation of the test package reference cube (correspondingly, the gyro input axis triad) with respect to inertial space. Thus, in a test, the package may be oriented by test tables in some predetermined rate sequence. The test package may then be realigned to the alignment reference position and the package-algorithm performance may then be evaluated. A porro prism was installed in the laboratory to provide the azimuth reference (5-arc-second accuracy). Two fixed targets housing Davidson autocollimators are used to align the Frame Reference Cube to an earth-fixed reference position (North, East and vertical). These optical standards then provide a prime reference from which the 4-axis test table readouts can be calibrated. Figure 4.3-17 shows the relative location of collimators and the porro prism in the laboratory.

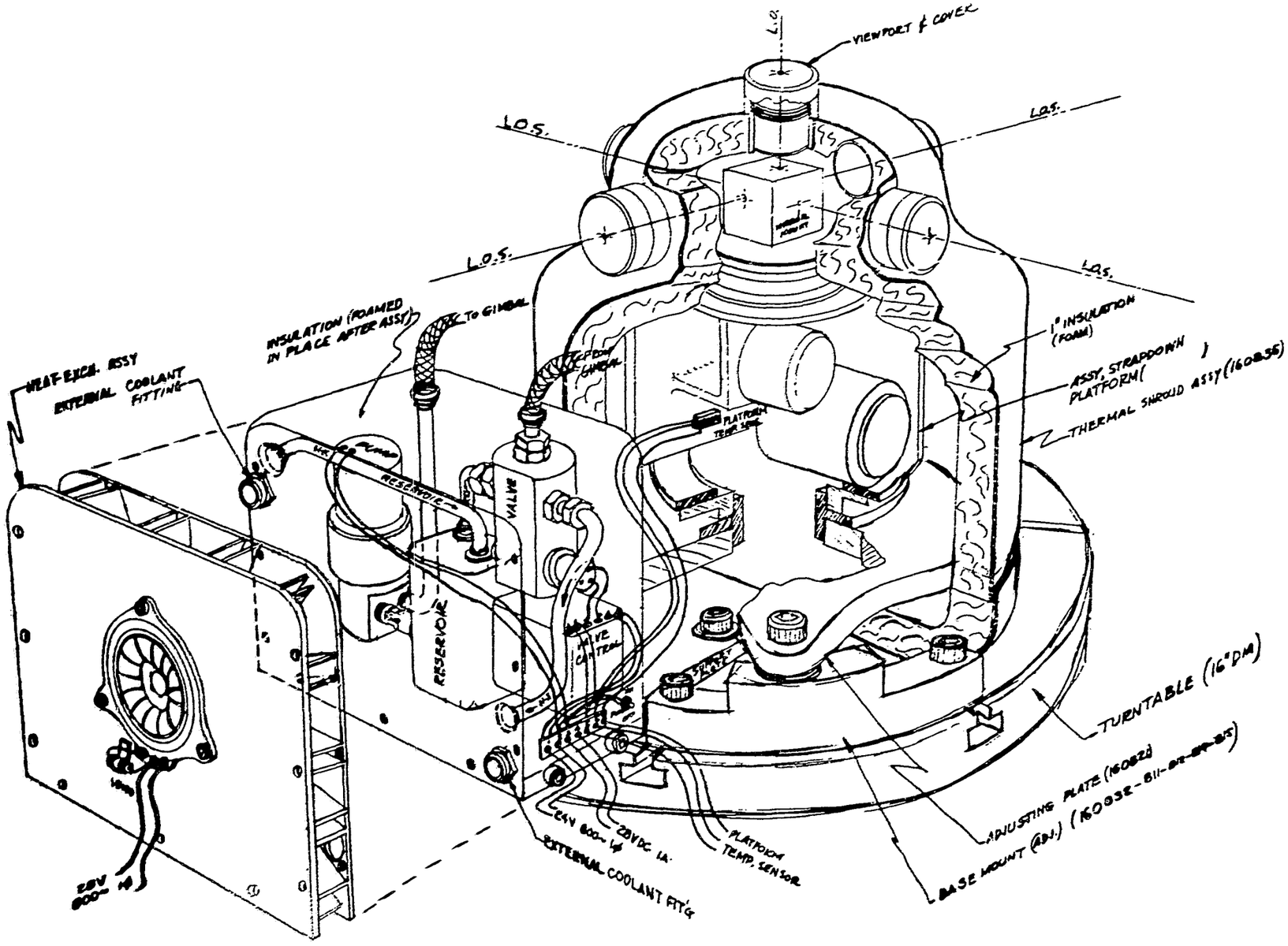

Fig. 4.3-14 Schematic pictorial of strapdown system (freehand perspective).

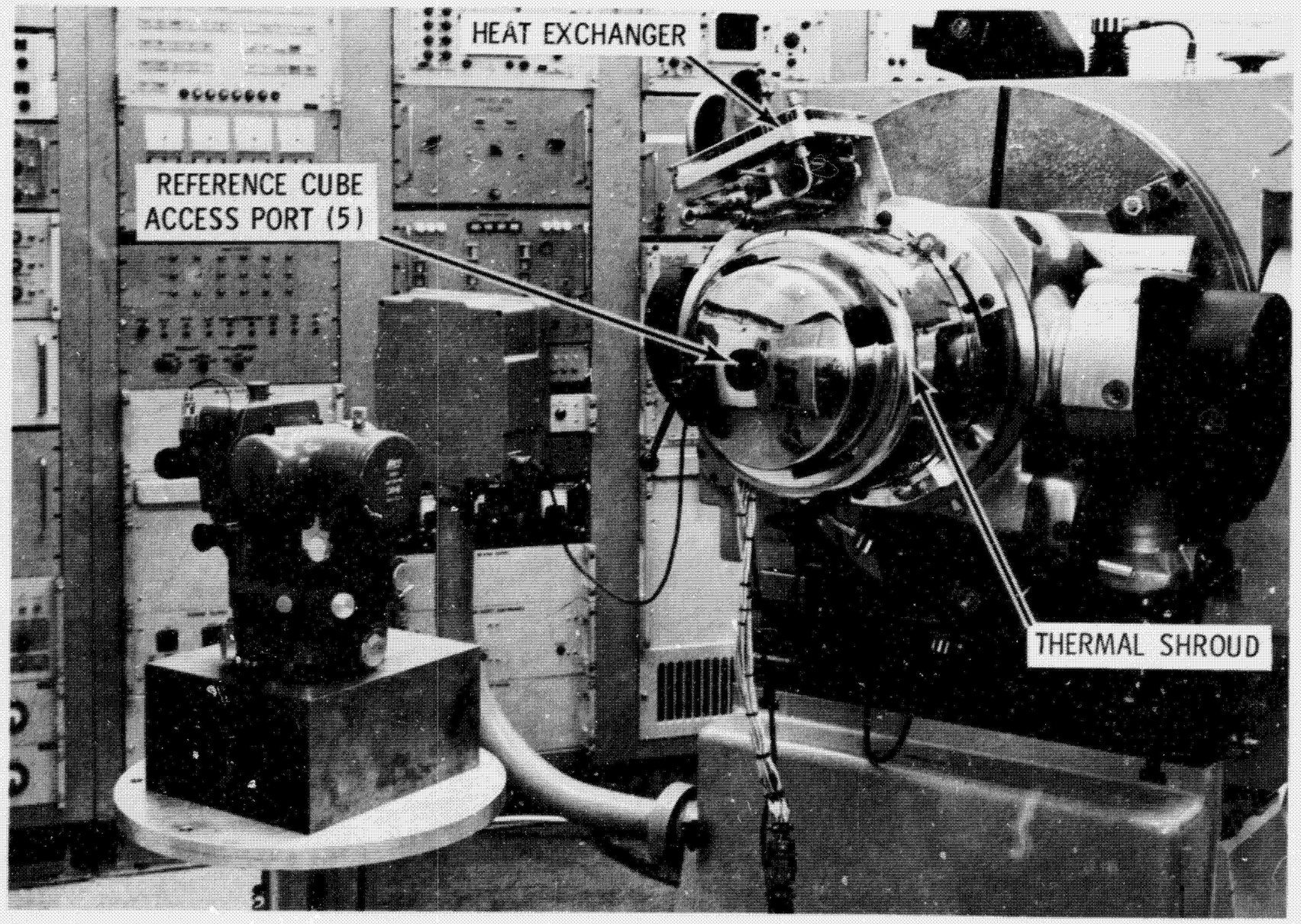

Fig. 4.3-15 Completely assembled test package on 16" table.

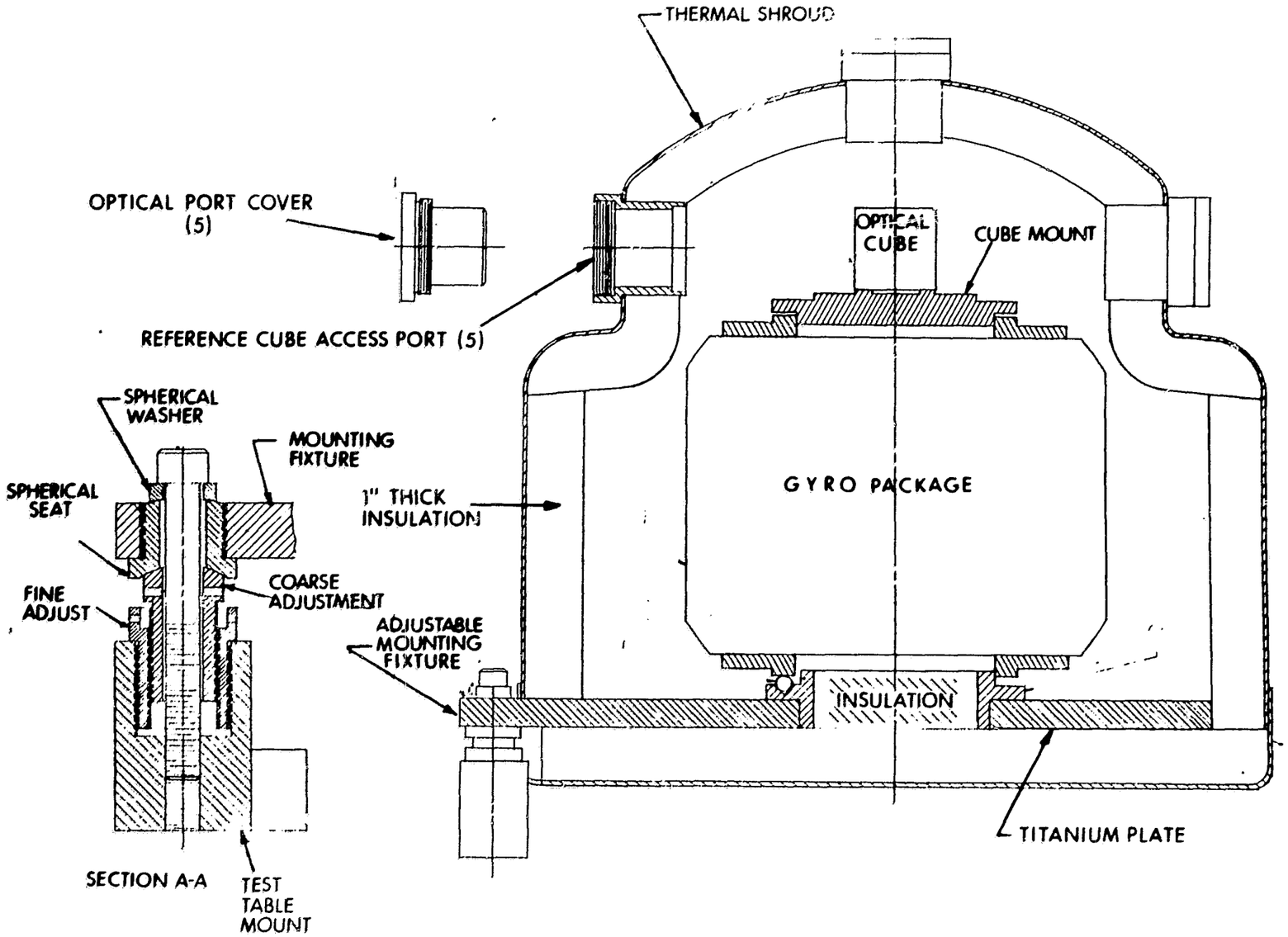

Fig. 4.3-16 Cut-away view gyro-package development test configuration.

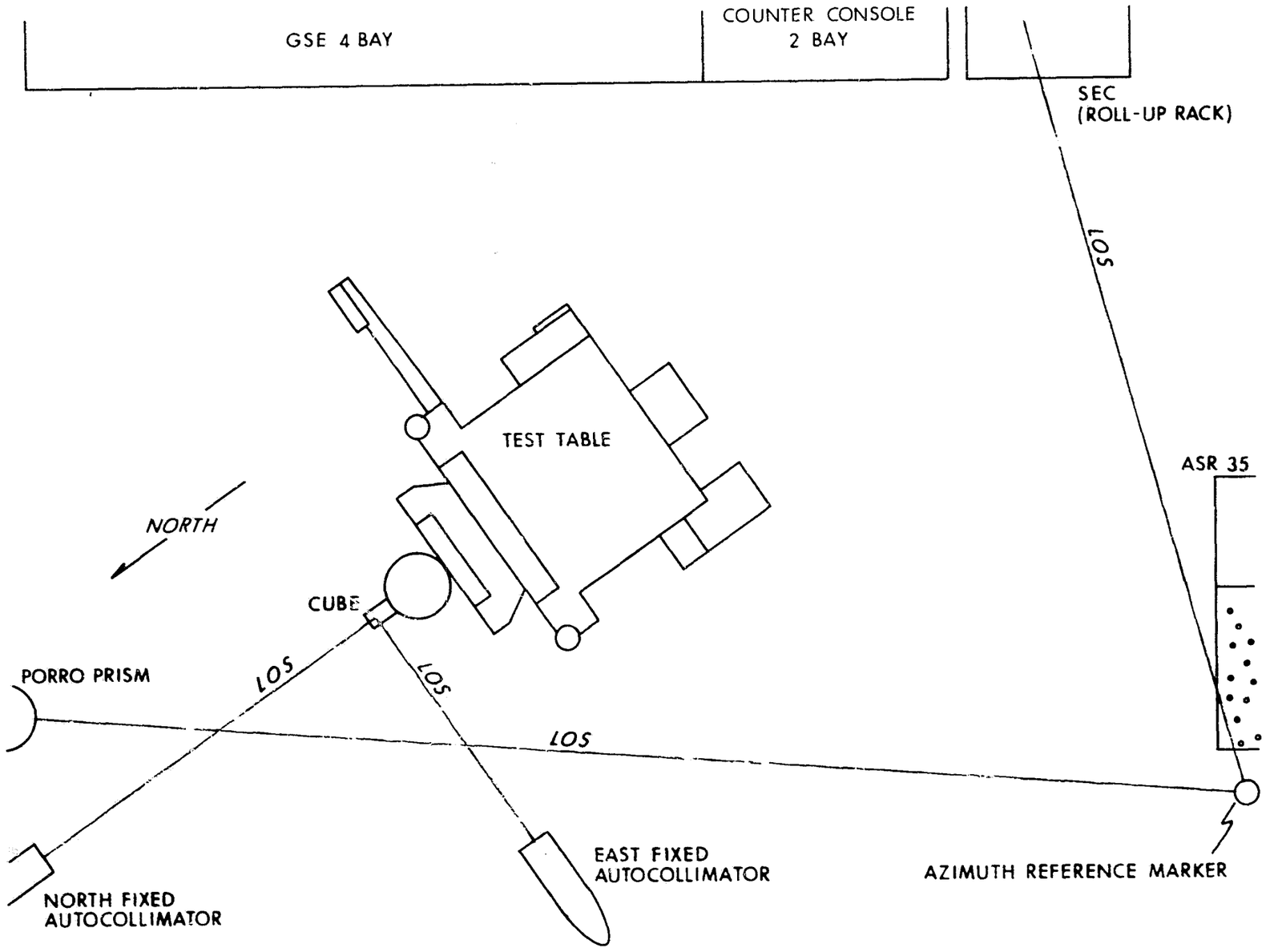

Fig. 4.3-17 Test facility - optical alignment references.

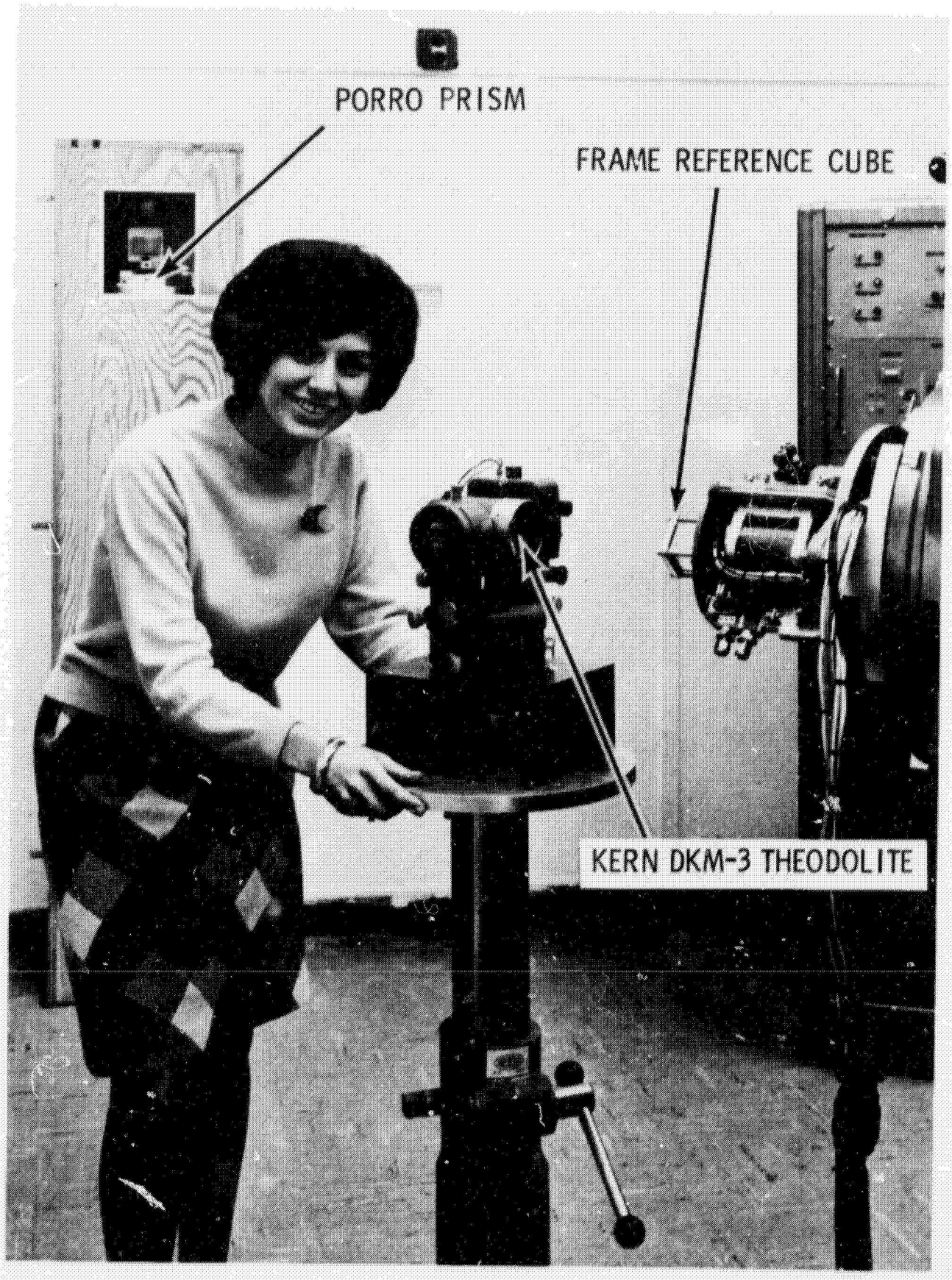

Fig. 4.3-18 System reference cube alignment using Kern DKM-3 theodolite (autocollimation).

Figure 4.3-18 illustrates a cube azimuth alignment using a Kern DKM-3 theodolite, the porro prism is shown in the background.

A 4-axis test table configuration consisting of two International Machine Tool Co. tables is used for static and limited dynamic tests. The upper table is a 16" modified with a rate drive on its rotary axis. Its trunnion is equipped with a manual drive provision. The lower table is a modified Apollo 32" table. The table rotary axis has been fitted with a hydrostatic bearing (installed to allow rate drive operation) and rate drive. The lower rotary axis is also equipped with an 18-bit (4.9 sec) optical encoder. The trunnion axis has a fixed rate drive capability. Both tables are equipped with precision optigons with read accuracy of 2 and 5 seconds of arc for the lower and upper tables, respectively. The lower table rotary rate range is 0.01 to 1 radian per second. Its maximum oscillatory capability is approximately 10 min of arc peak-to-peak at 10 cps. This table configuration was designed and assembled under NASA Contract 9-153.

The remaining major support and developmental test items: algorithm computer, electronics and power supplies, and supporting test equipment, test consoles and functions are described in subsequent sections of this chapter.

4.4 Real-Time - Algorithm Computational Capabilities

4.4.1 Introduction

Use of a real-time computer in the strapdown test laboratory is a necessary adjunct to comprehensive integrated system testing. To satisfy this objective, a small, scientific, general-purpose computer with state-of-the-art processing rate capability was sought. The computer application is discussed in Section 4.4.2 and the selection criterion for the computer is presented in Section 4.4.3. The programming effort necessary to allow real-time processing on the computer is then described. Finally, the special hardware development necessary to interface the strapdown test package with the computer is described in Section 4.4.5. The computer facility is shown in Fig. 4.4-1.

4.4.2 Use of a General-Purpose Computer

A general-purpose computer was selected because of its programming flexibility for data processing. For a real-time computer test application, the general-purpose computer programs which operate on the gyro data could be changed to evaluate not only different attitude maintenance schemes, such as the direction cosine matrix, the quaternion, and Euler angles, but would allow varying the program parameters to select

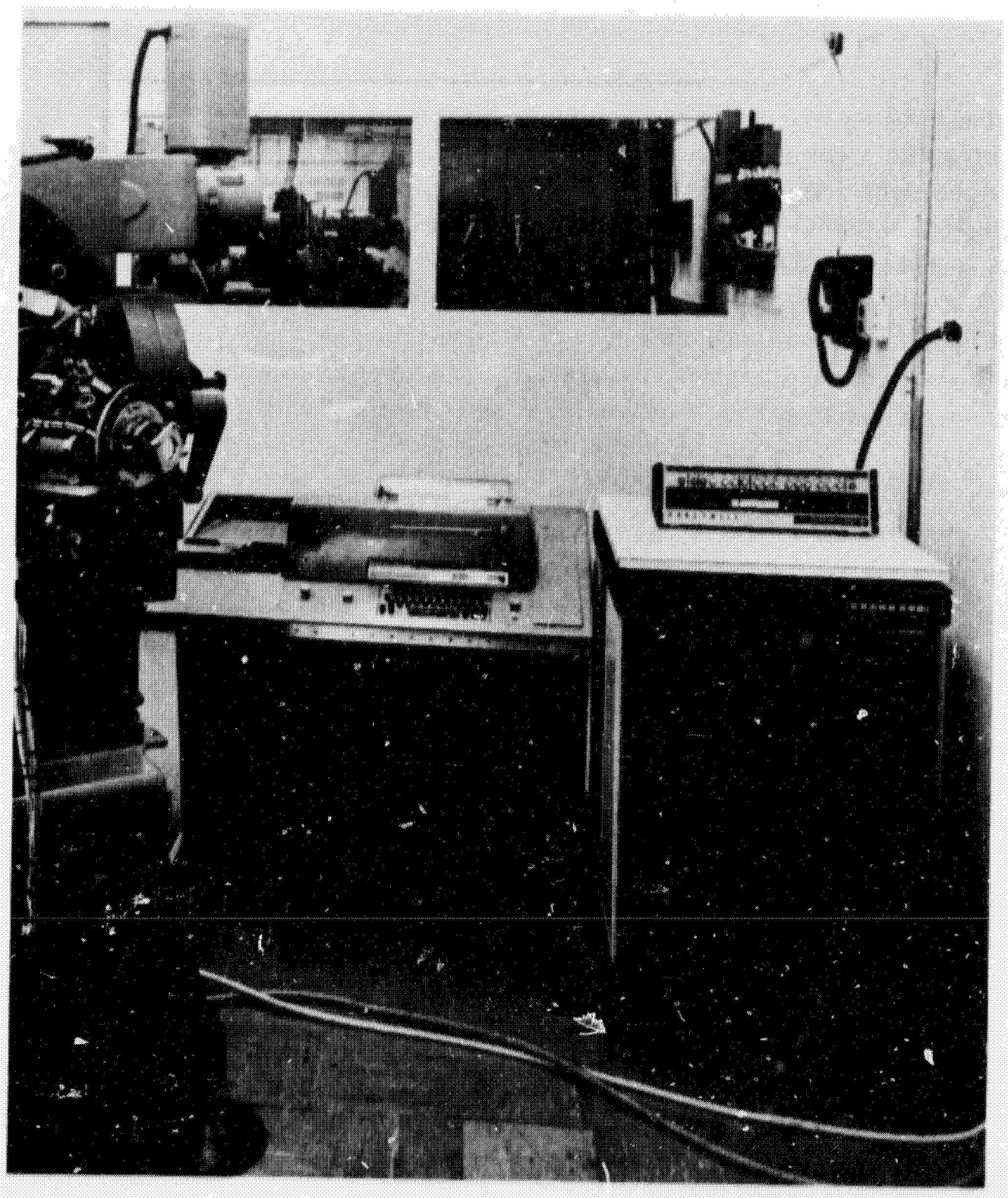

Fig. 4.4-1 Test computer.

those which best complement the performance of the gyro package itself. Some of the parameters which could be varied in the attitude maintenance program are the order of update, the frequency of update, the precision of the resultant matrix, and the time between orthogonalization and normalization of the matrix.

The real-time computer availability also allows simplification of gyro-package performance testing and adjustment by monitoring tests and printing performance results as soon as the data has been taken. Dynamic error analysis could be made if the true gyro platform orientation is known by the computer; that is, if the test table angles could be read by the computer, an instantaneous comparison of calculated orientation (using gyro data only) and true orientation could be made and stored.

4.4.3 Computer Capabilities

In order for the real time computer to perform its various tasks, requirements for the computer's speed, instruction complement, interrupt structure, and memory size were defined. The speed of calculation is generally proportional to the computer memory cycle time, since all instructions are stored in, and must be read from memory before execution in the central processor. Most instructions also involve data stored in memory. Thus, a state-of-the-art memory cycle time is desired, i.e., about one microsecond. The most common instructions appearing in an attitude maintenance algorithm are "Add," "Subtract," "Multiply," "Fetch," and "Store." In general, double-precision is necessary, i.e., 30 bits of accuracy.

In addition to the above considerations, several other application factors are also significant. For example, to allow the program running within the computer to be synchronized with the gyroscope data processing, an interrupt method must be available for the gyro electronics. Also, besides the real-time gyroscope operation, periodic transfer of data to and from a teletype and a magnetic type unit will be required. A waitlist clock will require a method to reinitiate a program delayed for a predetermined amount of time. The size of memory must allow storage for the real-time program and its data. Resident programs for teletype input/output data

conversions, task switching, interrupt determination, etc., must also be stored. Storage of a loader program in addition to the real-time program and servicing programs is desirable to allow insertion of new program segments without erasing the real-time program.

Recognizing these real-time computer capability requirements, a survey of small, commercially available general-purpose computers was made. Among those considered were the Varian DCI 620 and 620I, the Interdata INT. 3, the Raytheon model 703, the Scientific Data Corporation SDS Σ2, the SEL 810 A, and the Honeywell Computer Control Corporation DDP 516 and 416. The memory features of these units were considered adequate. Some of their other characteristics are shown in Table 4.4-1. The memory cycle and multiply times are shown in microseconds, and the availability of interrupt lines is indicated. The Honeywell DDP 516 was judged most suited for our application and a unit was received in November 1967.

The following is a brief review of the DDP 516's capabilities. The DDP 516 computer is a stored-program digital processor with a 2's complement numbering system. Addressing is direct, indirect, or indexed, or any combination of the three. The indexing of an address does not increase the execution time of an instruction. The coincident current ferrite core storage allows 8192 words of 16 bits each, and can be expanded to 16K or 32K with purchase of new memory packs. The hardware instruction capabilities are add, subtract, load and store both single-and double-precision, multiply, divide, and normalize. In addition, single word input (under program control) is allowed. Up to 16 peripheral devices may be connected to the input-output and interrupt lines, and the selection of allowable interrupts is programmable. The ASR-35 teletype unit is the primary input-output device furnished with the machine.

The speeds for various machine operations are as follows:

Memory cycle less than	1	microsecond
Load, Store, Add less than	2	"
DP Load, Store, Add less than	3	"
Multiply less than	6	"
Divide less than	12	"
1-word input/output	2	"

The ASR-35 teletype is used both for preparation of program source tapes and for loading of object programs into the computer's memory.

Table 4.4-1

Comparison of Computer Characteristics

TYPE	MEMORY CYCLE TIME, μ SEC	ADD μ SEC	MULTIPLY μ SEC	INTERRUPTS
SYSTEMS ENG. LAB. 810A	1.75	3.5	7	*
COMPUTER CONTROL CORP. 516	0.96	1.92**	5.28*	*
COMPUTER CONTROL CORP. 416	0.96	1.92**	NO	-
VARIAN DATA 620	1.8	3.6	18*	-
VARIAN DATA 620I	1.8	3.6	18*	-
RAYTHEON 703	2.0	4.0	*	1
INTERDATA 3	2.0	20	100	1
SCIENTIFIC DATA SYSTEMS Σ2	0.9	2.3	10	*

* OPTIONAL
** DOUBLE PRECISION WITH MULTIPLY OPTION

During real-time operation, the test engineer via the teletype keyboard will initiate and direct test or monitor programs. This computer capability will enhance test operations. (The interface hardware which connects the gyroscope package to the computer will be described later.)

4.4.4 Programming Requirements

The basic DDP 516 is not supplied with real-time software. This paragraph describes the programs developed for our application. Interrupt servicing requirements are presented and the initialization, data transfer (via interrupts), and data processing structure of programs are described. Examples of the maintenance of the attitude matrix and gyroscope performance programs are given. Finally, the real-time executive and the time-sharing teletype monitor program are explained.

During real-time operation, the computer, upon receipt of a program interrupt, will jump to a routine that was developed to determine which peripheral device issued the interrupt. This is done by commanding each device in sequence (through an SKS instruction), to return to voltage on the "device ready line" (within 2 microseconds) if it was not interrupting. The voltage causes a program skip to the next instruction. If no voltage is returned, the next instruction executed causes a jump to the program segment which services that device. Bookkeeping is also provided so that, after the interrupt is serviced, the interrupted program may be resumed.

Because more than one peripheral device is allowed to interrupt, and since these devices require program servicing to be completed within certain times, the interrupt service routine must be kept as short as possible. The criterion for timing is that two interrupt servicings (for different peripherals) be completed within the time allotment for the most critical device. For example, in the gyro test package operation, the gyro information may be updated every 104 microseconds and the servicing of the gyro data peripheral accumulators must be accomplished within this update period. Because of these interrupt time restrictions, a job-switching executive program with priorities is necessary. The gyro interrupts will, therefore, not only read gyro data, but also schedule the high priority gyro data use program.

A job using a peripheral device must be broken up into three sections: initialization, data transfer, and processing. The initialization section commands the peripheral to the appropriate mode, sets its interrupt mask, and tells the interrupt search program where the interrupt service routine for that device is located in memory. Following the initialization job, the data transfer phase begins. This phase operates entirely upon interrupt. This service routine determines when the data transfer is completed so that processing may begin.

In the case of an attitude maintenance program (the Algorithm), the initiation section will issue the "OCP" command (output control pulse, mode changes on/off, etc.) to the gyroscope interface hardware, initialize the attitude reference matrix, set the gyro mask (for interrupts), and store the address of the gyro reading (interrupt servicing) routine in a prearranged location. The initialization is then complete and it will return to the "end of task" section of the executive. The interrupt transfer section will read the three gyroscopes, store the data in prearranged data locations, and schedule the matrix update program through the executive. In addition, a short job will be scheduled which will restart the program that was in process when the interrupt occurred. The executive will then test the priorities of waiting jobs, and start the one with the highest priority. Usually the gyro data use program will carry the highest priority. The attitude algorithm then incorporates the latest set of gyro data into the attitude reference matrix. Upon completion, it returns to the "end-of-task" section to await the next set of gyro data. The attitude reference matrix will be available for printout, analysis, or velocity correction (when accelerometers are incorporated into the system). The signal to use or print the attitude matrix will be either programmed, for periodic reading, or attainable through a "start button interrupt" (an interrupt which occurs when the computer start button is depressed). The matrix will be printed when this interrupt occurs.

In a typical test, the programs described will be used to tell the computer (through the teletype keyboard) the test table's initial reference position and necessary inertial component compensation parameters. The test table is then repositioned and the computer calculates what the matrix should be, and compares it with the gyro data-produced matrix. The errors would be printed out using appropriate routines for data conversion and the teletype output. This teletype program has the same initialization, interrupt, and continue structure as the attitude matrix program. It involves less

computer action during interrupts, however, since only one word (one letter) is printed at each interrupt. The only processing is the acquisition of the word to be printed at the next interrupt.

If one wishes to perform a gyro performance test, the same general outline above would be used and, instead of calculating an updated attitude matrix, the gyro pulses would be accumulated. When enough time had elapsed (the computer would count the number of gyro interrupts to determine time), the interrupt schedules the drift calculation program and removes the gyro mask to prevent reading of any more data. The drift calculation program then determines drift terms from gyro pulse accumulations taken at several table orientations. Appropriate corrections for earth-rate, which is defined for each table orientation, are included. Data accumulated at each orientation is stored between orientation changes, and final processing and print-out takes place when the test sequence is over.

The executive program has been mentioned several times, and a more detailed description of it is in order. The scheduling section of the executive receives two pieces of data from the calling program. These are the priority of the job to be scheduled, located in the accumulator (A - register) by the calling program, and the address of the first instruction to be executed in the scheduled program, located in the low-order accumulator (the B-register). The scheduling section stores this data in a list, along with previously scheduled jobs, and sets up bookkeeping for the storage of the priority and location of the next job. It then returns control to the calling program. This scheduling consumes about 20 microseconds. Upon completion of a job, instead of issuing a halt (which will destroy any real-time work), it transfers control to the "end-of-task" section of the executive. This section enables the interrupt, does minor bookkeeping, and begins to search the waiting job list for the job with the next highest priority. During this time interrupts are allowed and are serviced normally. Should an interrupt which schedules a job occur during this search, the new job will be included in the search. After the highest priority waiting job has been found, the executive will readjust the job task waitlist as required, and start the new job.

Most programs need input, output, or both, from the teletypewriter. A time-sharing typewriter monitor program was written since program execution should not be prohibited because another will use the typewriter in the future. The DDP 516 supplied typewriter software was not compatible with our real-time system application, it has no provision for time sharing. The monitor forms a list containing the following data concerning the

typewriter: 1) address of calling program, 2) input or output?, 3) location of data buffer, 4) priority of calling program, 5) address of first interrupt service routine, 6) other data necessary for bookkeeping. When a call to the typewriter monitor is made, this data is stored, and the calling program is "put to sleep" (until the input or output data is transferred). The monitor then checks to see if the teletype is busy; if not, the input-output data transfer job is started. The transfer of data is then done under interrupt control; this allows time-shared processing with other jobs. When the final data transfer is done, the teletype-monitor program is scheduled to perform the translation of data or the resumption of the calling program. The busy flag is turned off, and the section of the monitor which searches the teletype waiting list is scheduled again.

The programmer's job is using the executive and the teletype-monitor is to know what data is necessary, and where it should be located. Because the program operates in real-time, routines which operate under inhibit interrupt must remain fairly short, and cannot contain loops of unknown length (such as one which asks if a peripheral is ready, and asks again if not). Such an unknown-length program may be operated under interrupt enabled mode, but it should have a fairly low priority.

The executive, teletype programs, and interrupt search programs have been written. At this time an attitude maintenance program using third-order quarternion update formula is in preparation.

4.4.5 Interface Hardware Development

As discussed in the program development section, the SKS instruction (skip if ready-line set) is used in the peripheral equipment search. In addition, the other input/output commands, OTA (output from accumulator), INA (input to accumulator), OCP (output a control pulse), and SMK (set interrupt mask flipflop) correspond to required voltages to transfer data and control information. In case of the ASR-35 teletypewriter, the interface logic, which uses signals from the computer and from the teletype unit, are furnished with the computer. The interface for the gyroscope electronics was designed and fabricated at MIT/IL using micropac circuit modules that are identical to the type used in the computer itself. This assured interface logic level compatibility and facilitated the design. The actual interface

hardware was assembled and installed in an unused area on one of the computers' swingdrawers shown in Fig. 4.4-2. A close-up of the gyro interface assembly is shown in Fig. 4.4-3. The computer power supply supports the logic power requirements for this assembly.

The instructions which were necessary are as follows:

INSTRUCTION	FUNCTION
INA'0017	Read X gyro counter
INA'0027	Read Y gyro counter
INA'0047	Read Z gyro counter & reset counters
OCP'0007	Reset counters and enable time scaler
OCP'1007	Disable scaler (turn off interface)
SMK'20	Set gyro interrupt mask if bit 12 of A is set
SKS'0107	Skip if gyro not interrupting

The major signal lines to and from the computer are as follows: the address bus (ADB) containing ten lines which specify which device and which function is to be accomplished, the 16-line input bus, the 16-line output bus, the device ready line (DRLIN-), and the interrupt line (P1L00-).

In addition to the interface logic itself, three up-down counters for the gyroscope $\pm\Delta\theta$ pulses, and one clock counter (scaler) are necessary. A block diagram of the complete gyroscope interface is shown in Fig. 4.4-4.

Figure 4.4-5 shows the timing of pulses issued by the computer to the interface electronics during an INA instruction.

The time scaler is an 8-bit binary counter with a parallel output. Any number of counts of the clock from 1 to 256 may be selected by performing a logical "and" for the desired bit configuration. For example, with 9600-Hz clock, select 96 counts for a 10-millisec interrupt.

The counter section has three 8-bit up-down counters. The + and - lines for each axis are separate and pulses will never occur simultaneously. A pulse on either line is used to select the counting direction. The pulse is delayed and shaped before arriving at the counter. On receipt of

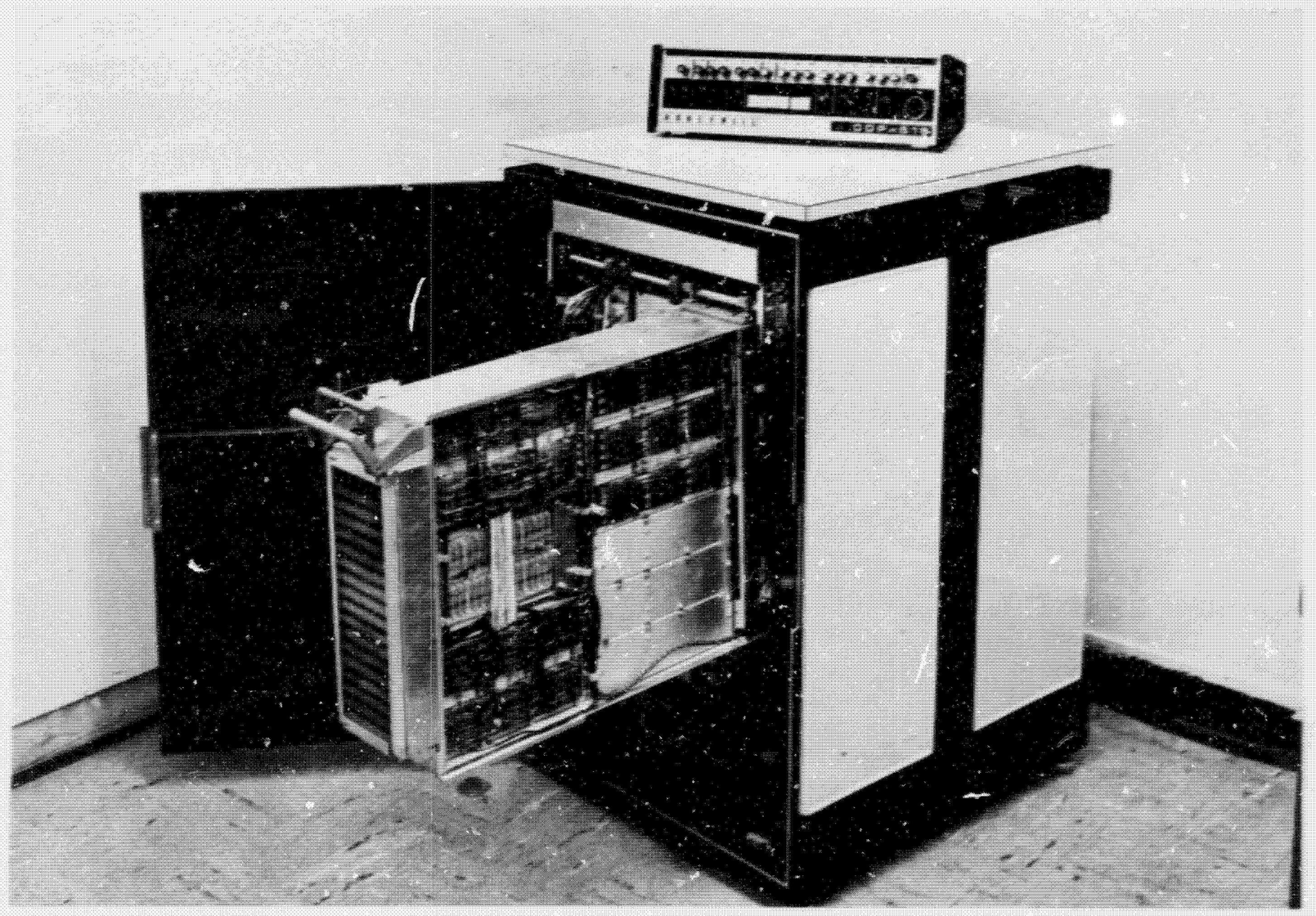

Fig. 4.4-2 Computer with interface modification.

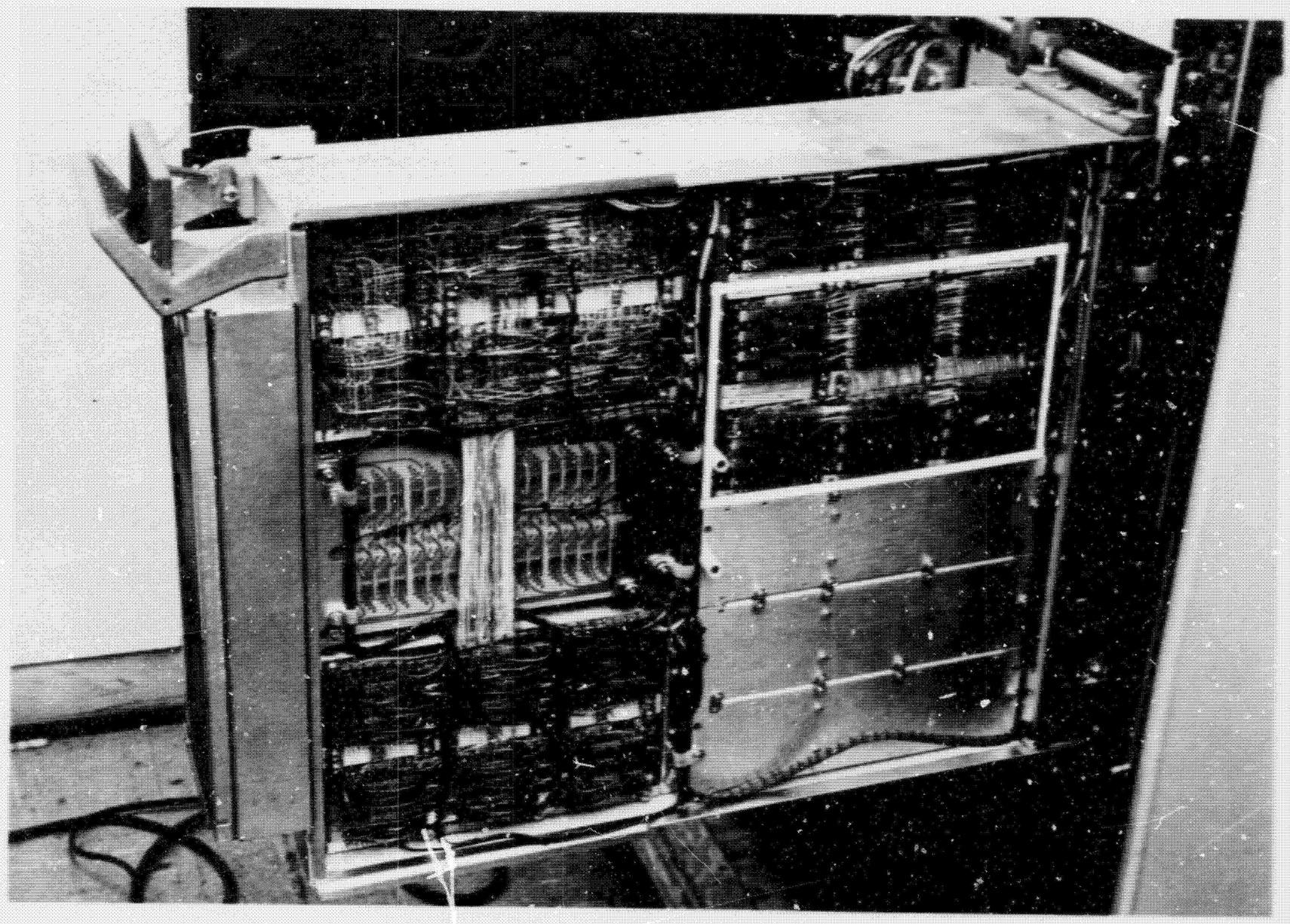

Fig. 4.4-3 Memory drawer with interface hardware outlined.

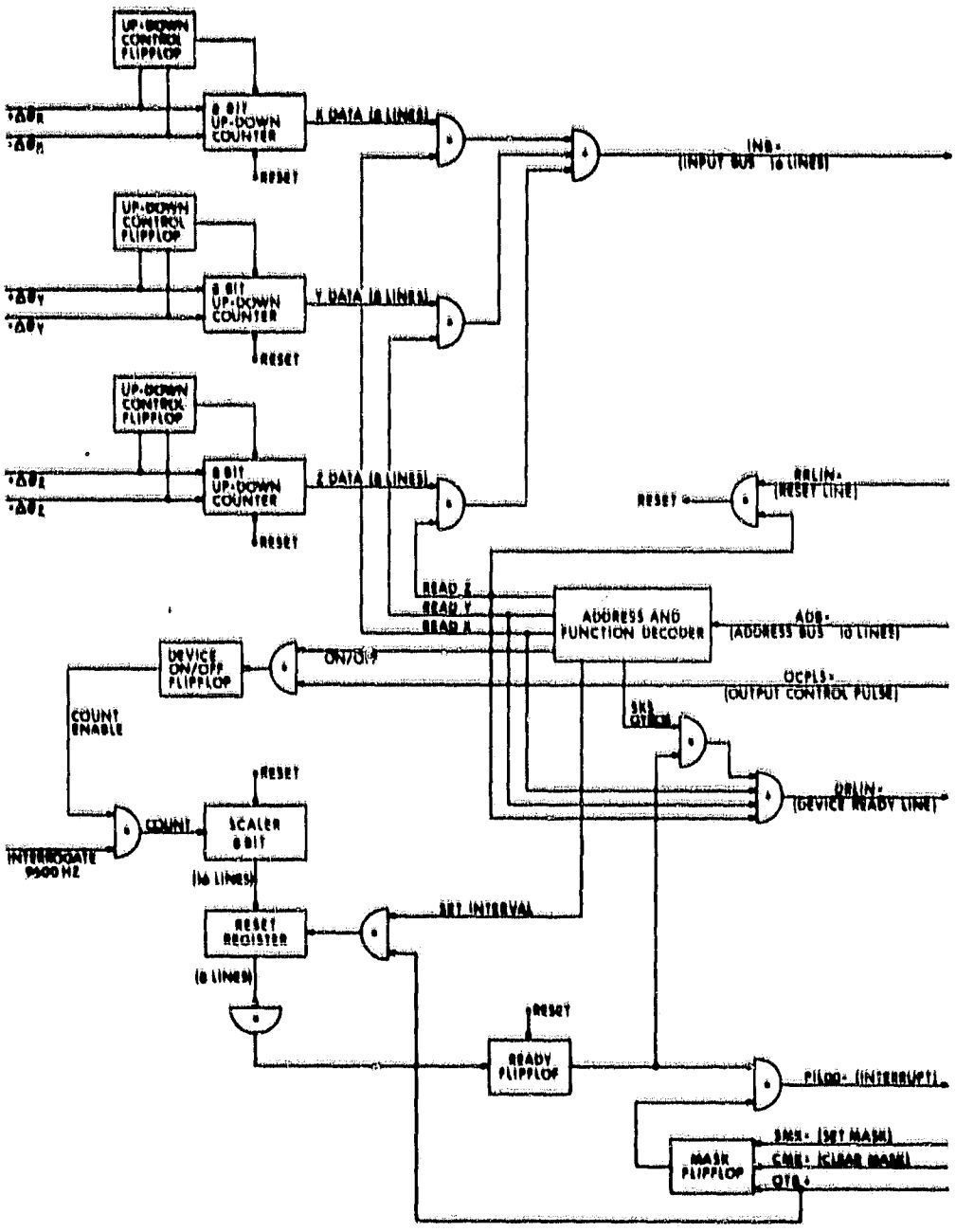

Fig. 4.4-4 Functional - block diagram gyro counter interface.

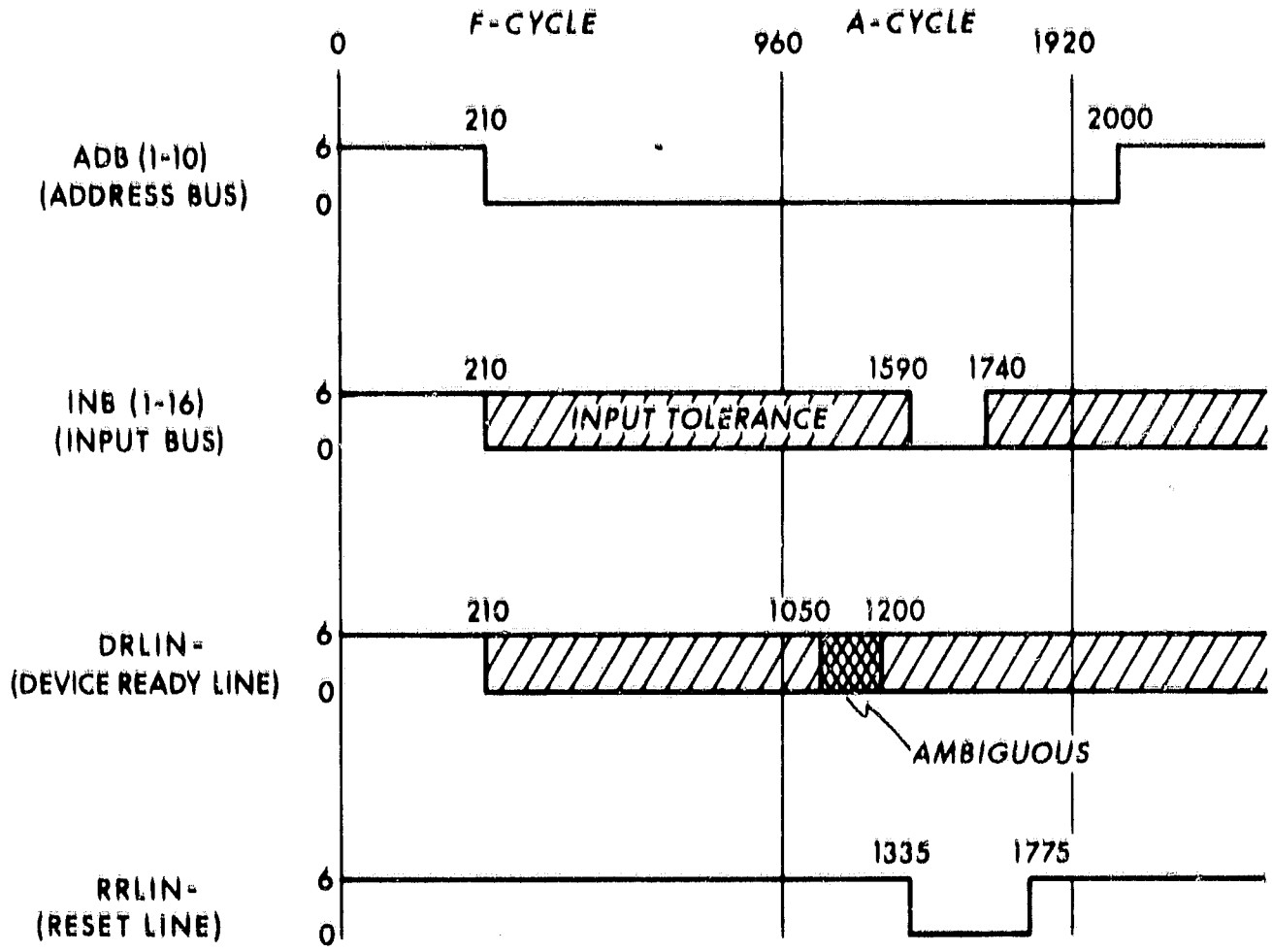

NOTE:

- IF DRLIN OCCURS BEFORE TIME 1050, DATA TRANSFER WILL OCCUR AND RRLIN- WILL BE ISSUED
- TIMES ARE IN NANOSECONDS

Fig. 4.4-5 Typical input/output instruction I/O control signal timing (typical)

interrupt 'bn', the computer will jump to a program sequence in which enabling signals are generated to bring the contents of the counters to the input bus. The timing of these signals is shown in Fig. 4.4-6.

In order to allow more flexibility in the gyro interface, three additions are being developed. The first is the capability to preset the time scaler to some value other than 96, which corresponds to 10 milliseconds. This option would simplify testing of different algorithm update rates. This would be accomplished by mechanizing an OTA 7 instruction, with the desired number of gyro clock counts in the accumulator. The time per update, then, could be adjusted from 104 microseconds (one pulse time at 9600 pps) to 26 milliseconds, or 256 counts. The second modification is of use in simulating a Digital Differential Analyzer with a DDP-516 program. This modification consists of putting data from all three gyros into one word. The gyros would be read every gyro clock pulse, and this modification would shorten the processing time for gyro data. At present, the gyro data is in 8-bit 2's complement form, whereas the computer uses 16-bit 2's complement form. The conversion from 8-bits to 16-bits takes 5-6 machine cycles per word, and a fairly simple modification to the gyro interface would eliminate this processing time.

The efficiency of the utilization of the computer facility from an operator or programmer standpoint will be greatly improved with addition of the high-speed input, output capability. An interface is being built which will allow the use of an incremental magnetic tape unit. This will increase the loading speed from 10 frames per second to 300 frames per second. The savings in loading speed is significant. The time for a full memory load would be reduced from 45 minutes to 1-1/2 minutes.

The DDP-516 does not have an interna. clock; a desirable addition to the facility would be a waitlist clock, that is, a hardware register which may be preset and counts up and interrupts on overflow. This would be useful for timing test durations and in rate calculations from position data.

In addition to programming for the DDP-516 Executive and System Testing routines, it would be desirable to expand the YUL compiler to assemble DAP language programs on the IBM 360. This would enable programming on cards, a useful storage and editing medium, and could provide correctly formulated tapes.

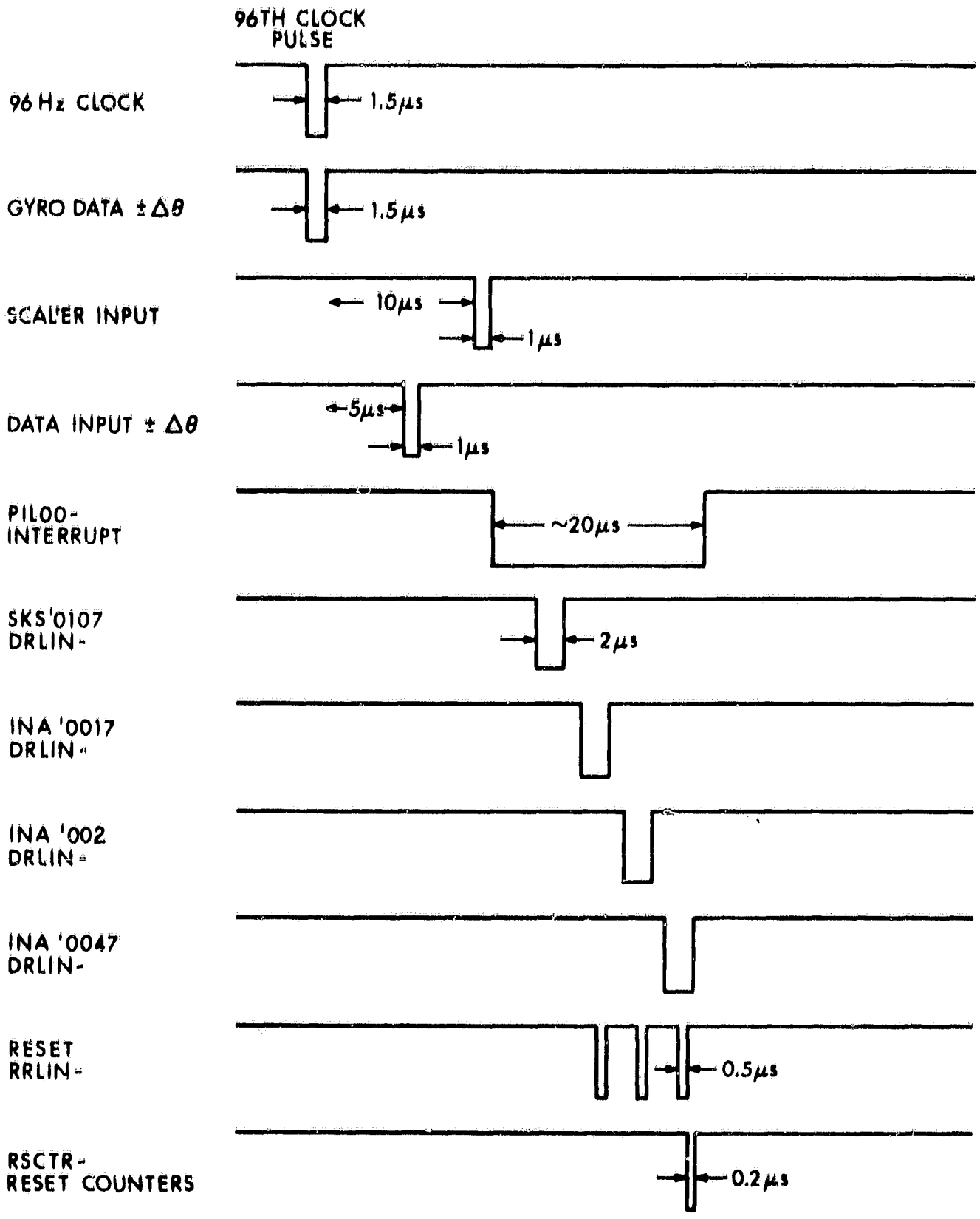

Fig. 4.4-6 Timing chart for gyro counter interface equipment.

4.5 Pulse Torque Control Loop and Power Supply Support Electronics

4.5.1 Introduction

The electronics is housed in a Support Electronics Console (SEC) and for the most part represent elements that are normally considered part of the airborne electronics. A photo of the console is shown in Fig. 4.5-1. Note that controls and monitoring provisions are included on the console that allow independent checkout and moding. In addition, provisions for remote GSE moding and monitoring are included. The upper panel includes control provisions for the frame heat exchanger (coolant loop) discussed in Section 4.3.

4.5.2 Summary

The major electronic elements of the SEC are:

1. Three Ternary Pulse Torque Electronics Control Loops

   This circuitry is used to provide closed-loop-ternary-pulse torquing to each of the system gyros. The present design allows a maximum torque output equivalent to a gyro input-axis rate of 0.3 radian per second. The torquing threshold and interrogation rates are adjustable.

2. Ducosyn Excitation Power Supply

   This power supply provides a 8V-rms 9600-Hz excitation for the gyro suspensions and signal generators. A transformer located on the gyro package fram steps the 26-volt-supply output down to 8 volts. A signal from the transformer secondary is fed back to the power supply and functions to regulate the excitation at the frame.

3. Two-phase Wheel Supply

   This unit delivers wheel power to the 3-system gyros. Its output voltage is 28V-rms at 800-Hz. Remote sensing from the gyro package is used to improve terminal voltage stability of the wheels.

4. A ± 15-Vdc Power Supply

   This supply provides excitation for the integrated amplifier circuits used in the individual gyro temperature controllers.

5. DC Torque Control

   A manually controlled torquer circuit is provided which permits open loop tests such as those for the determination of the IA misalignment angles.

A discussion of the operating features, design parameters, and functional concepts of each are discussed in the descriptions that follow.

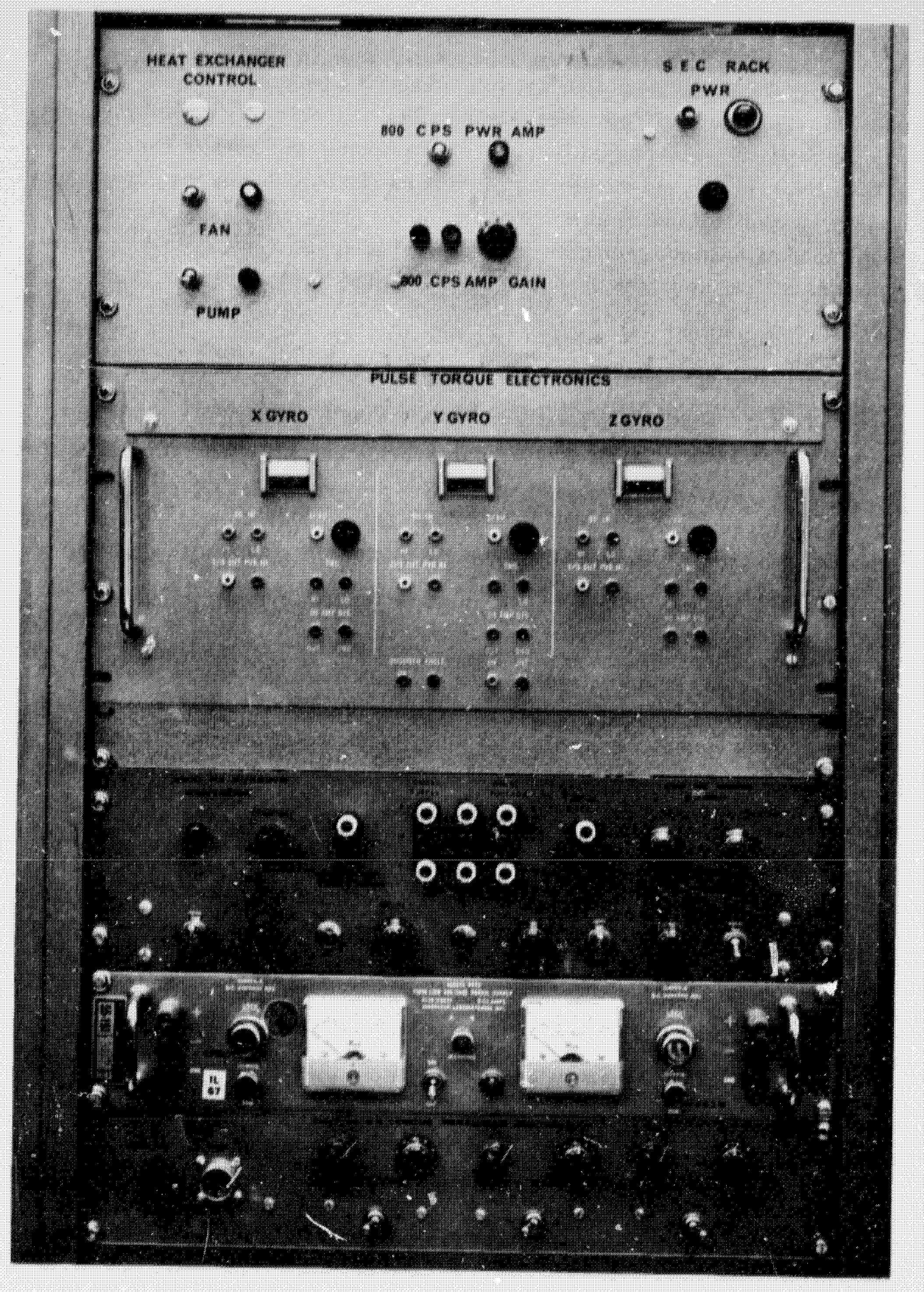

Fig. 4.5-1 Support electronics console.

4.5.3 Ducosyn Excitation Power Supply

The 9600-Hz ducosyn excitation power supply is composed of three basic sections:

Automatic Amplititude Control Section,
Filter,
Power Amplifier Section.

A block diagram is shown in Figure 4.5-2.

The A.A.C. (Automatic Amplitude Control) accepts the feedback signal from the gimbal-mounted transformer, converts it to dc, and compares it to a reference level. The output is then chopped at a 9600-Hz rate, supplied from the clock input, and applied to the filter.

The filter section is a constant, K, LC filter. The filter contains the trimming adjustments for phase control between the input and the output signal.

The power amplifier section is a class B push-pull amplifier with a transformer-coupled output. The power stages are driven by a preamplifier that receives its input from the filter section. Local feedback from the power amplifier output to the preamplifier is used for gain stability and reduction of distortion.

The design specifications for the power supply are:

Output Voltage:	26 volts rms at 9600 Hz.
Nominal Power Output:	6 watts
Voltage Regulation:	-0.2% to 0.3% with dc bus variations of 24 to 36 Vdc.
	-1.5% to +1.0% with temperature variations of -50° to 200°F.
Phase Angle Variation:	$+5^{\circ}$ to -3.5° for a temperature variation of -50° to 200°F.
Total Distortion:	1.2% of 26 volts.

4.5.4 Gyro Temperature Controller ± 15-Vdc Supply

The ±15-Vdc supply is a pulse width modulated supply which supports thermal control electronics.

The supply is composed of four basic sections:

Frequency Control Section,
Modulator Section,
Power Section,
Comparator Section.

A block diagram is shown in Fig. 4.5-3.

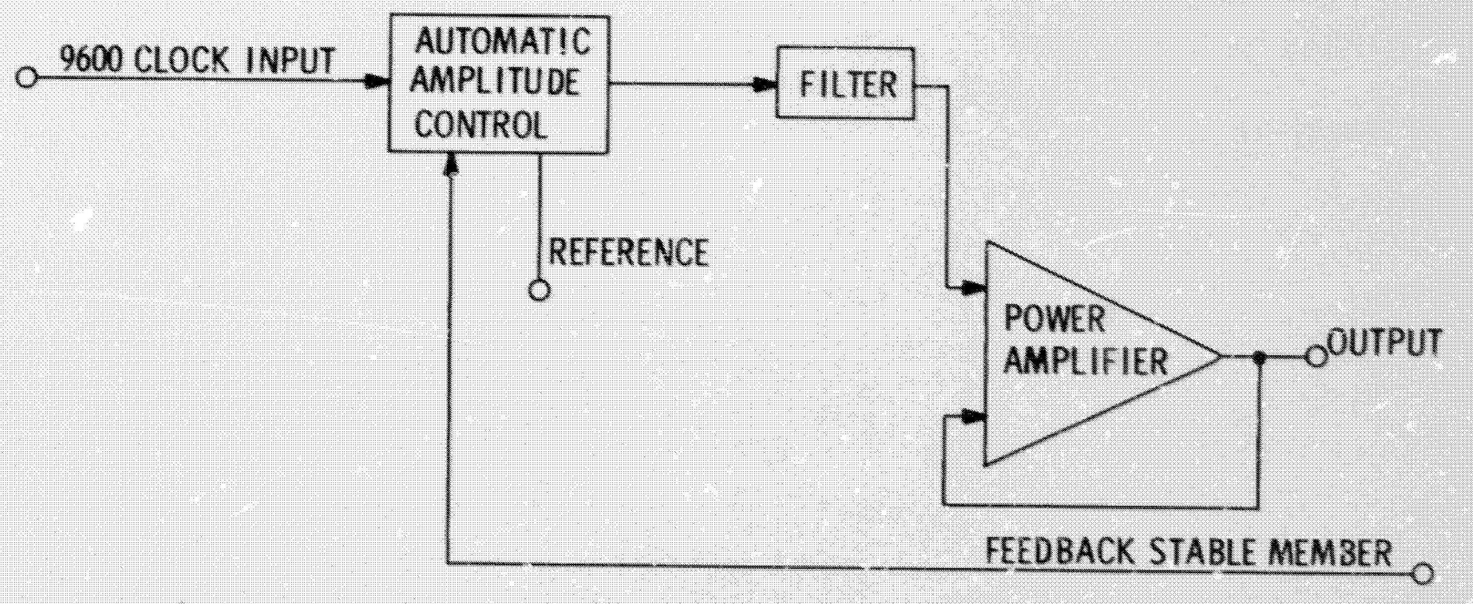

Fig. 4.5-2 Ducosyn 9600 cps power supply.

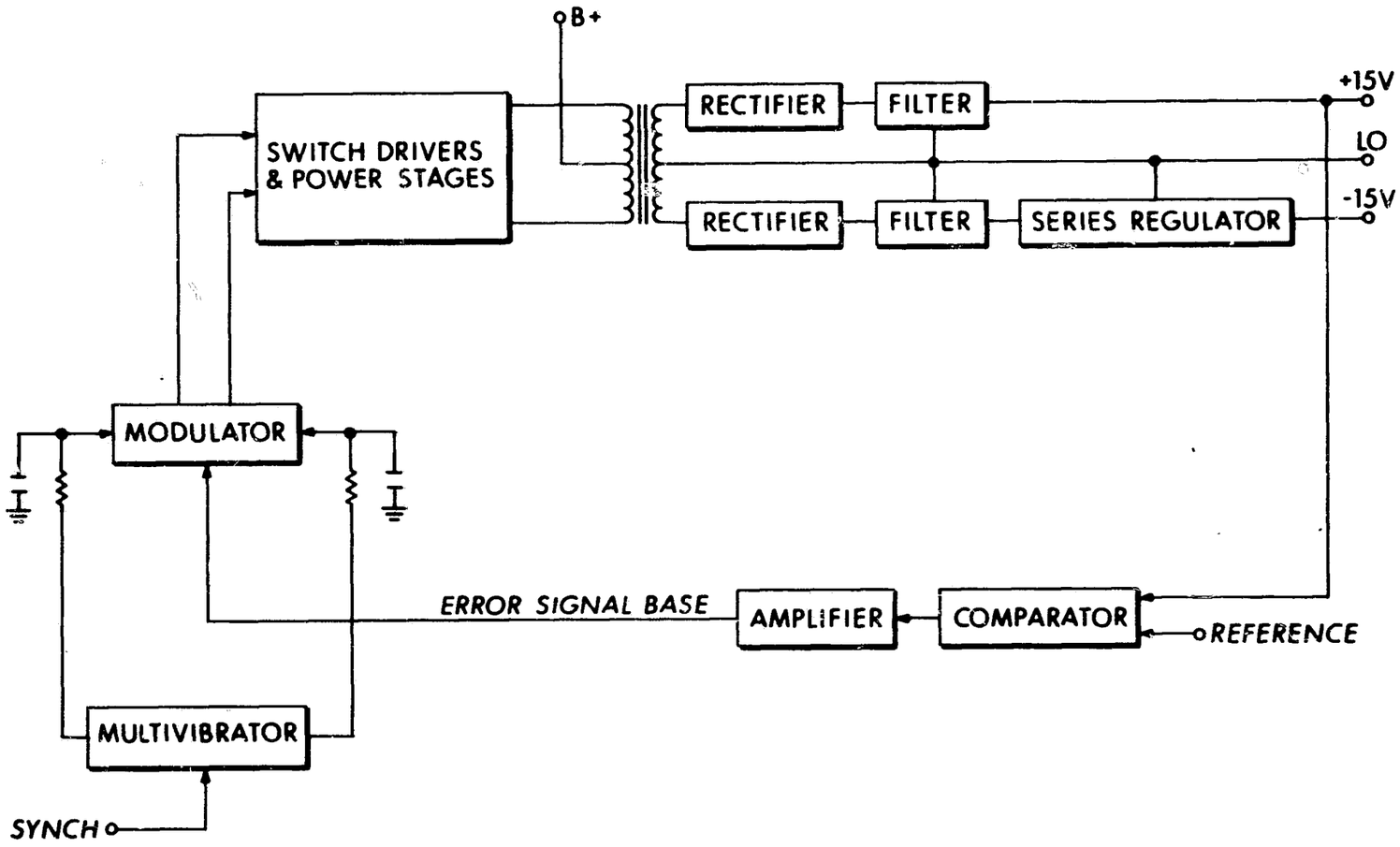

Fig. 4.5-3 ±15v supply.

The frequency control section is a free-running multivibrator which is synchronized at 51.2-k pps by an external input. The multivibrator output is integrated to produce a triangular-shaped wave form which produces the voltage slopes for pulse-width modulation.

The modulator section is a differential amplifier whose inputs are the integrated multivibrator outputs and the error signal bias from the comparator. The bias signal is applied to the emitters of the differential amplifier and controls where on the slope of the integrated wave forms the modulator operates. As this bias varies the output pulse width of the modulator varies.

The power section is a class B power stage, with drivers, which is transformer-coupled to the rectifier and filter sections of the output. The input to the power section is the variable pulse width output of the modulator. As loads or B+ vary the pulse-width input varies to maintain a constant output voltage from the filters.

The comparator section compares a feedback signal from the +15-volt output to a reference signal. The difference between the supply's output and the reference is amplified and used as the error-signal bias input to the modulator. A series regulator was added to the -15-volt output to provide the required regulation.

The design specifications for the power supply follow.

Output Voltage:	±15 Vdc
Maximum Power:	7.5 watts per side
Voltage regulation with buss variations of 22 to 36 volts (500-ma load):	-15 volts - 0.1%
	+15 volts - 1.7%
Load Regulation for 75-ma to 500-ma Variation:	-15 volts - 0.3%
	+15 volts - 0.1%

Output noise less than 100-mv peak.

4.5.5 800-Hz Wheel Supply

This supply is a 1% 800-Hz, 28V-rms supply based on the Block II electronics. It has an additional front panel amplitude control for flexibility. The supply is synchronized from an external clock, but has a free-running multivibrator for operation when sync is lost. The stability and distortion specifications are the same as the Apollo circuit's.

4.5.6 Pulse Torque Electronics

A) General

This description covers the basic operation of the gyro-pulse torque electronics, the design requirements for proper operation, and design specifications for each functional element. In addition, some of the control-loop problem areas which require further study and improvement are also reviewed. Figure 4.5-4 is a photograph of the three-axis pulse-torque control drawer located in the SEC.

A simplified block diagram of the gyro-pulse-torque electronics is shown in Fig. 4.5-5. As shown, the pulse-torque system mechanization is defined by two basic control loops: a dc current loop that maintains a precisely regulated torquing current and a torque-rebalance loop that detects gyro float motion and controls current switching to the gyro torquer to return the float to its null position.

The following sections describe the operational features of both the torque rebalance and current control loop. Nominal design parameters are outlined in Section E. A discussion of design problems and anticipated design improvements are reviewed in Section F.

B) Torque Rebalance Loop

The gyro float may be viewed as a torque summing element and an angular rate about the case input axis results in a torque which causes the float to rotate about its output axis. This rotation is sensed by the gyro signal generator (SG). The SG output magnitude, a 9600-Hz sine wave, is proportional to the float angle displacement from null and its phase (0 or π relative to the reference excitation voltage) is a function of the angular direction of rotation from the null position (positive or negative).

The torque command operates on the basis of the SG output to control the current to the torque generator via the operation of the current switch. The current polarity is set so that the torque produced rotates the float back towards the null position. The control loop is digital in nature and the torque generator is energized by current pulses of fixed amplitude and width.

The loop operation is such that the gyro SG signal is amplified and routed to positive - and negative-phase threshold-level detectors. A pulse (interrogate pulse) samples the level-detector outputs and is phased to correspond with the peak of the 9600-Hz SG output. The interrogate

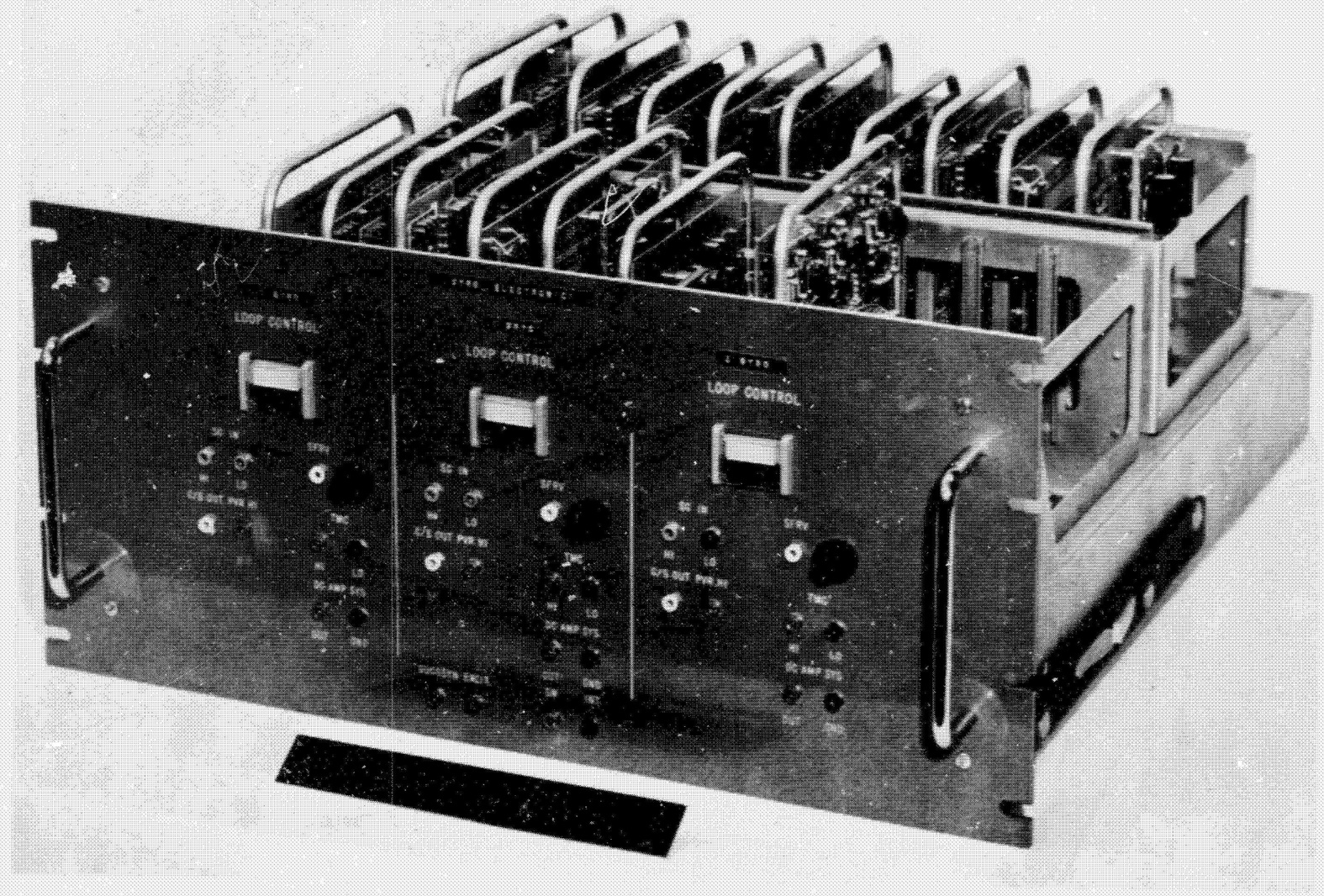

Fig. 4.5-4 Three-axis pulse torque control drawer.

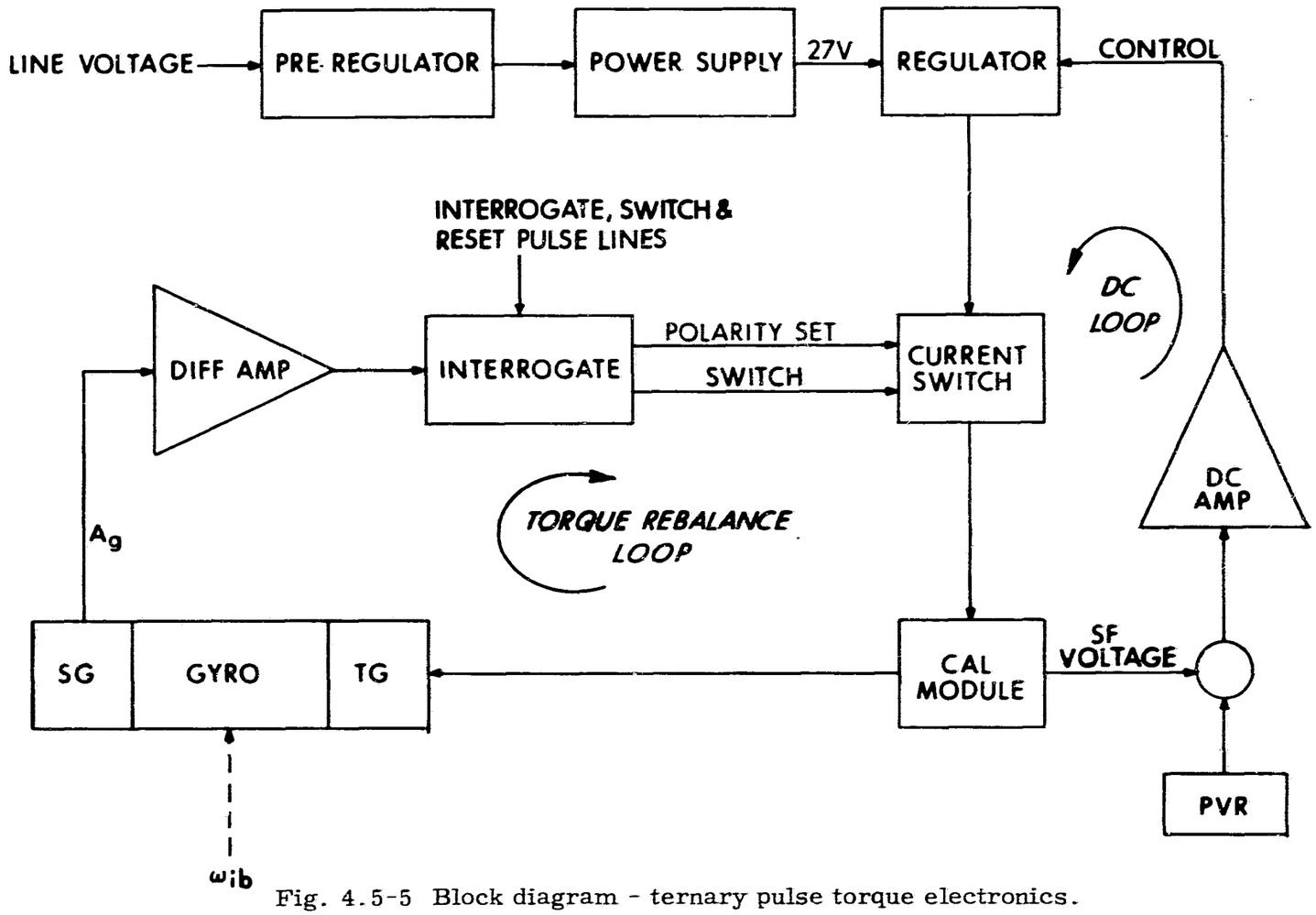

Fig. 4.5-5 Block diagram - ternary pulse torque electronics.

pulse rate may correspond to any integral submultiple of 9600 pps. (The test electronics, for example, have provisions for interrogation rates of 9600, 4800, and 3200 pps.) If the SG signal exceeds the level-detector threshold at the interrogation time, the logic sets the polarity (i.e., direction of flow) in the current switch. The polarity is selected so that the direction of current flow through the torque coil will result in a torque that drives the float back to the SG null position. After the polarity is set, a second pulse (switch pulse) turns the torquing current on. Before the next interrogate time a reset pulse occurs which turns the current switch off. The interval between the switch and reset pulse determines the duration of current flow, i.e. torquing-current pulse width. (In the test electronics used the interval between the switch and reset pulse is also selectable.) A functional diagram of the torquing control loop (interrogator) logic is illustrated in Fig. 4.5-6. (Relative timing pulses and control outputs to the current switch for an assumed SG output signal that exceeds the + level is also shown.) (The actual circuitry uses NAND-DTL logic.)

The current switch is illustrated in Fig. 4.5-7. The torquing polarity commands from the interrogator set diagonal opposite pairs of transistors of the "H" switch (Q_2 and Q_4 or Q_3 and Q_5). The transistors function as a double-pole double-throw switch that feeds current in one direction or the other dependent on the torquing polarity desired. Transistor Q_6 turns the torquing current on when a torque set command is received from the interrogator logic. Transistors Q_6 and Q_7 function as a single-pole double-throw switch so that, when no torque current is required, current is by-passed through a dummy load into the scale-factor resistor. The voltage across the scale-factor resistor is compared with a precision-voltage reference in the input stage of a high-gain dc amplifier. The amplifier is part of the dc control loop that maintains a precise fixed-current level. The current bypass minimizes load variations in the dc current control loop and assures that the loop does not go out of its linear operating region. Note also that an RC compensation network is connected across the torquer. It functions to tune the torquer so that the load seen by the switches and current loop is purely resistive.

In summary, the torquing loop operates such that current is applied as pulses and even at maximum commanded torque a short off period exists in every clock interrogation interval. The average restraining torque for a given measurement period is proportional to the number

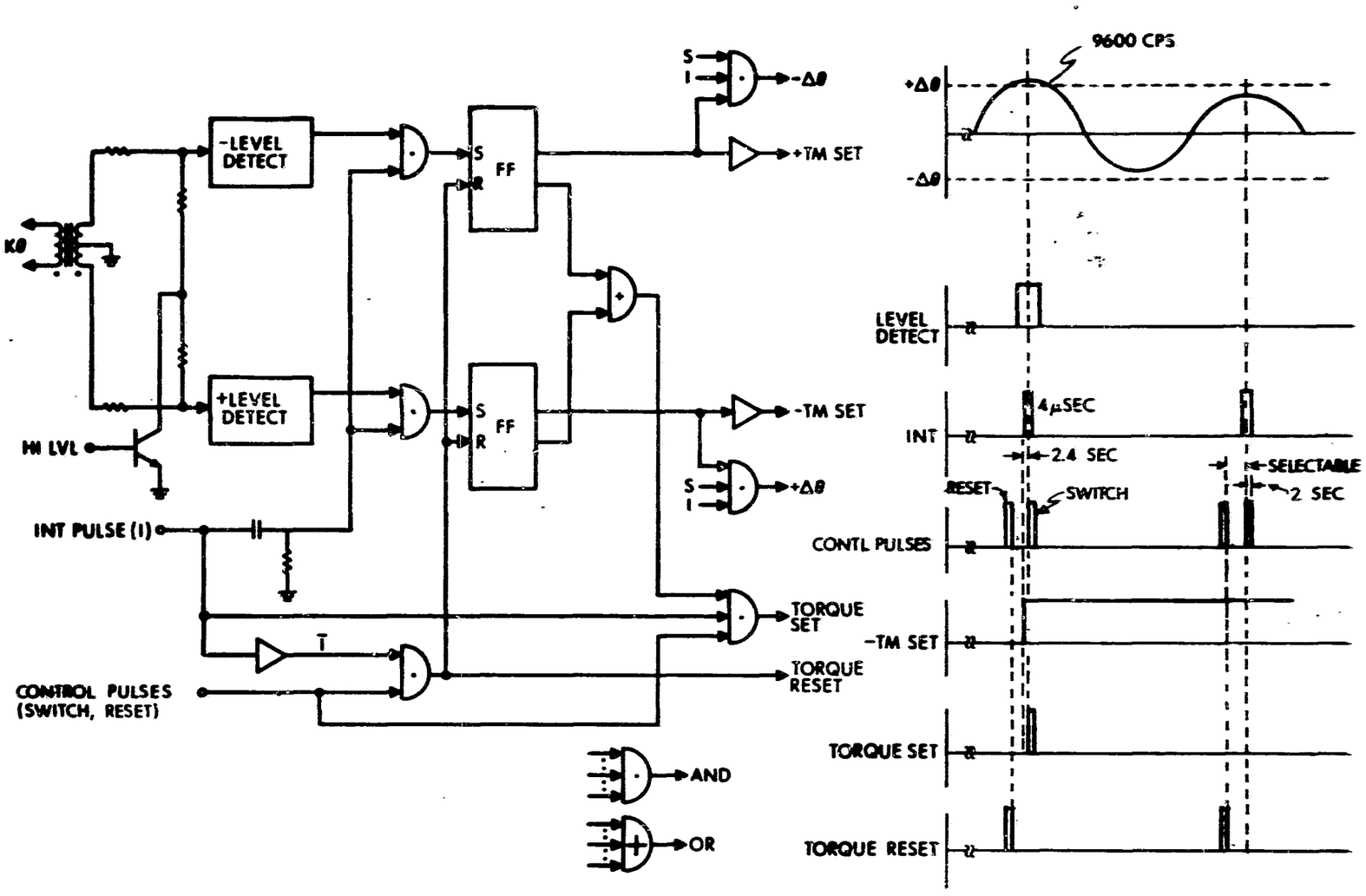

Fig. 4.5-6 Interrogator logic and timing.

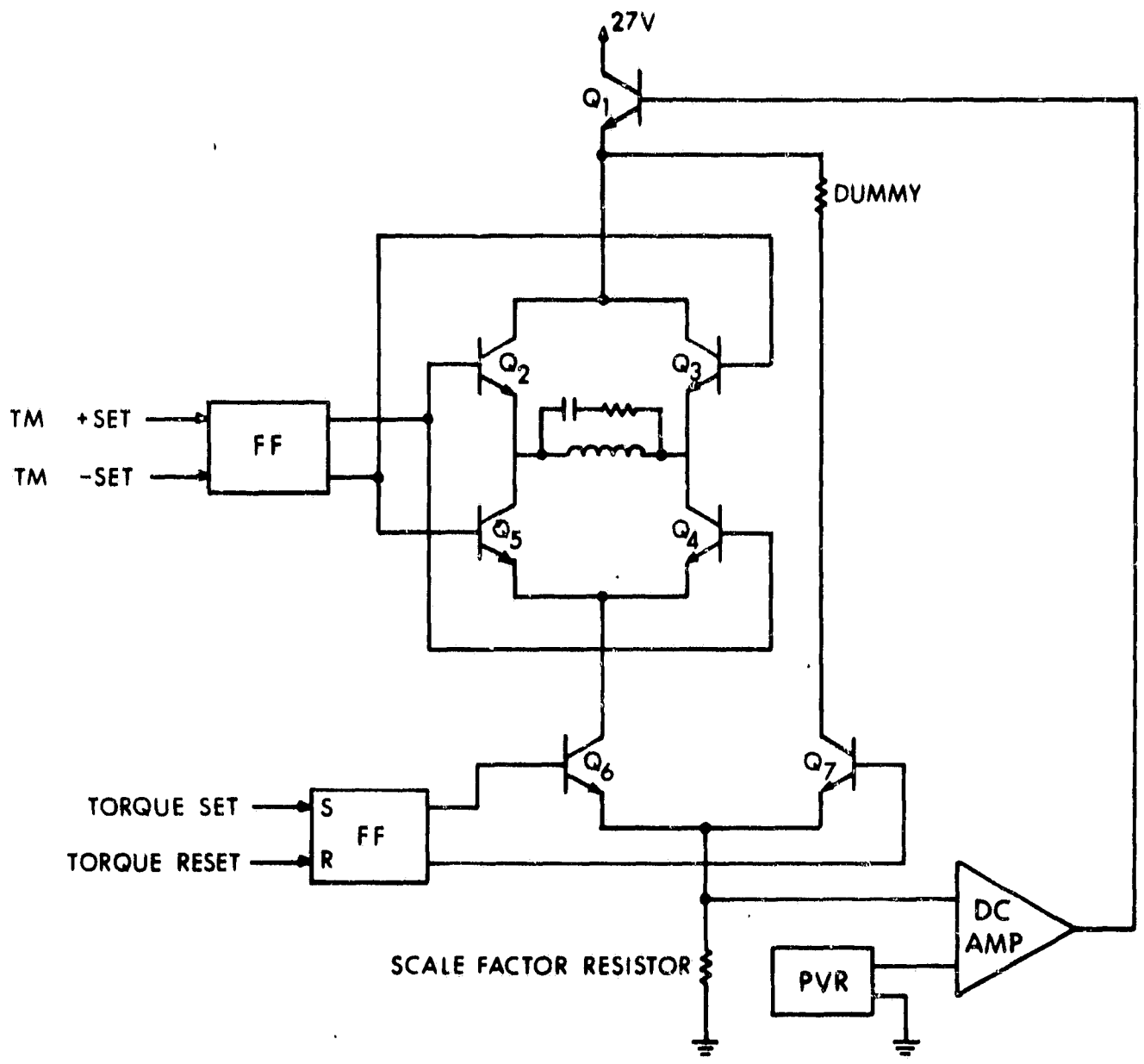

Fig. 4.5-7 Current switch.

of torque pulses applied during the period. Thus, an equivalent torquing pulse rate exists for each constant-level input rate to the gyro. For an ideal permanent-magnet torquer, however, the pulse rate has no effect on the amount of torque derived from each pulse or the float response to each pulse. Each torque pulse represents an equivalent increment of indicated float angle change, $\Delta\theta$. They are represented in the control loop mechanization by another pulse that is issued either on the $+\Delta\theta$ or $-\Delta\theta$ line for a torquing pulse that is commanded. The pulse line polarity is set to correspond to angular rates along the positive or negative sense of the instrument input axis, respectively.

C) DC Current Loop

The current loop operates to precisely regulate the torquing current magnitude to a fixed amplitude. A functional block diagram of the current loop is shown in Fig. 4.5-8. The series regulating transistor is controlled to maintain a constant current with load and power supply variations. The load variations result from changes in current polarity and switching between the torquer coil and dummy load. Current changes are detected by comparing the voltage drop across the scale factor resistor (R_{SF}) with a voltage developed by the precision voltage reference (PVR). Voltage differences are amplified by a differential amplifier and its output signal is then fed back to the current regulating transistor.

D) Design Parameters

The following is a brief summary of some of the nominal design parameters of the pulse torque electronics (refer to Fig. 4.5-9).

1. Gyro Preamp (differential amplifier)
Gain = 45V/V rms

2. AC Differential Amplifier

a) Gain = 45 for a 20 $\overset{\frown}{\text{sec}}$ threshold (3200-pps interrogation)

b) Gain = 130 for a 7 $\overset{\frown}{\text{sec}}$ threshold (9600-pps interrogation)

3. Interrogator

a) Trigger level 0.70-rms-matched with 10% for 0 and π phase inputs.

b) Pulse rise and fall time less than 60 nanosec for input interrogate, switch and reset pulse rise and fall time of less than 70 nanosec.

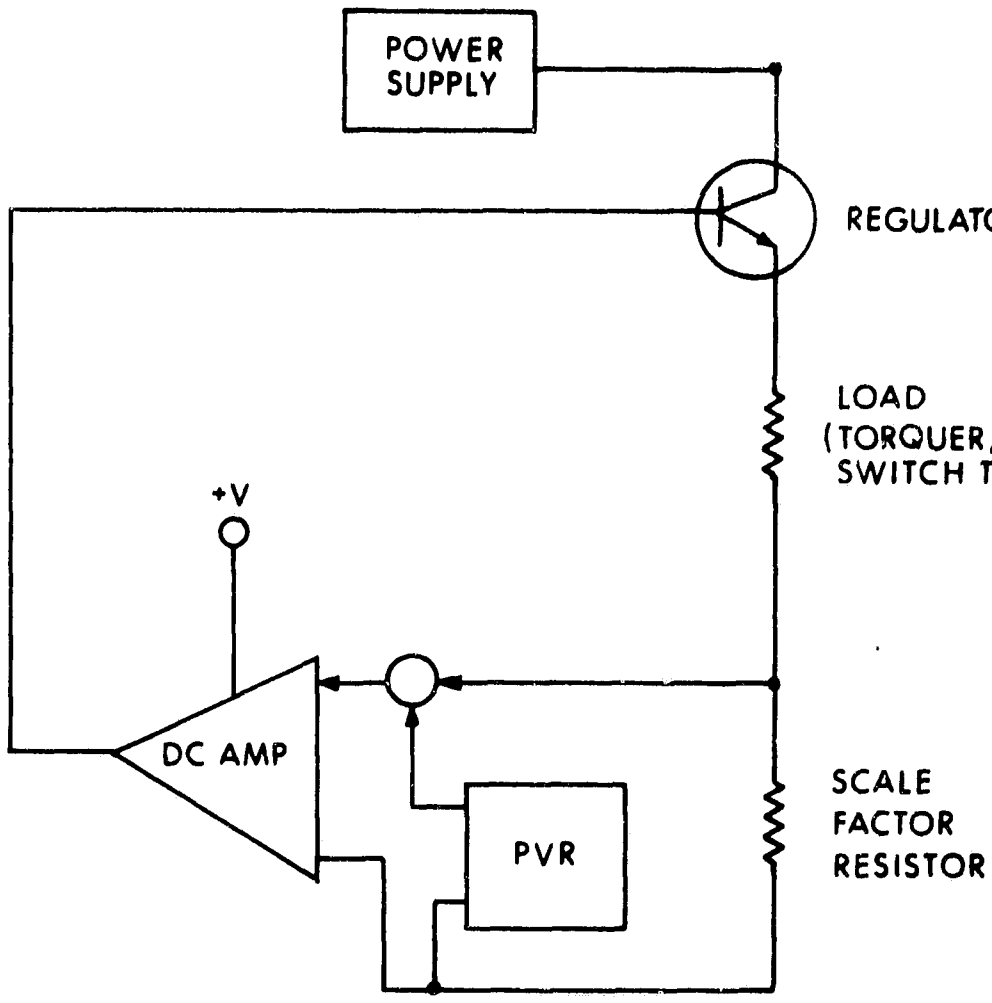

Fig. 4.5-8 DC current loop.

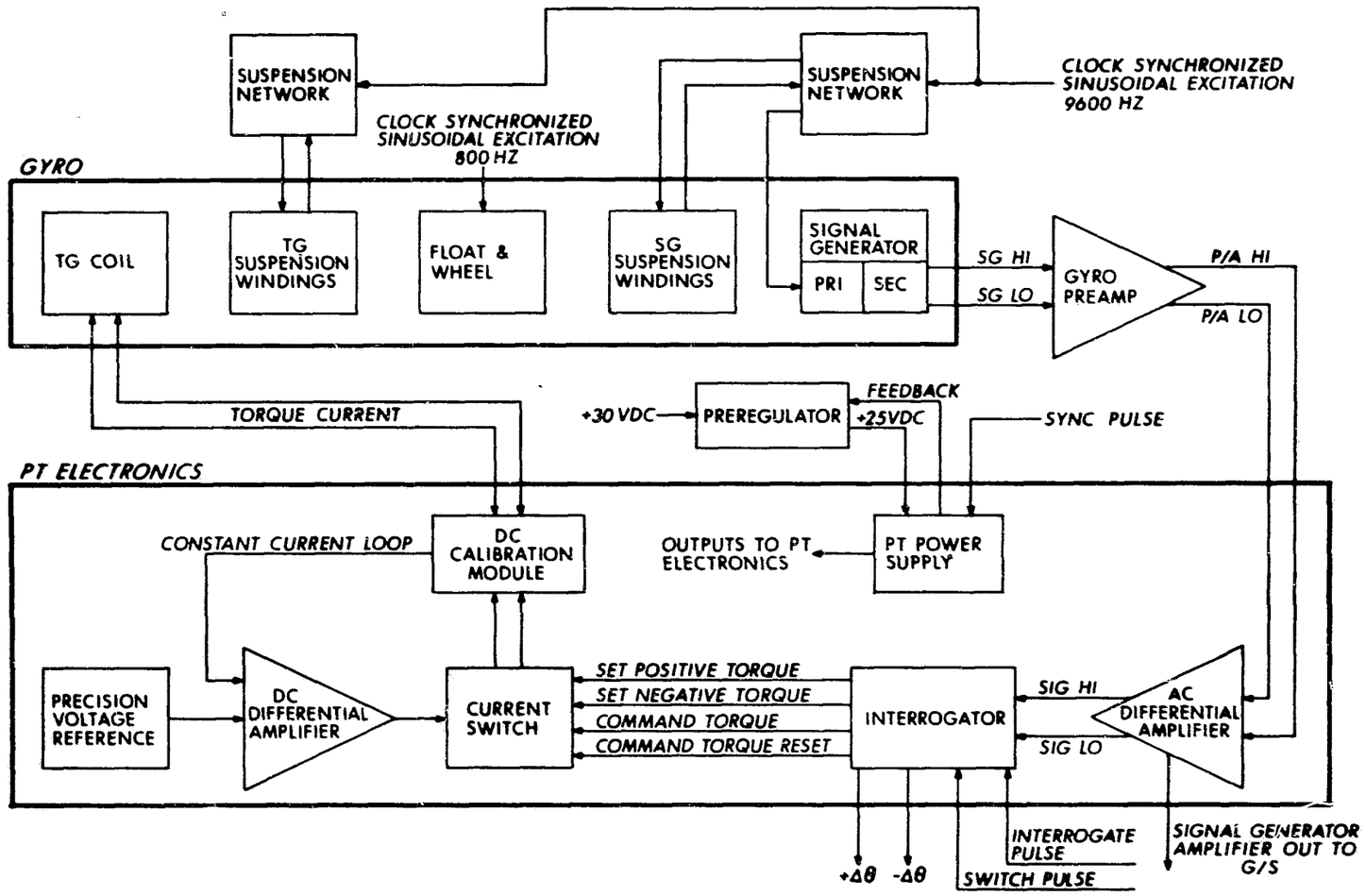

Fig. 4.5-9 Block diagram - PM pulse torque electronics.

a) Current level with 88-ohm scale factor resistor, 71 ma nominal, current spread for plus-minus polarity and dummy load conditions within 1 ppm.

b) Rise and fall time torquer current less than 0.4μ sec.

5. Pulse Torque Power Supply and Pre-regulator

a) Pre-regulator and power supply 27V ± 3% for line variations of 30 V ± 10%.

b) PVR supply of 15 Vdc ±1%.

c) The remaining outputs shall be as shown in the table below

TABLE 4.5-1

PULSE TORQUE POWER SUPPLY DESIGN PARAMETERS

Output	Tolerance
+ 8 Vdc	± 5%
+ 5 Vdc	± 5%
+10 Vdc	± 8%
-10 Vdc	± 8%

6. Precision Voltage Reference

Output voltage 6.0 Vdc stable to 1 ppm.

7. DC Amplifier

Gain > 10^5 V/V

Bandwidth > 400K Hz

Linear output ±2V

E) Discussion and Design Improvements

As indicated previously and reflected by some of the design parameters, the torquing scale factor stability is directly proportional to the torquing current pulse width and amplitude stability. For example, if we consider a nominal pulse amplitude of 70 milliamps and 300 microsec, current stability on the order of 3 nanoamps and pulse width stability of 6 nanosec is required for an rms scale factor uncertainty of 30 ppm. Clearly the rise time characteristics of the control pulses, logic networks, and current switching transistors are extremely critical in estabilishing accurate pulse width control. PVR and scale factor resistor stability in the ppm range are necessary for current-level control. Further, the dc amplifier gain operating range and bandwidth must be compatible with the load changes.

During instrument testing several operational problems were encountered that adversely affected control loop performance. These problems are reviewed below and, where applicable, design improvements are discussed.

1. Torquer Tuning (See Section 3.3.5C)

Tuning is required so that the torquer coil appears as a resistive load to the current-control loop. Inductance changes with pulse rate occur (referenced section) and result in degraded current-control loop performance. The dc amplifier cannot accomodate for the inductive transients with a single tuning network. Various combinations of parallel RC tuning networks were required in order to accomodate for the torquer nonlinearity.

2. Signal Generator Noise (See Section 3.3.6)

Various levels of pickup and noise modulation in the SG carrier signal output were observed. A filter in the gyro amplifier was required because of the excessive 800-Hz wheel power pickup. Modulation frequencies of 9600 ± 800- and 1600 - Hz could not be filtered since the frequency response of the loop would be adversely affected. This design change allowed reasonable performance at quantization levels of greater than 10 to 20 arc-seconds per pulse. However, the presence and amplitude of the modulation frequencies limit the ultimate level of loop quantization. Further improvement rests with the elimination of the modulation cause in the instrument itself (described in the referenced section).

3. Interrogator Timing (See Sections 3.3.10 and 3.4.7)

A "double-pulsing" phenomenon was observed in both gyro and PIP testing. The double-pulsing appears to be associated with noise coupling that occurs when the torque current is reset and results in an additional torque pulse (see Section 3.4.7). As indicated in the discussion of circuit operation, the present logic timing is such that a reset pulse proceeds each interrogation pulse. Thus, dependent upon the relative timing between the reset and interrogation pulse the noise coupling at the SG due to the current change in TG may cause erroneous torquing commands. An interim solution corresponds to setting up the pulse timing so that the reset pulse is spaced apart from the interrogation pulse by as much as possible, at least equivalent to a nominal torquer time constant. This influences the scale factor, however, since the

net effect is to reduce the torque current pulse width. A logic design change has been defined that alters the timing so that interrogation occurs prior to reset. This allows torquing command decisions to be made prior to resetting the torquer current. This change should eliminate the noise coupling influence.

4. Threshold-Level Detector

The present level detect circuitry employs logic circuit elements. The tolerance variation between thresholds can vary by as much as 20%. A more precise and interchangeable level-detection circuit should be designed.

5. Pulse Bursting (See Sections 2.5, 2.6, and 3.3.10)

Pulse bursting or moding is a dynamic characteristic associated with the interplay between the gyro float dynamics and the pulse rebalance control loop. Its influence on system performance is primarily dependent upon the type of attitude algorithm used, DDA or whole number. Its effect is to mask the desired quantization of the loop by the bursting of several pulses. The number of pulses vary as a function of the input rate. In the DDA mechanization this effect would limit the ultimate attitude indication performance. The affect upon whole-number computational performance should be minimal for low-update-rate higher-order algorithms. However, the relative phasing of bursts may cause a rectification error due to the noncommutative nature of the attitude algorithm.

Sections 2.5 and 3.3.10 describe the theoretical nature of the pulse-bursting phenomenon and some test findings. Section 2.6 describes a design technique that could be incorporated into the pulse-torquing electronics threshold-level detector that would eliminate the pulse bursting. Another advantage of the proposed design is that the noise susceptability of the torquing loop is significantly reduced.

6. One Radian/Sec Torquing

The present pulse-torquing electronics design is limited to a maximum current level of approximately 80 milliamps. With the present 18 IRIG torquer magnet configuration this current limitation will allow a maximum torquing rate of approximately 0.4 rad/sec. Even with the improved magnet design (Section 3.3.5D) the maximum torquing rate corresponds to 0.6 rad/sec. In order to achieve the 1-rad/sec torquing capability, design modification will be required. The increased current will necessitate a modification to the torquing power supply preregulator and changes in the current switch.

4.6 Test Program and Concepts

The test program and concepts described in this section are subdivided into three phases:

Preliminary System Functional Checkout (4.6.1)
Gyro Calibration and Long-Term Parameter-Stability Evaluation, (4.6.2)
System-Computer Real-Time Integrated Testing. (4.6.3)
Dynamic Tests (4.6.4)

Each represents a progressive level of test and evaluation capability.

4.6.1 Preliminary System Functional Checkout

Initial activity has been centered on function checkout and integration of the test-package electronic-support equipment (SEC) and the GSE. In the GSE, the 28-V power supply, temperature indicators, signal-scope monitors, counters and other monitoring equipments are initially adjusted and calibrated. Similarly, the SEC components, i.e., wheel supply, ducosyn-excitation and pulse-torque electronics, are given open-loop tests. Some of the sequences of turn-on operation that have been defined and instrumented are:

"Back-up" operation - system is maintained initially in this configuration until proper gyro temperature (132^{o}F) is reached.

Mode 1 - the ducosyn excitation (8-V rms at 9600-Hz) (airborne) 28-V supply verification and automatic switchover from backup operation.

Mode 2 - the gyro wheel-excitation phasing and amplitude verification.

Mode 3 - closed-loop pulse-torque-operation verification (monitoring of the amplified gyro error signal, the torquing threshold, approximately equivalent to one-$\Delta\theta$ for ternary-mode operation).

In addition, the instrument and frame temperature control loops are verified. The frame temperature stability is initially set to 115^{o}F by the frame heat exchanger. With wheels off, a stable temperature of 132^{o}F should be indicated. Wheels are turned on and off and gyro temperature should remain stable. The frame setpoint is adjusted so that positive temperature control will always result.

4.6.2 Gyro Calibration and Long-Term-Stability Evaluation

Prior to obtaining data for actual drift coefficients and scale factor computations, it is necessary to investigate the signal generator noise and torquing-loop stability.

1. Signal Generator Noise

In order to minimize cross-coupling errors due to float "hang-off", the pulse-torquing interrogator is set ideally to sense float rotation from null an amount equal to the pulse-torque quantization. For the 18 IRIG MOD B gyro, a $\Delta\theta$ of 6 arc-seconds is approximately equivalent to 0.18 mv rms, referred to the raw gyro null. Any noise greater than 0.18 mv will cause the loop to operate in a binary fashion rather than ternary. The interrogator threshold-levels could be widened but this would result in a larger float "hang-off" which would contribute to system cross-coupling errors. Possible noise pickup due to cross-talk between gyros, transients, and wheel and suspension power will be investigated and minimized.

2. Torque-Loop Stability

A measure of the torque-loop stability (this includes the electronic and gyro-drift uncertainties) is to be determined. The gyro net torque-to-balance uncertainties are dependent on the orientation of the gyro with respect to the acceleration vector (in this case - gravity). Thus, the position sensitivity must be taken into account in the calibration of instrument scale factor.

The gyro input axis is oriented (via the frame reference cube) parallel to the table-rate axis which is vertical. A minimum rate drive of approximately 2^{o} per second is selected. An integral number (n) of table revolutions would be used for collecting a preset number of $\Delta\theta$ pulses. This minimizes table-rate instability in- and measurement uncertainties in the scale factor determination.

Several runs would be taken to allow calculation of a 1-sigma value of stability. The number of table revolutions will be approximately defined so that only 2 or 3 of the lower-order bits of the preset $\Delta\theta$ count vary and an accurate 1-sigma value can be calculated.

3. Gyro Scale-Factor Calibration

The gyro remains aligned in the position used for determining the torque-loop stability. A rate drive of 2^{o} per second is used and a predetermined number (n) of table revolutions is selected. The GSE and/or computer are required to count both the elapsed time and the number of torque pulses for n table revolutions.

The equations for calculating the positive and negative scale factor are:

$$+ SF = \frac{2\pi n}{N^{+} - N_{ct}} \quad \text{(rad/pulse)}$$

$$- SF = \frac{2\pi n}{N^{-} - N_{ct}} \qquad (4.6.1)$$

where

N^{+} = pulse count for rates about the positive IA,

N^{-} = pulse count for rates about the negative IA, and

N_{ct} = total number of pulses due to the position-dependent gyro drift and the vertical component of earth rate; i.e., N_{ct} is determined by counting the number of pulses accumulated per unit of time interval with the table nonrotating and then calculating the total number of pulses that would be accumulated in time T_r (run duration).

The difference in the two scale factors for the PM Torquer is small (see gyro discussion Chapter 3). Provision for adjustment are included in the torquing-electronics calibration module.

4. Scale-Factor Linearity

Discrete table rates from 2^{o}/sec up to maximum torque capabilities of the pulse-torquing loop (at present 0.3 rad/sec) will be used to determine the scale-factor linearity. Linearity will be compared with that taken at the component level of testing.

5. Scale-Factor Stability

Scale-Factor stability will be obtained for both the short-term and long-term. Variations due to test moding, including system cool-downs and power transients, will be evaluated. At periodic intervals scale-factor calibration will be re-determined. From this data limits of allowable test environment changes will be determined.

6. Gyro Input-Axis Misalignment-Angle Determination

It is desired that the input axis form an orthogonal triad that is aligned to respective frame-reference-cube normals. The gyros will be aligned initially at the component level. This alignment will correct for the known misalignment of the frame mounting flats with respect to the cube normals. The system tests outlined in this section will determine the final alignment.

There are two basic techniques under consideration for determining the IA-misalignment angles. The first of these is presented here without great detail but will be used and compared with the results of the 2nd technique.

a) Torque-to-Balance Rate Method

The pulse-torque loop is closed and the gyro IA is aligned, via the respective reference cube normal, to be perpendicular to the table rate vector (ω). The table is then driven at about 5^{o}/sec. The change in the torque summation from a zero-rate input and the 5^{o}/sec-rate input is directly proportional to the misalignment of the IA with respect to the cube normal. Each "run" can determine one misalignment angle for each of two gyros. Since a total of 6 misalignment angles describes the location of all three IA's with respect to their cube normals, only three runs are required.

b) Open-Loop Method

This technique is more tedious than the one previously described, but is the same method that has been used successfully by the Inertial Sensor Group for component evaluation.

A gyro's IA misalignment with respect to its cube normal is defined by two angle; θ_{OA} and θ_{SRA}. To determine θ_{OA} the system is positioned as shown in Fig. 4.6-1.

The cube normals for IA, SRA and OA are designated as C_I, C_S and C_O, respectively. The system is orientated such that the cube normal C_S is parallel to the table-axis rate vector and the cube normals C_I and C_O lie in a plane perpendicular to the table axis.

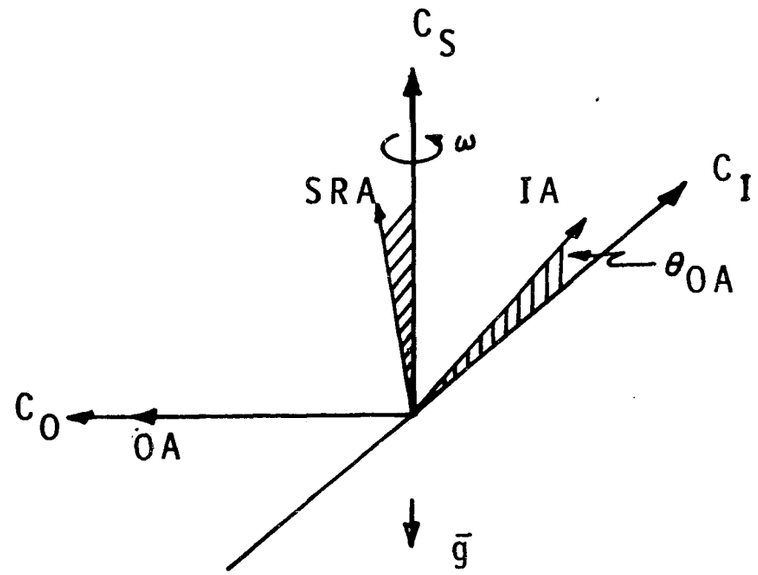

Fig. 4.6-1 Orientation for determining θ_{OA}.

The SG null is observed and a torquer current is used so that the SG signal remains at null. The table is then driven at a rate of approximately 5^{o}/sec. If a misalignment about OA exists, the float will precess off null and SRA will align itself with the table-axis rate vector. The amount the float moves off about OA is:

$$\theta_{OA} = \text{Gyro SG Sens.}\left(\frac{\widehat{\text{sec}}}{\text{mV}}\right) \times \text{SG output (mV)} = \widehat{\text{sec}} \quad (4.6.2)$$

To determine θ_{SRA}, the system is positioned as shown in Fig. 4.6-2.

The cube face C_I is placed parallel to the table rotary axis and C_O is placed parallel to the table trunnion axis (east-west line). The system is rotated about the trunnion axis such that the IA cube normal C_I is approximately parallel to the Earth Rate, W_{IE} vector. The float is nulled.

The table is now turned about the trunnion axis (-10^{o}) and the change in SG signal measured.

The test is done rapidly to minimize gyro-drift errors. The misalignment θ_{SRA} is then

$$\sin(\theta_{SRA}) = \frac{\theta_{OA}}{\theta_{trunnion}} \quad (4.6.3)$$

This test should be repeated several times in order to obtain an accurate-angle determination.

7. Gyro Drift-Coefficient Determination

For this test the gyros are operated in the pulse-torque-to-balance mode. At present only the bias and first-order terms will be determined, although if the magnitude of the 2nd-order terms, as found at the component level of testing, are appreciable, a multipoint step-tumbling test could be utilized to evaluate these terms.

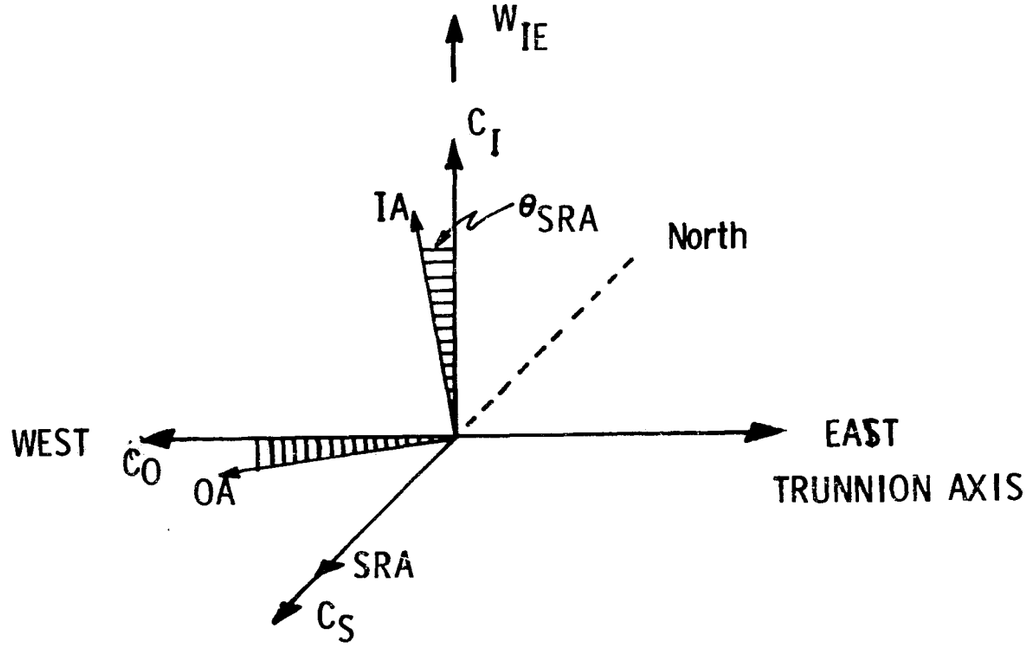

Fig. 4.6-2 Orientation for determining θ_{SRA}.

The bias and first-order terms are: NBD, ADOA, ADSRA, and ADIA. Figure 4.6-3 shows four possible system orientations that can be used to acquire the necessary torque summations. The drift terms comprising each torque summation are also indicated. Simultaneously solving the equations for each gyro will produce the desired drift terms. Twenty-five-minute test periods will be required for quarter-meru resolution.

The GSE is mechanized to accumulate the time for a preset number of torque pulses for each of the three gyros. For this test scheme, knowledge of the torque-pulse rate expected for each gyro in each orientation is required.

An integrated semi-automatic approach for effecting these tests using the Honeywell DDP-516 Computer is under development. For example, this test would be run in the following manner. The test program would be loaded into the computer and started. One of several test options would then be selected.

Each of these options requires the test package to be placed at various orientations for some period of time. The accumulated pulses for a specific position will be used to calculate the individual drift terms. The teletype will request necessary angles for each position and wait for a proceed signal indicating the angles have been set. The computer will then accumulate pulses for a pre-programmed time interval (on the order of 1/2-hour per position) and request that the operator move table to next desired position.

When the computer has accumulated sufficient data to determine the requested coefficients, they will be typed out on the teletype and computer will return to executive. Further development to allow the computer to automatically control table positioning would be desirable.

4.6.3 Integrated Gyro Package - Algorithm Testing

1. General

The test methods described in this section are conceptual in nature and are intended to provide a basis for integrated sensor package and algorithm computational performance evaluation. The gyro package is described in Section 4.3 and the algorithm computational processing is achieved using the Honeywell DDP-516 general-purpose computer described in Section 4.4.

CALIBRATION POSITIONS	X-GYRO	Y-GYRO	Z-GYRO
1	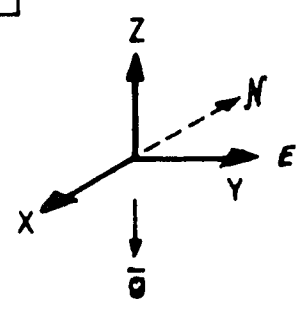	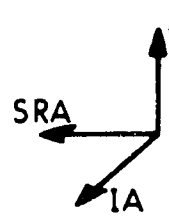	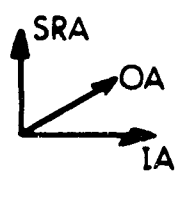	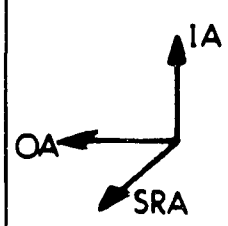
	W_{X_1} = -NBD-ADOA-W_{IEH}	W_{Y_1} = -NBD-ADSRA	W_{Z_1} = -NBD-ADIA+W_{IEV}
2	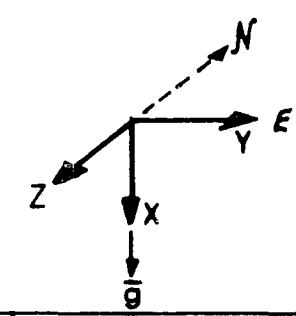	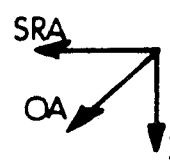	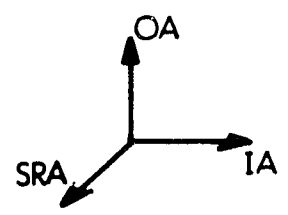	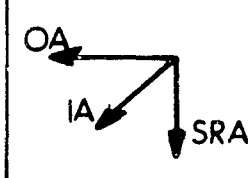
	W_{X_2} = -NBD+ADIA-W_{IEV}	W_{Y_2} = -NBD-ADOA	W_{Z_2} = -NBD+ADSRA-W_{IEH}
3	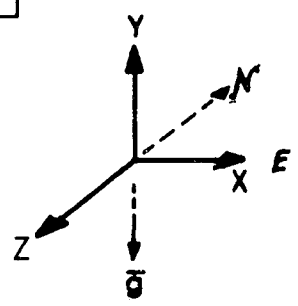	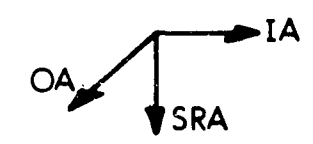	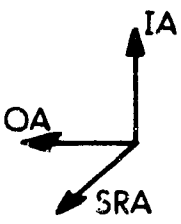	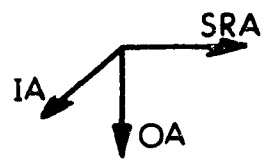
	W_{X_3} = -NBD+ADSRA	W_{Y_3} = -NBD-ADIA+W_{IEV}	W_{Z_3} = -NBD+ADOA-W_{IEH}
4	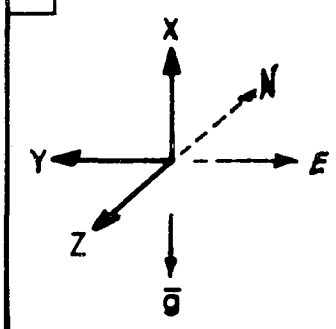	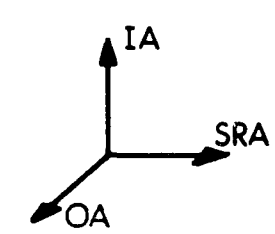	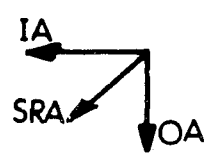	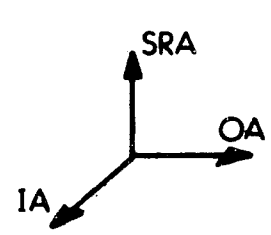
	W_{X_4} = -NBD-ADIA+W_{IEV}	W_{Y_4} = -NBD+ADOA	W_{Z_4} = -NBD-ADSRA-W_{IEH}

Fig. 4.6-3 Calibration positions for determining the gyro drift terms; NBD, ADOA, ADSRA, and ADIA.

The integrated test objectives are:

a) The development of critical test and analysis techniques for comprehensive and efficient evaluation of strapdown-system performance.

b) The evaluation of the interplay of system parameters on the performance capabilities and operational limitations of the strapdown system.

2. Test concepts

Both integrated static and dynamic environment tests are envisioned with a variety of algorithm implementations (quaternion and direction-cosine algorithms are described in Chapter 2). The interplay of algorithm order, update rates, and normalization techniques with sensor parameters and compensation (bias, output-axis coupling, etc.) techniques would be evaluated on a real-time basis. Trade-off studies relative to mission and performance objectives would then define an optimum configuration relative to hardware and software design complexity.

Tests are initialized with the body frame and the reference frame coincident. Typically, static performance comparisons are obtained with the package oriented with respect to earth rate or subjected to a sequence of rate inputs ending with the body frame returned precisely to the original reference position. In both of these cases the relative system drift is represented by the state of the computational algorithm sampled at random intervals for the earth-rate input or at the end of the test. Similarly, for fine-grain response and performance analysis during high-rate or mission-profile test-input sequences a dynamic test comparison is desirable.

For both the static and dynamic comparison it is necessary to have access to the algorithm state in the computer and to have precise knowledge of the test-package state with respect to the reference frame. In the static-test case the package test orientation at the desired comparison time is accurately defined. Maintaining knowledge of the reference-frame state (i.e., accounting for earth rate) represents a negligible computational load. Test monitoring and control access to the computer memory locations is readily attainable without conflict with the basic algorithm-processing requirements. Thus, for the static test the computer teletype writer (ASR-35) provides (using the special control interrupt program discussed in Section 4.4) a suitable input-output real-time test-control interface even though the data transfer is relatively slow (10 frames per second: four frames comprise one double-precision word).

Dynamic test comparison requires a high-speed input-output capability and a real-time test-table-angle interface. For this purpose a high-speed incremental tape-recorder interface, Digistore, with a 300-frame-per-second capability is being developed. During a test sequence the attitude matrix and corresponding table-position data will be stored at precise intervals. These data can then be outputted to the recorder during available program execution slots. The rotary axis of the lower table is equipped with a Wayne-George 2^{18} Digisec encoder. The output test tape may then be reprocessed through the 516 computer for data processing and teletype printout or used with available large-scale installation facilities (IBM 360) for processing and plotting.

In the development of the test sequence and programs for effecting this type of dynamic analysis, care must be exercised so that the data accumulation, processing and transfer does not jeopardize the integrity of the basic algorithm. Similarly, to be of value, sufficient interrogation of the algorithm-matrix components and test conditions must be recorded.

3. Instrument Error Correction

The discussions in Chapter 2 and 3 have identified both drift terms and dynamic instrument-error sources that are to be taken into account in the mechanization of the numerical algorithm. A major test objective is the evaluation of the performance interplay with the method and degree of parameter correction applied to the algorithm. Performance trade-offs with compensation update rate and complexity are essential outputs of this evaluation study.

Specifically, correction techniques for the following error sources and terms will be developed:

a) gyro bias drift
b) acceleration sensitive drift
c) scale factor
d) earth rate (test activity)
e) output axis coupling

Correction for the constant-bias term can be implemented by a simple iterative technique. If we assumed a 100-meru drift term, for example, a one-per-second update of one $\Delta\theta$ increment per gyro might be considered, at most. Similarly, the earth-rate influence represents a constant correction term modified (for the test latitude) by knowledge of the test-package orientation with respect to the earth-rate vector.

Correction for acceleration drift terms will require operation on the stored instrument constants by the measure of acceleration seen by them over finite measurement intervals. One approach is to determine the average acceleration seen by the instrument and compensate by indexing the lower-order bits of the appropriate direction-cosine terms prior to an algorithm update. In a practical sense, for a well-defined instrument, the acceleration-term magnitude should not exceed 20 meru. (By strict attention to assembly details it is possible to hold this magnitude within the uncertainty level by less than 5 meru.) If a one-arc-second correction increment were used in the one-g test environment, a maximum update every three seconds might be called for. With an integrating pendulous accelerometer as a system element, correction inputs can be keyed to the occurrence of a preset ΔV count for each associated accelerometer.

For test purposes it is reasonable to assume that the cw and ccw torquer SF can be adjusted within the stability uncertainties. Hopefully, compensation for SF linearity will not be required; evaluation testing at multiple rates will resolve this question. The scale-factor variation from nominal design should also be adjustable. However, numerical correction of this does not represent a significant burden. At most, a matrix correction based upon each gyro's net-pulse accumulation between updates may be considered. This does not represent a computational burden for the whole number 3rd-order algorithms and update rates under consideration.

Output-axis coupling is generally cited as a major error source requiring compensation. The simplest model postulated for the effective drift error (ω_D) due to angular acceleration of the gyro case with respect to the float ($\dot{\omega}_{OA}$) corresponds to

$$\omega_D = \frac{I_{OA}}{H} \dot{\omega}_{OA} \qquad (4.6.4)$$

where

I_{OA} is the float inertia about the output axis and H is the wheel angular momentum.

In Section 2.3.5 we have shown that the coupling effect more nearly exhibits both a wide- (Eq. 2.3.47) and narrow-band low-frequency response. At low-oscillatory rates the compensation required for the 18 IRIG is approximately 20% greater than at frequencies in excess of 0.01-cps. Thus, for extremely low frequencies, compensation using Eq. 4.6.4 is unsatisfactory. Similarly, for body-bending oscillatory inputs, it is more nearly correct. Over the dynamic range of spacecraft operations both frequency bands may be encountered.

An arbitrary selection of a wide-band compensation technique requiring estimates of the net change in angular rate (Δ rate) at high sampling frequencies is likely to compromise basic algorithm update capabilities. To be compatible with the quantized nature of the gyro data and the pulse-bursting phenomenon (Section 2.5), a smoothing process is implied. If smoothing is used, sizable rectification errors may occur if vehicle vibration, body-bending modes, or high-frequency attitude-manuever operations are evidenced.

The choice of OA coupling compensation technique is closely tied to the vehicle and mission environment. For low-rate large-attitude deadband control a low-frequency update is suitable. For short propulsion burns (higher-frequency modes are evidenced) no compensation at all may be indicated. For entry-type maneuvers the maximum accumulated $\Delta\theta$ error due to OA coupling during a roll maneuver may be on the order of a milliradian. A compensation of 10 updates per second would reduce these errors to negligible levels. The use of vehicle control system moding information (i.e., engine status, attitude control-mode limit-cycle deadband, etc., are normally available to the guidance computer) would be an aid in reducing the overall complexity of OA coupling compensation.

Compensation for gyro anisoinertia errors are not routinely considered. Basic gyro-design parameters should minimize these influences. Similarly, linear cross-coupling errors resulting from float offset angles should be limited by the torquing-control loop.

The present scope of this program is limited to gyro-algorithm performance-evaluation testing. The addition of accelerometers and their associated velocity algorithm would necessitate similar compensation considerations. These include the fixed compensation for bias, scale factor, and input-axis misalignments. For dynamic influences such as output-axis coupling, anisoinertia, linear and centripetal

coupling, the compensation considerations are similar to that of the gyro. For example, the output-axis coupling acceleration error (a_e) due to acceleration of the case with respect to the float output axis ($\dot{\omega}_{OA}$) is

$$a_e = \frac{I_{OA}}{p} \dot{\omega}_{OA} \qquad (4.6.5)$$

where

I_{OA} = is the float output-axis inertia

p = float pendulosity.

4.6.4 Dynamic Tests

Some of the typical inputs that are planned for instrument-package-algorithm testing are presented below.

The test described are not inclusive but do provide a basis for algorithm, compensation, and instrument-package evaluation. The influence of gyro quantization and pulse-bursting (discussion, Chapter 2), coupled with the suitability of various compensation techniques and their interaction with different algorithm orders and update rates, are of significant interest. The intent of the test sequencing is to provide a measure of the error-propagation characteristics of each of the system variables.

1. Constant-Rate Inputs

The system is initialized in the reference orientation (North and vertical). The test sequence then places the gyro-package orientation so that each gyro axis separately senses earth rate for finite periods. This allows definition of a performance baseline for bias and acceleration sensitive term correction and computational round-off errors. Tests conducted without various correction elements will allow direct comparitive evaluation.

Multiple axis-rate inputs of various magnitudes (0.03 to 0.3 rad/sec) will provide a measure of performance degradation due to slew errors (gyro quantization and algorithm order), algorithm constraint equation errors (orthogonality) and steady-state pulse-bursting.

2. Oscillatory-Rate Inputs

Output-axis coupling compensation and algorithm bandwidth is best evaluated with single- and multiple-axis oscillatory inputs. Controlled test inputs will sweep a frequency range from 0.01 to 10 cps per second.

Angular displacements of from 10^{o} to 0.5^{o} over the frequency range of 0.01-cps to 2-cps should correspond to worst-case spacecraft attitude-control deadband operation or body-bending inputs. Higher frequencies at amplitudes on the order of $1/10^{o}$ or less would be considered representative of higher-order bending-mode or vibratory inputs.

The adequacy of the OA-coupling compensation technique will be evidenced at the lower or operational frequencies. At intermediate test frequencies the error propagation due to the bandwidth limitations of the OA-coupling compensation delta-rate estimate will be evidenced.

The gyro test-package instrument orientation is shown in Fig. 4.6-4. Note that a completely orthogonal gyro-axes configuration has been selected. This mechanization allows maximum compensation-evaluation considerations and individual error-propogation analysis. For example, for OA-coupling compensation, the X gyro ω_{IA} corresponds to ω_{OA} about the Y gyro, ω_{IA} of the Y gyro corresponds to the Z-gyro ω_{OA} and the Z-gyro ω_{IA} is the X-gyro ω_{OA}.

The pulse-bursting phenomenon and basic gyro quantization will appear as performance phase lags. Noncommutativity errors resulting from these phase lags will be evaluated with various algorithm types, orders, and update rates. High-frequency inputs will probe performance limitations resulting from the interplay of instrument and algorithm bandwidth.

3. Coning

Coning-test inputs represent an effective means for both algorithm and instrument-package evaluation. Analysis methods allow one to project the theoretical system-performance limitations for algorithm order, update rate, instrument quantization, and computational word length as a function of coning frequency and amplitude (Chapter 2). Test comparisons with the projected performance allows fine-grain analysis of the error-propagation sources.

The coning input is mechanized by applying oscillatory test inputs about two of the test-package gyro axes. The input magnitudes and frequency are equal but their phase relationships are synchronized so that they are displaced by 90^{o}. The resultant motion is such that the third axis traces a cone whose amplitude and angular-rotational rate are equal to the angular displacement and frequency of the oscillatory input respectively (Fig. 4.6-5). The algorithm operates on the gyro data of the oscillatory axes to account for the kinematic

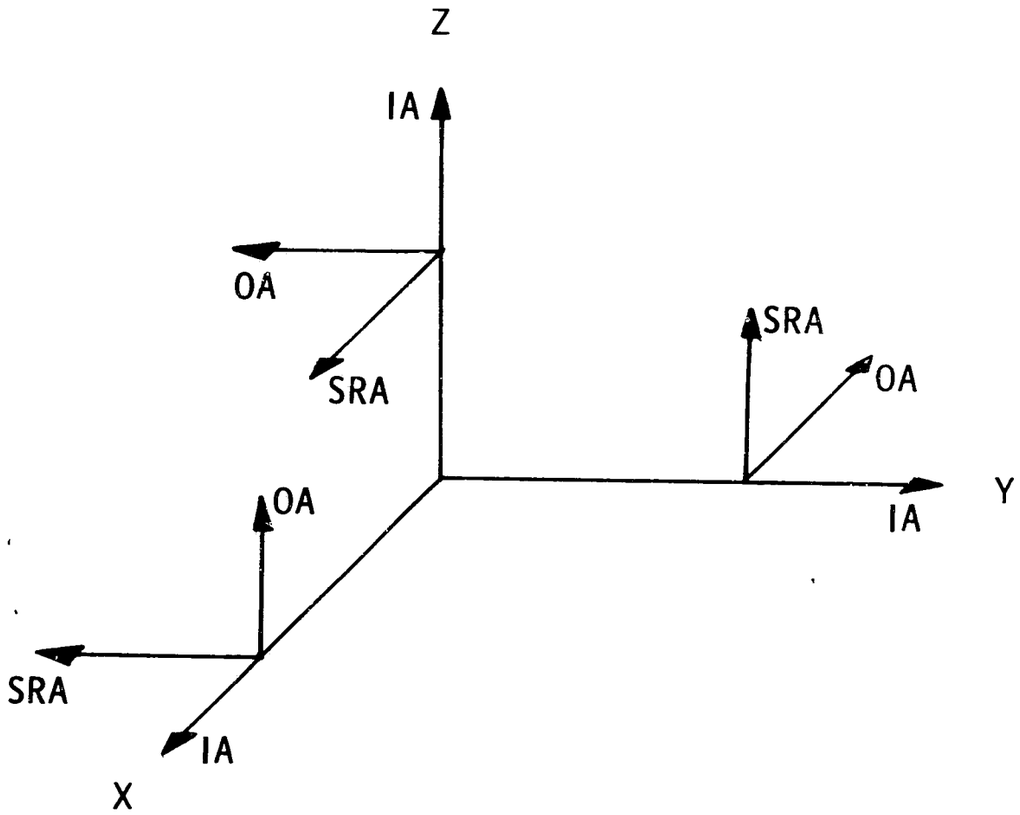

Fig. 4.6-4 Test package gyro axes orientation.

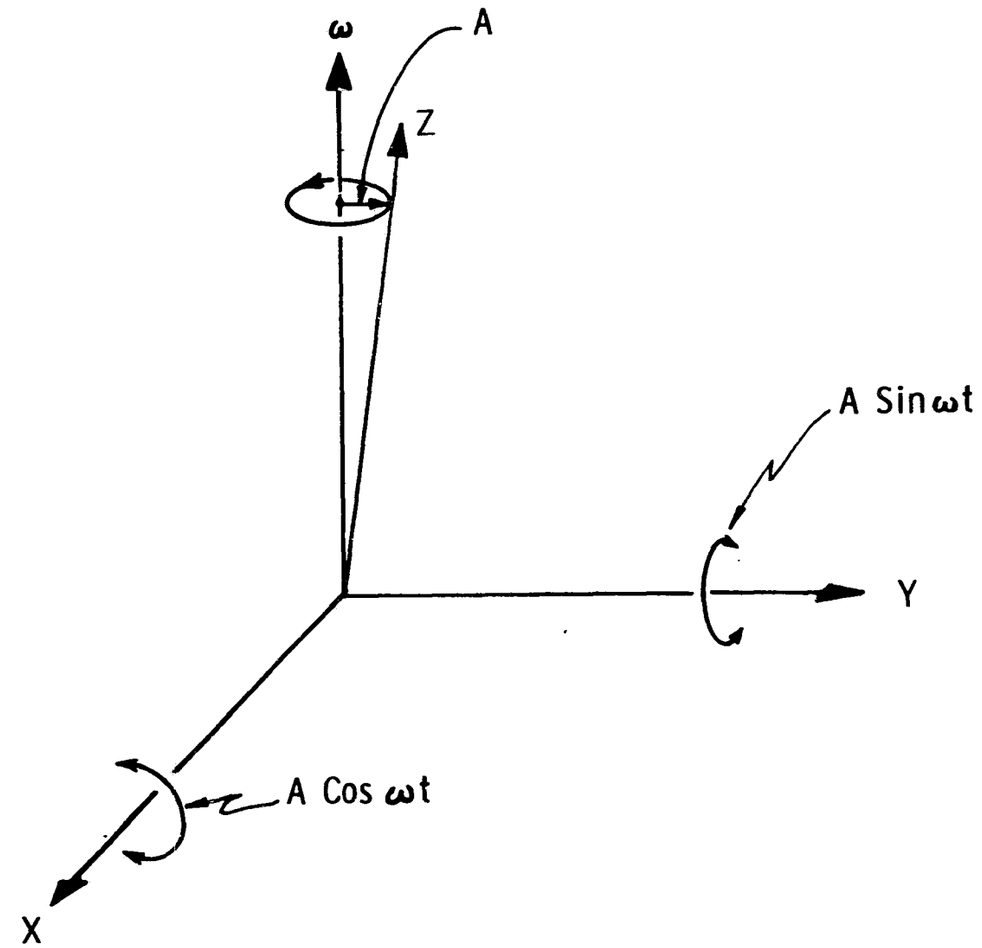

Fig. 4.6-5 Coning of the Z-gyro IA due to synchronized oscillations about X and Y.

coning drift of the third gyro axis. In an ideal system, if the bandwidth of the algorithm is greater than the coning frequency, the transformation matrix will exhibit no errors due to the coning drift. The measure of bandwidth performance with this coning-test input is directly evidenced by the drift rate of the coning axis as indicated by the algorithm output.

Coning inputs at frequencies of 1 to 10 cps allow evaluation of truncation errors for various algorithm orders at update rates of 100 to 250 times per second. The interplay of gyro-loop response limitations and its influence on algorithm performance is also exhibited in this frequency range. At lower input frequencies gyro quantization and compensation-error-propagation evaluation are facilitated.

4.7 Ground Support Equipment

This section covers the general design and construction features of the prototype ground support system developed to support the test and evaluation of an Advanced Guidance Strapdown sensor package.

4.7.1 General Design Concept

This Prototype GSE equipment was developed to have flexible control test modes, monitoring and compiling capabilities for support of strapdown sensor package development testing. It furnishes all necessary power and timing and incorporates fail-safe interlocks to protect against unsatisfactory test conditions. (Fig. 4.7-1).

4.7.2 Functional Description

This GSE was developed by modification and addition to the Apollo "Optical Inertial Analyzer" (OIA), and the computer test set. Layout drawings of the revised configurations are shown in Figs. 4.7-2 and -3. The actual equipment is shown in the photos of the facility area (Figs. 4.2-1 and -2). The following special purpose drawers and functions were developed.

4.7.2.1 Mode, Monitoring, and Timing Functions

a) Mode Control

This drawer was mechanized to control the transfer of power to the test package, and to control the operational modes during testing.

b) Counter Control

This function allows the test operator to remotely control all of the data monitoring sequences of the commercial preset counters and associated electronics that are necessary for use in processing the $\Delta\theta$ gyro pulses from the test package.

c) Digital Voltmeter Automatic Scan Control

This drawer functions so that a variety of test package critical voltage signals are automatically routed to a digital voltmeter. The sequencing allows continuous monitoring either prior to testing, or during the actual test phases.

d) Monitor Panel

This panel functions as a monitor of the test package operational status (i.e. wheel and ducosyn feedback voltages, bus dc power, clock pulse lines, etc.), and furnishes alarms, and system down mode discretes when necessary. Interlocks exist between the monitor and control panel to inhibit operation when alarms are issued.

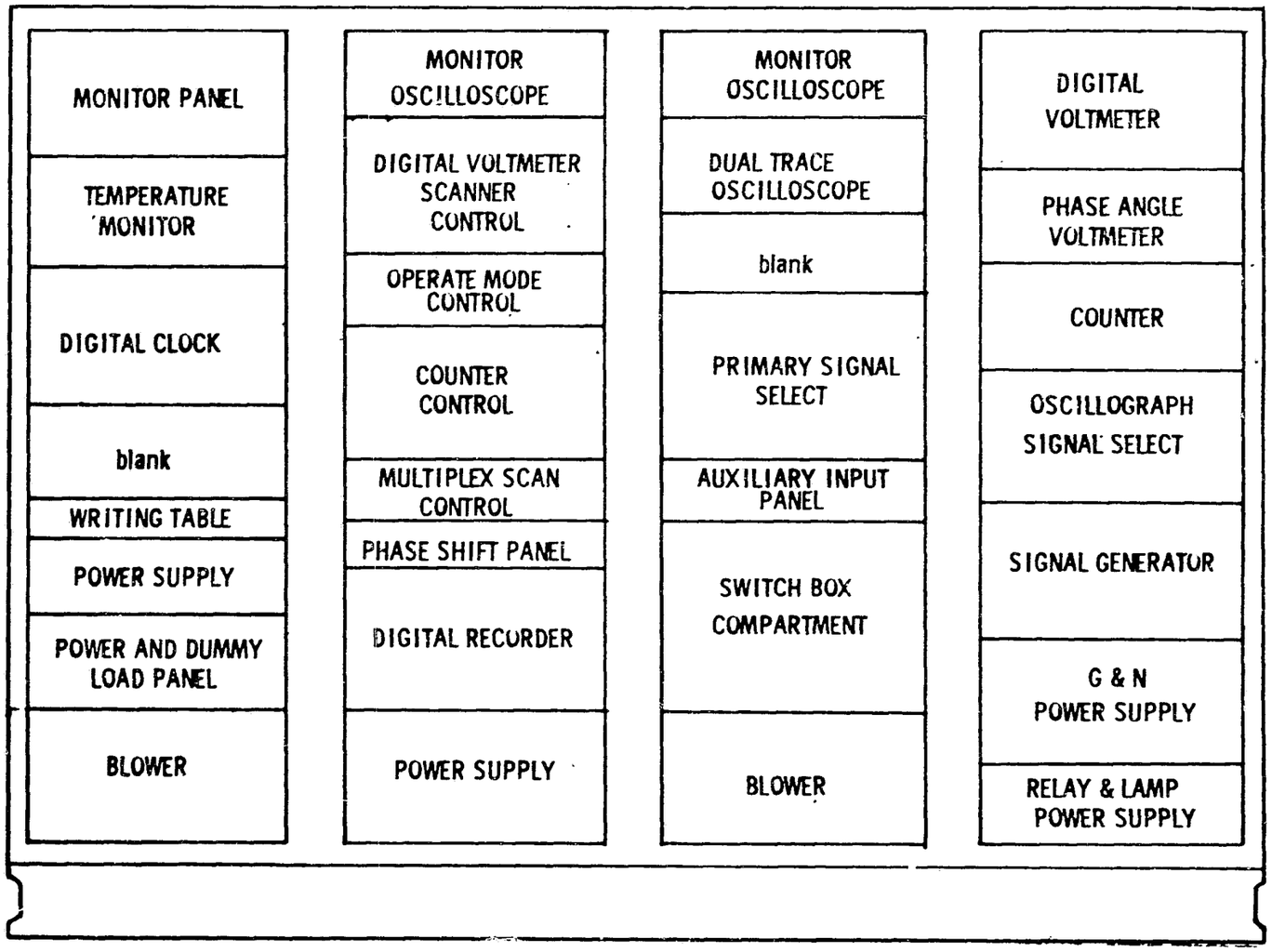

Fig. 4.7-1 Front panel layout of modified optics inertial analyzer.

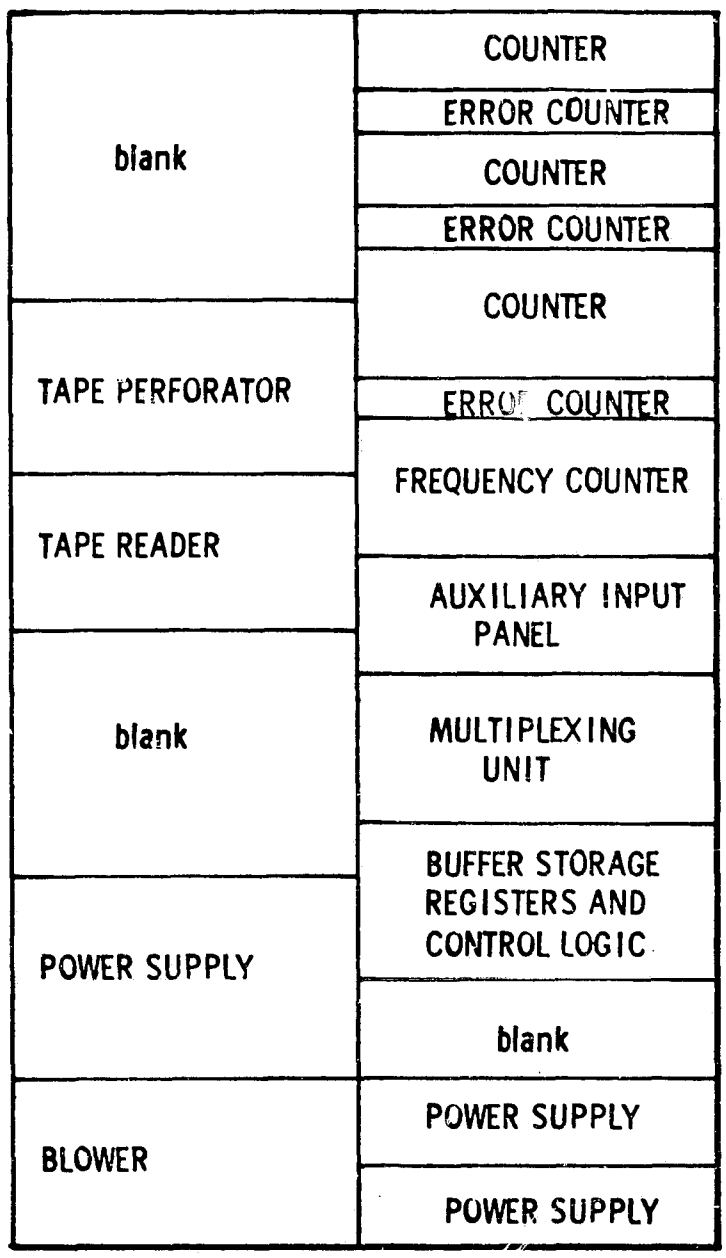

Fig. 4.7-2 Front panel layout of modified computer test set.

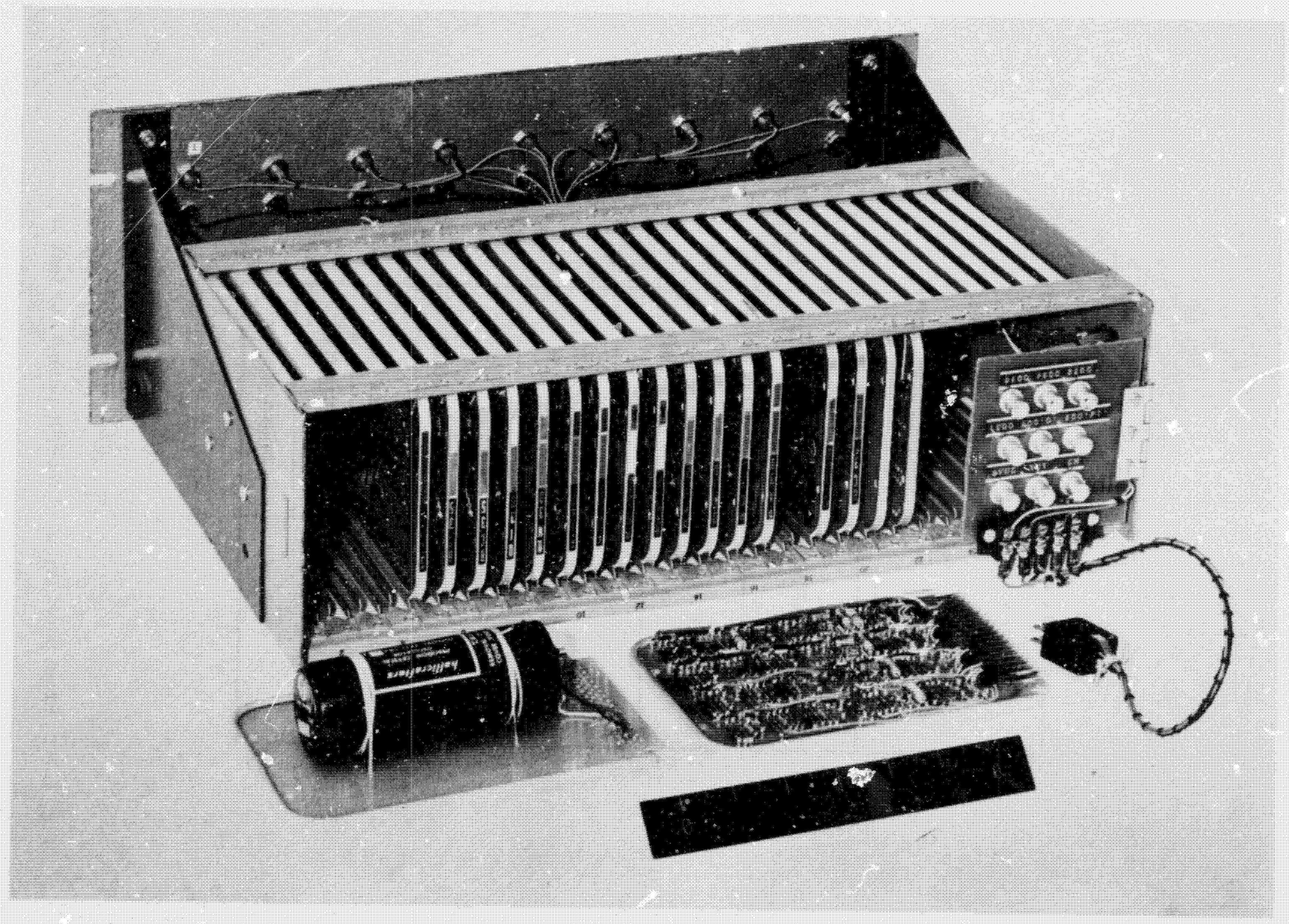

Fig. 4.7-3 Clock and scaler.

e) Temperature Monitor Panel

The temperature monitor panel for this system functions as an indicator only. It is designed to provide a compatible monitoring interface with each of the gyro individual temperature control loops, the frame and heat exchanger.

f) Digital Clock (Fig. 4.7-4)

This unit furnishes all timing pulses that are necessary for the test package electronic power supplies and torquing loops. It also furnishes a time base to the data aquisition system, for use when data is to be tagged as a function of real time.

g) Data Acquisition System

These GSE elements are used mainly for operational test data processing, storage, and transfer to recording equipment for test operator use.

1) Signal Multiplexing Unit

This unit contains the interface electronics for data transmission to recording equipment (tape punch and digital printer). It also provides storage for accumulated pulse counts and routes the DVM Scan data.

2) Multiplex Control Unit (Fig. 4.7-5)

This is the central control point for remotely controlling the output of the multiplexer. It provides indication as to when stored data is ready for transmittal and the sequence control for data transfer.

4.7.3 Operational Description

4.7.3.1 Mode Control

A block diagram illustrating the moding is shown in Fig. 4.7-6.

The standby mode (Mode #1) command, transfers the temperature controller from the overnight backup power to the test package dc power supply and at the same time excites the instrument suspension supply. An interlock exists between the mode control drawer and the monitor panel. This interlock inhibits the standby command if the output of the clock is not of the proper frequency and suspension supply output voltage amplitude is incorrect. If a "go" status exist (no failure detect indications) a "proceed" signal is indicated, and modes may be enabled.

"Operate" (Mode #2) is "wheels on" command in which the gyro wheels are interconnected to its 800-Hz supply. As in the standby

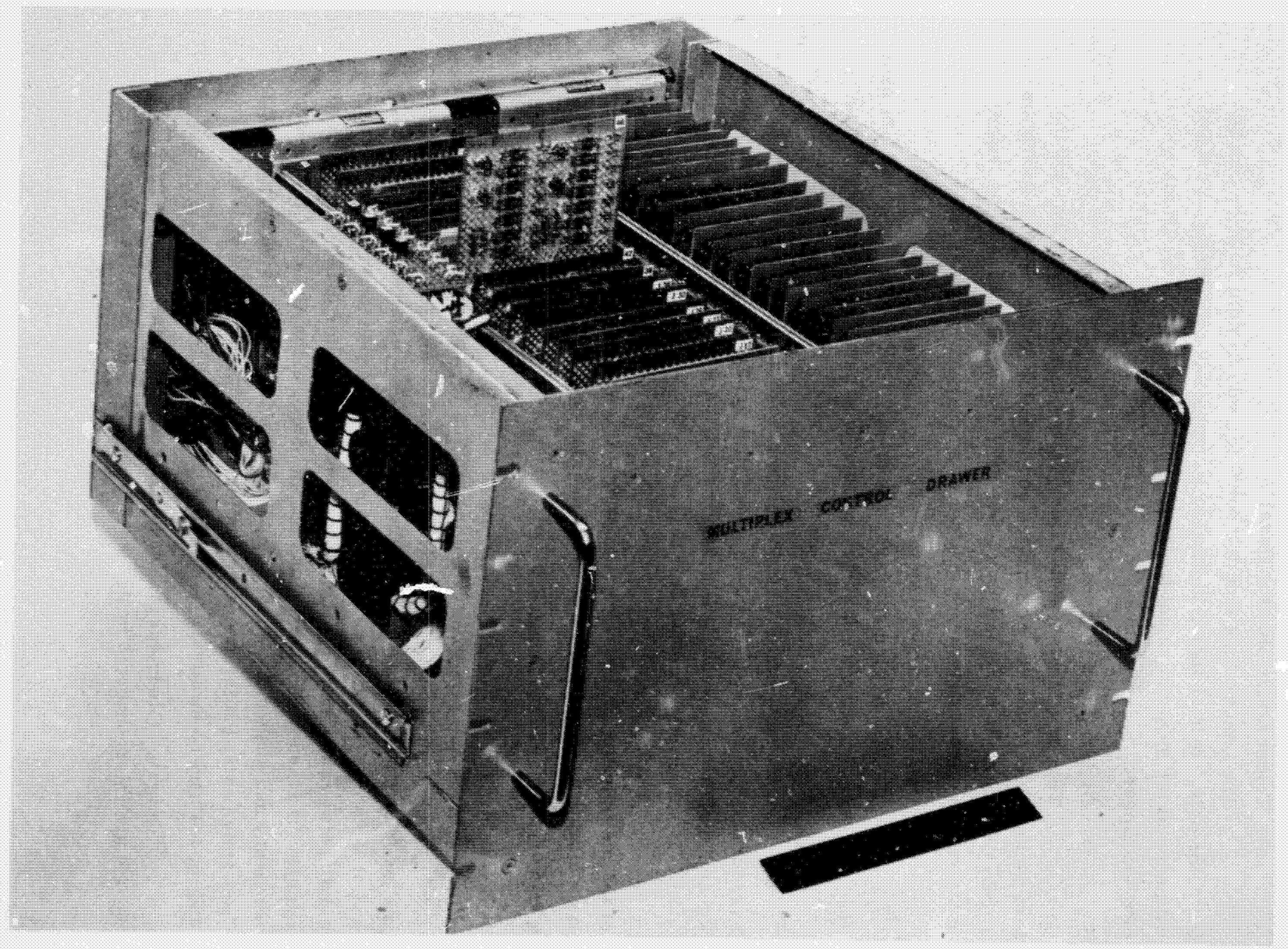

Fig. 4.7-4 Multiplex control drawer.

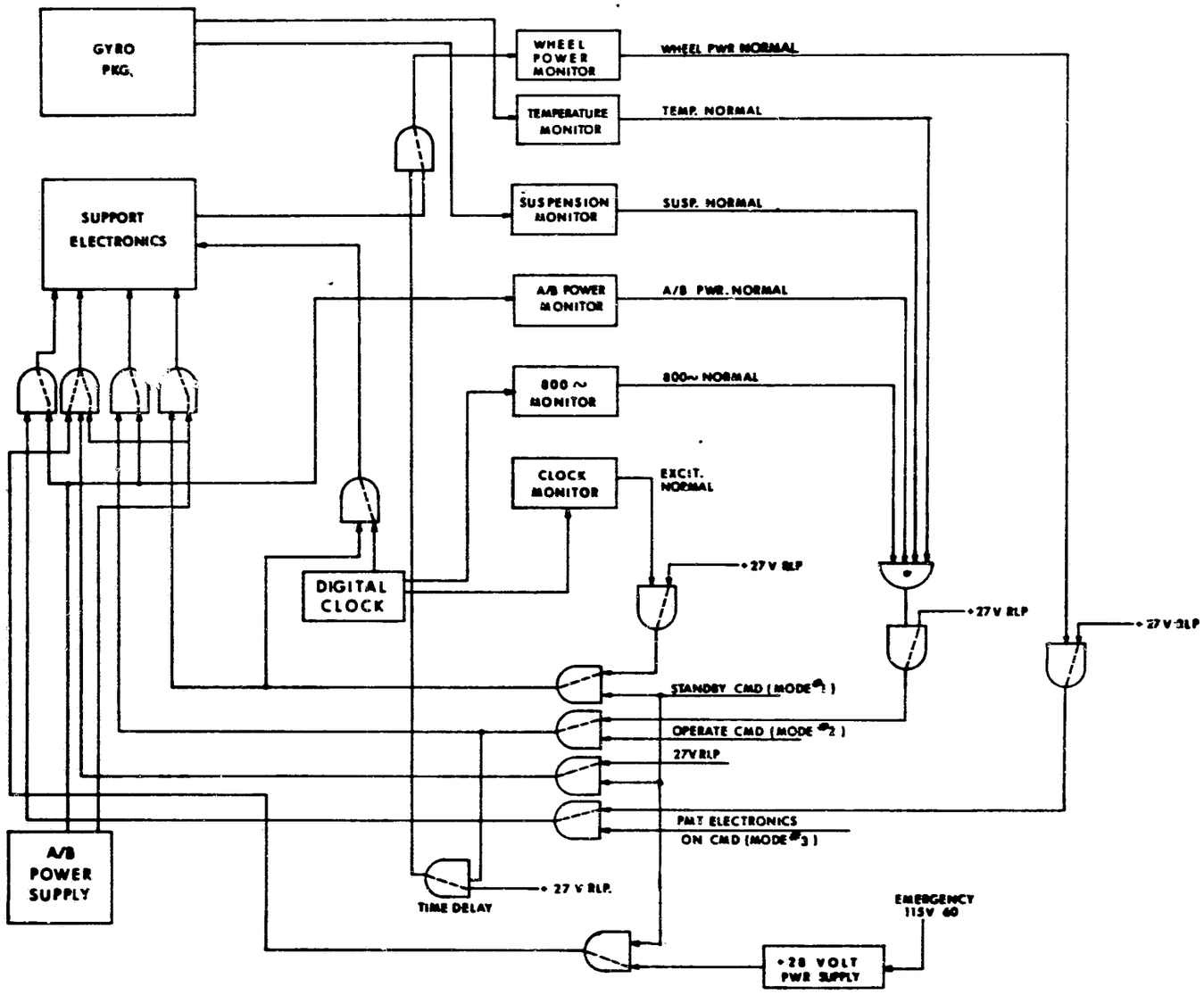

Fig. 4.7-5 Mode control, mech. diagram.

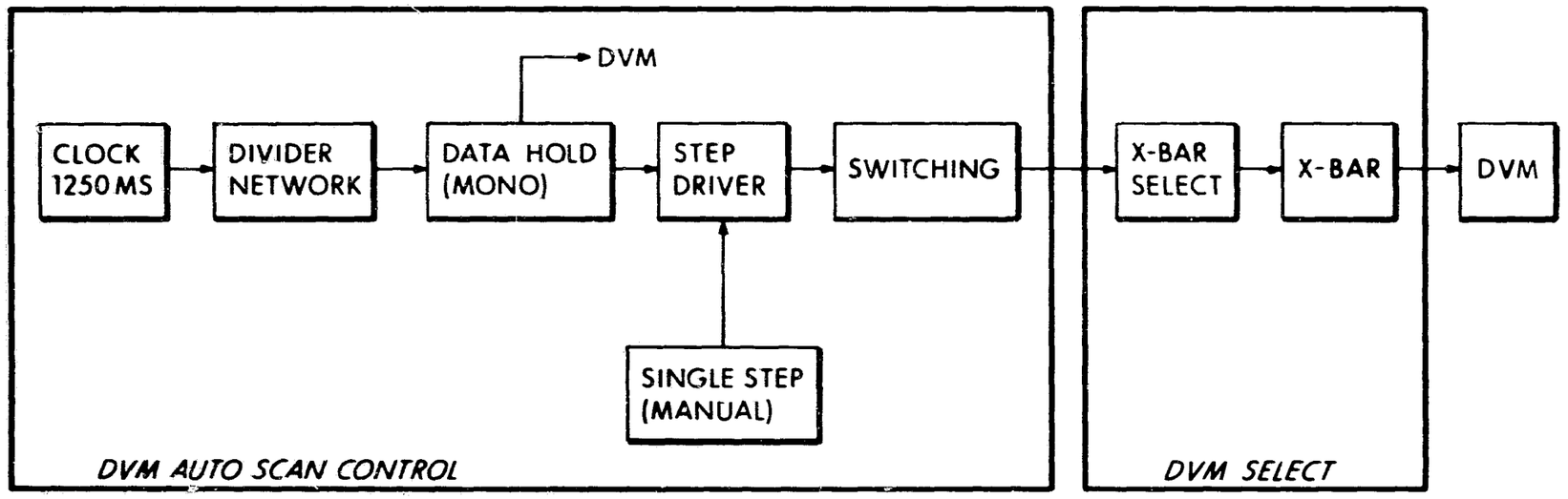

Fig. 4.7-6 DUM scan control

mode (#1), interlocks exist which will inhibit this command if a fault is detected. Another mode is provided that allows "wheels off" operation; an override feature simulates a "go" signal from the wheel power fault detector.

4.7.3.2 Digital Voltmeter Automatic Scanner:

This panel (block diagram Fig. 4.7-7) was designed to control the measurement of system voltages which have a direct bearing on data analysis, i.e.: gyro temperature, suspension excitation voltages, and wheel voltages, etc. The scanner will control the input to the DVM in a precise sampling sequence, thus relieving the test operator from the task of requesting these inputs on a one-at-a-time basis. The unit will scan prior to test start and/or during testing. The scan period for each input is selectable. Scanning may be accomplished at a 5-, 10- or 20-second sampling interval. The unit may scan continuously, in which case its data takes priority over all other data routed to the recording equipment. In the "single scan" mode the unit will scan the selected inputs once. An additional capability enables the operator to select a single input for repeated monitoring. These signals may then be continuously recorded to provide a log for detailed performance analysis and correlation.

4.7.3.3 Data Acquisition System

The data acquisition system consists of commercial monitoring and recording equipment, and the special multiplexing storage and control. An overall block diagram of this system mechanization is shown in Fig. 4.7-8.

The commercial equipments used are:

Four forward/backward counters,

one $10 \times 10 \times 6$ X-bar,

one tape perforator,

one digital printer.

The multiplex control drawer contains four 40-bit storage registers, a control logic for test control, parallel-to-serial converters, and timing for the readout sequence.

A counter control drawer permits the operator to control counter functions from a remote source. It enables the operator to control the counter input information (i.e.: $\pm\Delta\theta$'s or interrogator counts) from the test package, the test start/stop modes (i.e.: manual or automatic) and the test configuration (i.e., gyro coefficient and scale factor testing).

To illustrate the operational sequencing and signal flow, a hypothetical gyro coefficient test run will be described. Assume that

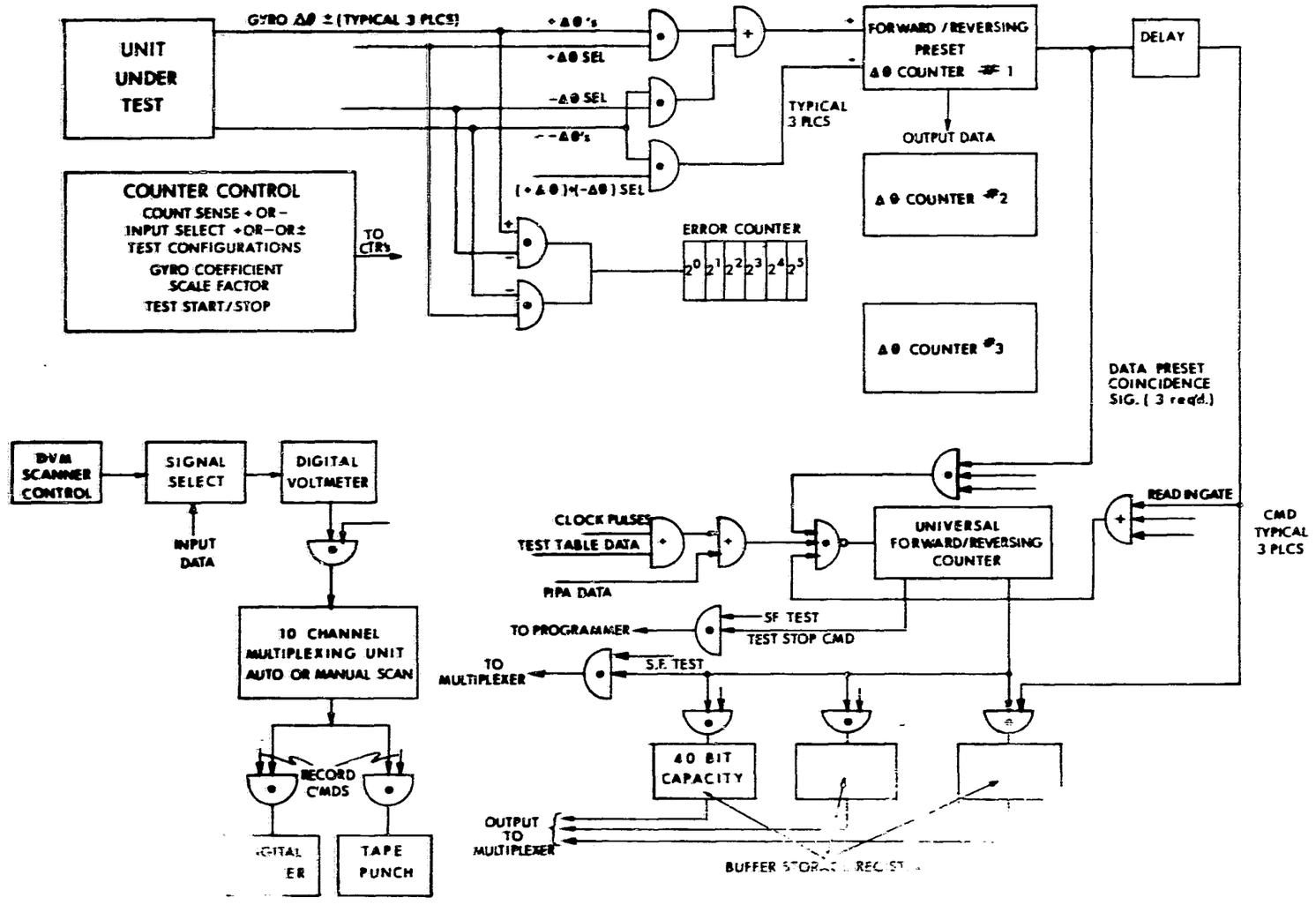

Fig. 4.7-7 Data acquisition mechanization.

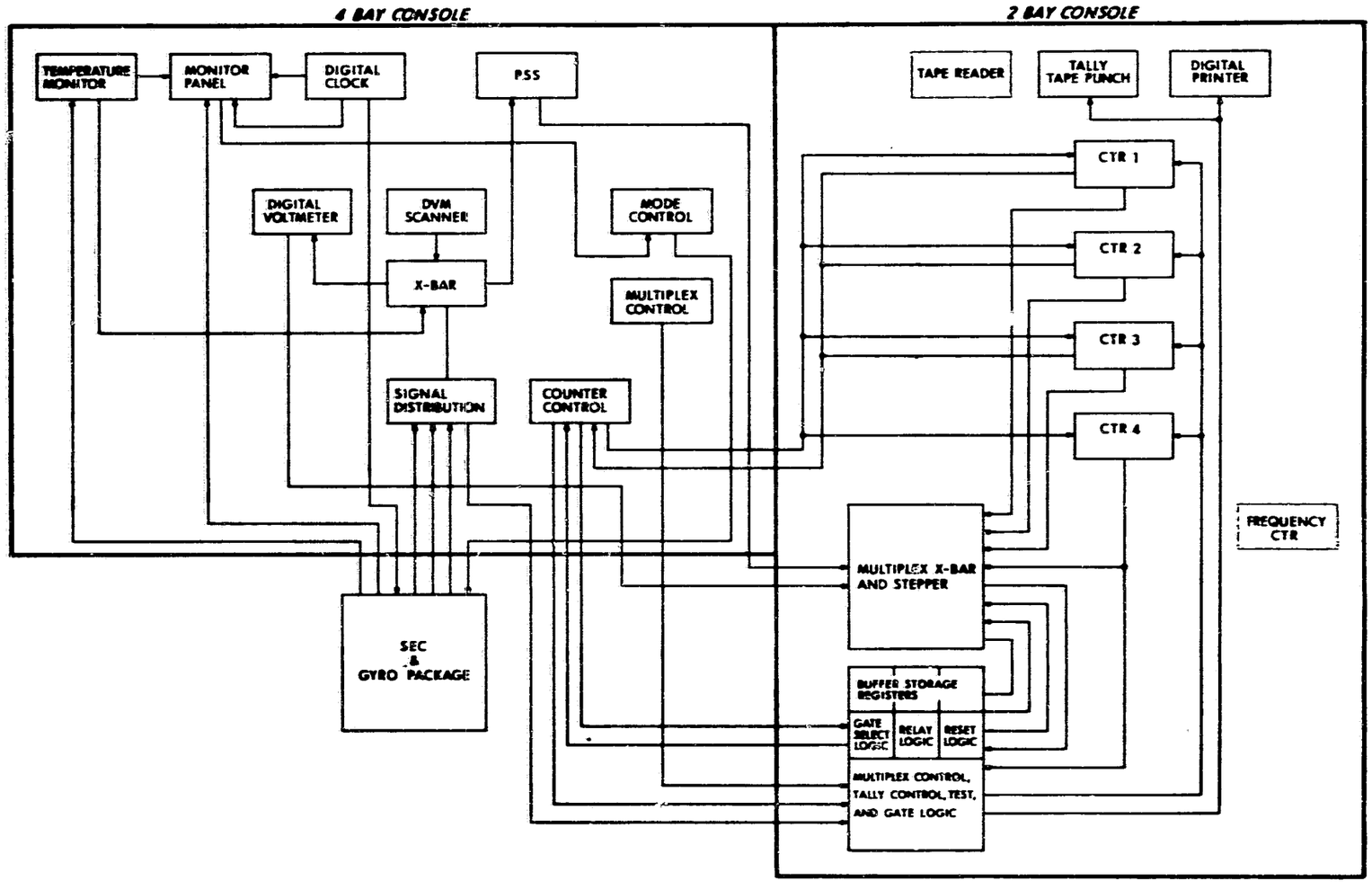

Fig. 4.7-8 Signal and control harness interface and block diagram - GSE for AGC and N System.

the test package is operating and the counters are preset to a previously determined number of desired input $\Delta\theta$ pulses. The direction of the counter accumulation is selected via the counter control panel. It is desired to accumulate time as a function of the preset pulse counts. Thus the gyro $\Delta\theta$ outputs are routed to the up/down counters by arming selected input gates, while the main timing frequency is routed to a fourth counter. Similarly, the DVM Scan is initialized and a pre-test scan is made and recorded. A low rate scan may also be selected. A test start signal is issued and the coefficient test is begun. Both the gyro $\Delta\theta$'s and the clock frequency are sampled. As each counter achieves the $\Delta\theta$ preset coincidence, a data-ready signal is issued to the control logic. This inhibits the time counter and the accumulated time is transferred to the storage registers. When the registers are filled, another ready signal is issued. This alerts the operator that the set of data is ready for recording. The selection of the recording sequence is made at the multiplex remote control panel, and, if the DVM is not recording, the scan sequence will start. The stored data is then transferred to recording equipment.

5. SUMMARY AND CONCLUSIONS

This report has presented the status of Advanced CG&N Inertial Subsystem studies and test evaluation effort covering the period of February through December 1967. The study focused upon the application and evaluation of strapdown inertial system techniques for advanced manned missions. A major objective was the development of a system mechanization that would yield reliability and performance consistent with extended spacecraft mission requirements. This conceptual effort was complimented by in-depth analysis and test evaluations to determine the performance capabilities and limitations of the strapdown inertial configuration. Thus, studies of instrument dynamic error sources, torque-to-balance loop techniques, and attitude algorithms were conducted. Concurrently development and test evaluations of state-of-the-art inertial instruments were conducted. Finally, a gyro package was developed with supporting test facilities, (including a real-time computational algorithm capability). Test evaluations to determine the potentialities of the strapdown configuration were programmed. Although many individual goals of this study were reached during the reporting period, considerable effort is still required if the overall study objectives are to be achieved. The following sections provide a brief summary of accomplishments in each of the major areas of investigation and test evaluation. Recommendations for continued effort are also included.

5.1 System Mechanization and Performance Model:

Mission analysis studies, for both transplanetary (section 1.2.2) and entry phases (section 1.2.3), using a strapdown system error mechanization were conducted and corresponding performance for strapdown system inertial components and software parameters were defined (section 1.2.4). One key area requiring further study is the terminal guidance portion of the interplanetary leg and its effects upon entry angle uncertainties. More comprehensive analysis reflecting vibration environments and the corresponding instrument dynamic error-source propagation would also be desirable.

In general, high reliability proved to be the overriding guidance system requirement for extended spacecraft mission applications. In view of this factor the selection of strapdown system mechanization concepts with their inherent reliability improvement potentials and ease of adaptability to redundancy techniques is confirmed. In fulfillment of the system mechanization objectives the study evolved a redundant modular sensor and electronics concept. The inertial reference unit that was formulated employes six single-degree-of-freedom gyroscopes and six linear accelerometers operated in a pulse-torque-to-balance control mode and configured in modular replaceable units. The instrument input axes are arrayed in a non-orthogonal configuration that corresponds to the unique symmetrical pattern defined by the normals to the faces of a regular dodecahedron. It was determined that this configuration achieved maximum reliability coupled with optimal performance for a six-sensor configuration. The analysis showed significant reliability improvement, even over orthogonal redundant configurations

that employ nine gyros and nine accelerometers. This study also formulated adaptive data processing techniques and self-contained failure isolation and detection methods for the system mechanization.

Continued effort in the area should pursue the development of a suitable engineering model of this mechanization. Feasibility of the entire concept could then be validated, modular techniques matured, and detailed problems of misalignment, dynamic error source correction, failure isolation sensitivities and criteria resolved. A timely initiation of this task would allow economical realization of hardware for projected advanced missions and avoids a simultaneous inefficient development and manufacturing program.

5.2 Instrument Model and Algorithm Development

Analytic studies formulated dynamic error source models for both the gyro and accelerometer (sections 2.3 and 2.4). Numerical dynamic errors for the 18 IRIG parameters using typical spacecraft environments was determined and are tabulated. An angular vibration environment test program is recommended to both validate this analysis and extend the knowledge of the behavior of a single-degree-of-freedom instrument in the body-mounted environment.

Studies, simulations, and tests of combined gyro-pulse-torque-to-balance operation were conducted. These studies served to illustrate the dynamic interplay of control-loop and gyro or PIP design parameters. The results (section 2.5) clearly demonstrated the factors influencing pulse-bursting operation as well as noise sensitivities. Control-loop synthesis techniques were then formulated (section 2.6) which eliminated pulse-bursting, minimized float hang-off, and reduced noise sensitivities. It is recommended these techniques be implemented to allow experimental verification of the analysis and simulations and evaluation of improvements in the gyro package test evaluation.

Whole-number higher-order quaternion and direction cosine attitude maintenance algorithms were developed and comparative error analysis for constant slew rates and coning inputs were formulated (section 2.2). Algorithm parameters such as computational update rate, data quantization and word length were evaluated. The analysis showed that a third-order algorithm operating at a moderate computational update rate (100/sec) with a gyro quantization of 6 arc seconds and word length of 34 bits would satisfy anticipated system requirements. Although no overwhelming advantage for either the direction cosine or quaternion was determined analytically, some advantages for the quaternion were evidenced, eg, a single-length normalization constraint rather than an orthogonalization requirement for the direction cosine. The analytic foundations of algorithm development were successfully completed during the study period. Evaluation of the theoretical findings through direct gyro test package-algorithm testing and computational simulations is recommended.

5.3 Instrument Evaluations:

In order to provide a realistic assessment and projection of strapdown system capabilities, the 18 IRID MOD B gyro and 16 PM PIP accelerometer were selected for development study and test evaluations. Both components are single-degree-of-freedom instruments with permanent magnet torquers that are operated in a pulse-restrained torque-to-balance loop. Particular emphasis was placed on the 18 Gyro (gas-bearing wheel package) and continued development of this instrument, specifically designed for the strapdown application, was funded under the scope of this program. In the testing of these instruments emphasis was placed upon torquer performance (i.e., SF stability and linearity, etc.) and instrument coefficient environment sensitivities.

Four 18 IRIG units were assembled during this reporting period. Two experienced hard-start difficulties and are being recycled. Unit #411 exhibited high quality inertial-grade performance and test results are described in sections 3.2 and 3.3. The fourth unit (#413) is in preliminary test and appears to be acceptable in all respects. Testing proved to be extremely valuable in that several application problems were uncovered (i.e., stop-bias hysteresis, eddy-current torquer sensitivity, SG noise, etc., sections 3.3.5 and 3.3.6) and corrective action for their resolution was initiated. In addition, improvements were conceived (TG magnet with a 40-50% increase in flux density, SG-to-TG alignment technique, etc.) that make a one-radian-per-second input rate measurement capability fully realizable. Implementation of recommended gyro design changes coupled with the torque-loop design improvements reviewed in section 4.5 appear to offer performance potentials that are consistent with the performance model requirements described in Chapter 1. Completion of the current 18 Gyro build and further comprehensive system application testing to both verify the test findings and allow three-axis gyro package testing is recommended. Continued development of the 18 IRIG is also recommended so that proposed design changes may be verified in a second-generation instrument-fabrication series.

Four 16 PM PIP units were fabricated and accepted for evaluation testing. One unit, SN-12, was furnished to NASA/MSC. Basic component performance testing on two units was conducted. Extremely stable high-quality inertial-grade performance was repeatedly attained and test results are described in section 3.4. Noise sensitivity problems were encountered and further investigation of instrument harness optimization appears to be warranted. Tests with malfunction type moding verified that the PM torquer was free of the magnetic type sensitivities (gaussing, etc.) exhibited in the Apollo PIP. However, suspension magnetic effects (ac hysteresis) still remain and are a source of bias instability. Further investigation in this area is desirable. Relative to the application of the PIP to a body-mounted environment a design improvement that would be desirable is a redistribution of the pendulous mass of the float to reduce the instrument's anisoinertia coefficient (section 2.4.2).

5.4 Body-Mounted Test Package and Real-Time Algorithm Test Evaluation:

The major effort in this area through this reporting period was the development of: a strapdown gyro test package; supporting electronics (torque loops, wheel and suspension power supplies); computational algorithm capabilities and interfaces; and supporting test facilities and equipment. These were designed and assembled during the reporting period and are described in detail in Chapter 4. Currently they are going through functional checkout and system integration testing. In parallel with this activity, static and dynamic test concepts were developed (section 4.6) that included real-time computational algorithm and compensation evaluations. To satisfy the on-line computational requirements a small general-purpose DDP-516 was secured. Software development was initiated and basic "housekeeping" programs (interrupt servicing, executive, and teletype monitor) necessary for real-time operations were developed and debugged. Algorithm, compensation, and test evaluation programming are in a preliminary stage of development. Continuation of this test evaluation activity is highly recommended. Testing should include multi-axes and oscillatory rate environments with several operational algorithms. The results of the test activity is expected to yield hardware-software trade-off performance criteria that will provide a realistic basis for the design of advanced strapdown configurations for future spacecraft application.

APPENDIX A

Quaternions

Sir William Rowan Hamilton first defined the concept of the quaternion as an extension of three-dimensional vector algebra. A quaternion is a quadruple of real numbers written in a definite order to represent a scalar and a three-dimensional vector.

If we let λ and Λ be the scalars and $\bar{\rho}$ and $\bar{P}$ be the vectors of two quaternions q and Q, we may write the formula defining quaternion multiplication as:

$$qQ = (\lambda + \bar{\rho})(\Lambda + \bar{P}) \tag{A-1}$$

The product is another quaternion whose scalar is the product of the two scalars less the vector dot product; and whose vector part is the scalar of the first times the vector of the second, plus the scalar of the second times the vector of the first, plus the cross product of the two vectors.

$$qQ = (\lambda\Lambda - \bar{\rho} \cdot \bar{P} + \lambda\bar{P} + \Lambda\bar{\rho} + \bar{\rho} \times \bar{P}) \tag{A-2}$$

Quaternion multiplication is not commutative. This can be shown by forming the reverse product in (A-2) and noting that the sign of the cross-product term will change. The quaternion of transformation may be thought of as a representation of a rotation of a body frame with respect to an inertial frame. Visualize a rotation of the body frame about the inertial frame described by some angle α about the rotational axis $\bar{1}n$. Then a unit quaternion describing this rotation is defined as:

$$q = \cos \alpha/2 + \bar{1}n \sin \alpha/2 \tag{A-3}$$

and its conjugate which corresponds to the opposite rotation can be represented as:

$$q^* = \cos \alpha/2 - \bar{1}n \sin \alpha/2 \tag{A-4}$$

Notice that by the definition of a unit quaternion a constraint has been imposed such that the scalar squared plus the vector magnitude squared is equal to one.

A similarity transformation using the quaternion can be formed which will describe an arbitrary vector being transformed from the body frame into the inertial frame as:

$$\bar{v}^i = q\,\bar{v}^b\,q^* \tag{A-5}$$

where $\bar{v}^i$ is an arbitrary vector in the inertial frame and $\bar{v}^b$ is the equivalent vector in the body frame.

To determine the rate of change of the rotation quaternion we may visualize the body frame oriented with respect to a reference frame at some time t_o. The quaternion Q may then be thought of as representing this relative orientation. An arbitrary nonrotating vector is then defined and expressed in quaternion form. The relationship between the vector in the body and the reference frame at time t_o, using the similarity transform (A-5) is:

$$\bar{v}^i = Q\,\bar{v}^b_{t_o}\,Q^* \tag{A-6}$$

Over a Δt time interval the body frame will have rotated to some new orientation, and Q_1 now represents the relative body frame orientation. The relationship between the same arbitrary vector in the body and reference frame is:

$$\bar{v}^b_{(t_o+\Delta t)} = Q_1^*\,\bar{v}^i Q_1 \tag{A-7}$$

Note that the vector representation $\bar{v}$ is not changing in the inertial frame. Substituting (A-6) in (A-7) we obtain:

$$\bar{v}^b_{(t_o+\Delta t)} = Q_1^* Q\,\bar{v}^b_{t_o}\,Q^* Q_1 \tag{A-8}$$

The quaternion Q^*Q_1 therefore represents a rotation quaternion (q) of the body frame during the Δt interval and corresponds to:

$$q = Q^*Q_1 = \cos\frac{\omega\Delta t}{2} + \frac{\bar{\omega}^b}{\omega}\sin\frac{\omega\Delta t}{2} \tag{A-9}$$

where $\bar{\omega}^b$ represents the vector describing the body frame rotation during the Δt interval and ω is its scalar magnitude. Premultiplying (A-9) by Q yields:

$$Q_1 = Q\left(\cos\frac{\omega\Delta t}{2} + \frac{\bar{\omega}^b}{\omega}\sin\frac{\omega\Delta t}{2}\right) \tag{A-10}$$

We may define the rate of change of rotation as:

$$\dot{q} = \frac{Q_1 - Q}{\Delta t} \tag{A-11}$$

Substituting (A-10) into (A-11) and noting that Q was selected arbitrarily and can also be expressed as a generalized rotation quaternion (q) (that corresponds to the rotation of body frame with respect to the reference frame that resulted in this orientation), we obtain:

$$\dot{q} = \frac{q\left(\cos\frac{\omega\Delta t}{2} - 1 + \frac{\bar{\omega}^b}{\omega}\sin\frac{\omega\Delta t}{2}\right)}{\Delta t} \tag{A-12}$$

The differential equation can now be simplified from (A-12) by converting the trigonometric functions to their small angle approximations. This results in:

$$\dot{q} = (\dot{\lambda} + \dot{\bar{\rho}}) = 1/2\ q\ \bar{\omega}^b = q\Omega \qquad \text{(A-13)}$$

where Ω has the quaternion form $(0 + \frac{\bar{\omega}^b}{2})$ and $q = (\lambda + \bar{\rho})$.
By effecting the indicated quaternion multiplication (A-13) and by equating the vector and scalar we obtain

$$\dot{\lambda} = \frac{\bar{\omega}^b \cdot \bar{\rho}}{2} \qquad \text{(A-14)}$$

$$\dot{\bar{\rho}} = \frac{\lambda\bar{\omega}^b - \bar{\omega}^b \times \bar{\rho}}{2} \qquad \text{(A-15)}$$

Equation (A-13) can also be written in a matrix equation form:

$$[\dot{q}] = [\dot{\lambda}\ \dot{\rho}_x\ \dot{\rho}_y\ \dot{\rho}_z] = \frac{1}{2}\begin{bmatrix}\lambda\\ \rho_x\\ \rho_y\\ \rho_z\end{bmatrix}^T \begin{bmatrix}0 & \omega_x & \omega_y & \omega_z\\ -\omega_x & 0 & -\omega_z & \omega_y\\ -\omega_y & \omega_z & 0 & -\omega_x\\ -\omega_z & -\omega_y & \omega_x & 0\end{bmatrix} \qquad \text{(A-16)}$$

where $[\Omega]$ is the anti-symmetric matrix representation of the angular velocity vector in the body frame and $\dot{\rho}_1$, $\dot{\rho}_2$, $\dot{\rho}_3$ are the rates of change of the magnitude of the vector components.

Now we may define the Taylor series expansion of q to allow formulation of an iterative update method. (The quaternion equation form is used.)

$$q\ (t + \Delta t) = q(t) + \dot{q}(t)\,\Delta t + \ddot{q}(t)\,\frac{\Delta t^2}{2} + \dddot{q}(t)\,\Delta\frac{t^3}{6} + \ldots \qquad \text{(A-17)}$$

Applying the chain rule of differentiation and using (A-13) we obtain:

$$\dot{q} = q\Omega;\ \ddot{q} = q\dot{\Omega} + \dot{q}\Omega = q(\dot{\Omega} + \Omega\Omega);$$
$$\dddot{q} = q(\ddot{\Omega} + \dot{\Omega}\Omega + 2\ \Omega\dot{\Omega} + \Omega^3) \qquad \text{(A-18)}$$

To use (A-18) to propagate the quaternion, it is necessary to find the relationship between the quantized $\Delta\theta$ outputs of the gyro loop and the Ω quaternion.

The $\Delta\theta$ increments of a single gyro can be defined in terms of equivalent body angular rates by expanding the incremental angle output $\theta(\Delta t)$ occurring at t from t to $t + \Delta t$ and by expanding the prior incremental angle output $\theta^*(\Delta t)$ from t to $t-\Delta t$. If $\omega(t)$ is represented by ω the results of these Taylor series expansions are:

$$\theta(\Delta t) = \omega\Delta t + \frac{\dot{\omega}\Delta t^2}{2} + \frac{\ddot{\omega}\Delta t^3}{6} + \ldots \qquad \text{(A-19)}$$

$$\theta^*(\Delta t) = -\omega\Delta t + \frac{\dot{\omega}\Delta t^2}{2} - \frac{\ddot{\omega}\Delta t^3}{6} + \ldots$$

These expansions could equally as well be defined as vector representations of ϖ, If we generalize them in this form (recall that Ω in (A-18) is the quaternion representation of ϖ), we may directly substitute the solutions for ϖ, $\dot{\varpi}$, and $\ddot{\varpi}$ (expressed in the quaternion form as Ω, $\dot{\Omega}$, and $\ddot{\Omega}$, respectively) as determined from substituting (A-19) into (A-18). Manipulation and substitution of these terms yields the exact solution of the third order quaternion in terms of the gyro loop $\Delta\theta$ increments:

$$q(t + \Delta t) = q(t)\ U(t, \Delta t) \qquad \text{(A-20)}$$

where

$$U(t + \Delta t) = \left[1 - 1/2\left(\frac{\bar{\theta}}{2} \cdot \frac{\bar{\theta}}{2}\right) + \frac{\bar{\theta}}{2} - \frac{1}{6}\left(\frac{\bar{\theta}}{2} \cdot \frac{\bar{\theta}}{2}\right)\frac{\bar{\theta}}{2} - \frac{1}{6}\left(\frac{\bar{\theta}^*}{2} \times \frac{\bar{\theta}}{2}\right)\right] \qquad \text{(A-21)}$$

APPENDIX B

Effects of Double Pulsing on Count Stability

Assume the ΔV output from a PM PIP is a train of pulses consisting of single pulses and pulse pairs. This ΔV pulse train is fed into a preset section of a counter which is used to control gating circuit on the counter accumulator. A precise time base (interrogator pulses) is then routed into the accumulator gate and a count is accumulated during the time the gate is open. The count represents time for the preset numer of ΔV's to occur. A count instability exists if the number of interrogator pulses accumulated for an equal number of ΔV's taken at random along the ΔV pulse train can vary for a constant input.

The test count relationship for an instrument subjected to a constant input is defined by Eq (B-1).

$$SF(X) - A_{in} N - C\theta = 0 \qquad (B\text{-}1)$$

where

- SF is the scale factor of the unit (expressed in cm/sec per ΔV pulse)
- X is the preset number of ΔV's
- A_{in} is the equivalent velocity input per interrogation pulse interval for a constant specific-force test orientation (expressed in cm/sec per interrogator pulse)
- N is the accumulated interrogator count
- C is the instrument viscous-damping coefficient
- θ is the net rotation of the float through the fluid during the interval in which the count is taken.

Since the product of the scale factor and the preset number of ΔV's is a constant, we note that the net change in rotation of the float represents a storage of data within the instrument during the count interval. This storage may be expressed as some equivalent percentage of the input velocity.

For a ΔV pulse train that exhibits the double-pulsing, three different interrogator counts may result as a function of the test start and stop conditions. They correspond to the present gate control operation which:

a) starts on a single ΔV or the first ΔV of a pair of ΔV's and ends on a single ΔV or the first ΔV of a pair of ΔV's,

b) starts on a single ΔV or the first ΔV of a pair of ΔV's and ends on the second ΔV of a pair of ΔV's,

c) starts on the second ΔV of a pair of ΔV's and stops on a single ΔV or the first ΔV in a pair of ΔV's.

For case (a) the test starts and stops with the float exactly at the same dynamic condition, $C\theta = 0$.

From Eq (B-1) it is evident that, if there is no storage, the test count is equal to

$$N = X \frac{SF}{A_{in}} \tag{B-2}$$

For condition (b) the float has received two consecutive torque pulses at the end of the count cycle and, as a result, has stored some increment of velocity:

$$k(SF) = + C\theta \tag{B-3}$$

Similarly, for condition (c) the float started with an increment stored velocity due to the previous torque pulse which existed just before the count was initiated and

$$k(SF) = - C\theta \tag{B-4}$$

The k is necessary to account for the fact that the input acceleration has acted for one interrogation pulse length in opposition to the applied ΔV torque pulse,

$$k = \frac{SF - A_{in}}{SF} \tag{B-5}$$

Stated another way, each ΔV pulse represents $\frac{SF}{A_{in}}$ interrogator pulses.

If we solve for N in Eq (B-1) and substitute the (C) term for conditions (b) and (c), the count shifts are

$$N = \frac{(SF) X \pm (SF - A_{in})}{A_{in}} \tag{B-6}$$

The output count variation (δN) from the no-storage test count Eq (B-2) corresponds to

$$\begin{aligned} &\text{case (b)} \quad \delta N = \frac{+ SF}{A_{in}} - 1 \\ &\text{case (c)} \quad \delta N = \frac{-SF}{A_{in}} + 1 \end{aligned} \tag{B-7}$$

Thus, if SF were scaled for a 10g capability and a 1g input were used, an 18-count deviation from the true count would occur.

REFERENCES

1. North American Rockwell, Space Division Staff, Final Report, Contract NAS-8-18025, A Study of Manned Planetary Flyby Missions Based on Saturn/Apollo Systems, August 1967.

2. The Boeing Company, Aerospace Group Staff, Phase 1 Briefing Report, Integrated Manned Interplanetary Spacecraft Concept Definition, 18 April 1967.

3. Battin, R. H., Astronautical Guidance, McGraw Hill Book Company, Inc., New York, 1964.

4. Martin, F. H., "Closed Loop Near Optimal Steering for Class of Space Missions", MIT ScD Thesis, May 1965.

5. Phillion, P. J., "Translunar Injection from Earth Parking Orbit", MIT Instrumentation Laboratory Guidance Performance Analysis Memo 504 #2-67, 10 January 1967.

6. Morth, R., Reentry Guidance for Apollo, MIT Instrumentation Laboratory Report R-532, January 1966.

7. Gilmore, J. P., A Non-orthogonal Gyro Configuration, MIT/IL Report T-472, January 1967.

8. Otten, D. D., Body Fixed, Three Axis Reference System Study, TRW Report 4499-6007-R0000, May 1966.

9. Reichenbacher, G. J., Jr., Multiplexing Scheme for Pulsed Torqued Inertial Components, MIT/IL Report T-491, September 1967.

10. Miller, J. and J. Feldman, Apollo Guidance, Navigation, and Control System Gyro Reliability, E-2141, June 1967.

11. Project Apollo Test Checkout Plan, Spacecraft 101 Launch Operations, FO-K-0203-SC101, Kennedy Space Center, May 1968.

12. Lunar Module for Apollo, LM Test and Checkout Plan for LM-3 Mission AS-503-LPL-673-1b, Kennedy Space Center NASA, Revised May 1968.

REFERENCES, (Cont.)

13. Webster's Seventh New Collegiate Dictionary, G. & C. Merriam Company, Springfield, Mass., 1963.

14. Control, Guidance, and Navigation for Advanced Manned Missions, R-600 (Vol II), Multiprocessor Computer Subsystem, January 1968.

15. Bumstead, R. M., and W. E. VanderVelde, Navigation and Guidance Systems Employing a Gimballess IMU, MIT/IL Report R-412, October 1963.

16. Broxmeyer, C., et. al., Vehicle-Fixed Component Inertial Guidance System Study, Final Report, AD617528, Raytheon S & ID, July 1964.

17. Ball, W. F., Strapped-Down Inertial Guidance, The Coordinate Transformation Updating Problem, U. S. Naval Ordinance Test Station, April 1967.

18. McKern, R. A., A Study of Transformation Alogrithms for Use in a Digital Computer, MIT/IL Report T-493, January 1968.

19. Otten, D. D., Body Fixed, Three Axis Reference System Study, Phase I Final Report, TRW #4499-6007-R0000, 2 May 1966.

20. Wiener, T. F., "Theoretical Analysis of Gimballess Inertial Reference Equipment Using Delta-Modulated Instrument", ScD Thesis, MIT Dept. of Aeronautics and Astronautics Engineering, (MIT Instrumentation Laboratory Report No. T-300), March 1962, p. 109.

21. Hayum, R., "Compensation of a Digital Integrating Accelerometer", S. M. Thesis, MIT Dept. of Electrical Engineering (MIT Instrumentation Laboratory Report No. T-209A), June 1959.
(The principal contribution is the concept of compensating to a pure integration, p. 29.)

22. Ibid., p. 49, pp 63-74.

23. Lory, C. B., "Compensation of Pulse-Rebalanced Inertial Instrument", S. M. Thesis, MIT Department of Aeronautics and Astronautics Engineering, (MIT Instrumentation Report No. T-485), January 1968.

24. Cooper, R. and J. Feldman, Inertial Components Reliability and Population Statistics, E-2252, March 1968.

25. Gilinson, P. J., W. C. Denhard, and R. Frazier, A Magnetic Support for Floated Inertial Instruments, MIT, Sherman M. Fairchild Publications Fund Paper No. FF-27, May 1960.